The Hashemite Kingdom of Jordan

Scientific Research Support Fund

The Hashemite University

JJEES

Jordan Journal of Earth and Environmental Sciences

Volume (17) Number (3)

Cover photo © Prof. Eid Tarazi

JJEES is an International Peer-Reviewed Research Journal

ISSN 1995-6681

jjees.hu.edu.jo

September 2026

Jordan Journal of Earth and Environmental Sciences (JJEES)

JJEES is an International Peer-Reviewed Research Journal, Issued by Deanship of Scientific Research, The Hashemite University, in corporation with, the Jordanian Scientific Research Support Fund, the Ministry of Higher Education and Scientific Research.

Submission address:

Manuscripts should be submitted electronically to the following e-mail:

jjees@hu.edu.jo

For more information and previous issues:

www.jjees.hu.edu.jo

The Hashemite Kingdom of Jordan

Scientific Research & Innovation Support Fund

The Hashemite University

Jordan Journal of Earth and Environmental Sciences

JJEES

An International Peer-Reviewed Scientific Journal

Financed by the Scientific Research & Innovation Support Fund

Volume 17 Number (3)

https://jjees.hu.edu.jo/

ISSN 1995-6681

The so-called "Lot's Wife statue," located within the Dead Sea Basin of the Jordan Rift Valley, consists of recent deposits of the Lisan Formation of Quaternary age. These deposits overlie older strata of the Nubian Sandstone sequence, including the Umm Ishrin Sandstone Formation of Cambrian age.
Photograph courtesy of Prof. Eid Tarazi, 2025.

JJEES
Jordan Journal of Earth and Environmental Sciences

JJEES

Jordan Journal of Earth and Environmental Sciences

JJEES (2026) 17 (3): 287-292
ISSN 1995-6681

Ionic Strength Prediction Using Selected Physicochemical Properties of Calcareous Soils: A Case Study from Al-Hashimya Area, Zarqa Governorate, Jordan

Mohammed Salahat* and Kholoud Mashal

Department of Land Management and Environment, Prince El-Hassan bin Talal Faculty for Natural Resources and Environment, The Hashemite University, Zarqa, Jordan

Received on 24 September 2025; Accepted on 26 January 2026

Abstract

Accurate estimation of ionic strength (I) is essential for predicting soil solution chemistry and ion interactions in calcareous soils, where carbonate equilibria dominate. Direct measurement of ionic strength requires full ionic analysis, which is costly and time-consuming; therefore, developing reliable, locally calibrated predictive relationships with easily measured soil properties is of practical value. This study aimed to establish empirical models linking ionic strength with electrical conductivity (EC) and sodium adsorption ratio (SAR) in calcareous soils from the Al-Hashimya area, Zarqa Governorate, Jordan. Forty-three surface soil samples (0–15 cm) from urban areas were analyzed for pH, EC, major cations and anions, and $CaCO_3$ content. Ionic strength was computed from measured ion concentrations and compared with EC-based models using linear and multiple regression. Results revealed that EC ranged from 1.3 to 63.8 dS m^{-1} and I from 0.025 to 0.94 mol L^{-1}, with a strong linear correlation ($R^2 = 0.91$) between EC and I. The best-fit model for these calcareous soils was $I = 0.0304 + 0.0155\ EC_{25}$, which yielded an R^2 22% higher than the widely used Griffin and Jurinak (1973) equation, reflecting the higher charge density and ion pairing characteristic of carbonate-rich systems. Incorporating SAR and key ionic species (Na^+, Cl^-, Ca^{2+}, Mg^{2+}, and HCO_3^-) further improved model performance ($R^2 > 0.95$). The locally calibrated model provides a practical tool for soil salinity assessment and irrigation management in the Al-Hashimya region, while highlighting the broader need for composition-aware ionic-strength calibrations across diverse calcareous soil systems.

Keywords: *soil salinity, ionic strength, calcareous soils, SAR, $CaCO_3$, Al-Hashimya, Zarqa*

1. Introduction

Calcareous soils are those soils containing abundant free $CaCO_3$ and often a calcic horizon. They are widespread across the world's drylands and are thought to make up more than one-third of the earth's land surface, according to FAO (2016). In the World Reference Base (WRB), such soils commonly fall within Calcisols, which are defined (among other criteria) by secondary carbonate enrichment and a calcium carbonate equivalent ≥ 15% over ≥ 15 cm of the profile. The amount of $CaCO_3$ in these soils can range from hardly detectable to 95% (Marschner, 1995). The prevalence of calcareous materials in arid and semi-arid regions reflects restricted leaching and frequent pedogenic carbonate accumulation, leading to alkaline pH, Ca–Mg–HCO_3-dominated solutions, and distinctive nutrient and physical behavior. The high accumulation of carbonates influences soil characteristics linked to plant growth, such as soil water relations and the availability of plant nutrients, as discussed extensively by Marschner (1995) and the contemporary soil chemistry literature.

Ionic strength (I) is the most critical attribute governing electrostatic interactions in soil solutions, and activity coefficients translate concentrations into thermodynamic activities. Accurate activities support predictions of mineral solubility, metal speciation, surface complexation/adsorption, and ion-exchange equilibria that regulate nutrient availability and contaminant mobility in calcareous settings.

Directly computing I from full-ion analysis is labor- and cost-intensive, particularly when routine monitoring or spatial mapping is required. By contrast, electrical conductivity (EC) is quick to measure, widely standardized (at 25 °C), and directly connected to salinity assessment in soil science and irrigation practice (e.g., ECe from saturated paste extracts and in situ ECa surveys). This has motivated long-standing efforts to infer comprehensive solution chemistry—including total dissolved solids, major-ion loads, and ionic strength—from EC. An influential contribution is the work of Griffin & Jurinak (1973), which linked ionic strength linearly to EC in natural waters and soil extracts. Variants of this relation (e.g., $I \approx 0.0127 \times EC_{25}$, with I in mol L^{-1} and EC in dS m^{-1} at 25 °C) remain embedded in practice and guidance. However, such calibrations are empirical and therefore sensitive to solution composition and temperature, with the original datasets dominated by monovalent Na–Cl systems, and do not account for the distinctive carbonate-rich composition of calcareous soil solutions.

Soil physicochemical characteristics chemistry, such as EC, SAR, and ionic strength, which are significant factors

* Corresponding author e-mail: mdsalahat@hu.edu.jo

influencing soil chemical characteristics, including clay dispersion and flocculation (Emerson, 1977; Goldberg & Forster, 1990; Miller et al., 1990). The osmotic stress between clay particles decreases as the electrolyte concentration rises, until it reaches a point where short-range van der Waals forces take control and lead to flocculation.

Despite the widespread occurrence of calcareous soils across drylands and their carbonate-dominated chemistry, composition-aware calibrations that translate routine measurements (e.g., EC, SAR, pH) into reliable estimates of ionic strength remain scarce in the peer-reviewed soil literature.

This study has three specific objectives:

1. To establish empirical, calibration-based relationships linking ionic strength (I) with electrical conductivity (EC) in calcareous soils of the Al-Hashimya area, Zarqa Governorate, Jordan;
2. To evaluate whether incorporating sodium adsorption ratio (SAR) and key ion species (Na^+, Cl^-, Ca^{2+}, Mg^{2+}, HCO_3^-) improves predictive accuracy beyond EC-alone models;
3. To provide a practical, composition-aware tool for rapid ionic strength estimation to support irrigation management and soil salinity assessment in the region.

2. Materials and Methods

2.1 Study area and sampling

Forty-three (n = 43) urban surface soils (0–15 cm) were collected across the Al-Hashimya area in the Zarqa Governorate, Jordan. The study was limited to urban surface areas to maximize accessibility and representativeness within a constrained geographic scope. Sites were purposively selected to span a wide range of pH, $CaCO_3$ content, and salinity to ensure adequate representation of the diversity of soil solution chemistry typical of the region. At each site, several scoops within ~10 m were composited, placed in labeled, airtight bags, and kept shaded during transport. In the lab, samples were air-dried at room temperature, gently disaggregated by hand, and passed through a 2-mm sieve. Subsamples for alkalinity and ion analysis were sealed in airtight containers to limit CO_2 exchange until extraction, following established soil salinity protocols (Rhoades, 1996; Corwin & Yemoto, 2017).

2.2 Saturated paste extract and analytical procedures

Saturated soil pastes were prepared and extracted under vacuum following USDA standard methodology (Richards, 1954). pH and electrical conductivity (EC) were measured immediately after extraction at ambient laboratory temperature and subsequently normalized to 25 °C using the standard temperature correction function. EC values are reported at 25 °C (EC_{25}). Filtered extracts were analyzed for Na^+, K^+, Ca^{2+}, Mg^{2+}, Cl^-, HCO_3^-, and SO_4^{2-}. Cations were measured by Atomic Absorption Spectrophotometry (AAS). Chloride and sulfate were determined by ion chromatography following standard EPA (1993) methods.

All electrical conductivity measurements throughout this manuscript refer exclusively to the electrical conductivity of saturated paste extracts normalized to 25 °C (EC_{25}). This standardization is essential because the validity of EC-I relationships depends critically on the extraction method and temperature normalization.

2.3 Soil and solution parameters

The values obtained from ion analysis were used to calculate two key descriptors:

Sodium Adsorption Ratio (SAR) following Richards (1954) and Ayers & Westcot (1985):

$$SAR = [Na^+] / \sqrt{(([Ca^{2+}] + [Mg^{2+}]) / 2)} \quad (1)$$

where cation concentrations are in mmolc L^{-1}.

Ionic Strength (I):

$$I = ½ \Sigma c_i z_i^2 \quad (2)$$

where z_i and c_i are the charge and molar concentration of the ionic species (Sposito, 2016), measured in mol L^{-1}.

2.4 Carbonate system speciation and activity coefficient calculations

The measurement of CO_3^{2-} directly in soil solution is analytically challenging due to its rapid equilibration with atmospheric CO_2 and its instability during storage and transport. Therefore, CO_3^{2-} concentrations were calculated from measured pH and HCO_3^- using the Henderson-Hasselbalch equation and carbonate equilibrium constants for the bicarbonate buffer system at 25 °C:

$$pH = pKa2 + \log([CO_3^{2-}]/[HCO_3^-]) \quad (3)$$

where, pKa2 = 10.33 (at ionic strength ≈ 0.1 mol L^{-1} and 25 °C; Sposito, 2016).

CO_3^{2-} was calculated as:

$$[CO_3^{2-}] = [HCO_3^-] \times 10^{(pH - pKa2)} \quad (4)$$

Assumptions underlying this approach:

1. Soil solutions are assumed to be in equilibrium with respect to the carbonate buffer system (Richards, 1954).
2. A fixed pCO_2 is not imposed; rather, the Henderson-Hasselbalch equation relies on the measured pH and HCO_3^- concentration, implicitly accounting for the solution's CO_2 buffering capacity (Sposito, 2016).
3. Deviation from equilibrium due to CO_2 loss during sampling was minimized by sealing subsamples in airtight containers until extraction and analysis, following established protocols (Rhoades, 1996).

Activity coefficients for all ionic species were calculated using the Davies equation (Davies, 1962) with ionic strength computed from Equation (2), following standard practice in soil chemistry (Sposito, 2016).

2.5 Modeling the EC_{25}→I relationship

To translate routine EC measurements into ionic strength, we evaluated:

- M_0: $I = 0.0127 \times EC_{25}$ (Griffin & Jurinak, 1973) as a historical baseline;

- M_1: $I = \beta_0 + \beta_1 EC_{25}$ (linear model, EC-only);
- M_2: $I = \beta_0 + \beta_1 EC_{25} + \beta_2 SAR$ (linear model with SAR);
- M_3: Multiple regression incorporating ion species and $CaCO_3$ content.

Models were fit by ordinary least squares (OLS) with robust standard errors; performance was summarized with R^2, root mean square error (RMSE), mean absolute error (MAE), and bias.

3. Results and Discussion

3.1 Soil salinity, sodicity, and basic chemistry

The electrical conductivity of the soil paste extract (EC_{25}) spanned nearly two orders of magnitude (1.3–63.8 dS m^{-1}), while pH ranged from slightly acidic to moderately alkaline (6.7–8.5). Sodium dominated the soluble cations (up to ~35 meq L^{-1}), followed by Ca^{2+}, whereas Cl^- exceeded SO_4^{2-} among the anions. Summary statistics (minimum, maximum, and coefficient of variation, CV) are reported in Table 1. The high coefficients of variation in EC_{25} (98.71%) and SAR (113.03%) indicate marked spatial heterogeneity typical of calcareous, irrigated arid soils where localized irrigation patterns, soil parent material variation, and differential salt accumulation create complex salinity distributions.

Table 1. Descriptive statistics of key soil-solution properties

Property	Min	Max	CV (%)
Ph	6.71	8.50	5.27
EC_p (dS m^{-1})	1.30	63.80	98.71
SAR	0.75	51.85	113.03
Ionic strength, I (mol L^{-1})	2.5×10^{-2}	0.94	91.72
Total anions	2.2×10^{-2}	0.66	94.11
Total cations	9.0×10^{-3}	0.75	119.10
Ion activity product, IAP = $a(Ca^{2+})\cdot a(CO_3^{2-})$	2.0×10^{-5}	3.1×10^{-3}	110.53
$CaCO_3$ (%)	26.64	62.41	23.74

3.2 Saturation state with respect to calcite

At 25 °C, the thermodynamic solubility product for calcite is:

$$Ksp = [Ca^{2+}] \times [CO_3^{2-}] = 10^{-8.42} \quad (5)$$

The saturation index (SI) indicates the stability of a mineral in a particular solution:

$$SI = \log_{10}(IAP/Ksp) \quad (6)$$

where IAP is the ion activity product. SI > 0 indicates supersaturation and a tendency toward calcite precipitation, whereas SI < 0 indicates undersaturation and potential dissolution.

The measured IAP range (2.0×10^{-5} to 3.1×10^{-3}) far exceeds Ksp, implying SI ≫ 0 and supersaturation with respect to calcite—consistent with carbonate-rich soils where high pH and low pCO_2 elevate CO_3^{2-} activities. Supersaturation indicates a tendency for secondary $CaCO_3$ precipitation and pedogenic carbonate accumulation. This finding explains the high $CaCO_3$ content (26.64–62.41%) observed in these soils and demonstrates the importance of understanding carbonate equilibria for predicting soil chemical processes, including the formation and stabilization of secondary carbonate horizons typical of calcareous soils in arid regions.

3.3 Linking ionic strength to EC and solution composition

Because ionic strength (I) governs activity coefficients via electrostatic screening, many practical models relate I to the easily measured EC. For natural waters and soil extracts dominated by monovalent ions (e.g., Na^+–Cl^- systems), the classic Griffin & Jurinak relationship is $I = 0.0127 \times EC_{25}$. This model was established using datasets that do not adequately represent carbonate-dominated systems with high divalent-cation content.

In the calcareous soils of this study, the best linear fit between measured I and EC_{25} was:

$$I\ (\text{mol L}^{-1}) = 0.0304 + 0.0155\ EC_{25}\ (\text{dS m}^{-1}),\ R^2 = 0.910 \quad (7)$$

Table 2. Linear relationships between ionic strength and EC from literature and this study

Relation	Reference	The relation between actual and predicted
I=0.016×EC I in mol/L and EC in dS/m	Ponnamperuma et al., (1966)	y = 3.5108x - 0.0243 R^2 = 0.9098
I= 0.0127×EC I in mol/L and EC in dS/m	Griffin and Jurinak (1973)	y = 0.7607x - 0.0053 R^2 = 0.9098
Is = 0.0446EC-0.000173 I in mol/L and EC in mS cm^{-1}	Gillman and Bell (1978)	y = 2.6097x - 0.0182 R^2 = 0.9098
I = 0.0304+0.0155*EC_{25} I in mol/L and EC in dS/m	Present study	y = 0.907x + 0.0241 R^2 = 0.9098

The slope of Eq. (7) is slightly higher than that of Griffin–Jurinak, reflecting the higher average charge density (greater divalent Ca^{2+} and Mg^{2+} content) and ion pairing in carbonate systems. Formation of ion pairs such as $CaHCO_3^+$ reduces the number of free ions in solution relative to total dissolved solids, affecting the EC-I relationship. This mechanistic insight explains why composition-aware models are necessary for accurate ionic strength prediction in systems with significant carbonate buffering.

3.4 Ionic composition and correlations

Model M_1 achieves 22.3% higher R^2 compared to the historical M_0 (Griffin & Jurinak, 1973) model, reducing RMSE by 51.6% (from 0.128 to 0.062 mol L^{-1}). The addition of SAR in M_2 provides marginal further improvement (ΔR^2 = 0.016; 2% increase), reducing RMSE from 0.062 to 0.054 mol L^{-1}. For rapid field or routine laboratory predictions when SAR measurements may not be readily available, the simpler M_1 (EC-only) model offers substantial practical improvements over existing methods. However, when SAR and ion speciation data are available, model M_2 offers the highest predictive accuracy.

Table 3. Performance metrics for different models

Model	Description	R^2	RMSE (mol L^{-1})	MAE (mol L^{-1})	Bias (mol L^{-1})
M_0	$I = 0.0127 \times EC_{25}$ (Griffin & Jurinak, 1973)	0.744	0.128	0.095	-0.032
M_1	$I = 0.0304 + 0.0155\ EC_{25}$ (locally calibrated linear)	0.910	0.062	0.048	+0.008
M_2	$I = 0.0298 + 0.0149\ EC_{25} + 0.0031\ SAR$ Linear with SAR	0.926	0.054	0.041	+0.003
M_3	$I = f(EC_{25}, SAR, Cl^-, HCO_3^-, Na^+, Ca^{2+}, Mg^{2+}, \%CaCO_3)$	0.958	0.018	0.012	+0.001

3.5 Ionic composition and correlations

Pearson correlations (Table 4) underline EC_{25}'s strong association with key soluble ions. The exceptionally high EC-Cl^- correlation ($r = 0.98$) indicates that chloride is the dominant anion controlling solution salinity in these soils, typical of salinized arid-region soils where irrigation with marginally saline water concentrates chloride. The strong EC-Na^+ correlation ($r = 0.93$) reflects co-mobilization of sodium with chloride (sodic-saline type salinity pattern). In contrast, EC shows moderate correlations with Ca^{2+} ($r = 0.65$) and Mg^{2+} ($r = 0.78$), indicating that divalent cations contribute substantially to ionic strength via their charge-squared weighting in Equation (2), even though their molar concentrations are lower than Na^+.

CEC and organic matter (OM%) show weak associations with EC_{25} in this dataset, consistent with salinity being driven primarily by the dissolved ion pool rather than by exchange capacity at the sampled spatial scale (urban surface soils with variable land use and irrigation history).

Table 4. Pearson correlations for selected soil parameters and ions

	pH	EC_{25}	Cl^-	HCO_3^-	Na^+	Ca^{2+}	Mg^{2+}	I calculated
pH	1.00							
EC_{25}	-0.46	1.00						
Cl^-	-0.48	0.98	1.00					
HCO3-	-0.013	0.29	0.27	1.00				
Na	-0.46	0.93	0.94	0.15	1.00			
Ca	-0.49	0.65	0.63	0.09	0.75	1.00		
Mg	-0.32	0.78	0.77	0.58	0.70	0.53	1.00	
I calculated	-0.47	0.95	0.95	0.41	0.94	0.76	0.87	1.00

The correlation of I with EC_{25} ($r = 0.95$) validates the strong predictive relationship captured by Equation (7) and justifies the use of easily measured EC as a surrogate for ionic strength in this calcareous-soil context.

3.6 Multiple regression incorporating ion species and carbonate content

Incorporating composition further improves prediction; multiple regression analysis identified Cl^-, HCO_3^-, Na^+, Ca^{2+}, Mg^{2+}, and $CaCO_3$% as significant covariates. The resulting model is:

$$I = -2.4\times10^{-2} + 1.7\times10^{-3}\ EC_{25} + 4.3\times10^{-4}[Cl^-] + 2.1\times10^{-3}[HCO_3^-] + 5.0\times10^{-4}[Na^+] + 9.1\times10^{-4}[Ca^{2+}] + 1.1\times10^{-3}[Mg^{2+}] + 5.6\times10^{-4}\ \%CaCO_3 \quad (8)$$

where,

- I: ionic strength (mol L^{-1})

- EC_{25}: electrical conductivity at 25 °C (dS m^{-1})

- $[Cl^-]$, $[HCO_3^-]$, $[Na^+]$, $[Ca^{2+}]$, $[Mg^{2+}]$: ion concentrations (mol L^{-1})

- $\%CaCO_3$: calcium carbonate content (percent by mass)

Note on Equation (8) application: All ion concentrations must be expressed in mol L^{-1}. Concentrations measured in other units (mmol L^{-1}, meq L^{-1}, mg L^{-1}) must be converted to mol L^{-1} using appropriate molecular weights before substitution into the equation.

This model achieves $R^2 > 0.95$, providing high predictive accuracy. The dominance of Cl^- and HCO_3^- coefficients reflects the importance of the primary dissolved salt composition in determining ionic strength through charge-concentration relationships. While pH, K^+, CEC, and OM were tested in the multiple regression, they were removed during model selection, indicating they do not significantly improve the prediction once major ion concentrations are accounted for.

3.7 Application of the derived I–EC model in spatial prediction

The locally calibrated ionic strength model was applied to interpolated EC values across the study area using ordinary kriging spatial prediction. EC values were interpolated to a regular grid using sample-based kriging with an exponential semivariogram model. Subsequently, the derived I-EC relationship [Eq. (7)] was applied to all interpolated EC grid values to generate spatially explicit predictions of ionic strength distribution.

The spatial analysis reveals distinct zones of high ionic strength ($I > 0.6$ mol L^{-1}) concentrated in the northeastern quadrant of the study area, corresponding to regions with the highest EC values. Moderate-salinity zones ($0.3 < I < 0.6$ mol L^{-1}) form a transition band, while low-salinity areas ($I < 0.3$ mol L^{-1}) occur predominantly in western and southern portions of the study area. This spatial heterogeneity reflects local variations in irrigation practices, soil parent material composition, and hydrogeological factors driving salt accumulation.

The spatial distribution of ionic strength directly informs targeted salinity management strategies. High ionic strength zones require the following practices:

1. Enhanced irrigation scheduling and salt leaching
2. Selection of salt-tolerant crop varieties
3. Potentially, separate water management protocols

Low-salinity zones may support a wider range of crops with minimal salinity constraints. This practical application demonstrates the utility of the locally calibrated I-EC model for region-specific irrigation planning and soil amendment strategies.

3.8 Study limitations and generalizability

This study has several important limitations that should be acknowledged:

1. Geographic scope: Sampling was limited to the urban Al-Hashimya area, Zarqa Governorate, Jordan. Results represent only surface soils (0–15 cm) from this localized region and cannot be directly generalized to calcareous soils in other geographic areas or different soil depths without independent validation.
2. Soil type specificity: The derived models are calibrated for the distinctive ionic composition of these particular soils (dominated by Na^{+}-Cl^{-} salinity with significant carbonate buffering). Different calcareous soil systems with alternative dominant salt compositions (e.g., Ca^{2+}- SO_4^{2-} systems) may require separate calibrations.
3. Model validation: The models presented are based on a single dataset (n = 43 samples) from one time period. External validation using independent samples from the same region, as well as comparison with other calcareous-soil regions, is recommended before widespread practical application.
4. Practical application scope: While Eq. (7) (M_1: simple EC-only model) provides substantial improvement over the Griffin & Jurinak (1973) universal equation, its use should be limited to the Al-Hashimya region where it was calibrated. Application to other regions should be preceded by local model development using the methodology described here.

Despite these limitations, this study provides:

- A methodological framework for developing composition-aware I-EC calibrations in carbonate-dominated systems
- Quantitative evidence that local calibrations substantially improve ionic strength prediction
- A practical tool specifically applicable to irrigation management in the Zarqa region

4. Conclusions

For calcareous soils in the Al-Hashimya area (Zarqa Governorate, Jordan), the locally calibrated model provides superior predictive accuracy compared to the widely applied Griffin & Jurinak (1973) equation, yielding a 22% improvement in explanatory power and reducing prediction error (RMSE) by 52%. This substantial improvement reflects the higher divalent-cation content and carbonate-induced ion pairing characteristic of these Zarqa region soils.

Incorporation of key ion species (Cl^{-}, HCO_3^{-}, Na^{+}, Ca^{2+}, Mg^{2+}) and $CaCO_3$ content further refined predictions to $R^2 > 0.95$, providing maximum predictive accuracy when complete ion analysis is available. For routine field applications where only EC and SAR are measured, adding SAR to the simple EC model (M_2) yields a marginal improvement ($\Delta R^2 = 0.016$) and may not always justify the additional measurement effort, depending on available laboratory resources.

The practical application of this locally calibrated model to irrigation management in arid regions is demonstrated through the spatial prediction of ionic strength distribution across the study area. The methodology presented here provides a template for developing similar composition-aware I-EC calibrations in other calcareous-soil regions, emphasizing that reliable ionic-strength prediction requires region-specific calibration rather than relying on universal equations that do not account for local compositional patterns.

References

Ayers, R. S., & Westcot, D. W. (1985). Water quality for agriculture. FAO Irrigation and Drainage Paper 29. Food and Agriculture Organization of the United Nations, Rome.

Corwin, D. L., & Yemoto, K. (2017). Salinity: Electrical conductivity and total dissolved solids. In E. A. Paul (Ed.), Soil microbiology, ecology and biochemistry (4th ed., pp. 417–435). Academic Press.

Davies, C. W. (1962). Ion Association. Butterworths, London.

Day, G. M., & Nightingale, H. I. (1984). Water-quality changes in dumpsites and landfills. Journal of Geotechnical Engineering, 110(2), 222–242.

Elgabaly, M. M. (1973). Soil and water salinity and the management of salt-affected soils. In B. Yaron, E. Kafkafi, & E. Sternberg (Eds.), Arid zone irrigation (pp. 235–258). Springer-Verlag.

Emerson, W. W. (1977). Physical properties of soils with particular reference to water relations and tilth. Soil Research, 15(2), 157–166.

EPA (U.S. Environmental Protection Agency). (1993). Methods for the determination of inorganic substances in environmental samples (EPA Method 300.0, Revision 2.1). National Exposure Research Laboratory, Cincinnati, OH.

FAO (Food and Agriculture Organization). (2016). Status of the world's soil resources: Main report. FAO, Rome.

Gillman, G. P., & Bell, L. C. (1978). The relationship between soil solution properties and soil physical and chemical properties. Australian Journal of Soil Research, 16(3), 331–343.

Goldberg, S., & Forster, H. S. (1990). Flocculation of reference clays and arid-zone soil clays. Soil Science Society of America Journal, 54(3), 714–718.

Griffin, R. A., & Jurinak, J. J. (1973). Estimation of activity coefficients from the electrical conductivity of natural aquatic systems and soil extracts. Soil Science, 116(1), 26–30.

Gustafson, H., & Behrman, A. S. (1939). Determination of total dissolved solids in water by electrical conductivity. Industrial & Engineering Chemistry (Analytical Edition), 11(6), 305–307.

Lewis, E. L. (1980). The Practical Salinity Scale 1978 and its antecedents. IEEE Journal of Oceanic Engineering, 5(1), 3–8.

Lind, C. J. (1970). Electrical conductivity of some standard solutions. Journal of Chemical & Engineering Data, 15(4), 499–502.

Lystrom, D. J., Rinella, F. A., & Knox, W. (1978). Definition of regional relationships between dissolved solids and specific conductance, Susquehanna River basin, Pennsylvania and New York. Journal of Research of the U.S. Geological Survey, 6(4), 541–545.

Marschner, H. (1995). Mineral nutrition of higher plants (2nd ed.). Academic Press.

McNeil, V. H., & Cox, M. E. (2000). Relationship between conductivity and analyzed major ions in Queensland streams: Application for resource monitoring and boundary classification. Hydrology and Earth System Sciences, 4(1), 139–149.

Miller, W. P., Frenkel, H., & Newman, K. D. (1990). Flocculation concentration and sodium/calcium exchange of kaolinitic soil clays. Soil Science Society of America Journal, 54(2), 346–351.

Mullins, C. E., MacLeod, D. A., Northcote, K. H., Tisdall, J. M., & Young, I. M. (1990). Hardsetting soils: Behaviour, occurrence, and management. Advances in Soil Science, 11, 37–108.

Oster, J. D., Shainberg, I., & Wood, J. D. (1980). Flocculation value and gel structure of sodium/calcium montmorillonite and illite suspensions. Soil Science Society of America Journal, 44(5), 955–959.

Polemio, M., Liguori, V., & Maggiore, A. (1980). Relationships between electrical conductivity and major ions concentration in the Salento Peninsula groundwaters (Southern Italy). Ground Water, 18(5), 465–473.

Pollak, M. J. (1954). The use of electrical conductivity measurements for chlorinity determination. Journal of Marine Research, 13(2), 121–133.

Rhoades, J. D. (1996). Salinity: Electrical conductivity and total dissolved solids. In D. L. Sparks (Ed.), Methods of soil analysis. Part 3: Chemical methods (pp. 417–435). Soil Science Society of America. https://salinity.outreachmm.com/wp-content/uploads/2023/05/Salinity-Electrical-Conductivity-and-Total-Dissolved-Solids-1996.pdf

Richards, L. A. (Ed.). (1954). Diagnosis and improvement of saline and alkali soils. USDA Agriculture Handbook No. 60. U.S. Government Printing Office. https://efotg.sc.egov.usda.gov/references/Public/AZ/HB60_saline_alkali_soils.pdf

Singh, K. P., & Kalra, Y. P. (1975). Solute concentration–conductance relationships for various salts in water. Journal of the American Water Resources Association, 11(5), 904–916.

Sposito, G. (2016). The chemistry of soils (3rd ed.). Oxford University Press. https://academic.oup.com/book/40684

Visconti, F., de Paz, J. M., & Rubio, J. L. (2010). What information does the electrical conductivity of soil water extracts of 1:5 ratio (w/v) provide for soil salinity assessment of agricultural irrigated lands? Geoderma, 154(3–4), 387–397.

Wilson, R. T. (1981). Electrical conductivity in the estimation of total dissolved solids in water. Journal of the American Water Resources Association, 17(1), 39–43.

JJEES

JJEES (2026) 17 (3): 293-302
ISSN 1995-6681

Jordan Journal of Earth and Environmental Sciences

Local QdF (Flood-duration-Frequency) Modeling of the Oued Mina Catchment in the North-West of Algeria

Aichoune Merzaka[1*], Yahiaoui Abdelhalim[2], Haddad Samir[2]

[1]*Faculty of Applied Sciences, Laboratory Processes for Materials, Energy, Water, and Environmental (PM3E), University of Bouira, Bouira 10000, Algeria.*

[2]*Institute of Technology, Department of Water Engineering, University of Bouira, Bouira 10000, Algeria.*

Received on 23 August 2025; Accepted on 28 January 2026

Abstract

The aim of this research paper is to develop a multi-duration and multi-frequency model that provides a more complete description of the basin's flood regime on both gauged and ungauged catchments in the range of observed and rare frequencies and answer the questions relevant to integrated river management. The approach adopted in this paper is based on the frequency analysis of multi-duration series using the exponential distribution. So, we have focused on the basic notions and concepts underlying the local QdF modeling of floods in the Oued Mina catchment in North-West Algeria. The local QdF modeling is directly drawn from statistical analysis of the average volume flow for multi-duration series, derived from annual hydrographs of the Oued El-Abtal station to the Exponential distribution, where the fittings of the series lead to the establishment of the relation between the average volume flow, the duration, and the return period. The developed QdF plot can be applied to estimate water availability over specific time intervals (aggregation periods) and across various return periods within the catchment. The obtaining QdF model would be useful in the study of the flooding in an ungauged catchment.

Keywords: *Average volume flow, Fitting, Flood prediction, QdF (Flood-duration-Frequency), Return period.*

1. Introduction

Floods are among the most significant natural hazards and affect almost all regions of the world. The study of floods has been the subject of several studies and research using different methods, such as flood frequency analysis (Hamed and Rao, 2000; Yahiaoui, 1997) and hydro-meteorological methods (Guillot and Duband, 1967; Magroume, 1992), such as GRADEX and AGREGEE. The accurate evaluation of river discharge and precipitation variability, along with the estimation of the frequency and magnitude of extreme hydrological events, represents a complex scientific challenge. This complexity arises from the profound influences of climate change and changes in land use and land cover, which substantially modify the dynamics and availability of water resources (Baran-Gurgul *et al.*, 2024). Hydrological modeling constitutes a fundamental scientific approach for simulating the movement and distribution of water within natural and managed environments. These models provide a quantitative framework for evaluating the effects of land-use transformations, climate variability, and extreme hydrometeorological events on hydrological processes. They serve as indispensable tools for formulating strategies for sustainable water resources management, flood risk mitigation, and environmental protection. The historical development and methodological advancements of hydrological modeling, from the 1950s to the present, are comprehensively examined in Singh's seminal work (Singh, 2018). In general, frequency analysis studies describe the flood event by its instantaneous peak flow. But when mapping a floodplain or designing a hydraulic structure, information about peak flow is essential yet insufficient (Di Baldassarre *et al.*, 2010). In addition, it is crucial to recognize that flood severity can be characterized by both its volume and its duration.

It is essential to give special attention to the concept of "duration" as a fixed parameter, since it plays a key role in many hydrological processes. The characterization of catchment flow, the assessment of water demand, and the evaluation of potential damage risks are all closely related to the temporal nature of hydrological events (Galea and Prudhomme, 1997). The conceptual foundations of the Flood-Duration-Frequency (QdF) model were introduced in the 1990s by Sherwood (1994), Balocki and Burges (1994) and Galea and Prudhomme (1997), who emphasized the role of duration in flood frequency analysis. These applications primarily address gauged catchments under non-stationary (Chen *et al.*, 2013; Cunderlik *et al.*, 2007) or stationary (Hachemi and Benkhaled, 2016) conditions, but the framework supports extension to ungauged areas via index-flood regionalization. QdF modeling also focuses on maximum instantaneous flows and on the analysis of characteristics related to different durations d to assign a frequency to the maximum average flow V_{CXd}.

The obtained QdF model can be used to construct probable flood hydrographs (Sauquet *et al.*, 2004), which can

* Corresponding author e-mail: m.aichoune@univ-bouira.dz

be used in the study of flood hazard.

The aim of this paper is to develop a local QdF model for the Oued Mina catchment in western Algeria by fitting the maximum flow series V_{CXd} of different durations d to the Exponential distribution, and determining the relationships between maximum flow, duration, and return period. The model QdF serves as a tool for flood hazard and vulnerability assessment.

2. Methodology

The methodology is applied to a specific catchment in western Algeria, selected due to its history of severe flooding (Lahlah, 2004) and representative semi-arid characteristics. The study area and available data are outlined in the following section.

2.1 Study area

The study has been conducted on the catchment of Oued Mina (Fig. 1), which is located in the North-Western part of Algeria, at about 300 km from Algiers, between 0° 20' and 1° 10' of East longitude and 34° 40' and 35° 40' of North latitude. The Oued Mina catchment drains an area of approximately 4900 km², and it is part of the large Chelif catchment. The stream of Oued Mina is the main tributary of Oued Chelif, with a distance of about 90 km between the Bakhada and Sidi M'Hamed Benaouda dams, with a South East-North West orientation (Touaibia *et al.*, 2003; Ghernaouet and Remini, 2017). The study area was selected as a case study due to the severe flooding in Oued Rhiou, Relizane, caused by heavy rainfall in October 1993 (Lahlah, 2004).

The Oued Mina catchment is characterized by a dominance of tertiary marls (Eocene, Miocene and Oligocene) very sensitive to erosion in the north, whose soils are generally bare and oversaturated, and Jurassic (upper, lower and middle) in the south, subject to less severe erosion (ANRH, 2010) where nearly 50% of its surface is covered by vegetation of varying density (6% of forests are dominated by young Aleppo pine plantations, 32% by "pistacia, olea, tetraclinis" scrubland and 12% by cereals) (Ghernaouet and Remini, 2014).

The catchment of Oued Mina is characterized by a Mediterranean climate, semi-arid to arid, with hot, dry summers and cold, humid winters. Annual precipitation averages 278 mm with high spatial and temporal variability, leading to alternating high-and low-water periods (Meddi, 1996).

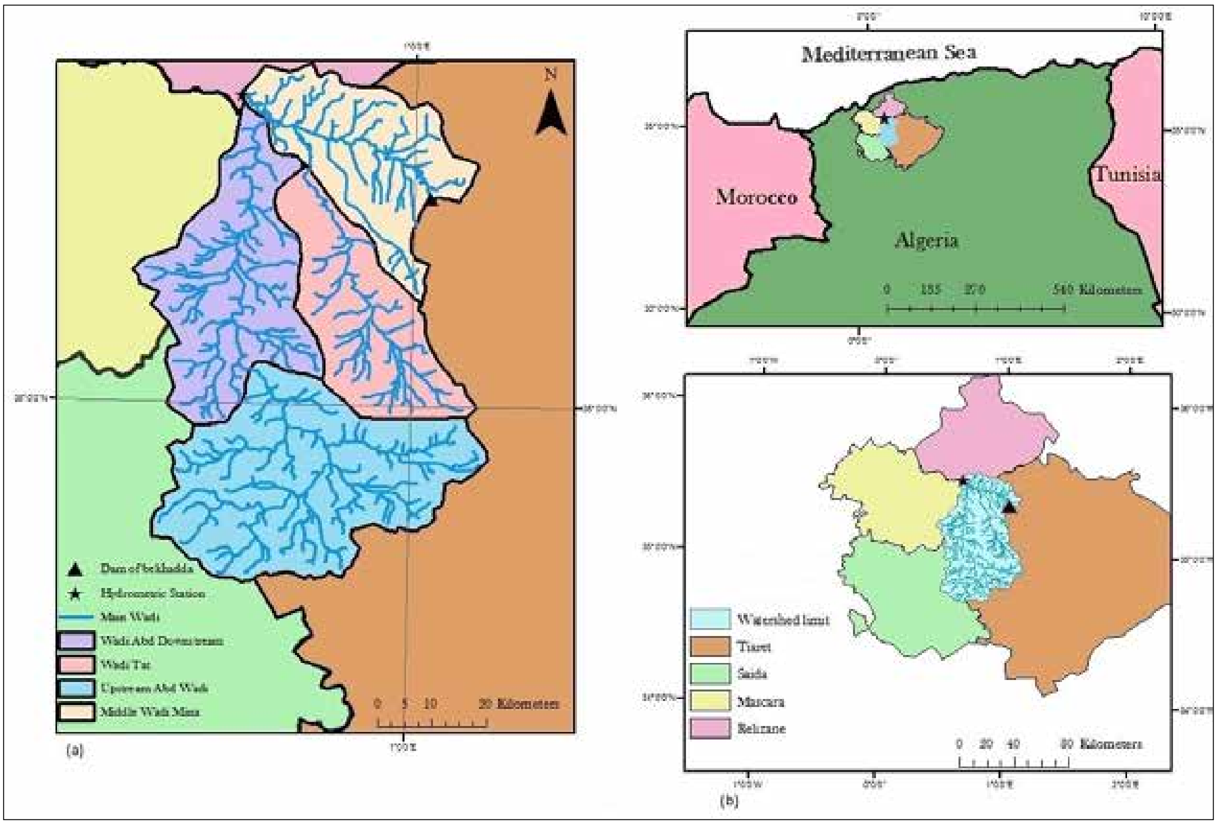

Figure 1. The Oued Mina catchment in North -West Algeria: (**a**) Hydrological network, sub-basin, and gauging station location; (**b**) Geographical location within Algeria.

The hydrometric data set used in this study was provided by the National Agency of Hydraulics Resources (ANRH) of Algiers. It consists of the records of instantaneous flood hydrographs recorded between 1953 and 2011 at the Oued El Abtal gauge station. The time series of annual maximum instantaneous discharge (Q_{IX}), which provides essential information for extreme event analysis, can be obtained (Fig. 2). This series has 57 observations, its mean and standard deviation are 309,65 m³/s and 242,80 m³/s, the min and max values are 31,85 m³/s and 962,65 m³/s, and the coefficient of skewness and kurtosis are respectively 1,06 and 3,15.

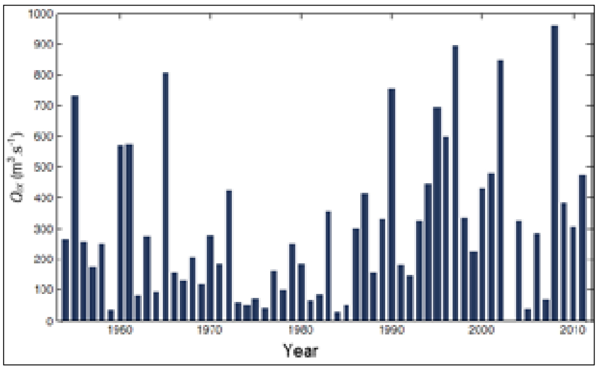

Figure 2. Annual instantaneous maximum discharges (QIX) in the Oued El Abtal station. *(Source: ANRH Algeria)*

By using the Wald-Wolfowitz test (Wald *et al.*, 1943), Mann-Whitney test (Mann *et al.*, 1947), Mann-Kendall test (Mann,1945 and Kendall,1938), and Grubbs test (Grubbs, 1949), the series of Q_{IX} is independent, homogeneous, stationary, and with no outlying values (Table 1).

Table 1. Sampling tests of the annual instantaneous maximum discharge series.

Type of the test	Calculated Value	Critical Value
Wald-Wolfowitz test for independence at 5%	1,314	1,960
Mann-Whitney test for homogeneity at 5%	1,770	1,960
Mann-Kendall test for stationarity at 5%	1,170	1,960
Grubbs test for outliers at 1%	2,692	3,538

These catchment characteristics and the validated Q_{IX} series provide the foundation for the QdF modeling approach. The materials and methods, including series extraction and distribution fitting, are detailed in the following section.

2.2. Material and method

2.2.1. Indices of the flood regime

The decision support system (DSS) was used (El Adlouni *et al.*, 2008), the curve of mean excess function (MFE) has a positive slope (Fig. 3), which implies that the underlying distribution is sub-exponential, so distributions considered in this section belong to the class D, which are represented by the Gumbel distribution, Gamma distribution, and Pearson Type III distribution. These include the method of moments (MOM), the maximum likelihood method (MLM), and the probability weighted moments method (PWM). These are practiced in fitting of distribution and compared by goodness-of-fit tests (Table 2 and Table 3). The main conclusion from the above analysis is that the Gamma distribution is the best model that will give a prediction estimation of the event's extreme.

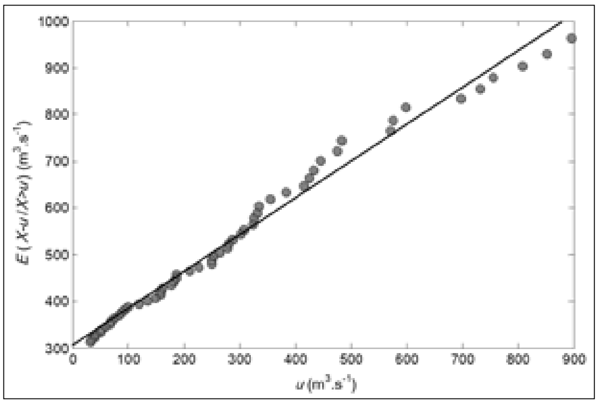

Figure 3. Mean excess function (MEF) for the annual instantaneous maxima peak flow series.

Table 2 shows the quantile estimates for the hydrometric station in the Oued Mina catchment using different distributions, and the following return periods were considered: 2, 5, 10, 20, 50, 100 and 1000 years. The results show the highest flow values. This result is due to several factors, including the geological nature of the region and the slope that facilitates the flow from elevations of 1933 meters to the lowest area, where the measuring station is located at an estimated elevation of 205 meters. We also note the vegetative cover and increased precipitation in this study area. These floods are characterized by irregular occurrence and strong destructive forces, so the engineer must design flood defense structures to withstand this force. Therefore, a suitable probability law for flood flows must be carefully chosen.

Table 2. Estimated Quantiles Q_{IXAT} for different return periods T.

Return period (Year)	Gumbel (MLM)	Gumbel (PWM)	Gumbel (MOM)	Gamma (MLM)	Gamma (MOM)	Pearson III (MOM)
2	264,67	268,76	269,18	246,75	248,21	266,78
5	460,88	485,56	483,74	475,39	474,05	491,13
10	590,80	629,11	625,79	**636.00**	632,02	634,60
20	715,41	766,80	762,06	971,20	784,65	767,39
50	876,71	945,03	938,44	991,62	981,38	932,82
100	997,58	1078,58	1070,61	1140,72	1127,58	1052,73
1000	1396,98	1519,89	1507,35	1626,37	1603,33	1430,91

The next step involves the estimation of goodness-of-fit. It is a different test which can be employed to determine the best theoretical probability distribution that can describe the annual instantaneous maxima peak flow series. So, the probability plot correlation coefficient test *(PPCC)*, Root Mean Square Deviation *(RMSD)*, and Kolmogorov-Smirnov *(KS)* were applied. Table 3 shows the results of the goodness-of-fit analysis. All the observed Kolmogorov–Smirnov values for the all distribution are less than 0,180 as theoretical value at 5% of significance and n = 57. The values of *PPCC* are near to 1, and all the values of *RMSD* are less than 1. Data analysis has shown that the goodness-of-fit of all distributions are accepted. To objectively distinguish between candidate distribution and select the most suitable one, we employed information criteria, such as the Akaike Information Criteria *(AIC)* (Akaike, 1974), and Bayesian Information Criteria *(BIC)* (Schwarz, 1979). Table 4 shows the distribution that yields the lowest AIC and BIC values, as these criteria penalize model complexity while rewarding goodness-of -fit.

Table 3. Goodness of fit test results

	PPC	*KS*	*RMSD*
Gumbel (MOM)	0,985	0,077	0,6244
Gumbel (PWM)	0,985	0,08	0,6499
Gumbel (MLM)	0,985	0,0753	0,4796
Gamma (MLM)	**0,989**	**0,056**	**0,1371**
Gamma (MOM)	0,98	0,06	0,1371
Pearson Type III (MOM)	0,988	0,081	0,1112

Table 4. Values of *AIC* and *BIC*

Probability Distribution	*AIC*	*BIC*
Gumbel (MOM)	776,13	780,22
Gumbel (PWM)	776,36	780,44
Gumbel (MLM)	775,18	779,27
Gamma (MLM)	**765,29**	**779,27**
Gamma (MOM)	765,31	769,4
Pearson Type III (MOM)	776,75	782,88

The use of the Gamma distribution is very suitable to fit the series of Q_{IX} (Fig. 4) because the lowest value of *AIC* corresponds to the Gamma distribution, as shown in Table 4, with parameter estimates *a* (scale) and *k* (shape), respectively equal to 1,58 and 0,05. Hence, the quantile of 10 years Q_{IXA10} is equal to 636 m^3/s, which is an important index of the flood regime of the catchment, high-lighting rapid, high-intensity floods, setting the stage for multi- duration QdF analysis.

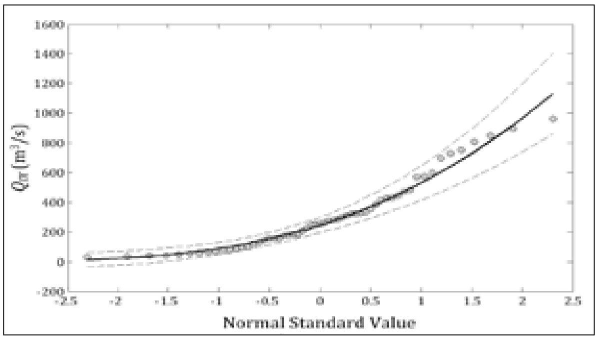

Figure 4. Observed and estimated flows at 95% confidence intervals for the Q_{IX} series.

According to the SOCOSE method of the French Technical Center for Rural Water and Forest Engineering (CTGREF, 1980), an observed flood hydrograph (Fig. 5) has two characteristics: the peak flow *Qs* and the duration ds during which half of *Qs* is continuously exceeded. For all observed flood hydrographs, the obtained data (*Qs*, *ds*) allow for drawing the mean between the ds and *Qs*. From the value of Q_{IXA10}, another index of the flood regime, *D* the duration of the characteristic flood of the catchment can be determined, which is approximately equal to 10 hours (Aichoune and Yahiaoui, 2024) (Fig. 6).

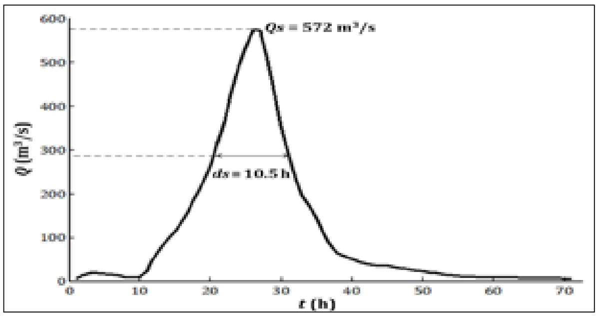

Figure 5. Flood hydrograph of 22 to 24 November 1959 recorded at Oued El Abtal station.

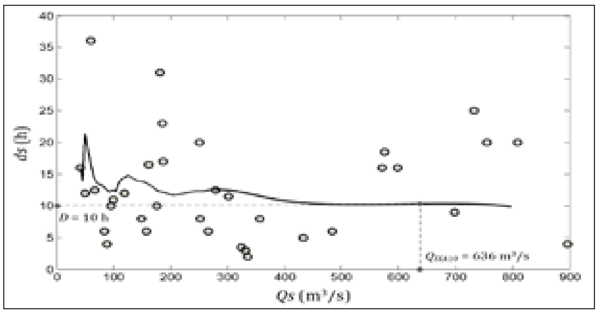

Figure 6. Estimation of the duration of the characteristic flood of the Oued Mina catchment.

With the V_{CXd} series extracted and the exponential distribution fitted using objective criteria (as detailed above), the key findings, including quantile estimates and the analytical QdF formulation, are presented and interpreted in the next section.

3. Results and Discussion

In this section, we present the main empirical results of the study, beginning with a description of the construction and fitting of the series of V_{CXd} by the exponential distribution, followed by a derived analytical formulation that provides a reliable tool for flood characterization in semi-arid catchments.

3.1. Construction and fitting of the series of V_{CXd}

The integration of the hydrograph *Q(t)* between t and *t+d* allows the volume of water *V* flowing for the duration *d*, where *D/2* ≤ *d* ≤ *5D*. Therefore, the corresponding characteristic average discharge rate is the volume V_{Cd} *(t)* flowing during this duration *d* is given by:

$$V_{Cd}(t)=\frac{1}{d}\int_{t}^{t+d} Q(\tau)\,d\tau \tag{1}$$

By analyzing all annual hydrographs, it is possible to construct, for each duration d (incremented in one-hour time steps), a sequence of average discharges *Vcd(t)*. From this time series, the maximum annual value V_{CXd} can be extracted, representing the annual characteristic maximum mean discharge corresponding to extreme flood episodes of duration d (Guilard, 1998). For the Oued Mina catchment, 46 V_{CXd} series were generated for durations ranging from 5 to 50 hours (d = 5, 6, 7, …, 50 h). In this study, the analysis focused on the ten representative durations (d = 5, 10, 15, 20, 25, 30, 35, 40, 45, and 50 hours). The mean, standard deviation, coefficient of variation, skewness, and kurtosis of each V_{CXd} series are summarized in Table 5. All series are independent, homogeneous, and stationary and show no outliers or anomalies, as confirmed by statistical sampling tests. The use of the exponential distribution in this study is consistent with previous hydrological studies that applied QdF or related flood-frequency frameworks in similar climatic and hydrological contexts. This study showed that in semi-arid Mediterranean climates, flood variables often exhibit strong skewness and rapid tail decay, conditions under which the exponential distribution provides satisfactory fits, especially for duration-dependent flood metrics. Ketrouci and Meddi (2015), by applying QdF modeling to Algerian basins, reported that the exponential distribution performs well for V_{CXdT} and provides reliable estimates across multiple durations. Other studies (Javelle and Ouarda, 2002; 2003; Ouarda *et al.*, 2001; Merz *et al.*, 2003) also support this finding.

Table 5. Table 5. Principal characteristics of the maxima flow series *(VCXd)* of Oued Mina.

d (h)	Mean (m³/s)	Standard deviation(m³/s)	Variation	Skewness	Kurtosis
5	201,23	193,79	0,96	1,24	3,00
10	177,14	169,94	0,96	1,29	3,09
15	152,83	147,48	0,97	1,53	4,40
20	140,59	131,60	0,94	1,41	4,05
25	123,66	114,30	0,92	1,46	4,34
30	110,67	100,75	0,91	1,52	4,64
35	100,62	91,09	0,91	1,53	4,75
40	91,03	81,47	0,89	1,61	5,13
45	83,49	74,33	0,89	1,68	5,44
50	77,12	68,36	0,89	1,74	5,80

So, the exponential distribution was identified for fitting the V_{CXdT} series corresponding to durations d = 5, 10, 15, 20, 25, 30, 35, 40, 45, and 50 hours (Fig. 7).

The probability distribution function of the exponential distribution with two parameters m_d and a_d is given by:

$$F(x) = 1 - \exp\left(-\frac{x - m_d}{a_d}\right) \quad (2)$$

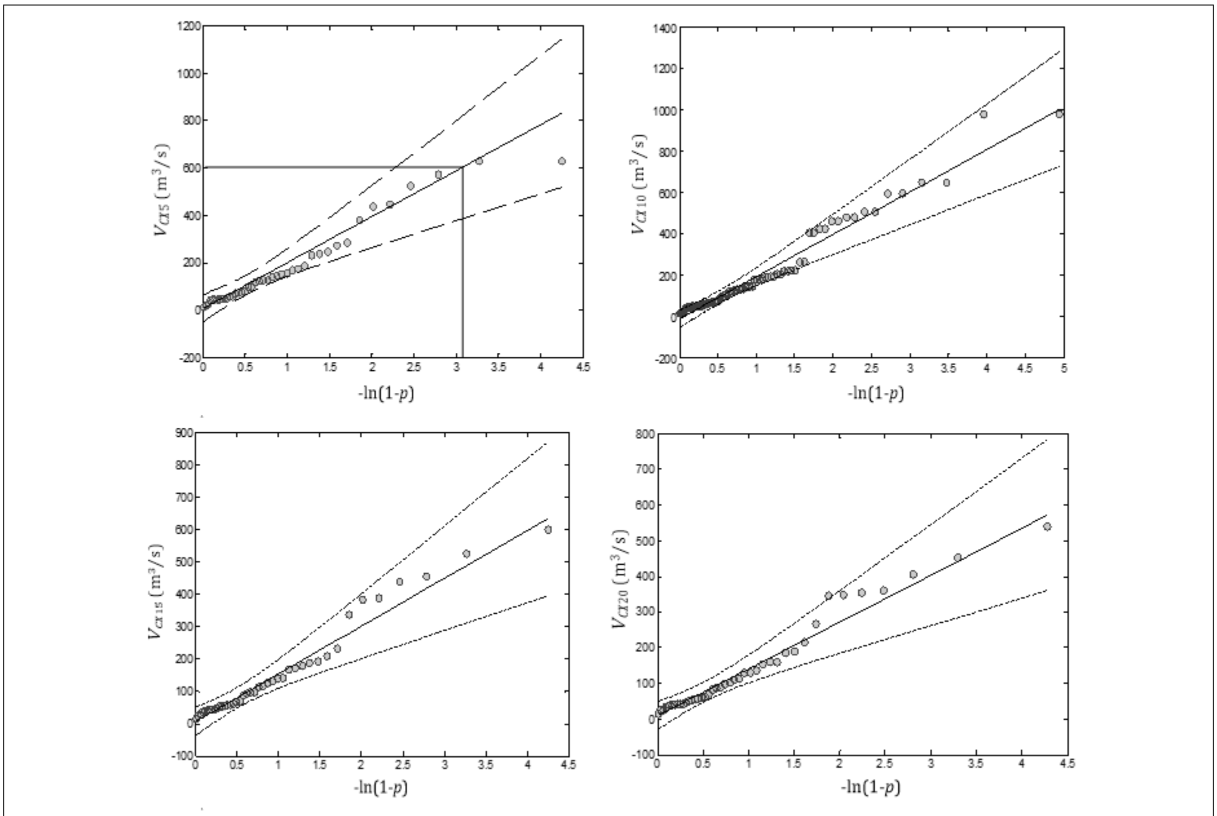

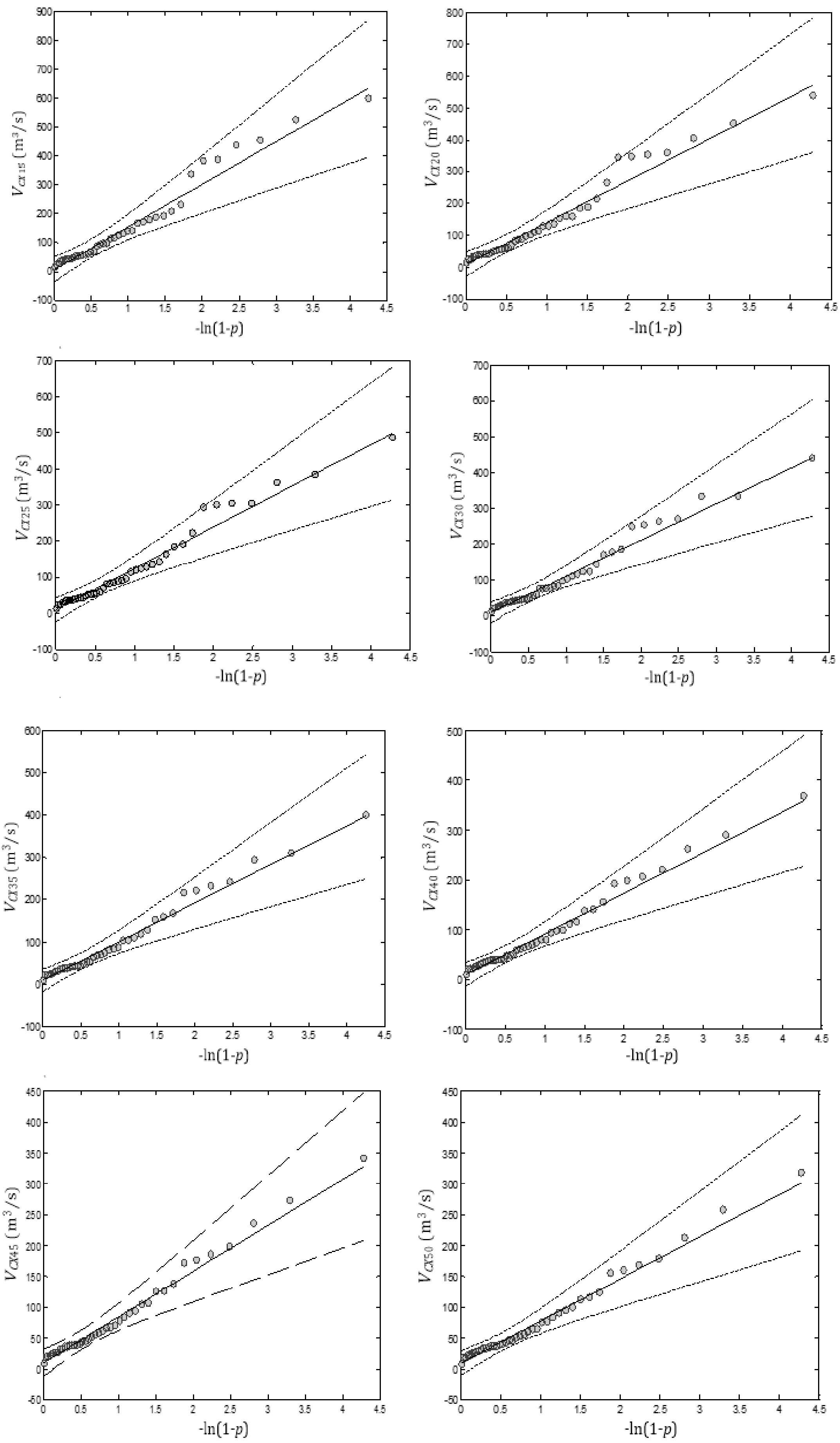

Figure 7. Figure 7. Fitting and confidence limits at 95 % of $_{VCXd}$ series (d = 5, 10 ..., 50 hours).

For the considered series of V_{CXd}, the parameters and are estimated by the method of moments, it was chosen for its simplicity unbiased estimation of location/scale in Exponential (small samples, n = 57), and robustness to outliers. This method performed well. It is recommended for Exponential in hydrological applications (Wilks, 2011). The results of estimation for the parameters and are given in the following table (Table 6). The results of the goodness-of-fit tests presented in Table 7 confirm the adequacy of the exponential distribution in modeling the V_{CXd} series for all considered durations. The Probability Plot Correlation Coefficient *(PPCC)* values are all greater than 0.98, indicating an excellent correlation between the observed and theoretical distributions. Moreover, the Kolmogorov–Smirnov *(KS)* statistics *(KS_{ob})* are systematically lower than the critical values *(KS_{th})* at the 5% significance level, which confirms that there is no significant difference between the empirical and theoretical distributions. Finally, the Root Mean Square Deviation *(RMSD)* values are very small and tend to decrease with increasing duration, suggesting a progressively better fit for longer flood durations. These results demonstrate that the exponential distribution provides a statistically reliable representation of the flood discharge behavior across all tested time scales.

Table 6. Estimated position and scale parameters for each V_{CXd} series.

d (h)	m_d (m³/s)	a_d (m³/s)
5	7,44	193,79
10	7,20	169,94
15	5,35	147,48
20	8,99	131,60
25	9,35	114,30
30	9,92	100,75
35	9,52	91,09
40	9,56	81,47
45	9,16	74,33
50	8,76	68,36

Table 7. Goodness of fit tests.

d(h)	5	10	15	20	25	30	35	40	45	50
PPCC	0,980	0,986	0,985	0,985	0,988	0,990	0,993	0,994	0,995	0,995
KS_{ob}	0,103	0,142	0,109	0,092	0,082	0,081	0,092	0,096	0,094	0,093
KS_{th}	0,210	0,210	0,210	0,207	0,207	0,207	0,210	0,207	0,207	0,207
RMSD	0,214	0,464	0,214	0,177	0,166	0,152	0,150	0,142	0,138	0,142

PPCC is the Probability Plot Correlation Coefficient (Filliben, 1975, Vogel, 1986, Kim *et al*., 2010) KS_{ob} and KS_{th} are the observed and theoretical Kolmogorov-Smirnov values (Massey, 1951) and *RMSD* is the Root Mean Square Deviation (NERC, 1975). So, the theoretical quantile V_{CXdp} of probability *p* is estimated for the Exponential distribution fitted with the method of moments is given by:

$$V_{cxdp} = m_d - a_d \ln(1-p) \tag{3}$$

Therefore, in term of return period *T*, the estimated quantiles V_{CXdT} is expressed as (Table 8):

$$V_{CXdT} = m_d + a_d \ln T \tag{4}$$

Table 8. Estimated quantiles V_{CXdT}

d(h)	*T* = 2	*T* = 5	*T* = 10	*T* = 20	*T* = 50	*T* = 100	*T* = 500	*T* = 1000
5	141,77	319,34	453,67	587,99	765,56	899,89	1211,78	1346,11
10	128,52	317,51	460,48	603,45	792,44	935,41	1267,37	1410,34
15	107,57	242,71	344,94	447,17	582,30	684,53	921,89	1024,12
20	100,20	220,79	312,00	403,22	523,80	615,02	826,82	918,04
25	88,58	193,32	272,54	351,77	456,51	535,73	719,69	798,92
30	79,76	172,07	241,91	311,75	404,06	473,90	636,05	705,89
35	72,66	156,13	219,27	282,42	365,88	429,03	575,64	638,78
40	66,03	140,68	197,16	253,63	328,28	384,75	515,87	572,34
45	60,68	128,79	180,31	231,83	299,93	351,45	471,08	522,60
50	56,14	118,78	166,16	213,54	276,17	323,55	433,57	480,95

3.2. V_{CXDT} Formulation

The equation (3), obtained by fitting the V_{CXd} series to the Exponential distribution, is represented in (Fig. 6) as a straight line on the semi-logarithmic plane. For the considered V_{CXd} series with durations d = 5, 10, 15, 20, 25, 30, 35, 40, 45, and 50 hours, all the fitted straight lines intersect at a common point (Fig. 8). This point of intersection can be determined graphically and is located approximately at the coordinates that can be determined graphically; $\ln(1-p_0) = -0{,}0154$ and V_{CX0} = 10,45 m³/s.

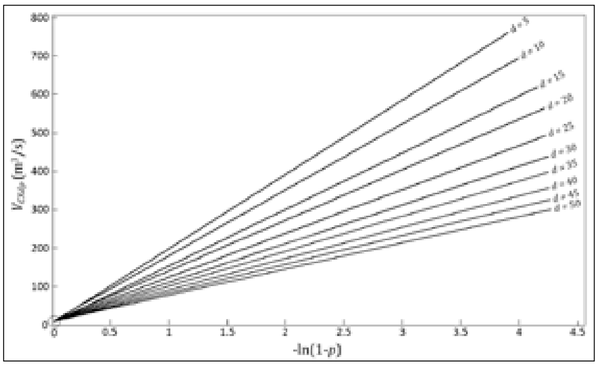

Figure 8. Straight lines of fittings of V_{CXd} series (d = 5, 10, 15, . . ., 50 hours).

It is possible to provide a continuous formulation of the quantiles V_{CXdT}. According to equation (3):

$$V_{CX0} = m_d - a_d \ln(1 - p_0) \quad (5)$$

And so, the difference between equation (3) and (5) gives gives an equation that depends only on the scale paramete a_d:

$$V_{CXdp} = a_d \left(\ln(1 - p_0) - \ln(1 - p)\right) + V_{CX_0} \quad (6)$$

a_d has a polynomial tendency of the second degree versus the duration d (Fig. 9) with a coefficient of determination R^2 = 0.999 expressed as:

$$a_d = 0.0461 d^2 - 5.2783\, d + 218.11 \quad (7)$$

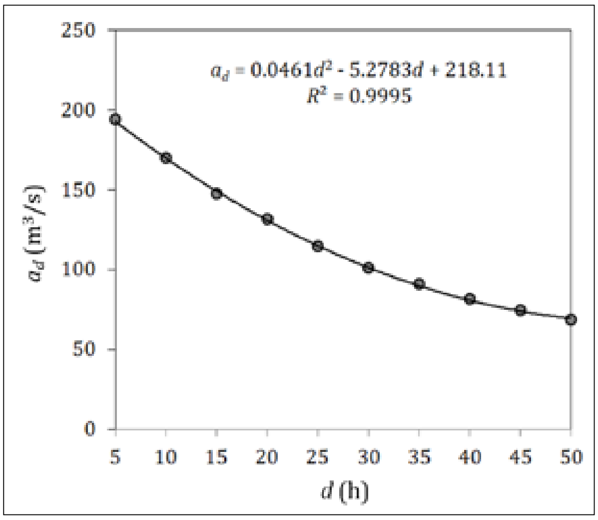

Figure 9. Polynomial tendency of a_d versus the duration d.

Thus, V_{CXdT} formulation as a quantile of flood depending on the duration d and the return period T is giving by:

$$V_{CXDT} = (0.0461\, d^2 - 5.2783\, d + 218.11) \times (\ln(T) - 0.0154) + 10.45 \quad (8)$$

It should be noted that Equation (8) provides a correction to the values of V_{CXdT} previously estimated using Equation (4) for different duration values. This analytical expression (Eq. 8) provides several advantages over discrete quantile tables (Table 5). It enables estimation of V_{CXdT} for any duration d and any return period T, slightly refines the discrete estimates by enforcing the observed convergence property, and facilitates the direct construction of smooth QdF curves (Fig.10). Interpretation of the QdF curves reveals key aspects of the catchment's flood regime: for short durations (e.g, 5-10 hours), discharges rise sharply with increasing return period, reflecting the torrential nature confirmed by Q_{IXA10} = 636 m³/s and d =10 hours. For longer durations, the curves flatten, indicating that extreme events are dominated by brief, intense peaks rather than sustained high flows. This pattern aligns with the semi-arid hydrology, where floods are typically flash-driven by connective storms (Meddi, 1996). Compared with traditional peak-flow analysis, this QdF model provides superior integration of magnitude, duration, and frequency, aligns with prior Algerian studies (Ketrouci and Meddi, 2015; Yahiaoui *et al.*, 2011; Hachemi and Benkhaled, 2016), and enhances applicability to ungauged sites through potential regionalization. The model's robustness supports advanced applications, such as probabilistic hydrograph generation and vulnerability assessments, which are crucial for mitigating risks in rapidly urbanizing semi-arid basins.

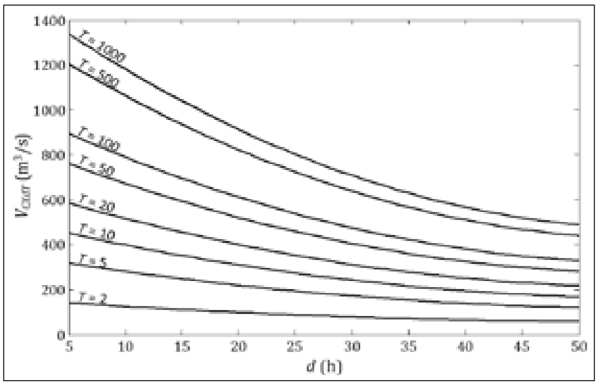

Figure 10. Flow-duration-Frequency (QdF) in V_{CX} curves of Oued Mina.

Compared with traditional peak-flow analysis, this QdF model offers superior integration of magnitude, duration, and frequency, aligns with prior Algerian studies, and enhances applicability to ungauged sites. In summary, the robust exponential fit and the derived analytical formulation provide a reliable tool for flood characterization in semi-arid catchments. The main conclusion of this study is presented in the following section.

4. Conclusion

The local QdF modeling is derived from statistical analysis of the average volume flow of the V_{CXdT} across multiple durations in the Oued Mina catchment. This methodology is based on fitting the Exponential statistical model. This selection is grounded in consistency with established QdF literature and hydrological principles, rather than subjective judgment. Previous studies have shown that flood quantiles expressed as mean discharges or volumes over fixed durations are adequately represented by parsimonious exponential-type models, particularly within the QdF framework (Javelle *et al.*, 2003).

These authors demonstrated that the Exponential distribution yields stable parameter estimates and satisfactory goodness-of-fit across multiple durations, especially when sample sizes are limited. Similar conclusions were reported in semi-arid Mediterranean catchments, where duration-dependent flood variables exhibit strong positive skewness and rapid tail decay (Ketrouci and Meddi, 2015). For this work, the *PPCC* values (0,980 and 0,995) indicate a strong correlation between observed and theoretical data, while the KS observed values remain below the critical thresholds confirming the model's adequacy. The *RMSD* values decrease with increasing duration, suggesting improved performance for longer aggregation periods. Overall, these results confirm the reliability of the exponential distribution for modeling the V_{CXd} data for *QdF* analysis. Therefore, the Oued Mina catchment's high quantile Q_{IXA10} = 636 m^3/s discharge values and the short flood duration (*D* = 10 hours) make it highly vulnerable to rapid torrential flooding.

Hence, the modeling of the flood regime is a major challenge in this case for predicting the extreme event. Moreover, the V_{CXd} series was constructed, and by fitting it to the exponential distribution, the following results were obtained: an analytical formula that gives the relationship of the characteristic extreme flow as a function of the duration and the return period. From the trend analysis, Construction of the QdF curves characterizing the Oued Mina catchment enables us to obtain finalized results integrating the great flows. It represents one of the most widely used hydrological tools in the management of water resources (Ketrouci, and Meddi, 2015; Ketrouci *et al.*, 2012; Hachemi and Benkhaled, 2016; Yahiaoui *et al.*, 2011) and they make it possible to carry out a frequency analysis of floods in a catchment area and flood forecasting for gauged or ungauged basins. Our findings could be valuable and can be helpful to decision makers to improve flood risk strategy in this region for protecting the lives of people and property. The increasing probability of flood occurrence is expected to pose substantial challenges to effective flood management. Accordingly, it is essential to reinforce mitigation and adaptation strategies to enhance human resilience within the Oued Mina catchment.

Acknowledgment

The authors express gratitude to the ANRH agents in Algeria for providing critical hydrometric data.

Conflicts of interest

The authors declare no conflict of interest.

References

Akaike, H. (1974). A new look at the statistical model identification. IEEE transactions on automatic control, vol. 19, no. 6, 716-723. Available from: https://doi.org/10.1109/TAC.1974.1100705.

ANRH (2010). Annuaires (données pluviométriques et hydrométriques) et cartes hydrologiques du bassin versant de l'Oued Mina. Ministère des Ressources en Eau, Algeria.

Aichoune, M., and Yahiaoui, A. (2024). Hydrological flood modeling and risk flooding evaluation methodology: Case of the Oued Mina catchment in the Wilaya of Relizane (North-West of Algeria). Algerian Journal of Chemical Engineering, 2, 8-17. Available from: http://doi.org/10.5281/zenodo.14805146.

Balocki J.B., Burges S.J. (1994). Relationships between n-day flood volumes for infrequent large floods J. Water Resour. Plan. Manag., 120 (6), 794-818. Available from: https://doi.org/10.1061/(ASCE)0733-9496(1994)120:6(794).

Baran-Gurgul, K., & Rutkowska, A. (2024). Water Resource Management: Hydrological Modelling, Hydrological Cycles, and Hydrological Prediction. Water, 16(24), 3689. Available from: https://doi.org/10.3390/w16243689.

Cunderlik, J. M., Jourdain,V., Ouarda, T.B.M.J. and Bobée, B. (2007). Local Non-Stationary Flood-Duration-Frequency Modelling. Canadian Water Resources Journal, 32(1), 43-58. Available from: https://doi.org/10.4296/cwrj3201043.

CTGREF, S., and Diame, S. H. (1980). Synthèse nationale sur les crues des petits bassins, fascicule 2: la méthode SOCOSE. Information technique no 38, vol. 2, Antony.

Chen, X., Zhang, L., Xu,C.Y., Zhang, J. & Ye, C. (2013). Hydrological design of nonstationary flood extremes and durations in Wujiang River, South China: Changing properties, causes, and impacts. Mathematical Problems in Engineering. 527461. 10 pages. Available from: https://doi.org/10.1155/2013/527461.

Di Baldassarre, G., Schumann, G., Bates, P. D., Freer, J. E. & Beven, K.J. (2010) Flood-plain mapping: a critical discussion of deterministic and probabilistic approaches. Hydrol. Sci. J. 55(3), 364–376. Available from: https://doi.org/10.1080/02626661003683389.

El Adlouni, S., Bobée, B. & Ouarda, T.B.M.J. (2008). On the tails of extreme event distributions in hydrology. Journal of Hydrology, 355(1-4), 16-33. Available from: https://doi.org/10.1016/j.jhydrol.2008.02.011.

Filliben, J.J. (1975). The probability plot correlation coefficient test for normality. Technometrics, vol. 17, no 1, 111-117. Available1from:https://doi.org/10.1080/00401706.1975.10489279.

Ghernaout, R., and Remini, B. (2017). Analysis of Suspended Sediment transport in Mina River Basin (NW Algeria). Houille Blanche. 103(3), 47-63. Available from: https://doi.org/10.1051/lhb/2017021.

Ghernaout, R., Remini, B. (2014). Impact of suspended sediment load on the silting of SMBA reservoir (Algeria). Environmental Earth Sciences, vol. 72, 915-929. Available from: http://doi.org/10.1007/s12665-014-3125-9.

Grubbs, F. E. (1949). Sample criteria for testing outlying observations. University of Michigan. Available from: http://doi.org/10.1214/aoms/1177729885.

Gilard, O. (1998). Les bases techniques de la méthode Inondabilité. Cemagref Edition.

Guillot, P., and Duband, D. (1967). La méthode du Gradex pour le calcul de la probabilité des crues à partir des pluies. IAHS. Publication n°84.

Galéa, G., and Prudhomme, C. (1997). Notions de base et concepts utiles pour la compréhension de la modélisation synthétique des régimes de crue des bassins versants au sens des modèles QdF. Revue des Sciences de l'Eau, 10(1), 83-101. Available from: https://doi.org/10.7202/705271ar.

Galéa, G., Javelle, P., Chaput, N. (2000). Un modèle débit-durée-fréquence pour caractériser le régime d'étiage d'un bassin versant. Revue des Sciences de l'Eau, 2000, 13(4), 421-440. Available from: https://doi.org/10.7202/705401ar.

Hamed, K. H. and Rao, A. R. (2000). Flood Frequency Analysis. CRC Press. 376 p. Available from: https://doi.org/10.1201/9780429128813.

Hachemi, A., & Benkhaled, A. (2016). Flood-duration-frequency modeling application to wadi Abiodh, Biskra (Algeria). LARHYSS Journal (27), 277-297.

Javelle, P. (2001). Caractérisation du régime des crues: le modèle débit-durée-fréquence convergent. Approche locale et régionale. UR Hydrologie-Hydraulique, Cemagref, groupement de Lyon. Thèse de doctorat, INPG (MMGE).

Javelle, P., Ouarda, T.B.M.J., Lang, M., Bobée, B., Galéa, G., & Grésillon, J. M. (2002). Development of regional flood-duration–frequency curves based on the index-flood method. Journal of Hydrology, 258(1-4), 249-259. Available from: https://doi.org/10.1016/S0022-1694(01)00577-7.

Javelle, M., Ouarda, T.B.M.J., & Bobée, B. (2003). Spring flood analysis using the flood-duration–frequency approach: application to the provinces of Quebec and Ontario, Canada. Hydrological Processes. 17(18), 3717-3736. Available from: https://doi.org/10.1002/hyp.1349.

Ketrouci, K., Meddi, M. and Abdesselam, B. (2012). Etude des crues extrêmes en Algérie : cas du bassin-versant de la Tafna. Science et Changement Planétaires-Sécheresse, 23(4), 297-305. Available from: https://doi.org/10.1684/sec.2012.0353.

Ketrouci, K., & Meddi, M. (2016). Application des modèles Débit-durée-Fréquence QdF pour l'estimation des crues rares en Algérie: Cas du bassin versant de la Tafna. Bulletin de l'Institut Scientifique, Rabat, Section Sciences de la Terre. 37. 45-54.

Kim, S., Shin, H., Kim, T., and Heo, J-H. (2010). Derivation of the probability plot correlation coefficient test statistics for the generalized logistic distribution. In: Proceedings of the International Workshop Advances in Statistical Hydrology.

Kendall, M. G. A. (1938). A new measure of rank correlation. Biometrika, 30(1-2), 81-93. Available from: http://doi.org/10.2307/2332226

Lahlah, S. (2004). Les inondations en Algérie Actes des journées techniques sur les risques naturels: Inondation, Prevision-Protection. Batna (Algeria) 15 and 16 December.

Margoum, M. (1992). Estimation des crues rares et extrêmes : le modèle AGREGEE. Conception et premières validations. Thèse de doctorat. ENMP, Paris.

Meddi, M. (1996). Study of annual mean flow in northern Algeria: proposed formulas to estimate the mean annual flow. Algeria Equip. Rev. 8, 5-8.

Mann, H, B., and Whitney, D, R. (1947). On a test of whether one of two random variables is stochastically larger than the other. The annals of mathematical statistics; p. 50-60. Available from: https://doi.org/10.1214/aoms/1177730491.

Mann, H. B. (1945). Non-parametric test against trend. Econometrika 13, 245–259. Go to original source. Available from: http://doi.org/10.2307/1907187.

Massey, F. J. (1951). The Kolmogorov-Smirnov Test for Goodness of Fit. Journal of the American Statistical Association, 46(253), 68-78. Available from: https://doi.org/10.2307/2280095.

Merz, R., & Blöschl, G. (2003). A process typology of regional floods. Water Resources Research, 39(12), 1340. Available from: https://doi.org/10.1029/2002WR001952.

NERC. (1975). Flood Studies Report. Hydrological Studies. National Environment Research Council London, Vol. 1-5. United Kingdom.

Ouarda, T.B.M.J., Girard, C., Cavadias, G. S., & Bobée, B. (2001). Regional flood frequency estimation with canonical correlation analysis. Journal of Hydrology, 254(1–4), 157–173. Available from: https://doi.org/10.1016/S0022-1694(01)00488-7.

Sauquet, E., Galéa, G., and Bessenasse, M. (2004). Caractérisation du régime des hautes eaux en débit-durée-fréquence: Application au contexte algérien. La Houille Blanche, vol. 90, no 5, 80-85. Available from: https://dx.doi.org/10.1051/lhb:200405010.

Schwarz, G. (1978). Estimating the dimension of a model, The annals of statistics, 6(2), 461-464. Available from: https://doi.org/10.1214/aos/1176344136.

Sherwood, J. M. (1994). Estimation of volume-duration-frequency relations of ungaged small urban streams in Ohio. Journal of the American Water Resources Association, 30 (2), 261-269. Available from: https://doi.org/10.1111/j.1752-1688.1994.tb03289.x.

Singh, V.P. (2018). Hydrologic modeling: progress and future directions. Geoscience letters, Vol. 5, article 15. Available from: https://doi.org/10.1186/s40562-018-0113-z.

Touaïbia, B. and Achite, M. (2003). Contribution à la cartographie de l'érosion spécifique du bassin versant de l'Oued Mina en zone semi-aride de l'Algérie septentrionale. Hydrological Sciences Journal, vol. 48(2), 235-242. Available from: https://doi.org/10.1623/hysj.48.2.235.44691.

Vogel, R. M. (1986). The probability plot correlation coefficient test for the normal, lognormal, and Gumbel distributional hypotheses. Water resources research, 1986, 22(4), 587-590. Available from: http://doi.org/10.1029/wr022i004p00587.

Wald, A. and Wolfowitz, J. (1943). An exact test for randomness in the non-parametric case based on serial correlation. The Annals of Mathematical Statistics, 14(4), 378-388. Available from: https://doi.org/10.1214/aoms/1177731358.

Wilks, D. S. (2011). Statistical methods in the Atmospheric Sciences. 3rd Edition. Academic Press, Amesterdam (or Elsevier), 676 p.

Yahiaoui, A. (1997). Contribution a une étude comparative des méthodes d'estimation des crues. Cas du bassin versant de Oued Mina w. Relizane. Thèse de Magister. École Nationale Supérieure de l'Hydraulique de Blida, Algérie. 120 p.

Yahiaoui, A., Touaïbia, B., Bouvier,C., and Dechemi, N. (2011). Modélisation du régime de crue en Débit–durée–Fréquence du bassin de l'Oued Mekerra dans l'ouest Algérien. Revue des Sciences de l'Eau, 24(2), 103-115. Available from: https://doi.org/10.7202/1006105ar.

JJEES

Jordan Journal of Earth and Environmental Sciences

JJEES (2026) 17 (3): 303-310
ISSN 1995-6681

Statistical Analysis for Assessment of Water Quality- Arkavathi River in India

Kalpana Polisetty

Department of Mathematics and Statistics, School of Applied Science and Humanities, Vignan's Foundation for Science, Technology and Research, Vadlamudi, Guntur, India-522213.

Received on 25 May 2025; Accepted on 17 February 2026

Abstract

This study assessed the water quality of the Arkavathi River in India across three time scales (2019, 2020, and the combined period 2019–2020) using the Weighted Arithmetic Water Quality Index (WAWQI). Thirteen physicochemical parameters were monitored twice a month at five sampling stations between August 2019 and July 2020. In all cases, only the Koggedoddy station met drinking water standards (WAWQI ≈ 45). In contrast, the other four stations were heavily polluted (WAWQI 60–90), with pollution severity following the order Thymasandra > Doddamuduvadi > Gogeredoddi > Tavarekere Bekuppe. Correlation analysis was conducted to characterize relationships among the parameters, which revealed that pH–DO (r = 0.815), EC–Na (r = 0.745), and EC–TDS (r = 0.71) were strongly related, indicating that ionic and oxygen-related factors largely control water quality. Moreover, ANOVA results revealed significant spatial differences in BOD, DO, pH, Cl, and F across the sampling stations. Hence, the study effectively identified the main causes of pollution in the Arkavathi River and showed which stations need quick action. Overall, the findings will help support effective river management and protection.

Keywords: *Arkavathi River, Water quality, WAWQI, Correlation analysis, One-way ANOVA*

1. Introduction

One of the pressing global issues is water quality, and continuously monitoring it presents a significant challenge for effective water resource management. To address this, water quality is typically assessed using three important parameters: physical, chemical, and biological. Understanding the interplay of these factors is crucial for determining whether water is safe for drinking, suitable for other uses, or unsafe for any purpose. Integrating the effects of various physicochemical and biological parameters into a single representative measure is only possible through the Water Quality Index (WQI).

Initially, WQI was proposed by Horton (1965); it was later improved by Brown et al. (1970) through the use of arithmetic weights, leading to the development of the Weighted Arithmetic Water Quality Index (WAWQI). In subsequent years, numerous studies have developed and applied different index aggregation functions, including the Chemical WQI, the Canadian Council of Ministers of the Environment WQI, the NSF WQI, the Oregon WQI, and the Overall Index of Pollution. However, several researchers have extensively applied the WAWQI to assess water quality in both surface and groundwater systems due to its ease of computation, flexibility, and ability to effectively provide an interpretable measure of overall water quality.

For example, WAWQI has been used to evaluate the water quality of the Gharraf River in southern Iraq (Ewaid & Abed, 2017), the Sabarmati River Basin (Kosha & Geeta, 2017), the Yamuna River (Anshu & Vinita, 2019), the Tigris River in Iraq (Chabuk et al., 2020), and the Arkavathi River and the groundwater around it (Bharath et al., 2024). It has also been applied to assess groundwater quality in Vijayawada, Andhra Pradesh (Satish et al., 2017), and South Gujarat (Divya et al., 2023). Other studies have examined the impacts of mining and industrial activities on water quality, such as gold mining areas in the southeastern region (Diop, 2023) and irrigation water in Basra City (Faroon et al., 2023). Additionally, many other researchers have used this approach (Tyagi et al., 2013; Oni & Fasakin, 2016; Kosha & Geeta, 2017; Kachroud et al., 2019; Tasneem & Mustafa, 2021; Khushbu et al., 2021; Sandra et al., 2023; Shirodkar et al., 2010; Lumb et al., 2011; Gazzaz et al., 2012; Dede et al., 2013). Collectively, these studies demonstrate the effectiveness of WAWQI in capturing spatial and temporal variations in water quality across diverse regions and sources.

Along with WAWQI, multivariate and statistical methods have been widely employed to analyze complex water quality datasets and identify pollution sources. Techniques such as Principal Component Analysis (PCA), Cluster Analysis (CA), and Discriminant Analysis (DA) have been applied to the Daliao River Basin (Zhang et al., 2009), Manchar Lake (Kazi et al., 2009), and the Haraz River Basin (Pejman et al., 2009) to identify potential pollution sources. Similarly, Ammar et al. (2017) applied CA and ANOVA to water samples from the Koudiat Medouar watershed to identify differences between sampling stations and assess the influence of pollution sources. VishnuRadhan et al. (2017) investigated the water quality of the Sg. Malim urban river in Peninsular Malaysia using various statistical approaches. In India, Loganathan and Ahamed (2017) assessed the Amaravati River using CA, PCA, and correlation analysis, while Prasad et al. (2020)

* Corresponding author e-mail: drkalpanastat@gmail.com

implemented an Internet of Things (IoT) based monitoring system for the Krishna River, using ANOVA to validate seasonal variations in water quality.

These studies highlight the usefulness of WAWQI, multivariate, and statistical methods for simplifying complex datasets, identifying key pollution sources, and supporting decisions on water quality management. Despite extensive studies on water quality using WAWQI and statistical analyses, the Arkavathi River, an important water source in the region, has not been systematically evaluated for various stations with different time intervals. This study addresses this gap by combining WAWQI, correlation, and ANOVA. The primary objectives of this study are i) to analyze physicochemical parameters, ii) to assess the river water status periodically, iii) to examine correlations between physicochemical parameters, and iv) to determine significant differences in parameters across sampling stations.

2. Material and Methods:

The Arkavathi River, a non-perennial river originating in the Nandi Hills of the Chikkaballapura district in Karnataka, southern India, is the focus of this study. Five sampling stations, namely Doddamuduvadi, Gogeredoddi, Thymasandra, Tavarekere Bekuppe and Koggedoddy, are selected. These stations are positioned along the river, spanning up to 5 km from its confluence. Data on 13 physicochemical characteristics: Bio-chemical Oxygen Demand (BOD), Dissolved Oxygen (DO), Nitrate (NO_3), pH, Electrical Conductivity (EC), Total Dissolved Solids (TDS), Total Hardness (TH), Chloride (Cl), Sulfate (SO_4), Iron (Fe), Fluoride (F), Boron (BH_3) and Sodium (Na) were collected twice a month from the Arkavathi River during the period from August 2019 to July 2020.

2.1 WAWQI method:

A notable feature of this method is that it classifies water quality based on the degree of purity as assessed through various water quality parameters (Singh et al. 2013; Kizar, 2018). This method contains three major components, which are the proportionality constant , unit weight factor (W_i), and sub-index or Ciphering water quality rating (Q_i) mathematical forms given below:

1. The proportionality constant is $K = \left(\sum_{i=1}^{n} \frac{1}{S_i} \right)^{-1}$
2. Unit weight factor is $W_i = \frac{K}{S_i};\ i = 1, 2, 3, \ldots n$
3. Ciphering the water quality rating is $Q_i = \left[\frac{V_i - V_{i0}}{S_i - V_{i0}} \right] X100$

Where,

V_i = Observed value of the i^{th} parameter of water for a particular sample station

V_{i0} = Ideal value of the i^{th} parameter of pure water

S_i = Standard acceptable value of the i^{th} parameter of water as per BIS 10500: 2012

n = Number of Physicochemical parameters

The mathematical expression of WAWQI is defined as

$$WAWQI = \frac{\sum_{i=1}^{n} W_i Q_i}{\sum_{i=1}^{n} W_i}$$

The ideal values (V_{i0}) are pH = 7.0 and DO =14.6 mg/L, and all other parameters are assumed to be zero. According to the WAWQI methodology, water quality is classified in five classes as follows: i) 0–25 indicates excellent quality; ii) 26–50 indicates good quality; iii) 51–75 indicates poor quality; iv) 76–100 indicates inferior quality; and v) above 100 indicates unsuitable for drinking (Yogendra and Puttaiah, 2008; Nayar, 2020).

3. Results and Discussion:

The measured physicochemical parameters of water at various stations of the Arkavathi River are analyzed using descriptive statistics and presented in Table 1. As per the results, the lowest BOD of 0.2 mg/L is recorded in June at Koggedoddy station, while the highest BOD of 38.4 mg/L is observed in September at Gogeredoddi station. The average BOD ranged from 2.15 mg/L at Koggedoddy to 13.15 mg/L at Gogeredoddi. All stations exhibited BOD levels exceeding 2 mg/L, indicating severe pollution of the river water.

The minimum DO of 1 mg/L is recorded in August at Gogeredoddi station, and the maximum DO of 9.4 mg/L is observed in February at Koggedoddy station. The average DO ranges from 2.26 mg/L at Gogeredoddi to 7.66 mg/L at Koggedoddy. Except for Koggedoddy station, the average DO levels at the remaining stations are below 5 mg/L, suggesting contamination of the river water. The lowest EC, 935 µS/cm, is recorded in June at the Doddamuduvadi station, and the highest, 1584 µS/cm, is observed in March at the Thymasandra station. The average EC ranged from 1172.8 µS/cm at Koggedoddy to 1273.4 mg/L at Doddamuduvadi.

The lowest TH of 198 mg/L is recorded in October at Tavarekere Bekuppe station, while the highest TH of 485 mg/L is observed in June at Koggedoddy station. The average TH ranged from 308.25 at Tavarekere Bekuppe to 349.2667 at Doddamuduvadi. Fe levels are consistently low, with the minimum recorded around 0.01 mg/L across all stations. The highest Fe concentration, 0.45 mg/L, was observed in October at the Tavarekere Bekuppe station. The average Fe concentration ranged from 0.0973 mg/L at Doddamuduvadi to 0.1313 mg/L at Koggedoddy.

Table 1. Descriptive statistics for measured physicochemical parameters of Arkavathi River (August 2019 – July 2020)

Parameters	Station	Min	Max	Mean	S.D.	Skewness	Parameters	Station	Min	Max	Mean	S.D.	Skewness
BOD	Doddamuduvadi	0.9	17.4	9.3357	5.5468	0.1621	Cl	Doddamuduvadi	138	246	214.4	27.3909	-1.9166
	Gogeredoddi	5	38.4	13.1526	7.6206	2.1191		Gogeredoddi	106	439	166.9	70.9948	3.4393
	Thymasandra	3.9	26.5	12.2368	5.4548	0.8924		Thymasandra	124	196	159.65	22.1858	-0.0127
	Tavarekere Bekuppe	2	25.3	11.5105	5.3807	0.6752		Tavarekere Bekuppe	126	202	163.35	24.4787	0.0511
	Koggedoddy	0.2	6.5	2.1526	1.9366	1.1140		Koggedoddy	122	225	170.65	33.2331	-0.3421
DO	Doddamuduvadi	1.5	5.5	3.3133	1.1127	0.1799	SO_4	Doddamuduvadi	14	58	29.6	10.7859	0.7124
	Gogeredoddi	1	4.8	2.2550	0.9568	1.2247		Gogeredoddi	21	55	36.1	9.9390	0.2354
	Thymasandra	1.7	5.3	3.345	1.1338	0.0870		Thymasandra	19	79	38.3	15.1468	1.3012
	Tavarekere Bekuppe	2	4.3	2.88	0.7218	0.4897		Tavarekere Bekuppe	19	77	36.85	15.2542	1.2420
	Koggedoddy	4.8	9.4	7.66	1.1476	-0.5747		Koggedoddy	15	85	33.55	16.4885	1.7013
NO_3	Doddamuduvadi	2.1	26.5	10.65	6.1226	1.5171	Fe	Doddamuduvadi	0.02	0.38	0.0973	0.1251	1.3635
	Gogeredoddi	0.5	64.5	9.7185	13.8246	3.8667		Gogeredoddi	0.005	0.4	0.1313	0.1194	0.882
	Thymasandra	0.6	36.5	10.6485	9.3623	1.7857		Thymasandra	0.009	0.42	0.117	0.1182	1.1655
	Tavarekere Bekuppe	1	63	15.2915	13.7394	2.6343		Tavarekere Bekuppe	0.001	0.45	0.1056	0.1203	1.6539
	Koggedoddy	3.5	31.2	15.6155	8.2343	0.3497		Koggedoddy	0.007	0.38	0.1019	0.1243	1.2819
pH	Doddamuduvadi	7.4	7.8	7.6533	0.1336	-0.1557	F	Doddamuduvadi	0.059	1.31	0.6053	0.3636	0.2245
	Gogeredoddi	7.2	7.9	7.655	0.1837	-1.1898		Gogeredoddi	0.05	0.714	0.3852	0.1706	-0.1440
	Thymasandra	7.3	7.9	7.71	0.1537	-0.9884		Thymasandra	0.052	0.779	0.4133	0.1667	-0.3643
	Tavarekere Bekuppe	7.3	7.9	7.715	0.1779	-0.8050		Tavarekere Bekuppe	0.053	0.795	0.4178	0.1856	-0.1524
	Koggedoddy	8.1	8.9	8.475	0.2433	-0.3807		Koggedoddy	0.082	1.21	0.6872	0.3369	-0.7107
EC	Doddamuduvadi	935	1447	1273.4	129.4565	-1.4085	BH_3	Doddamuduvadi	0.09	0.28	0.174	0.058	0.5562
	Gogeredoddi	967	1583	1272.05	196.3159	0.2465		Gogeredoddi	0.11	0.36	0.1955	0.0766	0.9308
	Thymasandra	996	1584	1272.45	194.4671	0.238		Thymasandra	0.1	0.29	0.187	0.0584	0.2599
	Tavarekere Bekuppe	965	1579	1271.05	194.9944	0.2216		Tavarekere Bekuppe	0.11	0.45	0.205	0.0860	1.4793
	Koggedoddy	954	1382	1172.8	148.623	-0.3551		Koggedoddy	0.06	0.4	0.191	0.1013	1.1117
TDS	Doddamuduvadi	570	1040	803.2	141.0984	0.2048	Na	Doddamuduvadi	84	156	124.1333	23.4127	-0.4866
	Gogeredoddi	544	1050	796.5	142.8258	0.1544		Gogeredoddi	83	181	129.85	29.2382	0.2861
	Thymasandra	548	1050	799.5	140.7067	0.1461		Thymasandra	90	200	133.55	29.6878	0.5153
	Tavarekere Bekuppe	540	1030	778.3	138.6416	0.3976		Tavarekere Bekuppe	94	194	133.25	29.3759	0.4939
	Koggedoddy	558	928	746.75	85.2212	-1.1614		Koggedoddy	48	181	125.5	36.8896	-0.5382
TH (as CaCO3)	Doddamuduvadi	267	465	349.2667	54.0763	0.7497							
	Gogeredoddi	202	404	318.25	58.9123	-0.3458							
	Thymasandra	213	423	318.3	53.2180	-0.0038							
	Tavarekere Bekuppe	198	377	308.25	47.6588	-0.5746							
	Koggedoddy	238	485	319.95	58.4488	0.8718							

Table 2. BIS and mean concentration values of physicochemical parameters of Arkavathi River

Parameters	BIS values	2019					2020					2019-2020				
		S1	S2	S3	S4	S5	S1	S2	S3	S4	S5	S1	S2	S3	S4	S5
BOD	2	8.06	14.24	11.36	13.32	2.98	12.53	11.94	13.21	9.5	1.23	9.3357	13.1526	12.23	11.5105	2.1526
DO	5	3.49	2.3	3.66	3.02	7.23	2.96	2.21	3.03	2.74	8.09	3.3133	2.255	3.345	2.88	7.66
NO_3	45	11.02	12.38	11.19	17	18.85	9.92	7.06	10.11	13.58	12.38	10.65	9.7185	10.6485	15.2915	15.6155
pH	8.5	7.69	7.64	7.75	7.7	8.42	7.58	7.67	7.67	7.73	8.53	7.6533	7.655	7.71	7.715	8.475
EC	750	1282.2	1203.7	1212.2	1209.9	1148.2	1255.8	1340.4	1332.7	1332.2	1197.4	1273.4	1272.05	1272.45	1271.05	1172.8
TDS	500	818.8	795.2	792.6	780.8	778.7	772	797.8	806.4	775.8	714.8	803.2	796.5	799.5	778.3	746.75
TH	300	336.1	296.7	316.5	295.2	303.3	375.6	339.8	320.1	321.3	336.6	349.2667	318.25	318.3	308.25	319.95
Cl	250	217.3	145.6	155.1	155.3	170.4	208.6	188.2	164.2	161.4	170.9	214.4	166.9	159.65	163.35	170.65
SO_4	200	32.7	34.4	34.6	32.2	33.3	23.4	37.8	42	41.5	33.8	29.6	36.1	38.3	36.85	33.55
Fe	0.3	0.09	0.14	0.11	0.11	0.09	0.11	0.127	0.126	0.103	0.112	0.0973	0.1313	0.117	0.1056	0.1019
F	1	0.59	0.36	0.38	0.39	0.55	0.65	0.41	0.44	0.45	0.83	0.6053	0.3852	0.4133	0.4178	0.6872
BH_3	0.5	0.18	0.19	0.18	0.22	0.22	0.17	0.2	0.19	0.19	0.16	0.174	0.1955	0.187	0.205	0.191
Na	200	129.4	122.7	123.3	123.2	128.2	113.6	137	143.8	143.3	122.8	124.1333	129.85	133.55	133.25	125.5

**Except pH and EC, all parameters are in mg/L*

The lowest NO_3 concentration, 0.5 mg/L, is observed in July at the Gogeredoddi station, while the highest NO_3 concentration,64.5 mg/L, is also recorded in November at the same station. The average NO_3 levels ranged from 9.72 mg/L at Gogeredoddi to 15.62 mg/L at Koggedoddy. The pH levels varied from a minimum of 7.2 in September at Gogeredoddi station to a maximum of 8.9 in August at Koggedoddy station. The average pH ranged from 7.65 at Doddamuduvadi to 8.48 at Koggedoddy.

TDS was lowest at 540 mg/L, recorded in July at Tavarekere Bekuppe station and highest at 1050 mg/L, observed in December at both Thymasandra and Gogeredoddi stations. The average TDS values ranged from 746.75 mg/L at Koggedoddy to 803.2 mg/L at Doddamuduvadi.

Cl concentrations ranged from a minimum of 106 mg/L in June at Gogeredoddi to a maximum of 439 mg/L in April at the same station. The average Cl levels ranged from 159.65 mg/L at Thymasandra to 214.4 mg/L at Doddamuduvadi. SO_4 concentrations ranged from a minimum of 14 mg/L in June at Doddamuduvadi to a maximum of 85 mg/L in February at Koggedoddy. The average SO_4 levels ranged from 29.6 mg/L at Doddamuduvadi to 38.3 mg/L at Thymasandra. F levels ranged from a minimum of 0.05 mg/L in August at Gogeredoddi to a maximum of 1.31 mg/L in November at Doddamuduvadi. The average F concentrations were 0.39 mg/L at Gogeredoddi and 0.69 mg/L at Koggedoddy. BH_3 concentrations ranged from a minimum of 0.06 mg/L in December at Koggedoddy to a maximum of 0.45 mg/L in September at Tavarekere Bekuppe. The average BH_3 levels were 0.17 mg/L at Doddamuduvadi and 0.21 mg/L at Tavarekere Bekuppe. Na concentrations ranged from a minimum of 48 mg/L in June at Koggedoddy to a maximum of 200 mg/L in March at Thymasandra. The average Na levels varied from 124.13 mg/L at Doddamuduvadi to 133.55 mg/L at Thymasandra.

The descriptive statistics reveals that the average levels of few variables at all stations are within the BIS standards (Table 2): NO_3 (<45 mg/L), pH (6.5-8.5), TDS (<500 mg/L), Cl (<250 mg/L), SO_4 (<200 mg/L), F (<1.5 mg/L), BH_3 (<1 mg/L) and Na (<200 mg/L). However, certain physicochemical parameters, such as BOD, DO, EC, TH, and Fe, exceed the acceptable limits set by the standards.

Various factors contribute to changes in their concentrations. For example, BOD and DO are mainly affected by the direct discharge of domestic sewage, industrial effluents, and other anthropogenic activities. Additionally, cooking cocoons in hot water during silk processing and filature operations in Ramanagara town, along with contamination of the Vrushabhavathi River, further increases organic and inorganic load, thereby influencing BOD and DO levels. Elevated EC, TH, and Fe values generally occur due to natural geological deposits, dissolution of minerals such as limestone and dolomite, and corrosion of iron-containing materials (Aghazadeh et al. 2017). Notably, the river flows through a rocky bed, which aids in the natural self-purification of water to some extent.

Also, some variables exhibit high variability, as indicated by their high standard deviations (S.D.), suggesting considerable differences between the samples. This variability can be attributed to various factors, including spatial and temporal variations, climatic conditions, and pollution sources. Additionally, skewness values provide insight into the distribution patterns. For instance, the BOD distribution is positively skewed toward higher concentrations at Gogeredoddi, followed by Koggedoddy. The dispersion results are very useful for understanding the factors contributing to variations in water composition.

These results suggest varying levels of contamination in the river water, making it unsuitable for drinking. However, findings provide an initial indication of water contamination; further analysis is necessary for a comprehensive understanding of the issues.

The mean concentration levels of physicochemical parameters of the Arkavathi River from five locations, along with the BIS standards for these parameters, are presented in Table 2 for WAWQI analysis. Based on these values, the data are categorized into three time scales (2019, 2020, and the combined period 2019–2020) to analyze the water quality status. The corresponding WAWQI values and water quality status are presented in Table 3, and their distribution across the study locations and time scales is shown in Figure 1.

Table 3. Periodical assessment of water quality status in the Arkavathi River based on WAWQI

Station	2019	Status of water quality	2020	Status of water quality	201-2020	Status of water quality
Doddamuduvadi	64.37	Poor water quality	83.02	Very Poor water quality	69.85	Poor water quality
Gogeredoddi	90.66	Very Poor water quality	82.48	Very Poor water quality	86.78	Very Poor water quality
Thymasandra	75.94	Very Poor water quality	86.51	Very Poor water quality	81.06	Very Poor water quality
Tavarekere Bekuppe	85.25	Very Poor water quality	70.06	Poor water quality	78.01	Very Poor water quality
Koggedoddy	48.46	Good water quality	45.86	Good water quality	47.32	Good water quality

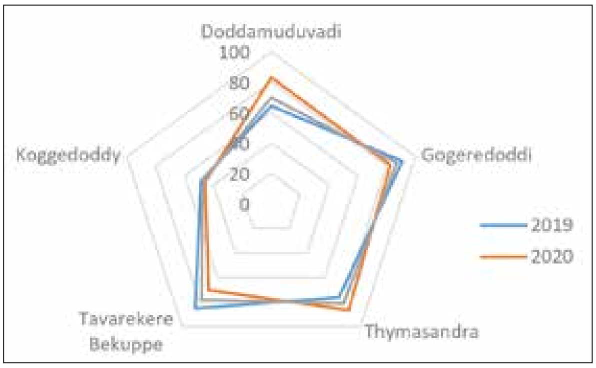

Figure 1. Comparison of WAWQI trends across stations and three-time scales

In 2019, the WAWQI analysis reveals that Gogeredoddi, with a measurement of 90.66, is categorized as exhibiting "very poor" water quality, followed by Tavarekere Bekuppe (WAWQI = 85.25) and Thymasandra (WAWQI = 75.94), both of which fall within the suboptimal water quality range. The Doddamuduvadi station, with a WAWQI of 64.37, is classified as having "poor" water quality. In contrast, Koggedoddy, with a WAWQI of 48.46, maintains "good" water quality, suitable for human consumption.

The 2020 WAWQI analysis shows that Thymasandra, with a WAWQI of 86.51, continues to exhibit "very poor" water quality, followed by Doddamuduvadi (WQI = 83.02), Gogeredoddi (WAWQI = 82.48), and Tavarekere Bekuppe (WAWQI = 70.06), all of which remain in the "poor" water quality category. Koggedoddy, with a WAWQI of 45.86, again shows "good" water quality, indicating lower contamination and suitability for drinking.

For the combined period of 2019-2020, Gogeredoddi recorded the highest WAWQI value of 86.7795, denoting "very poor" water quality, followed by Thymasandra (WAWQI = 81.06) and Tavarekere Bekuppe (WAWQI = 78.01), which also indicate "poor" water quality. Doddamuduvadi (WAWQI = 69.85) remains within the "poor" category. Conversely, Koggedoddy consistently demonstrated "good" water quality across both years, with a WQI of 47.32, signifying a consistently high standard of water purity and minimal contamination throughout the study period.

In all three analyses, all stations show that the river water is polluted and the water quality is generally very poor. Koggedoddy is a notable exception, with WAWQI values consistently below 50, indicating that the water quality there is good and suitable for drinking. The analysis focused on the results for 2020, as it offers accurate insights into water quality at various river stations. The findings reveal that the station Thymasandra has the poorest water quality, ranking highest in terms of contamination, followed by the stations Doddamuduvadi and Gogeredoddi, whereas Tavarekere Bekuppe station shows moderate contamination. In contrast, Koggedoddy Station's water is free from pollutants, with the quality being good. This higher water quality at Koggedoddy may be due to its proximity to the Cauvery River confluence, which likely enhances water quality at this site. The clear water near the confluence is crucial for both local residents and domestic animals.

The variability in water quality across stations highlights the fluctuating conditions in different parts of the river, with some stations showing a consistent decline while others maintain relatively better quality. Continuous monitoring and targeted interventions are essential to address these disparities and improve water safety. Despite the current challenges, there is potential for revitalizing the Arkavathi River. With focused efforts in water management and pollution control, the river's water quality can be significantly improved, ensuring both environmental sustainability and public health.

In addition, correlation analysis helps determine how variations in water quality parameters affect overall water quality across different sites. Here, average values from five sampling stations were used to analyze the relationships between 13 physicochemical attributes, and the results are presented in Table 4.

Table 4. Correlation matrix of thirteen parameters of water quality

	DO	NO_3	pH	EC	TDS	TH	Cl	SO_4	Fe	F	BH_3	Na	BCOD
DO	1												
NO_3	0.160	1											
pH	0.815*	0.153	1										
EC	-0.159	-0.099	-0.011	1									
TDS	0.016	0.142	0.048	0.711*	1								
TH	0.048	0.035	0.114	0.607*	0.414*	1							
Cl	0.070	-0.100	0.072	0.528*	0.369*	0.468*	1						
SO_4	0.001	-0.080	0.041	0.422*	0.331*	0.191	0.161	1					
Fe	-0.012	0.198	-0.141	-0.370*	-0.297*	-0.378*	-0.180	-0.009	1				
F	0.321*	0.251*	0.340*	-0.180	-0.279*	-0.040	0.025	-0.106	0.089	1			
BH_3	-0.040	-0.170	0.047	0.366*	0.142	0.232*	0.192	0.251*	-0.351*	-0.211*	1		
Na	-0.082	-0.146	0.087	0.745*	0.373*	0.058	0.369*	0.363*	-0.330*	-0.033	0.342*	1	
BOD	-0.576*	-0.180	-0.651*	0.181	0.058	-0.047	-0.097	0.163	-0.116	-0.313*	0.163	0.108	1

** Correlation is significant at 95% level (2-tailed).*

DO is strongly positively correlated with pH ($r = 0.815$, $p < 0.05$), weakly positively correlated with F ($r = 0.321$, $p < 0.05$), and moderately negatively correlated with BOD ($r = -0.576$, $p < 0.05$). NO_3 and F exhibit a weak positive association ($r = 0.251$, $p < 0.05$). pH shows a weak positive correlation with F ($r = 0.321$, $p = 0.05$) and a moderate negative correlation with BOD ($r = -0.651$, $p < 0.05$).

EC is moderately positively correlated with several parameters: TDS ($r = 0.711$, $p < 0.05$), TH ($r = 0.607$, $p < 0.05$), Cl ($r = 0.528$, $p < 0.05$), SO_4 ($r = 0.422$, $p < 0.05$), and BH_3 ($r = 0.366$, $p < 0.05$). EC shows a high positive correlation with Na ($r = 0.745$, $p < 0.05$) and a weak negative correlation with Fe ($r = -0.37$, $p < 0.05$). TDS exhibits weak associations with TH ($r = 0.414$, $p < 0.05$), Cl ($r = 0.369$, $p < 0.05$), SO_4 ($r = 0.331$, $p < 0.05$), and Na ($r = 0.373$, $p < 0.05$). TDS also has a weak negative association with Fe ($r = -0.297$, $p < 0.05$) and F ($r = -0.279$, $p < 0.05$). TH is weakly associated with Cl ($r = 0.468$, $p < 0.05$), Fe ($r = -0.378$, $p < 0.05$), and BH_3 ($r = 0.232$, $p < 0.05$).

Additionally, there is a weak positive association between Cl and Na ($r = 0.369$, $p < 0.05$), SO_4 and BH_3 ($r = 0.251$, $p < 0.05$), and Na ($r = 0.363$, $p < 0.05$). BH_3 shows weak positive associations with Na ($r = 0.342$, $p < 0.05$) and negative associations with F ($r = -0.211$, $p < 0.05$) and BOD ($r = -0.313$, $p < 0.05$).

From the overall analysis, the notable observation is that most physicochemical parameters show weak associations at the 95% confidence level. Also, both positive and negative associations are detected between the different types of variables. The positive correlations suggest that reducing certain parameter levels could help maintain permissible limits as directed by BIS (2012). The significant correlation coefficients identified in this analysis will aid in selecting appropriate treatments to reduce pollution levels in the Arkavathi River. To further interpret these relationships environmentally, the correlation analysis highlights the key factors influencing water quality and aquatic ecosystem health. Strong associations (DO–pH, EC–TDS, and EC–Na) indicate that oxygen availability and ionic content are primary drivers of water chemistry, directly affecting salinity and aquatic life.

Moderate correlations (DO–BOD, EC–TH, and EC–Cl) suggest secondary contributions from organic matter and mineral ions, reflecting combined natural and anthropogenic influences. Weak associations, such as those among fluoride, boron, and sulfate, indicate independent geochemical behavior, which has a limited impact on overall water quality. Collectively, these relationships emphasize that ionic strength, organic loading, and pH regulate the environmental quality of river water and its suitability for irrigation and other ecosystem services.

Moreover, One-way ANOVA with post-hoc (LSD) tests was used to compare physicochemical attributes among Arkavathi River stations, and the results are shown in Tables 5 and 6.

Table 5. ANOVA results of physicochemical parameters

Parameters	Sum of Squares	df	Mean Square	F	Sig.
DO	368.962	4	92.240	85.764	0.000
NO_3	624.555	4	156.139	1.379	0.247
pH	9.909	4	2.477	73.154	0.000
EC	155929.782	4	38982.445	1.211	0.312
TDS	41859.376	4	10464.844	0.550	0.700
TH	15539.406	4	3884.852	1.293	0.279
Cl	31990.276	4	7997.569	4.870	0.001
SO_4	787.532	4	196.883	1.017	0.403
Fe	0.014	4	0.003	0.244	0.913
F	1.416	4	0.354	5.818	0.000
BH_3	0.009	4	0.002	0.379	0.823
Na	1363.701	4	340.925	0.384	0.820
BOD	1495.200	4	373.800	12.365	0.000

Table 6. Post-Hoc (LSD) analysis of parameters across sampling stations

Parameters	Station		Sig.
BOD	Koggedoddy	Doddamuduvadi	0
		Gogeredoddi	0
		Thymasandra	0
		Tavarekere Bekuppe	0
DO	Doddamuduvadi	Gogeredoddi	0.004
	Gogeredoddi	Thymasandra	0.001
	Koggedoddy	Gogeredoddi	0
		Thymasandra	0
		Tavarekere Bekuppe	0
pH	Koggedoddy	Doddamuduvadi	0
		Gogeredoddi	0
		Thymasandra	0
		Tavarekere Bekuppe	0
Cl	Doddamuduvadi	Gogeredoddi	0.001
		Thymasandra	0
		Tavarekere Bekuppe	0
		Koggedoddy	0.002
F	Doddamuduvadi	Gogeredoddi	0.010
		Thymasandra	0.025
		Tavarekere Bekuppe	0.028
	Koggedoddy	Thymasandra	0.001
		Gogeredoddi	0
		Tavarekere Bekuppe	0.001

ANOVA revealed no significant average differences among the stations for NO_3, EC, TDS, TH, SO_4, Fe, BH_3, and Na. However, the remaining physicochemical parameters—BOD, DO, pH, Cl, and F—showed significant average differences ($p < 0.05$) among the five stations. The post hoc analysis was conducted to better understand the significant differences among sample stations for BOD, DO, pH, Cl, and F. This analysis identified which pairs of stations differed significantly. For instance, significant differences are observed between Koggedoddy and Doddamuduvadi, Thymasandra, Gogeredoddi, and Tavarekere Bekuppe for parameters such as BOD and pH.

4. Conclusion:

This study includes different physicochemical parameters that exceeded permissible limits of BIS, indicating water quality deterioration across the study stations. The overall water quality assessment requires a comprehensive approach using the WQI. To address this, the WAWQI was computed to assess contamination in the Arkavathi River. The spatial variations showed higher pollution in downstream stations, particularly near Thymasandra and Doddamuduvadi.

In addition, the correlation analysis identified substantial associations among the parameters. ANOVA revealed that some parameters (BOD, DO, pH, Cl, and F) had statistically significant differences at the 95% confidence level among the stations. These variations are due to human activities, and natural factors may also influence them. Overall results showed that Thymasandra, Doddamuduvadi, Gogeredoddi, and Tavarekere Bekuppe were grappling with significant pollution from multiple sources. Based on the results, local authorities or policymakers need to focus on periodic monitoring, stricter enforcement, and treatment interventions (effluent control, sewage management, and awareness programs) for polluted stations or design targeted clean-up plans. Despite these insights, the study is limited by a lack of microbiological and seasonal data, which could be added along with advanced pollution modeling to enhance understanding in future research.

Declarations

Ethics approval

The author has read, understood, and complied as applicable with the statement on 'Ethical responsibilities of Authors' as found in the Instructions for Authors.

Consent to participate

Not applicable.

Consent for publication

Not applicable.

Competing interests

The authors declare no competing interests.

Authors Contributions

The author is responsible for study design, data collection, analysis, interpretation, and manuscript preparation.

Funding

Not applicable.

Availability of data and materials

This study analyzed publicly available datasets.

References

Aghazadeh, N., Chitsazan, M., Golestan, Y. (2017). Hydrochemistry and quality assessment of groundwater in the Ardabil area, Iran. Applied Water Science 7: 35599-3616.

Ali, E., Amal, A.R. (2021). Assessment of Drinking Water Quality Index (WQI) in the Greater Amman Area, Jordan. Jordan Journal of Earth and Environmental Sciences 12 (4): 306-314.

Ammar, T., Noureddine, L., Abderrahmane, B. (2017). Assessment of the quality of water by hierarchical cluster and variance analyses of the Koudiat Medouar Watershed, East Algeria. Applied Water Science 7: 4197–4206.

Anshu, Y., Vinita, K. (2019). Dataset on assessment of River Yamuna, Delhi, India using indexing approach. Data in Brief: 22, 1–10.

Bharath, M., Arun Kumar, K., Syed A. (2024). Water Quality Index of Arkavathi River and Surrounding Groundwater. International Journal of Environmental Health Engineering 1-7.

BIS, Standard prescribed required desirable limits for drinking water, Bureau of Indian Standard. (2012).

Brown, R.M., Mcclelland, N.I., Deininger, R.A., Tozer R.G. (1970). A water quality index: do we dare? Water & Sewage Works 7: 339-343.

Chabuk, A., Al-Madhlom, Q., Al-Maliki, A., Al-Ansari, N., Hussain, H.M., Laue, J. (2020). Water quality assessment along Tigris River (Iraq) using water quality index (WQI) and GIS software. Arab Journal of Geosciences 13-654.

Dede, O.T., Telci, I.T., Aral, M.M. (2013). The use of water quality index models for the evaluation of surface water quality:

a case study for Kirmir Basin, Ankara, Turkey. Water Quality Exposure and Health 5 (1): 41–56

Diop, M., Ibrahima, M., Hadji, E.M.S., Tidiane, D., Liengsy, B., Cheikh, M. (2023). Development and application of water quality index (WQI) for the evaluation of the physicochemical quality of groundwater in gold mining areas of Southeastern Senegal. Journal of Water Resource and Protection 15: 33-50.

Divya, D.P., Darshan, J.M., Hazi, M.A., Mohdzuned, M.S., Shivendra, J., Upaka, R. (2023). Application of the Weighted Arithmetic Water Quality Index in Assessing Groundwater Quality: A Case Study of the South Gujarat Region. Water 15(19).

Ewaid, S.H., Abed, S.A. (2017). Water quality index for Al-Gharraf River, southern Iraq. Egypt Journal of Aquatic Research 43(2): 117–122.

Faroon, M.A., Dina, A.Y., Zainb, A.A.A.S. (2023). A New Modeled Equation of the Water Quality Index for Examination of the Water Quality of Treatment Plants in Basra City (Iraq). Journal of Environmental Research. Engineering and Management 79(1): 110–121.

Gazzaz, N.M., Yusoff, M.K., Aris, A.Z., Juahir, H., Ramli, M.F. (2012). Artificial neural network modeling of the water quality index for Kinta River (Malaysia) using water quality variables as predictors. Marine Pollution Bulletin 64 (11): 2409–2420.

Horton, R.K. (1965). An index number system for rating water quality. Journal of Water Pollution Control Federation 37(3): 300–306.

Kachroud, M., Trolard, F., Kei, M., Jebari, S., Bourrie, G. (2019). Water quality indices: challenges and application limits in the literature. Water 11(2): 01–26.

Kazi, T.G., Arain, M.B., Jamali, M.K., Jalbani, N., Afridi, H.I., Sarfraz, R.A., Baig, J.A., Shah, A. Q. (2009). Assessment of water quality of polluted lake using multivariate statistical techniques: A case study. Ecotoxicology Environmental Safety 72(20): 301-309.

Khushbu, K.B, Hymavathi, T., Mathuvanthi, C.N., Mavaja, N.A., Srinivasa, C.V. (2021). Impact of urbanisation on lakes a study of Bengaluru lakes through water quality index (WQI) and overall index of pollution (OIP). Environmental Monitoring Assessment 193: 408.

Kosha, A.S., Geeta, S.J. (2017). Evaluation of water quality index for River Sabarmati, Gujarat, India. Applied Water Science 7: 1349–1358.

Loganathan, K., Ahamed, A.J. (2017). Multivariate statistical techniques for the evaluation of groundwater quality Amaravathi River basin: South India. Applied Water Science 7: 4633-4649.

Lumb, A., Sharma, T.C., Bibeault, J.F. (2011). A review of genesis and evolution of water quality index (WQI) and some future directions. Water Quality Exposure and Health 3: 11–24.

Nayar, R. (2020). Assessment of water quality index and monitoring of pollutants by physicochemical analysis in water bodies: A review. International Journal of Engineering Research 9: 178–185.

Oni, O., Fasakin, O. (2016). The use of water quality index method to determine the portability of surface water and groundwater in the vicinity of a municipal solid waste dumpsite in Nigeria. American Journal of Engineering Research 5(10): 96-101.

Pejman, A.H., Bidhendi, G.R.N., Karbassi, A.R., Mehrdadi, N., Esmaeili, B.M. (2009). Evaluation of spatial and seasonal variations in surface water quality using multivariate statistical techniques. International Journal of Environmental Science and Technology 6 (3): 467-476.

Prasad, M.P., Harish, K., Raviraj, K., Umakant, P.K. (2020). Real-time water quality monitoring through Internet of Things and ANOVA-based analysis: a case study on river Krishna. Applied Water Science 10(22): 1-16.

Sandra, C., Paula, E.N., Naim, O., Youssef, E.R., Desiree, E.A. (2023). A comprehensive review of water quality indices (WQIs): history, models, attempts and perspectives. Reviews Environmental Science and Biotechnology 22 (2): 349-395.

Satish, C.S., Asadi, S.S. (2017). Estimation of water quality index by weighted arithmetic water quality index method: A model study. International Journal of Civil Engineering and Technology 8 (4): 1215-1222.

Shirodkar, P.V., Pradhan, U.K., Fernandes D., Haldankar, S.R., Rao, G.S. (2010). Influence of anthropogenic activities on the existing environmental conditions of Kandla Creek (Gulf of Kutch). Current Science India 98(6): 815-828.

Singh, P.K., Tiwari, A.K., Panigary, B.P., Mahato, K. (2013). Water quality indices used for water resources vulnerability assessment using GIS technique: a review. International Journal of Earth Science and Engineering 6: 1594-1600.

Tasneem, H., Mustafa A.K. (2021). Comparison between Weighted Arithmetic and Canadian Council of Ministers of the Environment Water Quality Indices performance in Amman-Zarqa Area, Jordan. Jordan Journal of Earth and Environmental Sciences 12 (4): 295-305.

Tyagi, S., Sharma, B., Singh, P., Dobhal, R. (2013). Water quality assessment in terms of water quality index. American Journal of Water Resources 1(3): 34-38.

VishnuRadhan, R., Zainudin, Z., Sreekanth, G.B., Dhiman, R., NoorSalleh, M., Vethamonv, P. (2017). Temporal Water quality response in an urban river: A case study in peninsular Malaysia. Applied Water Science 7: 923-933.

Yogendra, K., Puttaiah, E.T. (2008). Determination of Water Quality Index and Suitability of an Urban Waterbody in Shimoga Town, Karnataka. Proceedings of Taal2007: The 12th World Lake Conference: 342-346.

Zhang, Y., Guo, F., Meng, W., Wang, X. Q. (2009). Water quality assessment and source identification of Daliao River Basin using multivariate statistical methods. Environmental Monitoring and Assessment 152 (1-4): 105-121.

JJEES

JJEES (2026) 17 (3): 311-323
ISSN 1995-6681

Jordan Journal of Earth and Environmental Sciences

Surface Temperature and Evaporation Rates across the Gulf of Aqaba as Investigated from Landsat and Modis Data

Ibrahim M. Oroud* and Sattam Salem AlShogoor

Mutah University, Karak, Jordan

Received on 19 November 2025; Accepted on 12 March 2026

Abstract

Monthly surface temperature (ST) and evaporation rates across the Gulf of Aqaba (GOA) were derived using thermal images from Landsat 8 and near-surface meteorological data. Retrieved ST were compared with surface temperature from MODIS data for the same period, and both sets yielded similar results. Surface temperature of the GOA showed little annual range, with a minimum of ~20 ^{O}C in March and a maximum of 27 ^{O}C in August and September. However, the annual temperature range across the GOA is not uniform, varying from ~5.6 ^{O}C in the southern parts to ~9 ^{O}C in the northern parts, reflecting the flow regime from the Red Sea and the climate conditions across the GOA.

Average annual evaporation rate across the GOA, as calculated with the Penman equation, is ~2860 mm, giving a net water balance deficit for the entire GOA of ~ 8.8×10^9 m^3 annually. This deficit is compensated primarily via water flux from the Red Sea. Evaporation during April through September accounts for ~ one half of annual evaporation while the other half occurs during October through March. This evaporation characteristic is linked to the very large heat storage during the warming phase and its subsequent release in the cooling period of the annual cycle. A small evaporation gradient is noticed across the GOA, being more distinct in the cold season. The aerodynamic term represents a significant portion of evaporation during the low sun period, accounting for ~56% of total evaporation during December through February and ~28% from July through September. The annual trend of evaporation partitioning between energy and aerodynamic terms is attributed to the evaporation conversion efficiency of net radiation which increases as temperature increases. Thermal images have the potential to provide accurate measurements of surface temperature that can be used to understand climate dynamics and water balance across large spatial domains.

Keywords: *Gulf of Aqaba, evaporation rates, thermal images, atmospheric correction, marine environments*

1. Introduction

Evaporation is a crucial geophysical component of the energy and hydrological cycle over the Earth's surface. Around 77% of net radiation is dissipated via evaporation on a global scale (Budyko, 1974; Vonder Haar, 1994). The transformation of water from the liquid to the gaseous phase requires a large input of energy, and 2.45 MJ is needed to evaporate 1 kg of water. Unlike many other atmospheric elements, such as wind speed, air temperature, and relative humidity, which can directly be measured, evaporation is a derived element, and its rate is an integrated function of numerous interrelated surface elements and atmospheric forcings (Brutsaert, 1982; Allen et al., 1998; Foken, 2008). Until recently, sea surface temperature and turbulent fluxes were measured using conventional methods such as offshore sites and floating buoys to evaluate the annual cycle of temperature and spatial distribution of heat and mass transport across the sea-atmosphere interface (Stammer et al., 2002; Reynolds and Chelton, 2010; Gristey et al., 2021). These measurements provided valuable information of the spatial distribution of SST and vertical turbulent fluxes over the various parts of the world oceans (Vonder Haar, 1994; Kelkar, 2007). Although very informative and providing valuable background data, field campaigns are usually confined to point measurements, costly, and require large logistical investments. Furthermore, the spatial distribution of SST and turbulent fluxes obtained using field campaigns is deduced by interpolation rather than by direct measurements, entailing substantial smoothing and data approximation. The launch of satellites equipped with sensors having high spectral, radiometric, and spatial resolutions, along with their large synoptic scenes and relatively short time revisits, has revolutionized data gathering methods (Qin et al., 2001; Wang et al., 2015; Cristobal et al., 2018). Sensors onboard satellites can capture a large scene instantaneously, allowing for direct evaluation of processes in a static time domain (Sobrino et al., 2018; Diaz et al., 2021; Oroud, 2022; Oroud, 2025). Numerous investigators indicated that thermal satellite images yield high quality surface temperature with excellent spatial and temporal resolutions (Qin et al., 2001; Jimenez-Munoz and Sobrino, 2003; Jimenez-Munoz et al., 2014). The accuracy of atmospherically corrected surface temperature has been reported to be less than 1 K in relatively dry atmospheres with water vapor content below 2 g (Qin et al., 2003; Jiménez-Muñoz et al., 2009; Sobrino et al., 2018).

The Gulf of Aqaba (hereafter GOA), which represents

* Corresponding author e-mail: ioroud@mutah.edu.jo

the northern flank of the Red Sea, has received considerable attention due to its unique ecological habitats, the widespread tourist activity, the presence of numerous desalination projects and for understanding temperature structure, turbulent fluxes and water exchange with the Red Sea (Manasrah et al., 2006; 2019; Biton and Gildor, 2011; Ahmed et al., 2012; Faraj et al., 2022). Numerous studies were conducted in the GOA and the Red Sea to assess the energy budget, salinity, turbulent fluxes, and water exchange with the open seas (Assaf and Kessler, 1976; Paldor and Anati, 1979; Matsoukas et al., 2005; 2007).

The earliest attempt to assess evaporation from the GOA and the Red Sea was carried out by Neumann (1952) who indicated that evaporation rates were in the range 2000 mm a^{-1} in the GOA at 29^{O} N to 2350 mm a^{-1} in the southern parts of the Red Sea ~ 15^{O} N. Assaf and Kessler (1976) evaluated the annual flux of evaporation from the GOA based on hourly data collected in two sites situated in the northern parts of the GOA and indicated that evaporation was close to 3600 mm a^{-1}. Paldor and Anati (1979) investigated the monthly distribution of temperature and salinity across the GOA based on observations collected from 1974 through 1977 at nine sites distributed along the GOA. They found that surface temperature and salinity were high in summer ~26 ^{O}C, and 41 g kg^{-1} and low in winter ~21 ^{O}C and 40.5 g kg-^{1}.

Other relevant investigations were carried out in the Red Sea to assess turbulent fluxes across its surface; thus, the results obtained in this area are expected to be close to those encountered over the GOA because of the relative similarity in climate conditions. For instance, da Salva et al (1994) reported that the evaporation rate from the Red Sea is close to 1680 mm a^{-1}. Using a coarse spatial resolution of 2.5 × 2.5 degrees, Matsoukas et al (2007) indicated that evaporation over the Red Sea is ~2120 mm a^{-1} (see also Matsoukas et al., 2005). Based on the Penman equation, Dehwaha et al (2016) reported that evaporation from the Red Sea was close to 2600 mm a^{-1}. Numerous assumptions were made by the various investigators to reach the estimates presented above, such as the homogeneity of surface temperature and uniform weather conditions across the study sites. Furthermore, the various investigators did not take into account the suppression of evaporation caused by the salinity of seawater (e.g., Calder and Neal, 1984; Oroud, 2019a; Oroud, 2023). Thus, the objective of the present investigation is to examine the annual cycle of surface temperature and evaporation rates across the GOA using thermal images onboard Landsat 8 during the period February 2020 through January 2021. Surface temperatures retrieved from Landsat were compared with their corresponding values obtained from MODIS data. The present investigation is important for understanding the annual cycle of the sea surface thermal regime and the energy budget partitioning in a hyperarid marine environment, as well as for assessing water flux from the Red Sea.

2. Study area

The GOA forms the southern end of the Dead Sea Transform, created by the Sinai Peninsula's bifurcation of the northern Red Sea (Biton and Gildor, 2011). The Gulf of Suez occupies the western flank, while the GOA occupies the eastern one (Figure 1). The study area is located between 34.4 - 34.96 E and between 28 - 29.54 N. The north-south extension of the GOA is ~ 180 km, and its maximum width is ~ 28 km, with an area close to 3100 km^2. The gulf is semi-closed with an average depth of 800 m and a maximum depth reaching 1800 m (Biton and Gildor, 2011). This elongated, narrow gulf is an important marine site hosting unique assemblages of ecological habitats and supports a well-known coral reef ecosystem.

The GOA is situated in a hyperarid climate zone, and annual precipitation ranges from 20 to 30 mm a^{-1}, with some years passing without a single rainy event. Being located in a permanent subtropical high- pressure zone, the GOA receives substantial amounts of solar radiation year-round. Air temperature closely tracks solar radiation receipt, with average monthly air temperature varying from 15°C in January to 33°C in July and August.

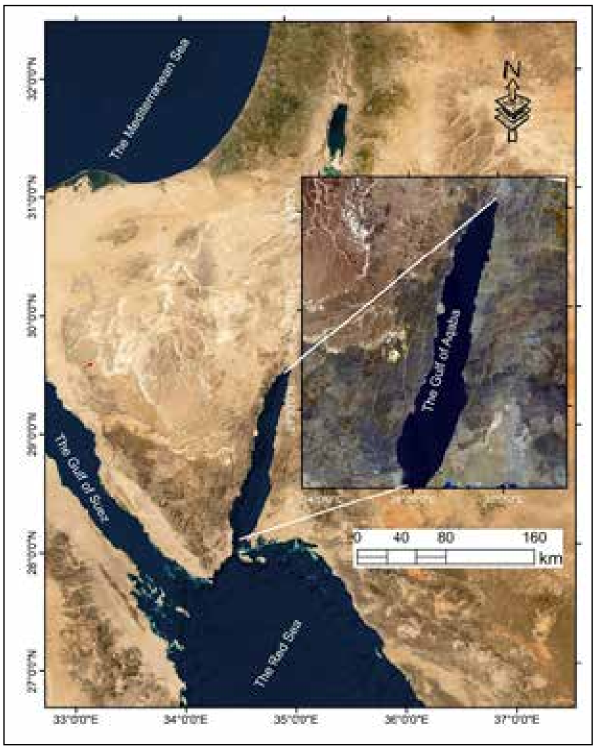

Figure 1. Location of the study area. The inset map is a pan-sharpened image taken in April 2020, showing the Gulf of Aqaba and surrounding terrain in greater detail.

3. Data and methods

A flowchart of the data requirements and processes involved in obtaining surface temperatures and evaporation rates across the GOA is presented in Figure 2. The first step was to estimate the kinetic temperature of the study area. After that, a series of processes were carried out to generate raster layers- e.g., incoming longwave radiation, solar radiation, upwelling thermal radiation- needed to estimate evaporation across the study area. A detailed discussion of the generated elements is presented in the flowchart.

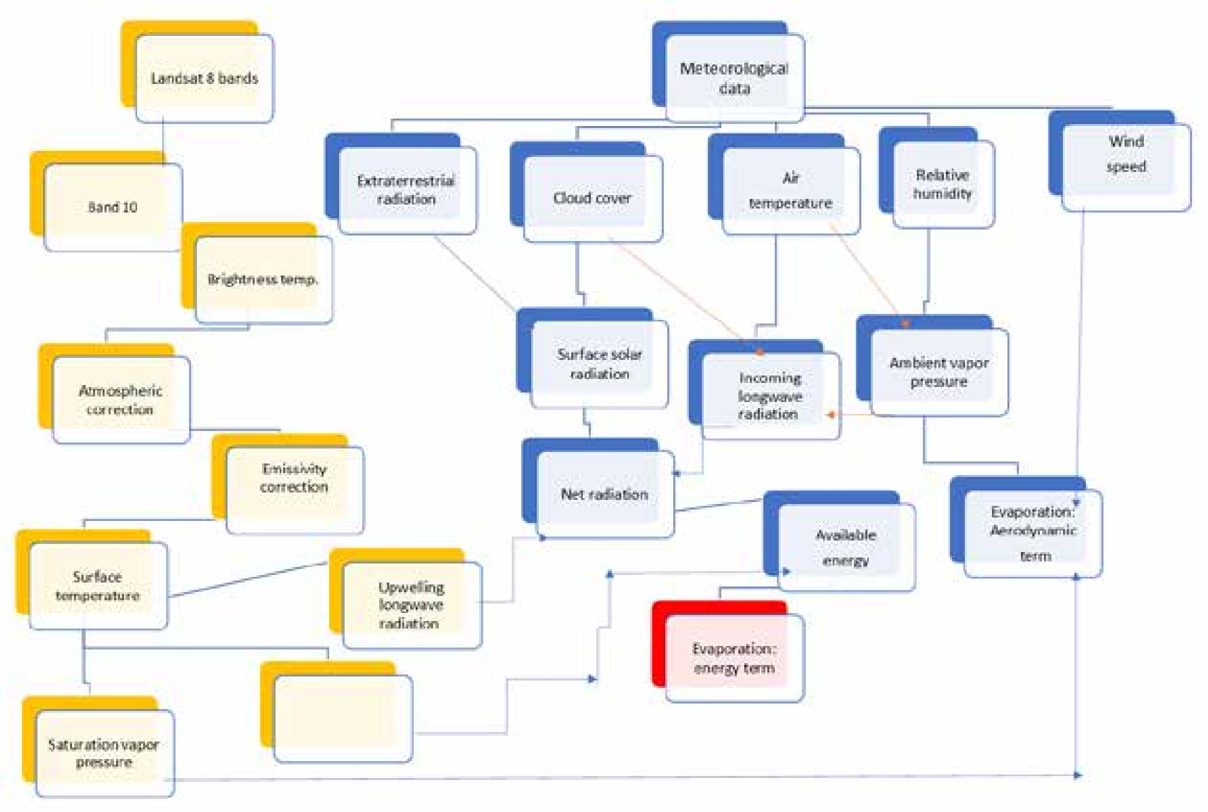

Figure 2. A flowchart showing data requirements and processes involved in obtaining surface temperature and evaporation across the GOA.

3.1 Meteorological data

Monthly meteorological data are obtained from archived data collected by the Department of Meteorology, Jordan, and from open sources. Solar radiation reaching the surface is evaluated from the extraterrestrial radiation and cloud cover observed in the northern tip of the Gulf. It is assumed that relative humidity, wind speed, and cloud cover over the GOA are well represented by observations in the northern parts, given the similarity in climate conditions across the study area. Table 1 displays the average monthly meteorological variables observed at the northern tip of the GOA.

Table 1. Average monthly weather conditions in the northern tip of the Gulf of Aqaba.

Month	So (MJ $m^2.day^{-1}$)	Ta (^oC)	RH (%)	U (m s-1)	C. cover (%)
J	14.88	15.0	53	6.0	23
F	18.96	16.7	45	6.0	22
M	23.45	20.0	37	6.7	20
A	27.00	24.4	30	6.7	23
M	29.15	28.9	29	6.9	19
J	29.95	31.7	31	7.5	3
J	29.61	33.3	33	7.1	2
A	28.11	33.3	38	7.1	1
S	25.32	31.1	44	6.8	2
O	21.43	27.2	47	5.9	13
N	17.43	21.7	48	5.9	24
D	14.65	16.7	53	5.8	27

3.2 Satellite data

3.2.1 Landsat data

8 OLI/TIRS has two thermal bands, 10 and 11, operating in the atmospheric window, 10-12.5 µm where atmospheric absorption and emission reach their minimum values. Band 10 operates in the spectral range 10.60–11.19 µm, with an effective wavelength of 10.904 µm, while band 11 operates in the spectral range 11.5-12.51 µm (Cristobal et al., 2018; Oroud and Balling, 2021). Thermal bands onboard Landsat 8 are captured at spatial and radiometric resolutions of 100 m and 12-bit, but are delivered to users at 30 m and 16-bit. Twelve images of the thermal band 10 covering the period February 2020 through January 2021, one for each month, were downloaded from the USGS site (https://earthexplorer.usgs.gov: path 174 Row 40). To ensure proper representation of surface temperature and to eliminate the influence of nearby terrain, the first 1 km along the shoreline was excluded.

3.2.2 MODIS data

Monthly SST from the Moderate Resolution Imaging Spectroradiometer (MODIS) onboard the Aqua satellite was downloaded for the study area from February 2020 through January 2021 to provide an independent check of the SST retrieved from band 10 onboard Landsat 8. MODIS sensors are sun-synchronous and flown on the NASA Terra and Aqua satellites, collecting imagery in 36 spectral bands for a wide range of applications in agriculture, forestry, meteorology, oceanography, and climate dynamics. This sensor is a key instrument designed as part of the Earth Observing System (EOS) to provide long-term global coverage of the Earth's land, ocean, and atmospheric properties. The MODIS SST product has high accuracy, with uncertainties of ~0.45 K at nadir and 0.56 K at 45°, as described in the Algorithm Technical Background Document (Brown and Minnett, 1999). This uncertainty range has been confirmed by other investigators (Qin et al., 2014; Ghanea et al., 2016; Cao et al., 2021). Thus, MODIS SST products can be used as a benchmark for SST validation. Retrieved SST was the average of daytime and nighttime readings, with a spatial resolution of 0.1 degree. All images were processed using ArcGIS Pro.

3.3 The brightness temperature

The spectral radiance emitted by a blackbody can be formulated using the Planck function (Menzel, 2006; Cristobal et al., 2018),

$$B\lambda(T) = \frac{hc^2}{\lambda^5 \mathrm{Exp}^{\left(\frac{hc}{\lambda kT}\right)} - 1} \tag{1}$$

where Bλ(T) is the spectral radiance (W m^{-2} sr^{-1} μm^{-1}), λ is wavelength (μm), h is the Planck's constant (6.626076 × 10^{-34} J s), k is the Boltzmann's constant (1.380658× 10^{-23} J K^{-1}), T is the blackbody temperature, and c is the speed of light. Radiance impinging on a satellite sensor (L_{TOA}) is expressed as (Menzel, 2006),

$$L_{TOA} = \tau\epsilon L_S + l_U + \tau(1-\epsilon)L_D \tag{2}$$

where τ is atmospheric transmission (-), LS is radiation emitted by the surface, ε is surface emissivity in the specified band (-), L_D and L_U are downwelling and upwelling atmospheric radiation, respectively; all terms are expressed in (Wm^{-2} sr^{1} μm^{-1}). Thermal radiance at a satellite sensor is converted to a brightness temperature using the following form,

$$TB = \frac{K2}{\mathrm{Ln}\left(\frac{K1}{L\lambda}+1\right)} \tag{3}$$

where TB is the at sensor or brightness temperature, K1 and K2 are constants obtained from the Landsat 8 manual.

The actual surface temperature is different from the brightness temperature due to atmospheric and emissivity effects (Menzel, 2006; Cristobal et al., 2018). The temperature difference between the kinetic temperature and the brightness temperature could reach several degrees depending on atmospheric conditions and the actual emissivity across a scene (Qin et al., 2003; Menzel, 2006; Cristobal et al., 2018). Emissivity effect could be large for bare sandy dry surfaces, but it is relatively small for water surfaces because the spectral emissivity of water within the band used to retrieve surface radiance is close to unity (e.g., Menzel, 2006).

Due to absorption and remission of longwave radiation, the atmosphere influences the radiance received by a satellite sensor (e.g., Salisbury and D'Aria, 1992; Faysash and Smith, 1999). The temperature of the intervening atmosphere is usually lower than that of the surface, leading to a reduction in the recorded radiance at the sensor level (Barsi et al., 2005; Menzel, 2006; Rosas et al., 2017; Oroud, 2020). The kinetic temperature of the sea surface or that of a ground surface is higher than the brightness temperature. The effect of the atmosphere on the retrieved temperature depends primarily on the vertical structure of humidity and temperature within the lower troposphere (Parata, 1994; Qin et al., 2001; Wang et al., 2015; Cristobal et al., 2018; Diaz et al., 2021). Numerous techniques have been used to correct for the atmospheric effect such as the radiative transfer equation like MOTRAN, in situ measurements or empirical equations. The algorithm presented by Barsi et al (2005) to correct for the atmospheric effect is implemented in the present investigation (http://atmcorr.gsfc.nasa.gov.)

3.4 Evaporation calculation

Evaporation from a water surface can be estimated using a variety of methods, such as the pan ratio method, the bulk transfer method, the Penman- Priestly method, the combination equation, and the eddy covariance (Allen et al., 1998; Bouwer et al., 2007; Metzger et al., 2018; Oroud, 2019a). The bulk transfer method, which is widely used, is quite sensitive to the transfer coefficient and vapor pressure deficit across the surface- atmosphere boundary, and thus this method will give an evaporation that synchronizes closely with water temperature. The combination equation accounts for radiative, convective, and storage terms and is therefore expected to provide a better representation of the annual course of evaporation from a deep-water body like the GOA. The Penman equation is written (Mundo and Gomez, 2017; Oroud, 2019a),

$$E = \frac{\beta\Delta(RN+QS)+\Psi f(u)(\beta e_w - e_a)}{\beta\Delta+\Psi} \tag{4}$$

where E is evaporation (Wm^{-2}), β is the activity coefficient of the water surface (-), Δ is the slope of saturation vapor pressure with respect to temperature (hPa K^{-1}), RN is net radiation (W m^{-2}), QS is the change in heat storage (Wm^{-2}), ψ is the psychrometric constant (hPa K^{-1}), f(u) is the wind function (Wm^{-2} hPa^{-1}), e_w and ea are vapor pressure at the water surface and in the contiguous air (hPa). All parameters comprising the Penman equation are presented below.

The energy balance at the surface- atmosphere boundary may be expressed as (Foken, 2008; Oroud, 2023),

$$Rn = S(1-\alpha) + L\downarrow - L\uparrow \tag{5}$$

where Rn is net radiation (W m^{-2}), α is surface albedo (-), are incoming and outgoing longwave radiation. Monthly solar radiation is estimated from extraterrestrial radiation and cloud cover (Iqbal, 1982)

$$S_G = \left(a + b\frac{n}{N}\right) S_{Ext} \tag{6}$$

where SG is solar radiation reaching the surface, a and b are empirical constants, n and N are actual sunshine hours and the theoretical daylight length, S_{EXT} is the daily extraterrestrial solar radiation (MJ m^{-2} day^{-1}), computed using the following form (Iqbal, 1983),

$$S_{EXT} = S_C\, D(\sin\emptyset \sin\delta + \cos\emptyset \cos\delta \sin\omega) \tag{7}$$

where SC is the solar constant, D is the inverse earth-sun distance, Φ is latitude, δ is solar declination, and ω is the sunset angle.

Down-coming longwave radiation is estimated using an expression presented by Brutsaert (1982),

$$L\downarrow = \epsilon_a \, \sigma T_a^4 (1 + cc^{\gamma}) \quad (8)$$

where ε_a is atmospheric emissivity (-), σ is the Stefan-Boltzmann constant (5.667×10^{-8} $Wm^{-2}K^{-4}$), T_a is near surface air temperature (K), cc is cloud fraction, and is a correction term for cloud cover contribution (Oroud and Nasrallah, 1998). Figure 3 shows the spatial distribution of the average air temperature in January and July across the GOA.

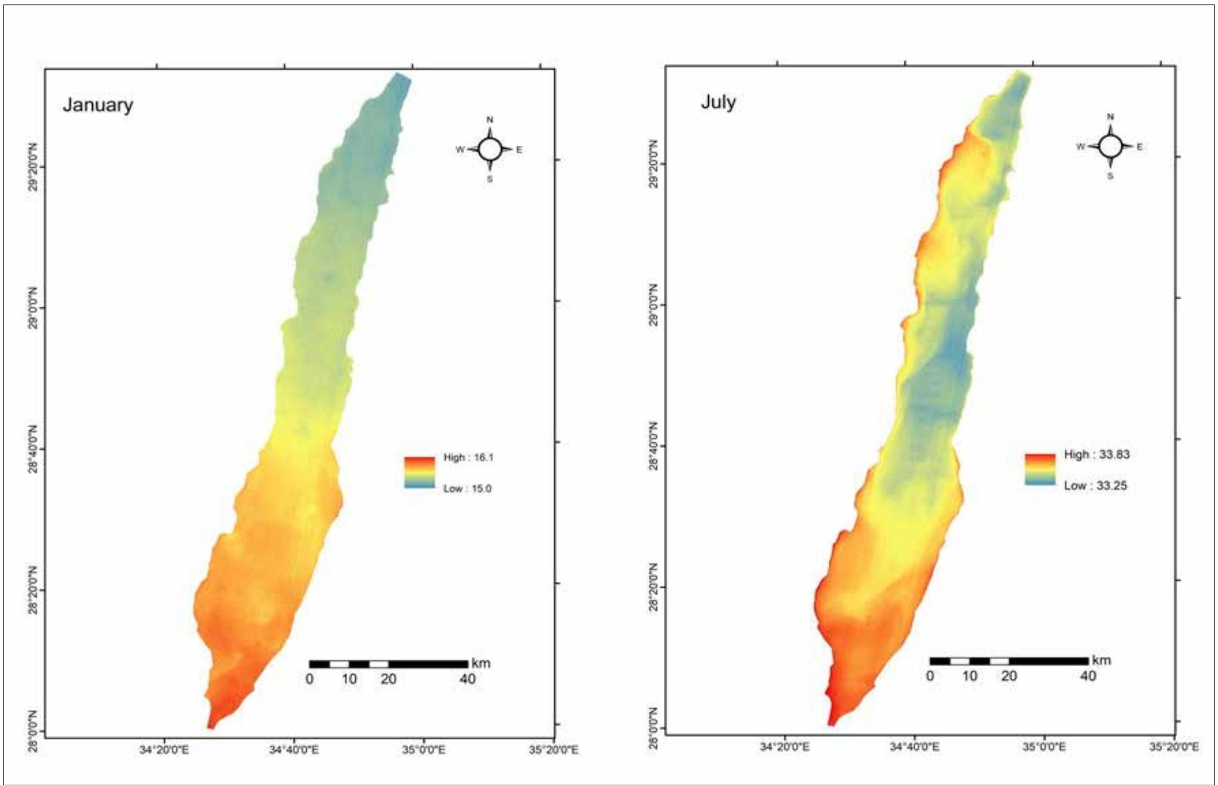

Figure 3. The spatial distribution of the average air temperature across the GOA in January and July.

The upwelling surface radiation from the sea surface is calculated using the following equation,

$$L\uparrow = \epsilon_S \, \sigma T_S^4 \quad (9)$$

where ε_s is surface emissivity, 0.97 for seawater, and T_S is surface temperature (K). Surface albedo over the GOA is assumed to be 0.05. All calculations of the various energy balance terms were performed on the raster layers using ArcGIS Pro.

The subsurface storage term is calculated assuming an effective mixed layer depth of 45 m (Oroud, 1997; Biton and Gildor, 2011),

$$QS = \rho_W \, C_W \frac{h(T_S^n - T_S^{n-1})}{\delta t} \quad (10)$$

where QS is subsurface storage (Wm^{-2}), ρw is water density ($kg\ m^{-3}$), CW is the specific heat of water ($J\ kg^{-1}\ K^{-1}$), h is the effective mixed layer depth (m), T_S^n and T_S^{n-1} are the surface temperature at the current and previous month, respectively, and δt is the time increment. The exact specification of the effective mixing depth does not influence the total annual evaporation as QS approaches zero for the annual cycle.

The wind function, which accounts for the aerodynamic term is expressed using the following form (Oroud, 2023),

$$F(u) = 3.6 + 2.5\,U \quad (11)$$

where U is wind speed ($m\ s^{-1}$).

The activity coefficient in Eqn. 4 accounts for the suppression of the saturation vapor pressure caused by dissolved salts. The activity of a saline solution may be expressed using the following form (Oroud, 2019a),

$$B = \frac{e_{w(Ti)}}{e_{f(Ti)}} \quad (12)$$

where e_w is the saturation vapor pressure of the saline solution and e_f is the saturation vapor pressure for freshwater at the same temperature. The average activity for the open seas and oceans is ~ 0.974, while it is for the GOA is ~ .97 because of its higher salinity. Water vapor pressure at the surface is calculated using the following expression (Brutsaert, 1982),

$$E_s = 6.1078 \exp\left(17.269 \frac{Tw}{237.3 + Tw}\right) \quad (13)$$

where Tw is surface water temperature in Celsius. The near-surface vapor pressure is calculated by (ea* RH), where the first term is the saturation vapor pressure at T_a and RH is the relative humidity.

4. Results

4.1 Retrieved temperature

An important point for further analysis is the accuracy of the retrieved surface temperature. Figure 4 displays a scatter diagram of satellite-retrieved skin temperature compared to corresponding values retrieved from the MODIS sensor.

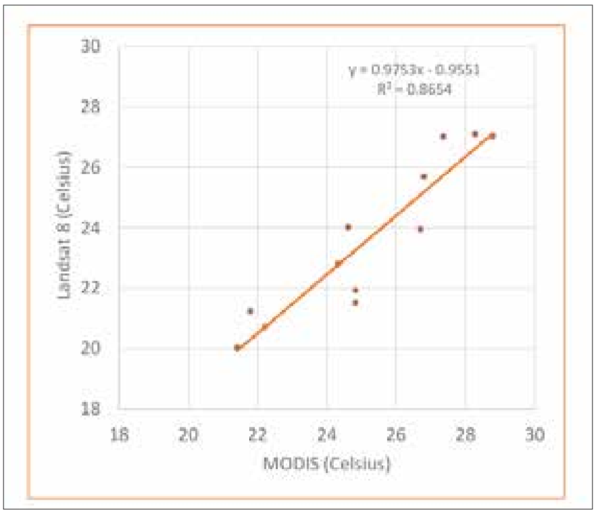

Figure 4. A scatter diagram of satellite-retrieved skin temperature versus that obtained from MODIS data.

There is close agreement between the satellite-retrieved temperatures and MODIS data, with a correlation coefficient of 0.94. Landsat 8 tends to slightly underestimate the surface temperature compared to MODIS as observed from Figure 4. This underestimation is likely linked to two main factors: 1- Landsat 8 observes the skin temperature around 10 AM when the temperature of the top water layer reaches its minimum values due to nocturnal cooling experienced the night before and the high thermal inertia of water, while the readings of MODIS are the average of observations taken at 1.00 PM and 1.00 AM. 2- MODIS data are slightly higher because of the slow heating of the upper water layer at 1.00 PM caused by the continuous flux of solar radiation and also due to the rise of the near-surface air temperature during the daytime hours. The temperature of the top layer at 1.00 AM is still warm due to the very slow cooling of water at night because the heat supplied to compensate for the net radiation deficit at night is drawn from a deep-water layer with very high heat capacity (heat capacity = $\rho_W C_{W.} h$: see Eqn. 11). In fact, cooling at the surface layer triggers strong instability as cooled water sinks downward and gets readily replaced by warmer water from beneath. Thus, the different timing of images taken for the two satellite platforms may explain the slightly cooler temperatures of Landsat 8 compared to those obtained by MODIS. The overall accuracy, however, is quite high, and surface temperature retrieved from the high-resolution thermal images onboard Landsat 8 can be used for operational purposes in lieu of observed values to investigate surface fluxes, thereby avoiding the restrictions imposed by measurement locality and the footprints of nearby terrain.

4.2 Surface temperature across the GOA

The spatial distribution of monthly surface temperature across the GOA in six selected months, three in winter and three in summer, is presented in Figure 5. The annual surface temperature varies from an average of 20 ^{O}C in March to 27 ^{O}C in August and September. A few distinct thermal features can be identified from the figures:

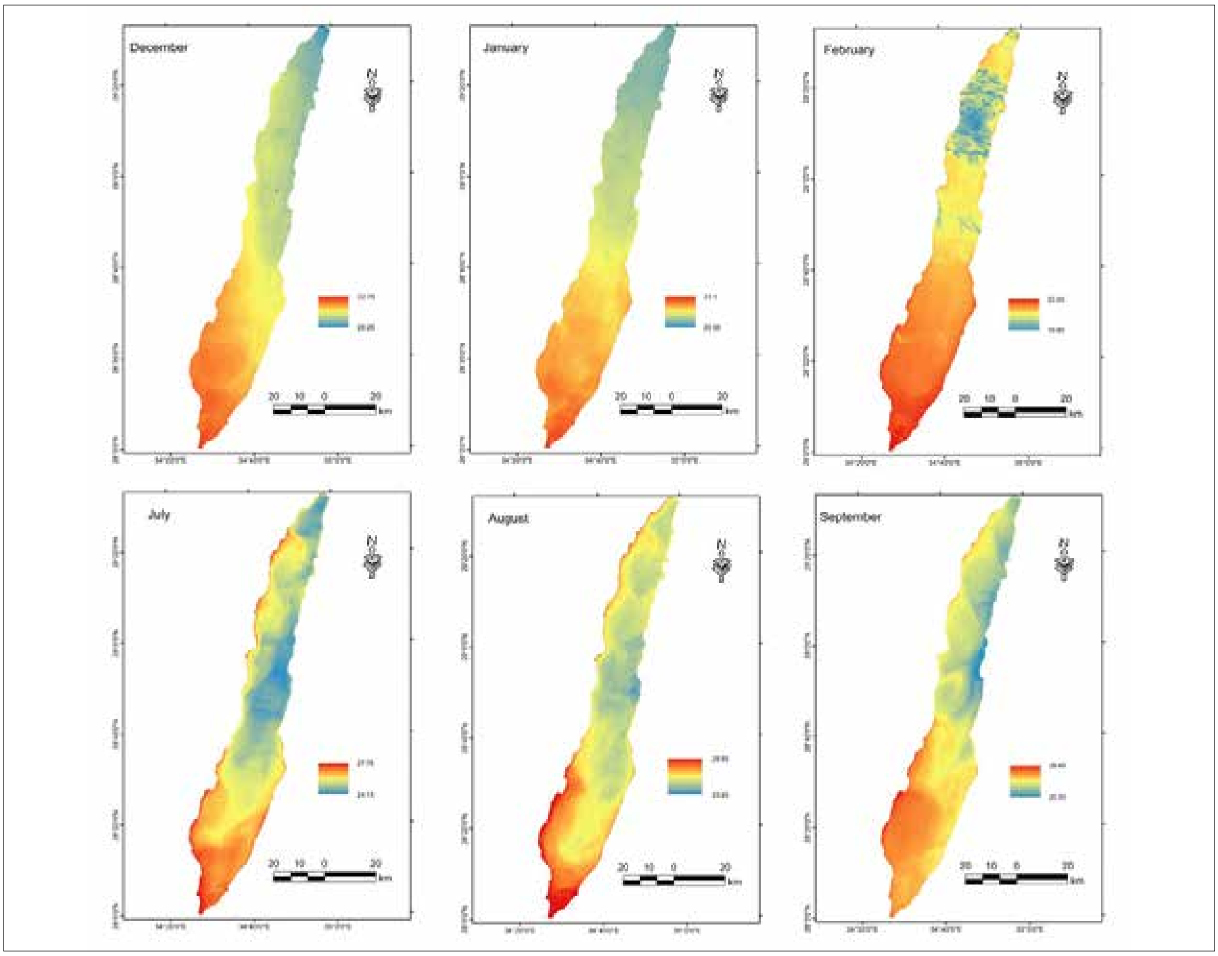

Figure 5. The spatial distribution of monthly surface temperature across the GOA in six selected months, three in winter and three in summer.

1- There is a clear north-south temperature gradient across the GOA. The temperature difference between the northern and southern parts is about 1.0-1.5 °C in winter and about 0.5 °C in summer. These seasonal differences are linked to hydrographic and meteorological forcings. Warm surface waters from the Red Sea feeding the GOA contribute to the observed warmer surface temperatures in winter in the southern parts. Furthermore, the southern parts have higher temperatures and receive more solar radiation during winter than the northern parts, as presented. Extraterrestrial radiation over the northern and southern parts of the GOA varies from about 20 MJ m^{-2} day^{-1} at the northern tip to 21.6 MJ m^{-2} day^{-1} in the southern portions in December, whereas this flux is relatively uniform across the GOA in summer (about 41 MJ m^{-2} day^{-1} in June).

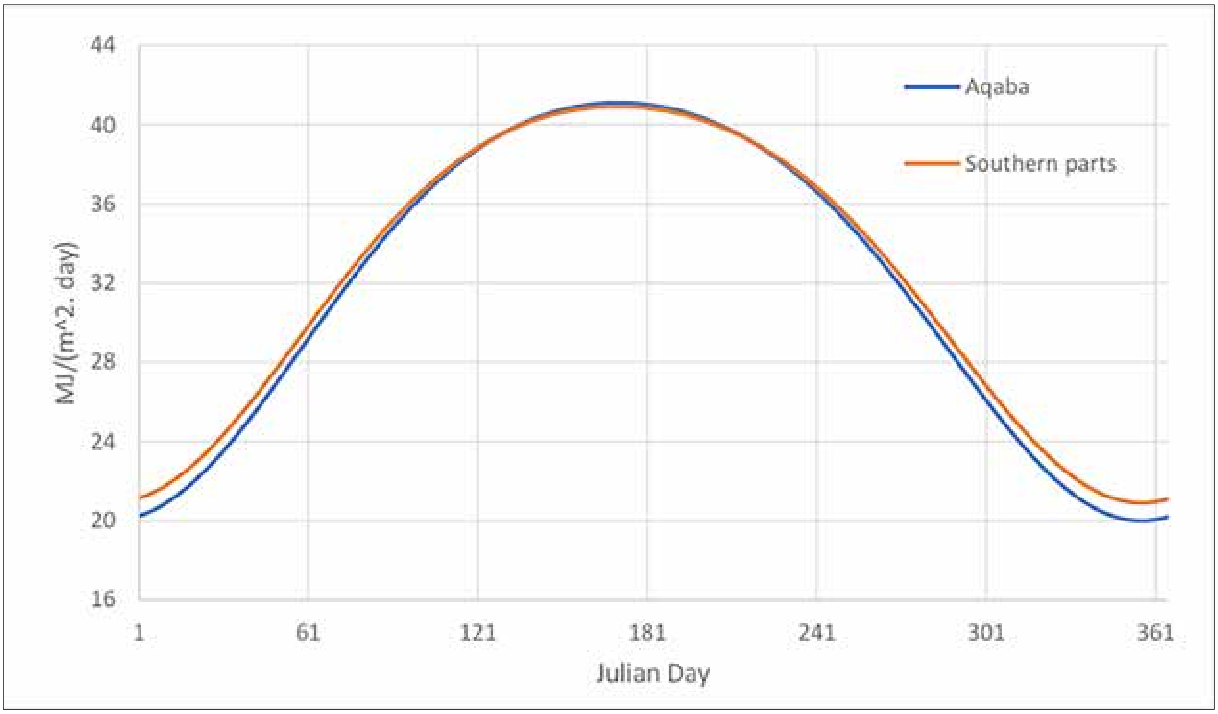

Figure 6. The annual cycle of extraterrestrial radiation over the northern and southern parts of the GOA.

2- The range of the annual SST in the GOA varies from ~5.6 ^{O}C in the southern parts to > 8 ^{O}C in the northern tip (see figure 7). This spatial temperature pattern is linked to hydrographic and atmospheric forcings. The southern parts receive a continuous flux of warm surface waters from the Red Sea, and thus the temperature there is expected to be close to that encountered over the northern Red Sea. Furthermore, solar radiation receipt over the southern portions and near-surface air temperature have less distinct annual cycles than the northern parts. The annual surface temperature range as demonstrated in Figure 7 is much smaller than those reported, for instance, in the Eastern Mediterranean- ~12 ^{O}C, the Dead Sea ~ 16 ^{O}C or the Gulf of Suez, ~ 11 ^{O}C (Berman et al., 2003; Manasrah et al. 2004; Biton and Gllord, 2011; Nykjaer, 2009; Oroud, 2019b; Oroud, 2023).

The above findings are substantiated by surface temperature retrieved from MODIS data. Figure 8 shows that the southern parts of the GOA as warmer than the northern part particularly at the end of year due to the influx of warm waters from the Red Sea, warmer air temperatures and higher solar radiation receipt as indicated in Figure 6. Landsat data provide finer details compared to the MODIS data, and thus thermal images onboard Landsat 8 are more suitable for detailed investigation of the energy balance components for small size areas like the GOA compared to coarse spatial resolution satellite platforms.

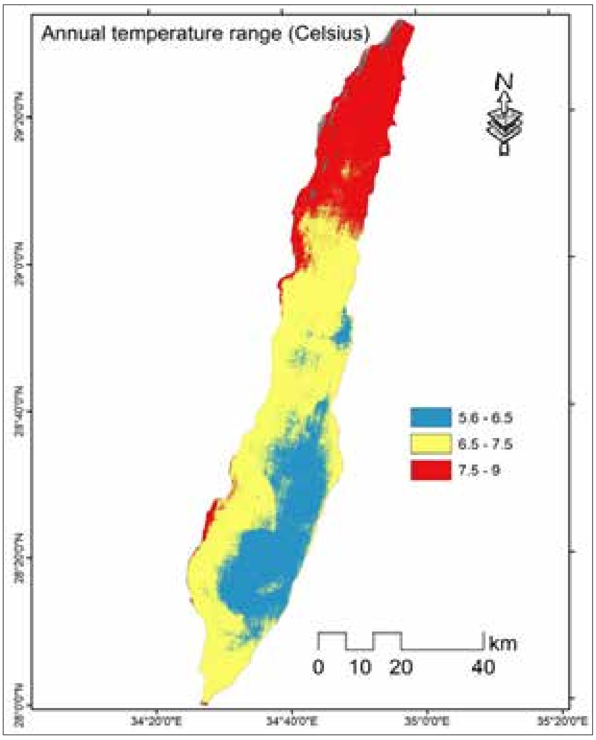

Figure 7. The annual surface temperature range across the GOA. The ST annual range is obtained by subtracting the temperature of March from that in August.

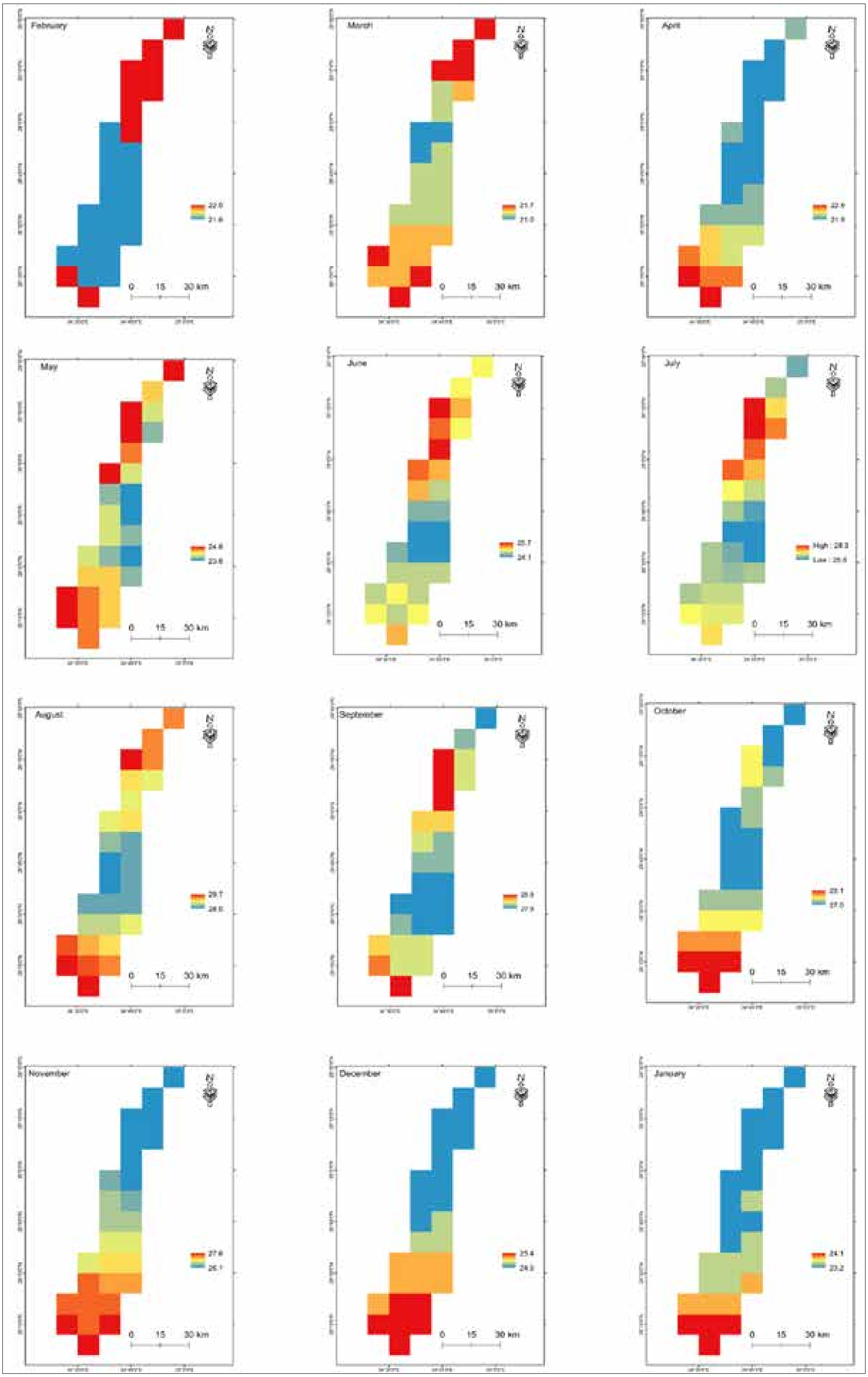

Figure 8. The spatial distribution of monthly surface temperature across the GOA as retrieved from the Moderate Resolution Imaging Spectroradiometer (MODIS) onboard the Aqua satellite during the study period.

5. Evaporation across the GOA

Evaporation across the GOA is quite high throughout the annual cycle. Figure 9 shows the spatial distribution of average daily evaporation for four selected months: two in summer and two in winter. Evaporation reaches its peak in late summer and early fall with average rates of 9.25, 10.24, and 9.57 mm day^{-1} in August, September, and October, respectively. During this period, the change in heat storage tends to be either close to zero, as in the case of August, or negative, as in the other months, and thus the available energy for evaporation is large. Despite the significant drop in air temperature and solar radiation during the low sun period, evaporation during the cold period of the year is relatively high. This pattern is due to the substantial subsurface heat release during the cooling stage of the GOA, which significantly increases available energy and thus evaporation.

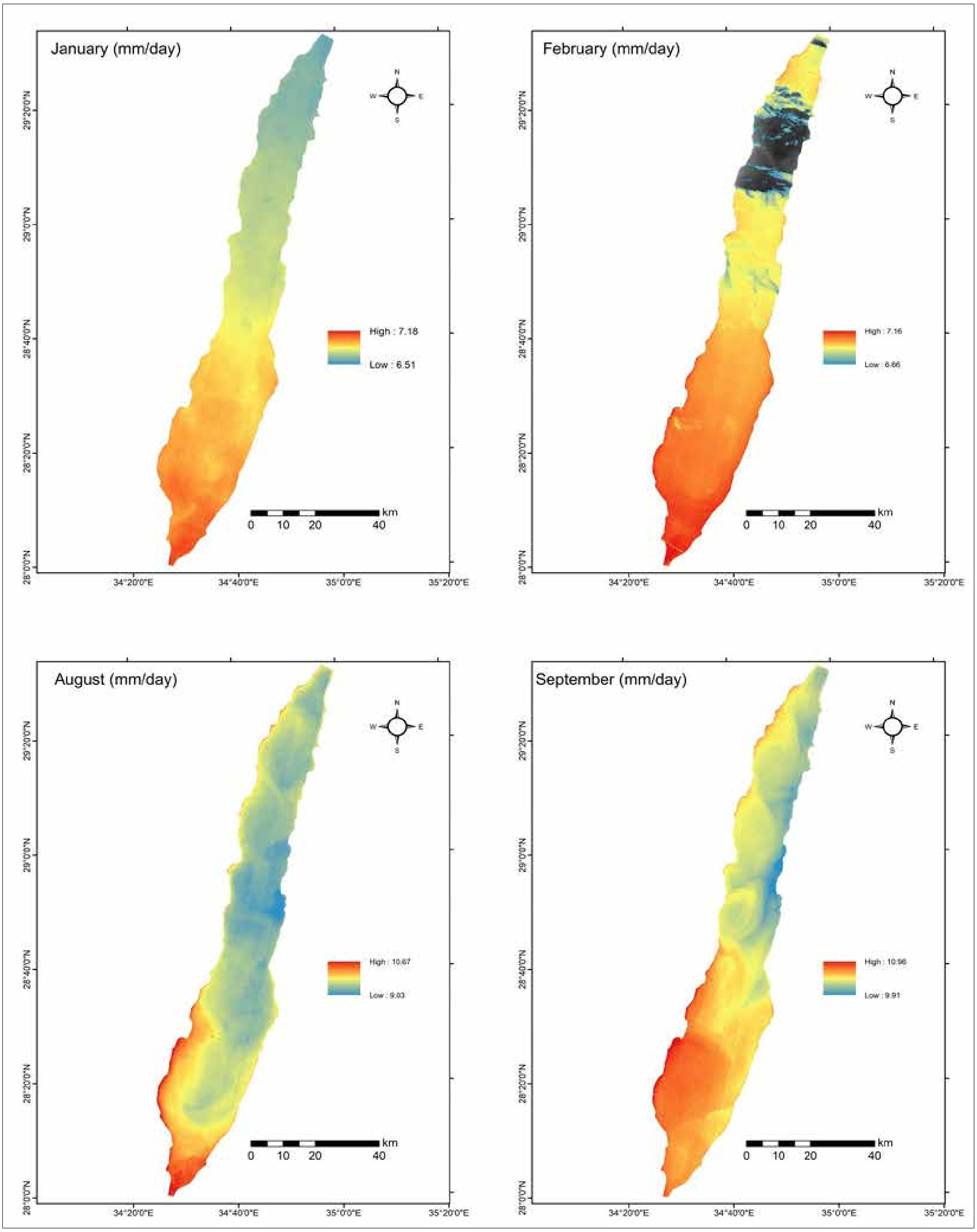

Figure 9. The spatial distribution of daily evaporation during four selected months, two in winter and two in summer.

The spatial distribution of evaporation rates from the GOA during April through September and October through March are presented in Figure 10. Average evaporation during the warm season, April through September, is 1465 mm -ranging from 1460 mm in the northern parts to 1550 mm in the southern parts-, while its counterpart in the low sun period, October through march is 1395 mm, varying from 1340 to 1450 mm across the GOA.

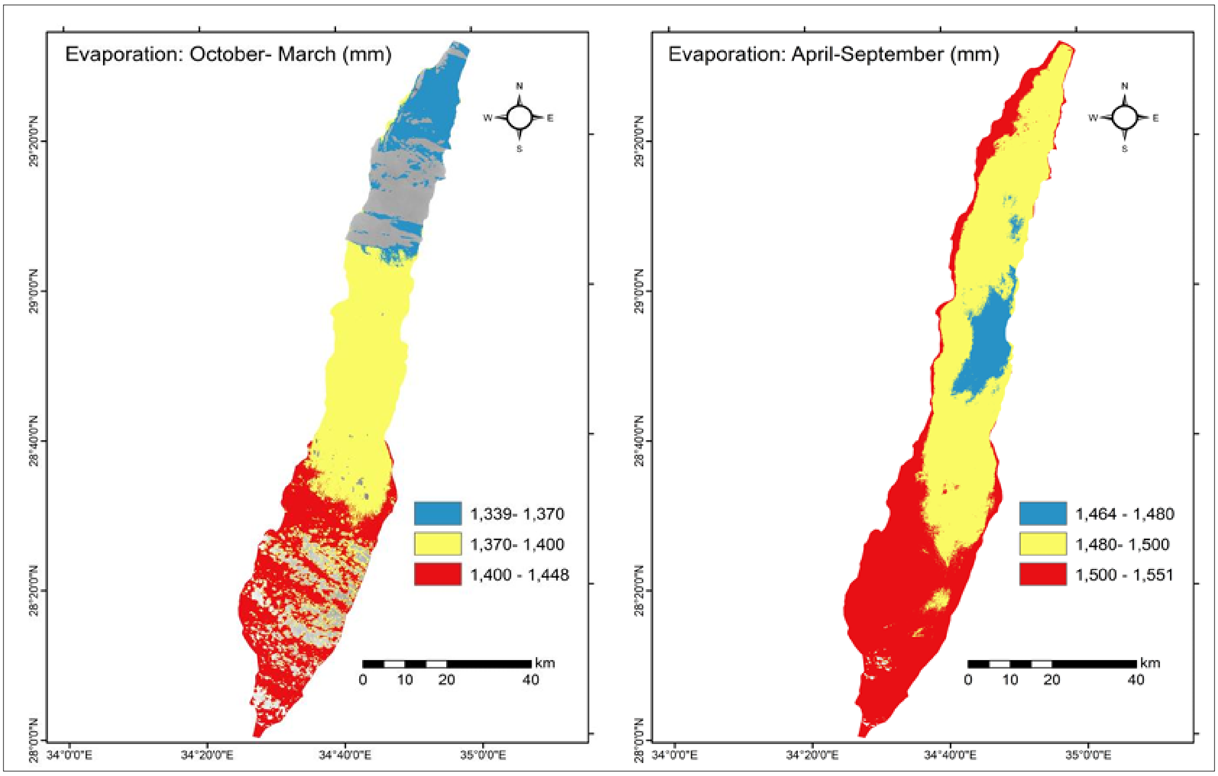

Figure 10. Total evaporation during the low sun period and the high sun period. Average evaporation for October through March is 1395 mm and the corresponding value for April through September is 1466 mm.

Although solar radiation and air temperature are relatively small in the low sun period, evaporation values across the GOA during this period are comparable to those in the warm period. This is linked to the very large subsurface heat storage during the warm period and its subsequent release in the cool period. Furthermore, the water temperature in the GOA does not vary much during the annual cycle, leading to high saturation vapor pressure deficit year-round. Evaporation across the GOA increases southward in both seasons, with the increase more pronounced from October through March.

Total evaporation across the GOA as calculated in this investigation is ~2860 mm a^{-1}. This figure is larger than those presented by da Salva (1994) and Matsoukas et al (2005; 2007), who indicated that evaporation from the Red Sea is ~1680 mm a^{-1} and ~2100-2200 mm a^{-1}, respectively. The estimates given by Matsoukas et al (2005; 2007) were based on coarse spatial resolution pixels- 2.5× 2.5 degrees. On the other hand, the calculated annual evaporation in this investigation is ~21 % lower than that reported by Assaf and Kessler (1976). Estimates presented by Assaf and Kessler were based on the bulk transfer coefficient, which is sensitive to the wind function and saturation vapor pressure deficit. Furthermore, Assaf and Kessler assumed uniform surface temperature and weather conditions throughout the GOA and neglected the effect of salinity on evaporation.

An important observation is the large contribution of the aerodynamic term in winter. The contribution of the aerodynamic term to total evaporation during the months December through March- is ~52%. On the other hand, the corresponding contribution for the period April through November is only ~ 32%, despite the larger saturation vapor pressure deficit during the warm period. Evaporation contributed by the energy term is relatively small in the cold months compared to the warm period. The physical explanation for this annual trend of energy and aerodynamic contributions is linked to the annual cycle of the energy conversion factor ($\Delta/(\Delta + \psi)$. The efficiency of the energy conversion factor increases appreciably as the temperature rises. Figure 11 shows the efficiency of the net energy conversion factor as a function of temperature. A temperature rise enhances the conversion of the available energy into evaporation but tends to suppress the aerodynamic term in the Penman equation due to the increased numerator in Eqn. 4. This tendency explains the large contribution of the energy term in the warm season and the enhanced contribution of the aerodynamic term in winter when temperature is relatively low. This tendency is expected to be larger for other locations like the Mediterranean, the Gulf of Suez or the Dead Sea due to the larger annual temperature range compared to the GOA.

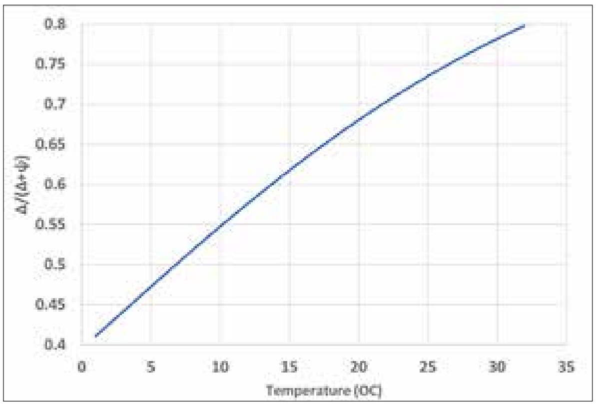

Figure 11. The efficiency of the net energy conversion factor as a function of temperature.

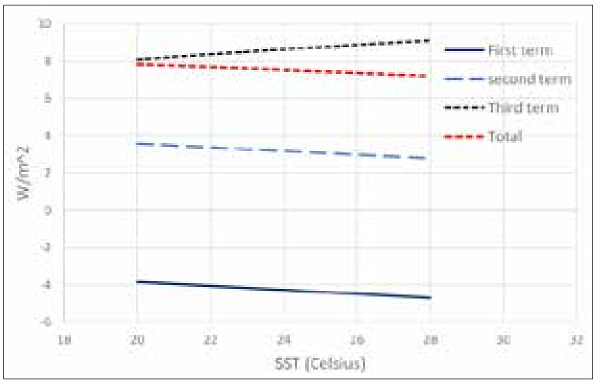

Figure 12. The sensitivity of evaporation as influenced by temperature departure at the environmental conditions encountered across the Gulf of Aqaba.

6. Sensitivity of evaporation to uncertainty in surface temperature

Surface temperature retrieved from Landsat 8 is consistent with field observations and those obtained from MODIS images, but uncertainty is expected to occur in SST which in turn influences evaporation estimates. The total effect of a temperature departure on evaporation as formulated by the Penman equation may be expressed using the following expression,

$$\frac{dE}{dT} = \frac{\partial E}{\partial Rn}\frac{\partial Rn}{\partial T} + \frac{\partial E}{\partial \Delta}\frac{\partial \Delta}{\partial T} + \frac{\partial E}{\partial e_s}\frac{\partial e_s}{\partial T} \qquad (14)$$

where all terms as indicated previously. A change in temperature has positive and negative feedback effects on evaporation (Oroud, 2019a). For instance, a departure in T reduces net radiation because of the enhanced upwelling radiation, while a temperature increase elevates the saturation vapor pressure and its slope at the surface-atmosphere boundary. The effects of these mechanisms on evaporation are nonlinear.

Figure 12 shows the response of evaporation as influenced by a one Celsius temperature departure as presented in Eqn. 14 for typical meteorological conditions encountered over the GOA. Assuming that the ambient conditions are unchanged, a temperature increase has mixed effects on evaporation. For instance, a temperature increase by one Celsius at 25 ^{O}C reduces net radiation by ~6 W m^{-2} ($-4\varepsilon\sigma T^3\delta T$) but increases the saturation water vapor pressure deficit which in turn enhances evaporation flux across the surface- atmosphere boundary. Figure 12 shows that the total evaporation response caused by one Celsius departure at the environmental conditions encountered at the GOA is close to 90-100 mm/year. It is clear that a small uncertainty in SST estimates is not expected to have a large impact on the calculated annual evaporation, as presented in this investigation. Evaporation departure is indeed very small and represents only ~3% of annual evaporation. The calculated evaporation uncertainty resulting from uncertainty in SST is smaller than uncertainties caused by other terms influencing evaporation estimates, like solar radiation receipt, the wind function or incoming longwave radiation.

7. Discussion and conclusion

Accurate estimates of surface temperature are essential for numerous geophysical investigations, such as mass and heat exchange across the surface atmosphere boundary. Results show that the surface temperature of the GOA varies from a minimum of ~20 ^{O}C during the low sun period to about 27 ^{O}C in August and September. The southern parts of the GOA are warmer than the northern parts year-round. The influx of warm water from the Red Sea is likely the main mechanism influencing this spatial pattern. The warmer climate and higher solar radiation, particularly in winter, in the southern areas, also contribute to this spatial temperature gradient.

Thermal images reveal that the average annual temperature range over the GOA varies from ~5.6 °C near the Red Sea to >8 °C in the northern parts of the gulf. This spatial pattern demonstrates that the GOA does not have a uniform annual temperature range. The annual temperature range in the GOA is relatively smaller than that encountered in nearby lakes and open seas. For instance, the southeastern Mediterranean has an annual range of 12 ^{O}C while the Suez Canal, which forms the western extension of the Red Sea, was reported to have an annual temperature range close to 11 ^{O}C, and the Dead Sea has an annual temperature range in excess of 16 ^{O}C.

The annual evaporation from the GOA is quite large, reaching ~ 2860±100 mm a^{-1}. Being hyperarid and receiving no flow from nearby terrains, the large water deficit of the Gulf of Aqaba is compensated by the continuous flow of water from the Red Sea. Based on the evaporation results presented in this investigation and the area of the Gulf of Aqaba, total annual flow from the Red Sea to the Gulf of Aqaba is close to 8.86 billion cubic meters. This massive flux keeps the salinity and water temperature of the Gulf of Aqaba very close to those encountered over the northern parts of the Red Sea. This investigation provides insight into the energy, water, and salt balances across the Gulf of Aqaba, and also offers a better understanding of processes shaping the marine environment of the Gulf of Aqaba.

An important relevant point regarding the difference between Landsat and MODIS in calculating temperature and evaporation rates is illustrated. The Landsat program and the Moderate Resolution Imaging Spectroradiometer (MODIS) are widely used to estimate evaporation from both land and water surfaces, although they differ in their overpass times. Landsat is commonly applied to derive surface temperature and evaporation rates for terrestrial areas, lakes, and reservoirs, whereas MODIS sensors aboard Terra and Aqua are designed to monitor temperature and evaporation over broad regions due to their wide swath coverage. Landsat typically passes at about 10:15 a.m., while Terra and Aqua (MODIS) overpass at approximately 1:30 p.m.

Surface temperatures over land are highly sensitive to the timing of satellite overpasses because of pronounced diurnal heating cycles. In contrast, sea surface temperature shows minimal diurnal variation. This stability is primarily due to water's high thermal capacity and the involvement of a relatively deep, well-mixed surface layer generated by wave action. The large heat capacity of seawater (density × specific heat × depth) means that substantial energy is required to raise its temperature even slightly. Consequently, the precise timing of a satellite pass over has little effect on measured sea surface temperature and associated evaporation rates.

Author Declarations:

-Funding (no funding is provided)

-Conflicts of interest/Competing interests (there is no conflicting or competing interests)

-Ethics approval/declarations (not applicable)

-Consent to participate: authors agree to the conditions stipulated in the Journal guidelines

-Consent for publication (yes)

-Availability of data and material/ Data availability (data is available upon reasonable request).

-Code availability (not applicable)

References

Ahmed, A., Abou-Elhaggag, M., El-Badry, H. (2012) Hydrodynamic modeling of the Gulf of Aqaba," J. Environ. Protection, 3, (8A), 2012, 922-934. doi: 10.4236/jep.2012.328107.

Allen, R.G., Pereira, L.S., Raes, D. and Smith, M. (1998) Crop Evapotranspiration—Guidelines for Computing Crop Water Requirements. FAO Irrigation and Drainage Paper 56. Food and Agriculture Organization, Rome.

Assaf G, Kessler J. (1976) Climate and energy exchange in Gulf of Aqaba (Eilat). Mon Weather Rev 104:381–385, https://doi.org/10.1175/1520-0493(1976)104<0381:CAEEIT>2.0.CO;2

Barsi, J. A., Schottb, J. R., Palluconic F. D., Hook J. H. (2005). Validation of a Web-Based Atmospheric Correction Tool for Single Thermal Band Instruments, Earth Observing Systems X, edited by James J. Butler, Proceedings of SPIE Vol. 5882 (SPIE, Bellingham, WA, 2005), https://doi: 10.1117/12.619990

Berman, T., N. Paldor, N., Brenner, S. (2003) Annual SST cycle in the Eastern Mediterranean, Red Sea and Gulf of Elat, Geophys. Res. Lett., 30(5), 1261, https://doi:10.1029/2002GL015860.

Bernardello R, Serrano E, Coma R, Ribes M, Bahamon N (2016) A comparison of remote-sensing SST and in situ seawater temperature in near-shore habitats in the western Mediterranean Sea. Mar Ecol Prog Ser 559:21-34. https://doi.org/10.3354/meps11896

Biton, E., Gildor, H. (2011) The general circulation of the Gulf of Aqaba (Gulf of Eilat) revisited: The interplay between the exchange flow through the Straits of Tiran and surface fluxes, J. Geophys. Res., Oceans, https://doi.org/10.1029/2010JC006860

Bouwer, L., Biggs, T., Aerts, C. (2007) Estimates of spatial variation in evaporation using satellite-derived surface temperature and a water balance model, Hydrolo. Process, https://doi.org/10.1002/hyp.6636

Brutsaert, W. (1982) Evaporation into the Atmosphere. Theory, History and Application. D. Reidel Publishing Co., Dordrecht, Boston, London.

Budyko, I. (1974) Climate and Life. Academic Press.

Calder, I.R., Neal, C. (1984) Evaporation from saline lakes: a combination equation approach. Hydrol. Sci. J. 29, 89–97, https://doi.org/10.1080/02626668409490924

Cao, M., Mao, K., Yan, Y., Shi, J., Wang, H., Xu; T; Fang, S; Yuan, Z. (2021) A New Global Gridded Sea Surface Temperature Data Product Based on Multisource Data, Earth Syst. Sci. Data, https://doi.org/10.5194/essd-2021-6

Cristobal J, Jimenez-Munoz J, Prakash A, Mattar C, Skokovic D, Sobrino J. (2018) An improved single-channel method to retrieve land surface temperature from the Landsat-8 thermal band. Remote Sens 10: 431. https://doi.org/10.3390/rs10030431

da Silva, A., Young, A., Levitus, S. (1994), Atlas of Surface Marine Data 1994, vol. 1, Algorithms and Procedures, NOAA Atlas NESDIS, vol. 6, NOAA, Silver Spring, Md.

Dehwaha , A., Jadoona , K., Al-Mashharawia , S., Missimer, T. (2016) Effects of nearshore evaporation rates on the design of seabed gallery intake systems for SWRO facilities located along the Red Sea shoreline of Saudi Arabia, Desalination and Water Treatment, 57:48-49, 22726-22733, https://doi.org/10.1080/19443994.2015.1098796

Diaz, L.R.; Santos, D.C.; Käfer, P.S.; Rocha, N.S.d.; Costa, S.T.L.d.; Kaiser, E.A.; Rolim, S.B.A. (2021) Atmospheric Correction of Thermal Infrared Landsat Images Using High-Resolution Vertical Profiles Simulated by WRF Model. Environ. Sci. Proc., 8, 27. https:// doi.org/10.3390/ecas2021-10351

Faraj, T. K., Tarawneh, Q. Y., Oroud, I. M. (2022) The applicability of the tourism climate index in a hot arid environment: Saudi Arabia as a case study, International J. Env. Sci. Techno. https://doi.org/10.1007/s13762-022-04228-.

Faysash D, Smith E. (1999) Simultaneous land surface temperature- emissivity retrieval in the infrared split window. J Atmos Ocean Technol 16:1673–1689, https://doi.org/10.1175/1520-0426

Foken, T. (2008) Micrometeorology. Springer.

Folchitto, S. (1991) Seawater as salt and water source for solar ponds. Sol. Energy 46, 343–352

García-Monteiro, S., Sobrino, J.A., Julien, Y., Sòria, G., Skokovic, D. (2022) Surface Temperature trends in the Mediterranean Sea from MODIS data during years 2003–2019, Regional Studies Marine Sci., 49, doi.org/10.1016/j.rsma.2021.102086

Gristey, J.J.; Su, W.; Loeb, N.G.; Vonder Haar, T.H.; Tornow, F.; Schmidt, S.K.; Hakuba, M.Z.; Pilewskie, P.; Russell, J. (2021) Shortwave Radiance to Irradiance Conversion for Earth Radiation Budget Satellite Observations: A Review. Remote Sens. 13(13), 2640; https://doi.org/10.3390/rs13132640

Iqbal M (1983) An introduction to solar radiation. Academic, New York

Jimenez-Munoz, J.C., Sobrino J. A. (2003) A generalized single-channel method for retrieving land surface temperature from remote sensing data. J Geophys Res 108. https://doi.org/10.1029/2003JD003480

Jimenez-Munoz, J., Sobrino, J., Skokovic, D., Mattar, C., Cristobal, J. (2014). Land surface temperature retrieval methods from Landsat-8 thermal infrared sensor data. IEEE Geosci. Remote Sens. Lett. 11, 10. https://doi.org/10.1109/LGRS.2014.23120232

Kelkar, R. R. (2007) Satellite Meteorology, BS Publication, Hyderabad, India, 267 pp.

Kidd, C., Levizzani, V., Bauer, P. (2009) A review of satellite meteorology and climatology at the start of the twenty-first century, Progress in Physical Geography 33(4), 474–489 DOI: 10.1177/0309133309346647

Manasrah, R., Rasheed, M., Badran, M. (2006) Relationship between water temperature, nutrients and dissolved oxygen in the northern Gulf of Aqaba, Red Sea. Oceanologia, 48, 237–253, http://www.sciencedirect.com/journal/oceanologia

Manasrah, R., Abu-Hilal, A., Rasheed, M. (2019). Physical and Chemical Properties of Seawater in the Gulf of Aqaba and Red Sea. In: Rasul, N., Stewart, I. (eds) Oceanographic and Biological Aspects of the Red Sea. Springer Oceanography. Springer, Cham. https://doi.org/10.1007/978-3-319-99417-8_3

Matsoukas, C., Banks, A. C., Hatzianastassiou, N., Vardavas, I. (2005) The seasonal energy budget of the Mediterranean and Red Seas, Geophys. Res. Abstract, 7, 04596, https://doi.org/10.1029/2004JC002566

Matsoukas, C., Banks, A. C., Pavlakis, K. G., Hatzianastassiou, N., Stackhouse Jr, W. Vardavas, I. (2007) Seasonal heat budgets of the Red and Black seas, J. Geophys. Res., 112, C10017, https:// doi.org/10.1029/2006JC003849

Menzel, W. P. (2006). Remote sensing applications with meteorological satellites, NOAA satellite and information service, Univ. Wisconsin, Madison.

Metzger J, Nied M, Corsmeier U, Kleffmann J, Kottmeier C. (2018) Dead Sea evaporation by eddy covariance measurements vs aerodynamic, energy budget, Priestly-Taylor, and Penman estimates. Hydrol Earth Syst Sci 22:1135–1155. https://doi.org/10.5194/hess-22-1135-2018

Mundo-Molina, M., De Coss-Gomez, E. (2017) Physical-Mathematical Foundations of the Penman Equation from the Perspective of the First Law of Thermodynamics and Energy Balance Theory. Journal of Water Resource and Protection, 9, 1377-1390. https://doi.org/10.4236/jwarp.2017.912088

Neumann, J. (1952). Evaporation from the Red Sea. Israel Exploration Journal, 2(3), 153–162. http://www.jstor.org/stable/27924478

Nykjaer, L. (2009) Mediterranean Sea surface warming 1985–2006, Clim. Res., 39, 11–17, 2009 https://doi.org/10.3354/cr00794

Oroud, IM. (1997) Diurnal evaporation from fresh and hypersaline shallow ponds in a hot, dry environment. Phys Geog. 18(4):363–382, https:// doi.org/10.1080/02723646.1997.10642625

Oroud IM. (2011) Evaporation from the Dead Sea and its implications on its water balance, Theor. Appl. Climatol, 106, 523–530, https://doi.org/10.1007/S00704-0452-6.

Oroud, IM. (2018) Global warming and its implications on meteorological and hydrological drought in the southeastern Mediterranean. Environmental Processes 5, 329–348. https://doi.org/10.1007/s4071-018-0301-z.

Oroud, IM. (2019a) Evaporites: relative humidity control of primary mineral facies revisited. Hydrol. Process 33(3):395–404. https://doi.org/10.1002/HYP.13334

Oroud, IM. (2019b) The utility of thermal satellite images and land- based meteorology to estimate evaporation from large lakes. J Great Lakes Res. https://doi.org/10.1016/j.glr.2019.05.004

Oroud, IM. (2020) Spatial and temporal surface temperature patterns across the Dead Sea as investigated from thermal images and thermodynamic concepts. Theor. Appl. Climatol. 142(1–2):569–579. https://doi.org/10.1007/s00704-020-03343-9

Oroud, IM (2023) The future fate of the Dead Sea: Total disappearance or a dwarfed hypersaline hot lake? J. Hydrolo, 623, https://doi.org/10.1016/j.jhydrol.2023.129816.

Oroud, IM., Balling, R. C. (2021) The utility of combining optical and thermal images in monitoring agricultural drought in semiarid Mediterranean environments, Journal of Arid Environments, https://doi.org/10.1016/j.jaridenv.2021.104499.

Oroud, I.M. (2025) The Relative Impact of Urbanization Expansion and Climate Change on Flood Hazard in Amman City. Jordan J. Earth Environ. Sci. 2025, 1, 96–107.

Paldor N, Anati DA (1979) Seasonal variation of temperature and salinity in the Gulf of Elat (Aqaba). Deep-Sea Res 26:661–672, https://doi.org/10.1016/0198-0149(79)90039-6

Parata, A. J. (1994) Land surface temperature determination from satellites, Adv. Space Res. 14, No. 3, pp. (3)15-(3)26,

Qin, Z., Karnieli, A., Berliner, P. (2001) A mono-window algorithm for retrieving land surface temperature from Landsat TM data and its application to the Israel-Egypt border region. Int. J. Remote Sens. 22, 3729–3746, https://doi.org/10.1080/01431160010006971

Rosas, J., Houborg, R., McCabe, M. F. (2017) Sensitivity of Landsat 8 surface temperature estimates to atmospheric profile data: A study using MODTRAN in dryland irrigated systems, Remote Sens. 2017, 9, 988; https://doi.org/doi:10.3390/rs9100988

Reynolds, R. W., Chelton, D. B. (2010) Comparisons of daily sea surface temperature analyses for 2007-08. J. Climate, 23. 3545-3562, https://doi.org/10.1175/2010JCLI3294.1

Salisbury J, D'Aria D (1992) Emissivity of terrestrial materials in the 8-14 µm atmospheric window. Remote Sens Environ 42:83–106, https://doi.org/10.1016/0034-4257(92)90092-X

Sobrino, J., Jimenez-Munoz, J. (2014) Minimum configuration of thermal infrared bands for land surface temperature and emissivity estimation in the context of potential future missions. Remote Sens. Environ. 148, 158–167, https://doi.org/10.1016/j.rse.2014.03.027

Stammer, D., Wunsch, C., Giering, R., Eckert, C., Heimbach, P., Marotzke, J., Adcroft, A., Hill, C. N. and Marshall, J. (2002) The Global Ocean Circulation during 1992–1997, Estimated from Ocean Observations and a General Circulation Model. Journal of Geophysical Research, 107(27) , https://doi.org/10.1029/2001JC000888

Vonder Haar, T. H. (1994) The global energy budget and satellite observations, Advances in Space Research,14, 131-144, https://doi.org/10.1016/0273-1177(94)90362-X.

Wang, F., Qin, Z., Song, C., Tu, L., Karnieli, A., Zhao, S., 2015. An improved mono-window algorithm for land surface temperature retrieval from Landsat 8 thermal infrared sensor data. Remote Sens. 2015 (7), 4268–4289. https://doi.org/10.3390/rs70404268.

Yang, J., Gong, P., Fu, R. et al. (2013) The role of satellite remote sensing in climate change studies. Nature Clim Change 3, 875–883 (2013). doi.org/10.1038/nclimate1908.

JJEES

JJEES (2026) 17 (3): 324-337
ISSN 1995-6681

Jordan Journal of Earth and Environmental Sciences

Desertification and its Effects in Iraq: A Review

Emad Telfah Abdel Ghani[1*], Wael F. A. Alshamary[2], Husam Naji Mukhlif[3], AbdulKarem A. M. Alalwany[3], Atheer Saleem Almawla[1], M S Jumaah[4], Bilal Muayad Abdulrahem Alalosy[1]

[1] The Upper Euphrates Centre for Sustainable Development Research, University of Anbar, 31001, Iraq.
[2] The College of Agriculture, University of Kirkuk, 36001, Kirkuk, Iraq.
[3] Higher Institute of Desert Sciences, University of Anbar, Ramadi, 31001, Iraq.
[4] Department of Soil Science and Water Resources, College of Agriculture, University of Anbar, Ramadi 31001, Anbar, Iraq.

Received on 3 May 2025; Accepted on 30 March 2026

Abstract

Desertification is an environmental process in the world which leads to degradation of land, decrease in agricultural productivity and biodiversity. In Iraq, 55.5% of the territory (≈96,500 km²) would be desertified or undergoing such process/state, while 23.2% would be classified as experiencing full desertification (≈40,400 km²). This growth has been fostered by climate change, mismanagement of water, and unsustainable land use. Effects include decreased food security, rural to urban migration, and increased frequency of sandstorms damaging both public health and economic activities. Efforts to halt desertification, including afforestation, better irrigation and sustainable farming, have made a difference but are not enough in the absence of more robust policy measures and international co-operation. This review compiles recent (2023–2024) developments and the growing significance of the desertification situation in Iraq, as well as its requirement for sustainable connected action that not only slows down/combats desertification but also ensures a stable socio-ecosystem.

Keywords: *desertification, drought, sand dunes, Geographic Information Systems (GIS), Remote sensing, Iraq.*

1. Introduction

Global desertification is one of the world's dilemmas, exacerbated by water shortage as well as climate change. The United Nations Convention to Combat Desertification (UNCCD, 2024), indicated that globally over one-third of our planet's land is affected (Awadh S.M. 2024).

Desertification is closely associated with rainfall variability and climate change in arid and semi-arid regions, leading to a redistribution of potential for land productivity and the development of soil erosion (Salahat & Al-Qinna, 2015).

Wind erosion is one of the notable processes in the desertification phenomenon that occurs in arid environments, resulting in the removal of fine particles and organic matter from soil structure which deteriorates fertility and water retention capacity of soil (Abdelwahab ve Mustafa, 2021, Ide vd., 2025). As a result, desertification is not just an environmental issue; it represents a development concern that impacts upon food security and the sustainable utilization of natural resources.

Destruction of the vegetation cover by drought and over-grazing results in an increase in the susceptibility of the soil to wind erosion and water. It is conducive to the loss of fertile topsoil and threatens the long-term sustainability of ecosystems (Al-Sababhah & Al-Maqablah 2023)

The crisis in Iraq is even more severe. The Iraqi Ministry of Planning (2024) indicated that 55.5% of Iraq is desertified or under threat of desertification, as well as 23.2% already totally deserted in iraq shafaq. com). This indicates a marked increase from the previous year, 2021, in which the total desertified area was found to be 27,200 km² (Alkhateeb et al., 2019; Al-Shamary et al., 2021). The spread of the desertified areas is associated with decreasing water levels in Tigris and Euphrates rivers, increasing temperatures, and soil salinization resulting from inefficient use of irrigation waters (Lateef et al., 2024).

Quantitative analyses indicate that vegetation degradation has rapidly intensified in, for instance, the provinces of Babil and Al-Qadisiyah in the period between 2000 and 2023 under land-use change impact and climate stress (Alsultan et al., 2023; Alobaidy et al., 2024).

In this context, a detailed framework in the form of an integrated scientific investigation is direly needed in Iraq. The purpose of this review is to offer a synthesis up-to-date on the topic of desertification, including its causes, impacts and potential countermeasures, with an emphasis on sand dunes as a crucial defacing aspect in Iraq.

2. Methodology

As a review paper, this study performs systematic literature research and analysis to synthesize the recent research on desertification in Iraq. The approach is based on three main parts:

2.1 Databases and Sources

Relevant literature was searched from international

* Corresponding author e-mail: emadabdulghani@uoanbar.edu.iq

databases (Scopus, Web of Science, Google Scholar), as well as local journals and reports issued by Iraqi entities (UNCCD, 2024; Iraqi Ministry of Planning, 2024).

2.2 Search Strategy

Search keywords were "desertification Iraq", "sand dunes Iraq", "climate change Iraq", and "soil degradation Iraq", and the OR Boolean operators were used to focus the search results. Publications from 2000 to 2024 were considered, with an emphasis on studies from recent years (2023–2024) to ensure contemporariness (Alkhateeb et al., 2019; Al-Shamary et al., 2021).

2.3 Inclusion and Exclusion Criteria

- Inclusion: Peer-reviewed articles, government reports, and conference papers addressing desertification drivers, impacts, or mitigation strategies in Iraq.
- Exclusion: Non-English publications without translation, non-peer-reviewed sources, and articles lacking methodological transparency.

2.4 Analytical Framework

The selected studies were categorized into thematic clusters:

- Drivers of desertification (climatic, anthropogenic, geological).
- Impacts (agricultural, ecological, socio-economic).
- Mitigation strategies (afforestation, water management, sustainable agriculture).
- Comparative synthesis was conducted to highlight regional variations within Iraq and to evaluate the effectiveness of current policies (Safriel, 2009; Rasul, 2016).

3. Desertification concept

Desertification is when an area that was fertile is eroded into a desert because of human actions (Becerril-Pio and Mastachi-Loza, 2021). Sivakumar (2007) and Reynolds (2013) claim this is an ongoing global concern and severely affects nature and productivity in the contemporary world, which seems to have become a reason for concern for many people. Other countries, including Iraq, are also facing this environmental challenge (Al-Obaidi et al., 2022). In a statement by the UNCCD (United Nations Convention to Combat Desertification) on desertification, they estimate that it surpasses 1/3 the total surface area of land, which is the reason behind land degradation, which in itself is an astonishing loss or reduction in biologically productive land or economically useful land. This phenomenon usually leads to the degradation of biodiversity and plant and animal life, in addition to the depletion of social value, poverty, and unrest (Eltaif et al., 2024).

This takes place in arid and semiarid regions which is caused by climate changes along with overgrazing and inappropriate land utilization (Sombroek & Sene, 1993).

A section is also described as becoming increasingly more arid, which makes the area susceptible to maximum land degradation, termed desertification.

Desertification is defined by (Vogt et al 2011) "as a process of land degradation in which a region becomes increasingly arid, resulting in loss of biological productivity and economic value"- it's a biological problem which has complex causes linked to human and natural factors. Climate change, overgrazing, and poor land management also contribute to emerging deserts (Wairiu, 2017). Desertification has become a serious environmental problem worldwide due to its havoc caused environmentally and humanly (Thomas, 1997).

3.1 Factors of Desertification

The causes of desertification are multifaceted and include climate change, overgrazing, deforestation, and irrigation practices that deplete water resources (Darkoh, 2018). These factors often act in combination, and it may be impossible to determine a single cause.

The loss of arable land is one of the major effects of desertification. This can be disastrous for agriculture, as it limits the quantity of space available for crops and increases the risk of crop failure. This can also cause food insecurity to become more intensified and problematic in this area, with growing difficulties to produce enough food required by the local population (Tokbergenova et al., 2018).

Besides the influence on agriculture, desertification can bring severe consequences for the environment. Reduction in plant cover can result in erosion and soil degradation, subsequently encouraging the expansion of desertification. It may also cause loss of biodiversity as most plant and animal species cannot survive the harsh environment resulting from desertification (Kassas, 1995).

There is a number of initiatives to tackle desertification. The UNCCD has initiated a variety of programmes and projects to address desertification and encourage sustainable land use. These include the Great Green Wall Initiative to plant a barrier of trees across Africa as part of an effort to reverse desertification, and enhance food security, and the Land Degradation Neutrality Fund that financially supports projects for land restoration initiatives (Reynolds et al., 2007).

Sustainable management of water resources is crucial in arid countries, and the importance of flood hazard mapping using dam break scenarios is highlighted for reducing risks (Al-Weshah, Al-Salahat, & Al-Omari, 2024).

Even then, desertification is still widespread across the globe. In order to effectively deal with desertification, holistic solutions will be required that can address the multiple factors contributing to desertification and the particular circumstances of communities experiencing this phenomenon (Safriel, 2009).

In Iraq, desertification is a major issue as it has an arid and semi-arid climate that suffers from drought and soil degradation. The issue is compounded by factors such as population explosion, urbanization and environmental deterioration. These have resulted in the depletion of flora, disturbance of soil, and lower productivity of soil that has eventually affected local people's lives negatively as well as decreasing environmental health (Al-Kasoob et al., 2024).

Other significant reasons for the desertification of the land in Iraq include overgrazing. This is a widespread phenomenon in many areas of the nation, especially northern and central regions, where there are limited water points and pasture. Overgrazing results in soil and vegetation degradation, can contribute to soil erosion, and decrease biodiversity (Al-Turaihi et al., 2023).

Another significant reason for desertification in Iraq is bad land use management. Improper land use is forced on many parts of the country - for example, crops that are planted in areas that cannot or should not bear agriculture. This can contribute to soil degradation and erosion, as well as loss of vegetation and habitats for wildlife (Maitima et al., 2009).

Several measures have been tried to solve the problem of desertification in Iraq, such as land management and conservation practices, sustainable agriculture, and irrigation projects. Nonetheless, a lot more must be done to reduce the fundamental reasons for the issue and make sure that its natural resources are not only protected but also compatible with long-term management and use (Rasul, 2016).

Evidence from Jordan on urbanization and its sustainability implications reveals that the changes in land use/land cover have significant relevance for environmental change (Abusmier & Al-Kofahi, 2024).

3.2 Types and forms of desertification:

There are several types of desertification, including:

- Climatic desertification: This type of desertification is caused by changes in the climate, such as prolonged drought or extreme temperatures. These changes can lead to the loss of vegetation and soil erosion, making the land less productive and more vulnerable to further degradation.
- Anthropogenic desertification: This type of desertification is caused by human activities, such as overgrazing, deforestation, and poor land management practices. These activities can lead to the loss of vegetation, soil erosion, and salt accumulation in the soil, making the land less productive and more vulnerable to further degradation.
- Geological desertification: This type of desertification is caused by geological factors, such as tectonic activity or the erosion of mountains. These factors can lead to the loss of vegetation and soil erosion, making the land less productive and more vulnerable to further degradation.
- There are also several forms of desertification, including:
- Physical desertification: This form of desertification is characterized by the loss of vegetation, soil erosion, and the accumulation of salt in the soil. It can lead to the formation of sand dunes, which can reduce land productivity and increase vulnerability to further degradation.
- Biological desertification: This form of desertification is characterized by the loss of biodiversity, which can have negative impacts on the ecosystem and the communities that rely on it. It can be caused by the loss of vegetation, soil erosion, and the introduction of invasive species.
- Chemical desertification: This form of desertification is characterized by the accumulation of pollutants and other harmful substances in the soil, which can make the land less productive and more vulnerable to further degradation. It is associated with human activities such as the use of insecticides and fertilizers, and industrial and agricultural pollution.
- All things considered, desertification is multidimensional problem and can cause many adverse effects to the natural environment and local communities. Policy makers and communities alike should therefore seek a solution to the cause, while employing effective solutions to mitigate against it (Pal et al., 2023).

3.3 Desertification's landforms:

There are some landforms related to desertification. Certainly the most prolific is the sand dune. Dunes A dune is a mound of sand that wind has blown into. They may be as small as several feet high or as tall as hundreds of feet in height and are typically located in dry or semi-dry areas.

3.3.1 Sand dunes:

The most common problem in desertification areas is sand dunes, which obstruct roads and prevent people from reaching water resources and other resources (El Gamri, 2020).

Salt pans are also a feature of desertification. Salt pans are flat lands with deposits of salt and other minerals, usually found in arid regions. They form when water from a salt lake or sea evaporates, leaving behind a crust of salt. Salt direns are a significant issue in the regions going through desertification as they may render the soil infertile and very challenging for any plant growth (Zade et al., 2021).

A related landform type is the playa, which is a wet basin that forms in arid environments, either through drying of an alkaline lake or accumulation and concentration of bleached silts. Playas are level, dry areas located in deserts. They tend to be salt- and mineral-coated, and are typically located at the bottom of valleys or in basins. Playas are a serious concern for the process of desertification because they cause land to be non-cultivable, and due to environmental contamination, plant and animal habitats become both ecologically harmful and hazardous (Abdelfattah et al., 2009).

In conclusion, desertification is one of the key environmental and economic problems facing millions of people worldwide. It is attributed to a number of factors, including global warming, overgrazing, deforestation and bad land management. Desertification.

The landscape in desertified areas includes sand dunes, salt pans, and playas, all of which can render soil infertile and unsuitable for the support of plants and animals Logsdol & Klopcic, 2017).

3.3.2 Desertification landforms in Iraq:

Environmental Situation Desertification is a serious issue for Iraq with long-term effects on the natural environment and the human population of that country. Desertification has had a great effect on the Iraqi natural environment, and its people. Desertification in Iraq. From a UNDP report, desertification in Iraq is driven by overgrazing, deforestation, and sub-optimal irrigation techniques (Chasek etal, 2019).

Among the most visible effects of desertification in Iraq are dunes that reach a maximum height of fifty meters. These sand dunes, called "ergs," form when the wind blows loose sand from the floor of the desert into piles. Ergs are most common in Western and Southern Iraq, and have the effect that they force out agricultural land and make access to water and resources difficult for people (Shahid & Alsumaiti, 2022).

Loss of vegetation cover is another effect of desertification in Iraq, resulting in soil erosion and low water retention in the soil. This has, in fact, hindered farmers from cultivating crops, increasingly contributing to food insecurity and economic crisis in a large number of rural areas (Minelli, 2016).

Efforts to combat desertification in Iraq have involved reforestation and afforestation projects, along with sustainable land management schemes. Yet the UNDP report adds that these initiatives have been undermined by continued conflict and insecurity in the country, as well as inadequate funding and resources (Chasek et al., 2019).

Overall, it can be argued that desertification has always been a major issue in Iraq, affecting the natural landscape and the livelihood of Iraqi people. Addressing these will require coordinated action by government, non-government organizations (NGOs), and other agencies to implement sustainable land management practices (WHO 1992).

Sand dunes:

Sand dunes are active, dynamic land forms that constantly shift and change under the influence of wind and water. Natural distribution in Iraq Dwaras of sand dunes are distributed in various thrust-sanders, including the western desert, eastern desert, and the south desert of Manifesto.

These sand dunes can move in a variety of ways, including through the process of saltation, which is the bouncing and hopping movement of grains of sand as they are blown by the wind (Sissakian et al., 2013). Sand dunes are among the main features of the earth's surface and are a prominent presence in arid and semi-arid environments in different regions of the world, due to the availability of appropriate environmental conditions for their formation in these environments, as arid and semi-arid ecosystems are characterized by fragile systems that are vulnerable and respond to various degradation factors, especially after the climatic changes that the planet is witnessing due to the erosion of the ozone layer by the impact of greenhouse gas emissions, or the so-called (global warming phenomenon), and the resulting increase And the recurrence of drought years, the lack of rainfall, and a rise in the temperature of the earth, which affected its natural system and disrupted its ecological balance, and then its degradation, and the activity of wind erosion processes from transport, sedimentation and formation of sand dunes in different regions of the world (Agam & Berliner, 2006).

Sand dunes in Iraq are primarily controlled by the wind and one of its main features is force and direction. Dunes generally come about in the direction of the prevailing wind and move with a similar size and shape, which is impacted by periodicity and the strength of gusts. For instance, dunes in the Western desert of Iraq are predominantly formed under the influence of the northwest wind that prevails over the region during winter seasons (Jourdain et al., 2006).

Another cause that may affect the advancing desertification in IRAQ is the existence of vegetation. Vegetation in the form of vegetation cover on sand dunes stabilizes the dune and prevents of further erosion. Dry, non-vegetated dunes are easier to shape by wind and erode with less resistance (Goudie & Middleton, 2006).

Dyani Brown Climate change can contribute to shifting sand dunes in Iraq. Wind and water regimes in the area might be altered by temperature increase or changes in precipitation patterns, this could also affect how the sand dune system is formed and works (Eklund & Pilesjö, 2012).

Several research works have been done on the dynamics of sand dunes in Iraq. The results of one such study appeared in the journal "Geomorphology," and looked at sand dunes' shapes in western Iraq, reporting that the dynamics of these landforms depend on wind direction, vegetation cover, and topography. In addition, the research identified locations susceptible to sand dune advance and transport and suggested that understanding these dynamics might be helpful for interpreting predictions about how such advances could affect infrastructure and human habitation (Al-Naji & Al-Shammery, 2019).

Desertification Desertification has reached to one of the study material that has been drawn attention of humans all over the world, and concern by international organizations that have made a lot of efforts to reduce it and try to find appropriate solutions for soil, water and natural vegetation This is due to lack of effective sources Which can be defined as limited natural wealth with importance in global level experiencing steady population growth throughout recent years (Adamo et al., 2018).

Overall, sand dunes in Iraq are active landforms under the influence of multiple factors, including wind, water, and vegetation. As such, they can pose a threat to infrastructure and human settlements, and understanding the patterns and processes that drive their movement can be crucial for mitigating these risks (Goudie, 2018).

3.3.3 The concept of sand dunes:

The definition of sand dunes varied from one world to another and from one group to another, where it is defined as the wind blowing rock debris to then gather to form small shapes, circular or longitudinal shape sometimes, irregular shape at other times, known as sand dunes (Longwell, 1949). On the other side, Bagnold (1954) defined sand dunes (a mound of sand rising to a single peak), while Rasmussen (2024) defined sand dunes as a collection of sand-sized materials blown by the wind. Furthermore, (Stone, 1967) believed that sand dunes are a topographic phenomenon of air origin consisting of grains of sand from a natural source deposited on the side far from the direction of the wind. While Steven Fryberger et al. 1979) defined sand dunes as (collected in the form of a series of deposits blown by the wind), they have a slight slope facing the wind and another steep slope on the obscured side, called the façade of the slide (Al-Jashaami et al., 2024).

3.3.4 Hazards of sand dunes:

1. People migrate to other places to search for a source of livelihood and life, which leads to instability.
2. Lack of visibility when walking on the roads during sandstorms and various disasters.
3. Disruption of air traffic and the resulting fatal and tragic accidents.
4. Damage to agricultural crops and filling irrigation canals and drains with sand, and the resulting losses.
5. Ecological imbalance in the sand dune area in everything related to man and the biosphere.
6. Health problems that result from the inhalation of air loaded with dust and dust by humans, and the deaths that occur.

3.3.5 Benefits of sand dunes (Ati, 2021):

1. Sand dunes are used in the manufacture of glass.
2. Mixing sand with clay produces fertile soil for planting.
3. They act as groundwater reservoirs because they have high permeability.

3.3.6 Forms of sand dunes in Iraq:

3.3.6.1 Barchan (Crescent) Dunes

Crescent dunes arise when the wind blows in one direction and a sufficient amount of sand is available, and this type of dune is similar in general shape to the crescent with the two arched ends pointing in the direction of the wind departure, as they indicate the direction of movement of the dune and the direction of the prevailing winds (Al-Trabulsy, 1993). Crescent sand dunes are formed when the sand piles or sand gathering reach maturity, and then begin to move with the direction of the wind, as they begin to form the ends of the thin dune that are less resistant than the centre of the dune in the form of two wings up to their length and arch to the degree that the wind resistance is equal to the degree of resistance of the middle part of the dune and when the crescent dune is formed, it remains in its shape as long as the prevailing winds remain in the same direction (Figure 1).

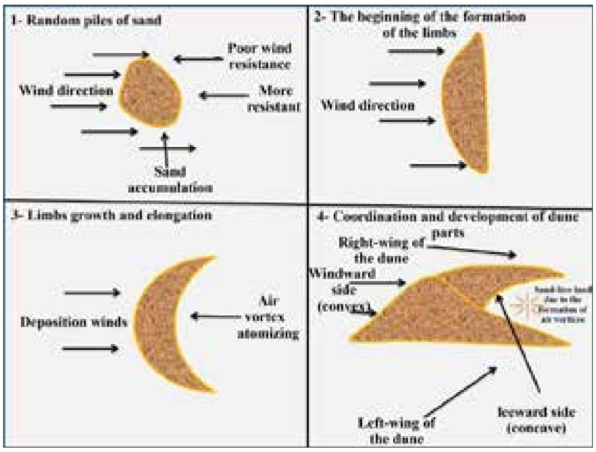

Figure 1. Stages of formation of the crescent dune (Barkhan)

3.3.6.2 Longitudinal sand dunes (composite):

The basis of these dunes is the crescent dune, which, when exposed to winds intersecting the prevailing winds in the region, can cut the wings of the crescent dune, making one longer than the other. Wind eddies carry the remnants of these dunes, causing the edges to lengthen and the formation of longitudinal dunes from the previous crescent shape. Bagnold saw that these dunes may be the result of air currents associated with strong winds that blow permanently in one direction and extend their axes parallel to these winds, but he stressed that the compound dunes begin their life cycle as crescent dunes due to their exposure to side winds that intersect with the permanent direction of them, which leads to the elongation of one of the sand dune sides (Al-Jashaami et al., 2024).

When studying this type in the field, it is observed that compound dunes result from the merging of crescent dunes. The merging of dunes aligned in a longitudinal orientation is also observed, creating a wind barrier in the dune-merger area, leading to sedimentation and the filling of these areas with sand particles (Figure 2).

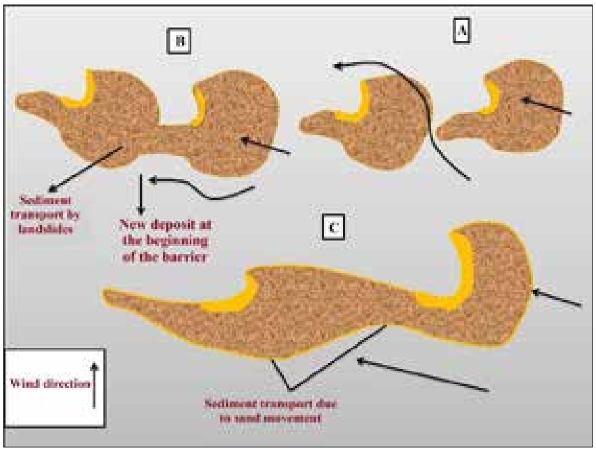

Figure 2. Stages of formation of the longitudinal dune (composite)

3.3.6.3 Nebkas sand dunes:

This type of sand dune forms when a sand-laden wind encounters an obstacle, such as plants, especially desert shrubs, or a massif, which acts as a barrier. This causes the wind to deposit its sediment load around the plant or massif (Wang et al., 2002). Continued accumulation of sand grains on the plant leads to cohesion, forming a triangular shape whose head points in the direction of the wind. It grows until it becomes a dune known as a Nebka. The plant is eventually covered, leading to its death and decay, especially in annual plants. The sand grains then become loose and are easily winnowed, carried, and transported by the wind again. These dunes move slowly and cohere with the roots of plants (Sabah Baji Diwan, 2013) (Figure 3).

Figure 3. A picture showing the formation of the dunes of Nebkas

Wide sand dunes:

The reason why this type of dune is called by this name is because it intercepts the movement of the prevailing winds as they are perpendicular to them. This type arises when there is an abundance of sand, and the area is devoid of vegetation. The transverse dunes consist in two sides (as in the crescent dunes), extending in opposite directions. The first is a slope and takes a concave shape at an angle ranging between (15-32) (Gaur et al., 2023).

Figure 4. A picture showing the formation of the wide dunes

3.4 Movement of sedimentary particles of sand dunes

Grains and sand sediments move in three ways, which are chemical:

1. Creeping: Moving in this way, coarse grains that cannot be carried by the wind, rolling grains moving on the surface of the earth for short distances, and when moving, may collide with other grains lead to their movement is the other, and the size of the grains that move in this way ranges from (1 – 2 mm) (Baas, 2019).
2. Saltation: The grains move in this way to close distances from the surface of the soil, due to direct wind pressure on the grains. As the grains rise to the top, then down, then to the top again after blowing new air again, and the size of the grains that move in this way ranges between (0.05 – 1 mm) (Bass 2019).
3. Suspension: very fine grains of sand, less than 0.05 mm in diameter, which are very soft, are carried in this way in the upper layers of the atmosphere and can travel very long distances, up to 3000 – 4000 km. They remain suspended in the air for a long time and are then deposited when wind speed and strength weaken due to low atmospheric pressure (Al-Guralry & Al-Zubaidi, 2023).

3.5 The negative effects of sand dunes and ways to control them:

Sand sediments affect when they move and sedimentation on many human facilities, especially agricultural and industrial activity, services, and conductor roads, as well as having a role in the activity of dust phenomena, suspended dust, and rising dust, which have negative effects represented in the following:

3.5.1 Effects on soil:

Sand dunes lead to the loss of large amounts of soil, the change in its properties, and a decrease in its ability to retain organic matter, which leads to the loss of soil fertility and thus a lack of plant growth. The process of wind splashing repeats, splashing small particles, and then desertification begins, which leads to a change in the properties of the soil and a decrease in its productivity, and thus the loss of large areas of agricultural land.

3.5.2 Impact on agricultural lands, irrigation channels, and natural pastures:

The encroachment of sand dunes on agricultural land is one of the most serious problems, as it leads to the landfilling of arable land, altering the characteristics of its soil, spreading loose, dry soils over it, eliminating its vegetation cover, exposing it to various erosion factors, and ultimately converting it into land unsuitable for agricultural production by transferring the characteristics of dry desert soils, and over time converting it into a desert.

Figure 5. Showing the landfilling of irrigation channels due to the movement of sand dunes

3.5.3 Impact on transport and connectors ways:

Sand dunes are one of the factors affecting transport routes in areas near the sand dunes, as they affect the main tiled roads and other unpaved secondary roads.

Figure 6. The encroachment of sand dunes on land roads

3.5.4 Impact on the industrial facility (gravel and sand quarries in the region):

The effect of sand dunes on these quarries is in two forms: The first is a direct effect where the sand dunes crawl on these quarries, which leads to the difficulty of controlling them, while the second form has an indirect effect through the creep of sand dunes on the road that leads to the quarries and thus the difficulty of reaching the load cars to the quarries that transport gravel and sand from these quarries and thus stop working in them.

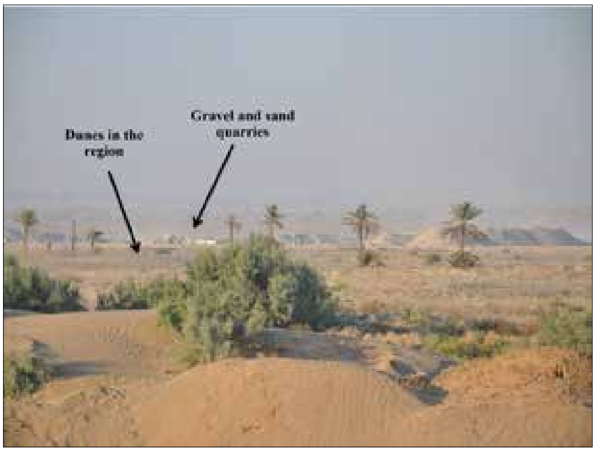

Figure 7. The effect of sand dunes on quarries directly

3.5.5 Impact on residential villages in the region:

The neighboring villages near the sand dunes suffer from sand creeping toward their homes, with sand grains and rising dust colliding with their doors and windows, leading to the deposition of sand particles inside. In some cases, this may lead to residents migrating or leaving their homes during the summer due to the intensity of the winds and the dryness of the region, as well as the mental health damage it causes, such as feeling suffocated and not opening the doors because of sand particles entering the house. This can leave a person feeling as if they are living an abnormal life, as if they are in the middle of a barren desert.

3.6 Ways to reduce the effects of sand dunes

Several methods are used to stabilize the sand dunes, including mechanical and other biological methods, which are as follows:

3.6.1 Mechanical methods (temporary methods):

1. Earth mounds: The main purpose of establishing earth mounds is to establish defensive lines and barriers that resists sand encroachment towards the facility to be protected, such as irrigation projects, roads, cities, agricultural lands, etc. In addition to stopping the sand creep and preventing its access to the facility to be protected, the berms are intersecting with the prevailing wind direction in the region, The distance between one berm and another depends on the density of the sand dunes in the region, where the distance is low if the sand dunes are dense, and earthen mounds help to create suitable conditions for the growth of natural plants and the success of afforestation due to hindering the creep of the sand dunes. They also work as fences that prevent the entry of animals for grazing in the region and are often at a height of (2-3 m). Mechanisms are used in the work of these berms (Hereher, 2010).

2. 2- The work of fences: It is the work of fences made from plant residues, such as palm fronds, reeds, and papyrus, that act as bumpers to reduce wind speed in front of the sand dunes. However, because of the limited capacity of the area that contains the sand dunes in the study area, this method has become useless, as it requires large quantities of plant residues, a long time, and high labor costs.

3. Modification and levelling of sand dunes (mechanical potential): It is a method used in areas where the sand dunes are newly formed, provided that they are planted with agricultural crops, as they must be close to water sources, as the windbreaks were established in them after they were modified and ploughed deep tillage through which the sand mixes with agricultural soil, and then it is planted and afforested and this process takes place in the winter, where the movement of sand is almost stopped.

4. Mulching: The sand dunes are covered with a heavy layer of clay from the areas adjacent to the sand dunes by machinery (bulldozer), where the thickness of this layer is (20-30 cm), As it works to stop the movement of the dunes completely, because it is a heavy soil (clay) that is difficult to transport by the wind and when rain falls, it holds together and works to protect the sand underneath, as well as its pressure due to heavy machinery on it during the covering process. This method is characterized by its ease and speed of completion and does not need extensive experience and low costs compared to other means, as well as it helps to develop vegetation cover for water retention (Figure 8). But if the areas

are vast, it is necessary to switch to coverage, using oil (black oil) to treat the movement of sand dunes in lands where agricultural activities cannot be used, because oil derivatives have a negative impact on agricultural land, and this method is rehabilitated and defects are repaired after a period not exceeding five years (Scherr & Satya Yadav, 1996).

3.6.2 Biological methods (permanent means of prevention):

This method is one of the approaches that provide sustainability in the stabilization of sand dunes, and the presence of vegetation means the permanent stability of the sand dunes. The removal of vegetation cover by humans helped form sand dunes, and the re-vegetation of such areas can eliminate the problem of moving sand dunes, if managed in ways that suit the special environmental conditions of those areas, such as exploiting types of trees that tolerate drought and soil salinity and using trees in the study area (Tamarisk, eucalyptus) for easy propagation, as well as their ability to withstand drought and salinity. These methods in the study area are as follows:-

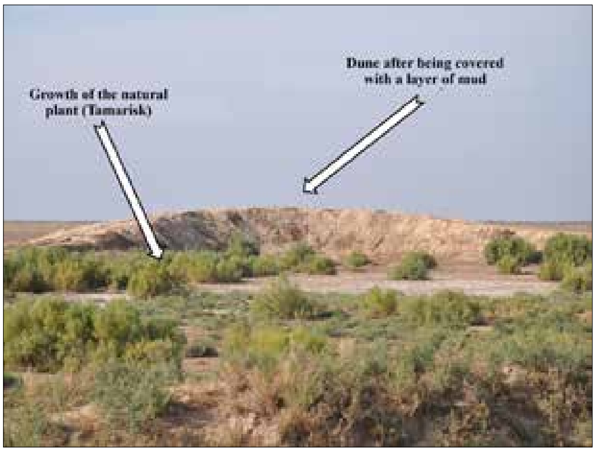

Figure 8. The dunes covered with a layer of clay

1. Development of natural herbs:

It is a method that comes naturally after the sand dune is covered with clay soil, where vegetation is grown on it when appropriate conditions are available, and it is also important to protect it from overgrazing, because the presence of animals on the sand dune removes vegetation cover and destroys the clay layer, which leads to its deterioration again. This requires preventing the entry of animals for grazing purposes. The most important of these plants are Tamarisk, Anabasis, and Saltwort.

2. Cultivation of windbreaks (green belts):

Planting trees in areas with moving sand dunes is important because they act as bumpers to reduce wind speed and improve natural conditions for the growth of native plants in these areas. If planted systematically, they further reduce wind speed and soil erosion. After completing mechanical methods, green belts and windbreaks are planted in sand dune areas, with trees selected for their ability to withstand drought and soil salinity, as mentioned earlier. In the study area, tree types such as Tamarisk and Eucalyptus are planted, among others, and then irrigated only in the first year.

3.6.3 The use of remote sensing and geographical information systems to monitor desertification:

In a study of spatial extensions of the sand accumulations significantly for the years (2000-2005-2013-2019), on the pastoral lands of two regions in the Western Desert of Iraq, depending on the techniques of remote sensing and geographic information system, this covered an area of (1826.5 km^2) (harbi Ibrahim & Said, 2023). The researcher (Alalwany et al., 2021) explained in his study the patterns of sand movement in the Western Desert in Egypt and its impact on the environment in the study area, where the accumulations move 40 meters in three broad directions during the year. The movement of these sand accumulations is related to the prevailing wind system within the region. (Hereher, 2010) Studied the economic risks of sand dune movement and its impact on agricultural development in southern Siwa Oasis in Egypt, he also calculated the area affected by sand dune movement has arrived 50,629 acres, and the cost of economic losses from the seriousness and effects of sand accumulation movement has arrived L.E 3206.7 million. The researcher (Abo, 2015) pointed out in his study of the Ratqa Valley basin, which is part of the Hammad Basin, it can be agriculturally exploited, and the lands of the basin of this valley suffer from the problem of gathering dunes that threaten agricultural areas within the basin of this valley, as well as agricultural lands in the district of Al -Qaim.

Figure (9) illustrates the time trend of the decline in the vegetation cover index (NDVI) in Iraq during the period 2000–2023, reflecting the deterioration of vegetation cover associated with the increasing severity of desertification, drought, and climate change.

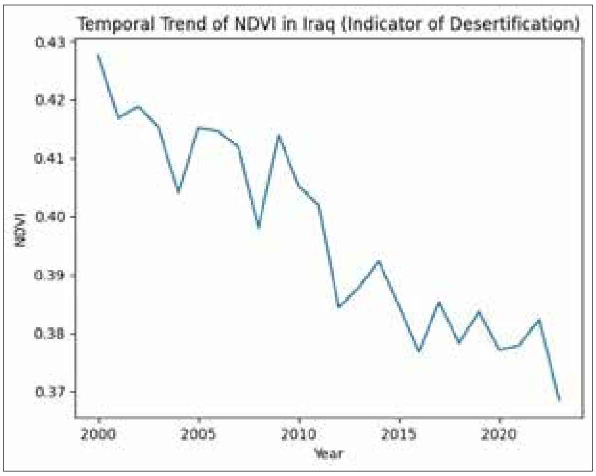

Figure 9. Temporal trend of NDVI in Iraq as an indicator of desertification. Source: MODIS satellite data; adapted following land degradation monitoring approaches by Al-Ansari et al., 2021 reported in JJEES.

Desertification was incorporated into the Sustainable Development Goals outlined in the 2030 Agenda for Sustainable Development in order to address its possible effects on the economy, ecology, and society. The main objective of Sustainable Development Goal 15 is to safeguard, restore, and promote the sustainable use of land-based ecosystems, effectively manage forests, prevent desertification, and halt and reverse land degradation and biodiversity loss (Yousef et al., 2025). According to projections of future climate change, desertification will increase globally due to changes in temperature, precipitation, carbon sequestration, and atmospheric carbon dioxide levels. Sustainable Development Goal 15.3 aims to rehabilitate land and soil degraded by desertification, drought, and floods. The primary objective is to attain a state of balance by 2030, when restoration activities effectively offset the adverse impacts of land degradation. Addressing desertification is essential for reducing global poverty and mitigating the negative impacts on biodiversity and climate change resulting from human activities (Mukhlif, 2015). Remote sensing technology, by analyzing multispectral images, allows you to monitor climate, soil, and vegetation dynamics of a territory. By means of spectral indices NDVI (Normalized Difference Vegetation Index), MSAVI (Modified Soil-Adjusted Vegetation Index), NDMI (Normalized Difference Moisture Index), NBR (Normalized Burn Ratio), Spectral Albedo values (BRDF) of Liang, BSI (Bare Soil Index), LST (Earth's surface temperature), and the GIS technology, is possible to accelerate the acquisition of spatial-environmental data. The authors started out with research about the use of the aforementioned spectral data, considering the study area Mussomeli Municipality (Caltanissetta Province, Sicily), to evaluate the sensitivity of the area to desertification, in a short period (year, season). In this study, the satellite data are considered in MEDALUS (Mediterranean Desertification and land use) protocol, which adopts data attributable to four Macro factors: protection, soil, climate, and land management (Bolch et al., 2021). The use of geospatial data and Geographic Information Systems (GIS) technologies for monitoring and mapping desertification processes has become essential for understanding landscape dynamics, assessing environmental change, and informing strategies for sustainable land management (Mussumeci et al., 2024).

The Mirzachul was chosen as a desertification monitoring case study. To identify the soil types present in the case study area, Landsat imagery for 1994-2024 and the Soil Map of Uzbekistan served as auxiliary data. We concentrated on the NDVI, SAVI, and WDVI. The trends of sandy bare soil and steppe were also significantly different in 1994, with approximately 830 ha and 3800 ha (Yuan-he et al., 2016), respectively. However, by 2024, the area of sandy bare soil had decreased sharply by about 50% to 1.5 million hectares, while the area of steppe had increased to 2 million hectares (Abdimuminov et al., 2024).

Using information drawn from remote sensing, various aspects of desertification can be analyzed, monitored, and predicted. Over –the years, there have been several approaches to studying desertification using RS. This paper explored the global-scale prevalence and chronology characteristics of research that applied RS to study desertification. Moreover, the research also considered the main methods and elements used to study desertification through remote sensing data analysis. 1991 Desertification Research on the Theme of RS and Application in Desertification Research began from 22.The early application of remote sensing in the research on desertification originates from 22. From 2015 to 2020, more than 40 papers were published on average annually, and this represents a significant increase in the use and availability of remote sensing (RS) technology for desertification assessment (Abdimuminov et al., 2024).

Assessment of Land Degradation Risks. Remote sensing and GIS, as well as tools, are powerful for assessing such risks in different fragile ecosystems, for example, Al Gadeer. The methodology is tested in A by using this combination of remote Sensing, where (Mazahreh et al., 2012). 2019) applied different data and maps as an input to (GIS) to generate potential suitability for various Land Utilization Types (LUTs). Suitability assessment. Land suitability mapping has been developed by integrating soil and climate information within a novel approach.

The monitoring and prediction of desertification in arid areas are important for the solution of environmental and social problems. Supplemental to remote sensing for monitoring land surfaces and ecosystems. The objective of this research is to monitor and predict desertification in the Sistan Plain using raw data from remote sensing, based on a data screening method. The satellite data for the study included images from Landsat 5 and 8 captured in June each of 10 years (1990–2020). The remote sensing-based indices such as LULC map, normalized differential vegetation index (NDVI), enhanced vegetation index (EVI), VCI, TCI, MNDWI, and SI were utilized in the study. Central satellite data, SPI, and SDI environmental indices were also included for analysis (Yousef et al., 2025).

The researcher (Hashemi et al., 2024)pointed out in his study the role of modern technologies in monitoring desertification, as he used Remote Sensing (RS), Geographic Information Systems (GIS), and Global Positioning Systems (GPS) technologies, which have proven their importance in studying soil surveys, as they save time and effort and provide continuous information and values for soil characteristics and their spatial and temporal variations in a comprehensive manner, where risks can be predicted and then the necessary measures taken to reduce them and preserve resources.

Change detection is the process of determining the difference in observing the phenomenon over different time periods. Modern technologies have enabled monitoring and observation of changes in vegetation cover across very large areas at different times. To control and monitor the density and distribution of vegetation in desert environments with unlimited boundaries, repeatedly and continuously integrated by means of remote sensing, is considered important in the preservation of this ecosystem and its maintenance and the preservation of what is deteriorating for the purpose of developing implementation plans to maintain that wealth (Abdulhameed et al., 2022).

4. Desertification in Iraq

Desertification in Iraq is driven by multiple climatic and anthropogenic factors. To provide clarity and synthesis, the following tables summarize the main drivers and impacts across Iraqi regions, as well as the mitigation strategies currently applied and their effectiveness.

Figure 10 and Table 1 show the relative importance of the main factors causing desertification in Iraq, where low rainfall, high temperatures, and soil salinity are among the most influential factors, in addition to overgrazing and poor land management.

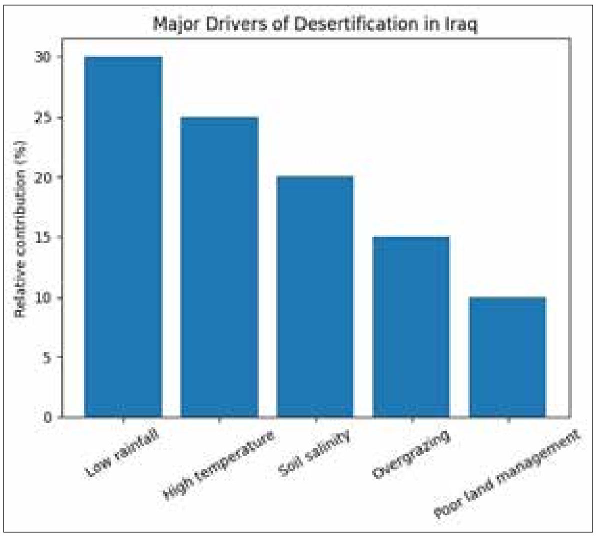

Figure 10. Major drivers of desertification in Iraq. Source: FAO (2020), UNCCD (2022), Salah and Salahat, 2020, JJEES.

Table 1. Main drivers of desertification in Iraq and their regional impacts. Adapted from Alkhateeb et al., 2019; Al-Shamary et al., 2021; Abdulrahman, 2025.

Driver	Most affected region	Main impact
Declining rainfall & rising temperatures.	Southern and central Iraq.	Loss of vegetation cover, increased sandstorms.
Mismanagement of water resources (salinization, evaporation).	Southern provinces (Basra, Dhi Qar).	Soil salinity, reduced agricultural productivity.
Overgrazing.	Northern and central Iraq.	Rangeland degradation, biodiversity loss.
Deforestation .	Anbar and Diyala.	Soil erosion, loss of vegetation.
Population growth & urbanization.	Baghdad and peri-urban areas.	Pressure on resources, unregulated urban expansion.

Several strategies have been adopted to mitigate desertification in Iraq, as shown in Table 2. This shows the effectiveness of each strategy.

Table 2. Mitigation strategies against desertification in Iraq and their effectiveness. Adapted from Rasul (2016), Safriel (2009), UNCCD (2024), Chasek et al. (2019).

Strategy	Application in Iraq	Effectiveness	Notes
Afforestation/reforestation.	Limited campaigns in Anbar and southern Iraq.	Moderate.	Lack of funding and sustainability.
Water management (modern irrigation, water harvesting).	Pilot projects in Kirkuk and Najaf.	High.	Requires scaling-up and government support.
Sustainable agriculture (biochar, soil amendments).	University research and small-scale trials.	Moderate.	Scientifically effective but not widely adopted.
International cooperation (UNDP, FAO projects).	Small-scale initiatives.	Low.	Hindered by instability and limited resources.

Desertification in Iraq is depicted in Figure 11, showing the areas most affected and the environmental impacts of climate change and water shortage.

- The government has launched efforts to address the problem, but is hampered by large hurdles.

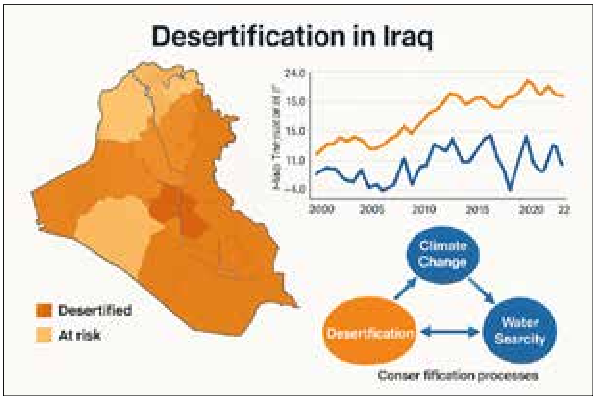

Figure 11. Desertification in Iraq. Adopted from https://masae-analytics.com/

5. Conclusions

The results in Tables 1 and 2, as well as Figs. 9–11, illustrate the intricate relationships of both climatic fluctuations and human activities in shaping desertification across Iraq. The data provided to us is evidence that desertification is a consequence not only of climate change, but also as a result of bad land use and water management … and due to the fact that the people seem to cut off the branch they sit on.

Policy Analysis

Existing policies in Iraq to combat desertification are not coherent and adequate. Reforestation programs remain meritorious but are handicapped by inadequate friend-foe identification, weak community involvement. Water management measures, such as dam building and traditional irrigation based on water-demanding crops, have frequently exacerbated soil salinity and declining groundwater recharge. Additionally, institutional harmonization is insufficient among the Ministries of Agriculture, Environment, and Water Resources, leading to duplication of roles and lack of effective implementation.

Drivers and Impacts

The distribution (Figure 11) shows that desertification hotspots are mainly located in the western and southern sides, where there is the most precipitation decline and temperature increase. These changes in climate, coupled with overgrazing and deforestation, have contributed to increased soil erosion and loss of vegetation.

Effectiveness of Mitigation Strategies

Table 2 indicates that although the strategies have been implemented in some cases – afforestation and sustainable agriculture, for instance – their implementation has low effectiveness due to insufficient funding and lack of farmer participation. While international cooperation (including with its neighbours on transboundary water management) is lacking, Iraq remains exposed to upstream states' water policies.

This assessment verifies that desertification in Iraq is not just an environmental problem, but a strategic issue which affects the ability of the country to ensure food security and sustainable development. The research identifies three main factors for the decline, including poor management of water resources, climate change, and unsustainable land use. Appropriate actions, consequently, effective responses also call for an integrated national policy on management of land and water, the launching of public-awareness campaigns, and the introduction of modern techniques to limit soil degradation. The results presented will be useful in the context of both scientific discussions on desertification and policy-making and development activities in Iraq. In addition, the present work pinpoints areas that would need further investigation in the future, especially technically and economically viable solutions which can enhance Iraq's ability to combat desertification and meet sustainable environmental development.

6. Recommendations

To face these challenges, Iraq needs to consider an integrated approach that encompasses environmental, social, and economic dimensions. Key recommendations include:

1. Establishing early warning systems for drought and desertification.
2. Promoting modern irrigation techniques (e.g., drip irrigation) to reduce water waste.
3. Enhancing regional cooperation with Turkey and Iran on shared water resources.
4. Empowering local communities to participate in afforestation and land restoration projects.
5. Aligning national strategies with UNCCD frameworks and the Sustainable Development Goals (SDGs).
6. Expansion in the studies of using remote sensing and geographic information system as early warning to monitor desertification especially in Iraq.
7. Using the recent technologies to mitigate the creeping of sand dunes towards agricultural lands.
8. Using all means to retain soil moisture which prevent sand particles from transport to other areas.
9. Appropriate use of water harvesting techniques to mitigate desertification.
10. Limiting pastoralists' overgrazing in places that are likely to turn into deserts.
11. Establishing laws to preserve desert plants.
12. Working on afforestation of desert areas with heat-tolerant plants.

References

Abdelfattah, M. A., Dawoud, M. A. H., & Shahid, S. A. (2009). Soil and water management for combating desertification: Towards implementation of the United Nations Convention to Combat Desertification from the UAE perspectives. Proceedings of the International Conference on Soil Degradation, Riga, Latvia. https://www.researchgate.net/publication/259178629_Soil_and_water_management_for_combating_desertification_-_towards_implementation_of_the_United_Nations_Convention_to_Combat_Desertification_from_the_UAE_perspectives

Abdimuminov, B., Mamatkulov, Z., Allanov, K., Abdunazarav, H., Umarova, M., & Choriev, A. (2024). Monitoring and mapping of desertification process using geospatial data and GIS technologies in Mirzachul area. E3S Web of Conferences. https://doi.org/https://doi.org/10.1051/e3sconf/202459003008.

Abdulhameed, I. M., Alhadeethi, I. K., Jabir, A. A., Fayyadh, A. S., Mohammed, A. S., Kamel, A. H., Ghani, E. T. A., Mutar, H. A., Al-Esawi, J. S. E., & Almafrchi, K. Y. (2022). Guideline of Iraqi valleys development. Upper Euphrates Basin Developing Center. https://www.researchgate.net/publication/361007080_Guideline_Of_Iraqi_Valleys_Development_1_Wadi_Horan

Abdulrahman, S. A. (2025). Iraq's Desertification: The Complication of Environmental Security Issues. Natural Built Social Environment Health, 1(01), 81-98. https://doi.org/10.63095/NBSEH.25.720252.

Abdelwahab, M., & Mustafa, M. (2021). A review Research on

Wind Erodibility of Some States and Their Interrelationships in Sudan. Jordan Journal of Earth & Environmental Sciences, 12(4). https://jjees.hu.edu.jo/files/Vol12No4/JJEES_Vol_12_No_4_P9.pdf

Abo, R. S. A.-S. (2015). Sand dunes movement and its impact on development plans, Siwa Oasis. International Journal of Research in Economics and Social Sciences, 5(11), 124–133. https://www.academia.edu/30072199/Sand_dunes_movement_and_its_impact_on_development_plans_Siwa_Oasis?auto=download.

Abusmier, S. A., & Al-Kofahi, S. D. (2024). Examining land use/land cover dynamics in Zarqa Governorate major districts: Implications for urban and environmental sustainability. Jordan Journal of Earth and Environmental Sciences, 16(1), 45–60. https://www.researchgate.net/publication/389891405_Examining_Land_UseLand_Cover_Dynamics_in_Zarqa_Governorate_Major_Districts_Implications_for_Urban_and_Environmental_Sustainability.

Adamo, N., Al-Ansari, N., Sissakian, V. K., Knutsson, S., & Laue, J. (2018). Climate change: Consequences on Iraq's environment. Journal of Earth Sciences and Geotechnical Engineering, 8(3), 43–58. https://iraqi-forum2014.com/wp-content/uploads/2018/05/Vol-8_3_3.pdf.

Agam, N., & Berliner, P. R. (2006). Dew formation and water vapor adsorption in semi-arid environments: A review. Journal of Arid Environments, 65(4), 572–590. https://doi.org https://doi.org/10.1016/j.jaridenv.2005.09.004.

Ahmed, A. D., Abdulhameed, I. M., Ghani, E. T. A., & Ibrahim, M. K. (2020). Selection of water harvesting sites in Horan valley. IOP Conference Series: Materials Science and Engineering. https://doi.org/10.1088/1757-899X/881/1/012183?urlappend=%3Futm_source%3Dresearchgate.net%26utm_medium%3Darticle.

Al-Gurairy, A., & Al-Zubaidi, A. (2023). Climate change and its impact on the expansion of the phenomenon of sand dunes and desertification of agricultural lands in Iraq for the period 1984–2022 (Governorates of Al-Qadisiyah, Al-Muthanna, and Dhi Qar). Israa University Journal of Applied Sciences, 7(1), 75–96. https://doi.org/10.52865/YJPI8019.

Al-Jashaami, S. H., Almudhafar, S. M., & Almayahi, B. A. (2024). Desertification and its impact on agricultural production in Iraq. Library of Progress – Library Science, Information Technology & Computer, 44(3). https://www.researchgate.net/publication/385291236_Desertification_And_Its_Impact_On_Agricultural_Production_In_Iraq

Al-Juboori, J. M. Y., Khairo, A. M., & AlShamary, W. F. (2023, April). The thermal conductivity and matric potential (moisture tension) relationships for soils of different gypsum content. In IOP Conference Series: Earth and Environmental Science (Vol. 1158, No. 2, p. 022007). IOP Publishing. https://doi.org/10.1088/1755-1315/1158/2/022007

Al-Kasoob, G. F., Al-Sulttani, A. H., Al-Quraishi, A. M. F., & Hussein, R. N. (2024). Monitoring drifting sand using spectral index and Landsat TM/OLI datasets in Bahr An-Najaf area, Iraq. In Natural Resources Deterioration in MENA Region: Land Degradation, Soil Erosion, and Desertification (pp. 241–260). Springer. https://doi.org/ https://doi.org/10.1007/978-3-031-58315-5_12

Al-Naji, A. J., & Al-Shammery, T. A. (2019). Mineralogical study of sand dunes fields in Najaf Governorate, Southern Iraq. Iraqi Journal of Science, 239–254. https://doi.org/10.24996/ijs.2019.60.2.6.

Al-Obaidi, J. R., Yahya Allawi, M., Salim Al-Taie, B., Alobaidi, K. H., Al-Khayri, J. M., Abdullah, S., & Ahmad-Kamil, E. (2022). The environmental, economic, and social development impact of desertification in Iraq: A review on desertification control measures and mitigation strategies. Environmental Monitoring and Assessment, 194(6), 440. https://doi.org/10.1007/s10661-022-10102-y.

Mazahreh, S., Bsoul, M., & Hamoor, D. A. (2019). GIS approach for assessment of land suitability for different land use alternatives in semi arid environment in Jordan: Case study (Al Gadeer Alabyad-Mafraq). Information Processing in Agriculture, 6(1), 91–108. https://doi.org/10.1016/j.inpa.2018.08.004

Al-Shamary, W. F. A., Alkhateb, B. A. A. H., Abd Al-Jabbar, M. S., & Kahlel, A. S. (2021, May). Impact of date residues, humic acid and the level of irrigation in growth and yield of onions (Allium cepa L.). In IOP Conference Series: Earth and Environmental Science (Vol. 761, No. 1, p. 012011). IOP Publishing. https://doi.org/10.1088/1755-1315/761/1/012011

Al-Shamary, W. F. A., Alkhateb, B., Ghani, E. T. A., Al-Antary, T. M., & Kahlel, A.-M. S. (2021). The influence of perlite and irrigation management on the properties of potatoes in gypsiferous soil. Fresenius Environmental Bulletin, 30(5), 4771–4778. https://www.researchgate.net/publication/352440377_THE_INFLUENCE_OF_PERLITE_AND_IRRIGATION_MANAGEMENT_ON_THE_PROPERTIES_OF_POTATOES_IN_GYPSIFEROUS_SOIL_CIRCADIAN_RHYTHMS_View_project_Agricultural_patterns_View_project_THE_INFLUENCE_OF_PERLITE_AND_IRRI

Al-Trabulsy, H. A. M. (1993). Investigation of some astronomical phenomena in medieval Arabic chronicles [Doctoral dissertation, Durham University. https://etheses.dur.ac.uk/5691/1/5691_3107.PDF?UkUDh:CyT.

Al-Turaihi, A. S., Al-Zubaydi, J. H., & Manii, J. K. (2023). Engineering and Minerological Characteristics of Sand Dunes of Babylon Governorate, Iraq. The Iraqi Geological Journal, 247-258. https://doi.org/10.46717/igj.56.1E.19ms-2023-5-29

Alalwany, A., Mukhlif, H., & Abdulkareem, B. (2021). A study of the distribution of sand sheet on some pastures in the Western Desert of Iraq. IOP Conference Series: Earth and Environmental Science. https://doi.org/10.1088/1755-1315/904/1/012002

Alkhateeb, B., Alshamary, W., & Aljumily, A. (2019). The role of perlite and irrigation management in water consumptive, growth and yield of potato (Solanum tuberosum L.) in sandy loam soil. Biochemical & Cellular Archives, 19(2). DOI: 10.35124/bca.2019.19.2.4063

Alobaidy, A. S., Tahir, H. T., & Alshamary, W. F. (2024). The role of the use of some soil enhancers and the type of subsurface drip irrigation tube in some of the physical properties of the soil and the efficient use of water for the growth and yield of eggplant crop under protected farming conditions. Sciences, 15(4), 40–51. https://iasj.rdd.edu.iq/journals/uploads/2024/12/03/699c811f25f990d82b10a2400f72e216.pdf

Alshamary, W., Aljumily, A., Ghani, E. T. A., & Alkhateb, B. A. (2021). The influence of binary irrigation (BI), humic acid (HA), and various saline water on water consumption (WC), water use efficiency (WUE) of corn (Zea mays L.). Ecology, Environment and Conservation, 27(1), 316–322. https://www.envirobiotechjournals.com/EEC/v27i121/EEC-46.pdf

Alsultan, R. M. H., Al-Shamary, W. F. A., Ibrahim, M. A., & Kahlel, A. S. (2023). Effect of biochar and amino acid (steam) on growth and green yield of onion (Allium cepa L.) variety (Karbala). IOP Conference Series: Earth and Environmental Science. https://doi.org/10.1088/1755-1315/1259/1/012047

Alsultan, M., Alobaidy, H., & Ahmed, S. (2024). Rainfall anomalies and temperature rise in Iraq: A 20-year analysis. Iraqi Journal of Environmental Science, 18(1), 33–47. https://doi.org/10.1007/s00704-022-03976-y

Al-Tameemi, N., Xuexia, Z., Shahzad, F., Mehmood, K., Linying, X., & Zhou, J. (2025). From Trends to Drivers: Vegetation Degradation and Land-Use Change in Babil and Al-Qadisiyah, Iraq (2000–2023). Remote Sensing, 17(19), 3343.

https://doi.org/10.3390/rs17193343.

Al-Sababhah, N., & Al-Maqablah, M. (2023). Integrated evaluation of soil erosion-prone areas and land degradation risk. Jordan Journal of Earth and Environmental Sciences, 14(2). https://jjees.hu.edu.jo/files/Vol14/No.2/JJEES_Vol_14_No_2_P8.pdf

Al-Weshah, R., Al-Salahat, M., & Al-Omari, S. (2024). Flood hazard mapping from dam break: A case study of King Talal Dam. Jordan Journal of Earth and Environmental Sciences, 16(1), 61–72. https://jjees.hu.edu.jo/files/Vol16/No1/JJEES_Vol_16_No_1_P4.pdf

Ati, A. A. S. S., Al-Daraji, R. A. H., & Al-Ghuraibi, I. M. (2021). Climate change and combating desertification. Methodological book. Ministry of Higher Education and Scientific Research – University of Baghdad – College of Agricultural Engineering Sciences. Unavailable online.

Awadh, S.M. (2024). Drought and Desertification Hazard in Iraq. In: Abd el-aal, A.ea.K., Al-Enezi, A., Karam, Q.E. (eds) Environmental Hazards in the Arabian Gulf Region. Advances in Natural and Technological Hazards Research, vol 54. Springer, Cham. https://doi.org/10.1007/978-3-031-71836-6_14.

Baas, A. C. (2019). Grains in motion. Aeolian Geomorphology: A New Introduction, 27-60. https://doi.org/10.1002/9781118945650.ch2.

Bagnold, R. A. (1954). Experiments on a gravity-free dispersion of large solid spheres in a Newtonian fluid under shear. Proceedings of the Royal Society of London. Series A. Mathematical and Physical Sciences, 225(1160), 49–63. https://royalsocietypublishing.org/rspa/article-media/9364/pdfviewer/48449

Becerril-Piña, R., & Mastachi-Loza, C. A. (2021). Desertification: Causes and countermeasures. In Life on Land (pp. 219–231). Springer. https://doi.org/10.1007/978-3-319-95981-8_81

Boer, B., & Hannam, I. (2021). Restoration of ecosystems and land degradation neutrality. In Fulfilling the Sustainable Development Goals (pp. 392–404). Routledge. https://doi.org/10.4324/9781003144274-30?urlappend=%3Futm_source%3Dresearchgate.net%26utm_medium%3Darticle

Bolch, E. A., Hestir, E. L., & Khanna, S. (2021). Performance and feasibility of drone-mounted imaging spectroscopy for invasive aquatic vegetation detection. Remote Sensing, 13(4), 582. https://doi.org/10.3390/rs13040582

Chasek, P., Akhtar-Schuster, M., Orr, B. J., Luise, A., Ratsimba, H. R., & Safriel, U. (2019). Land degradation neutrality: The science-policy interface from the UNCCD to national implementation. Environmental Science & Policy, 92, 182–190. https://doi.org/10.1016/j.envsci.2018.11.017

Darkoh, M. B. (2018). The nature, causes and consequences of desertification in the drylands of Africa. Land Degradation & Development, 9(1), 1–20. https://doi.org/10.4324/9781315192963-10?urlappend=%3Futm_source%3Dresearchgate.net%26utm_medium%3Darticle

Diwan, S. B. (2013). Spatial analysis of the distribution and forms of sand dunes in Maysan Governorate. Al-Ustad Magazine, 8(205), 113. https://search.mandumah.com/Record/466794

Eklund, L., & Pilesjö, P. (2012). Migration patterns in Duhok Governorate, Iraq, 2000–2010. Open Geography Journal, 5, 48–58. https://doi.org/10.2174/1874923201205010048

El Gamri, T. (2020). Sand dunes: Mechanisms, impacts and control measures in the Sudan. Environment and Natural Resources International Journal (ENRIJ), 5, 1–16. https://www.researchgate.net/publication/349378038_Sand_Dunes_Mechanisms_Impacts_and_Control_Measures_in_the_Sudan

Eltaif, N.I., Gharaibeh, M.A., Fadhil Al-Quraishi, A.M. (2024). Impact of Climate Change on Iraq: Severe Water Scarcity and Desertification. In: Al-Quraishi, A., Negm, A., Benzougagh, B. (eds) Climate Change and Environmental Degradation in the MENA Region. The Handbook of Environmental Chemistry, vol 136. Springer, Cham. https://doi.org/10.1007/698_2024_1100.

Gaur, M. K., Wadhawan, S. K., & Dhir, R. (2023). Geomorphological characteristics of sand dunes and evolution of aeolian landscape for sustainable future in western Thar Desert, Rajasthan, India. In Sand dunes of the Northern Hemisphere (pp. 246–277). CRC Press. https://doi.org/10.1201/9781003125426-19?urlappend=%3Futm_source%3Dresearchgate.net%26utm_medium%3Darticle

Steven Fryberger, Breed C.S., McKee E.D. (1979). A study of global sand seas: Glossary. Prepared in cooperation with the National aeronautics and Space administration, United States Department of Interior, Publisher: U.S. Geological Survey.

Goudie, A. S. (2018). Human impact on the natural environment: Past, present and future. John Wiley & Sons. https://tuannguyenweb.wordpress.com/wp-content/uploads/2017/04/andrew-s-goudie-the-human-impact-on-the-natural-environment_-past-present-and-future-wiley-blackwell-2013.pdf

Goudie, A. S., & Middleton, N. J. (2006). Desert dust in the global system. Springer Science & Business Media. https://doi.org/10.1007/3-540-32355-4

Harbi Ibrahim, I., & Said, Y. H. (2023). Food security policy in Iraq and the challenges of response after 2003. Tikrit Journal for Political Science, 3(pic4), 287–314. https://doi.org/10.25130/tjfps.v3ipic4.238

Hashemi, Z., Sodaeizadeh, H., Mokhtari, M. H., Ardakani, M. A. H., & Aliabadi, K. K. (2024). Monitoring and forecasting desertification and land degradation using remote sensing and machine learning techniques in Sistan plain, Iran. Journal of African Earth Sciences, 218, 105375. https://doi.org/10.1016/j.jafrearsci.2024.105375

Hereher, M. E. (2010). Sand movement patterns in the Western Desert of Egypt: An environmental concern. Environmental Earth Sciences, 59(5), 1119–1127. https://doi.org https://doi.org/10.1007/s12665-009-0102-9.

https://shafaq.com/en/society/Over-half-of-Iraq-now-at-risk-of-desertification-ministry-warns.

Ide, I., Abdourhamane Toure, A., Rajot, J. L., Marticorena, B., Noma Adamou, S., Pierre, C., ... & Garba, Z. (2025). Wind Erosion Dynamics Associated With Land Use on Sandy Soils Under Heavy Anthropogenic Pressure (Southwestern Niger). Land Degradation & Development. https://doi.org/10.1002/ldr.70037

Iraqi Ministry of Planning. (2024). Annual report on desertification and land degradation in Iraq. Baghdad: Government of Iraq. https://wfp.tind.io/record/130575/files/ELR%203541.pdf

Kassas, M. (1995). Desertification: A general review. Journal of Arid Environments, 30(2), 115–128. https://doi.org /10.1016/S0140-1963(05)80063-1.

Lateef, N. S., Ghani, E. T. A., Alnedawi, I. S., & Alshamary, W. F. (2024). Effects of binary irrigation and humic acid on maize yield in saline conditions. International Journal of Design & Nature and Ecodynamics, 19(5), 1725–1732. http://iieta.org/journals/ijdne

Longwell, C. R. (1949). Sedimentary facies in geologic history: Conference at meeting of the Geological Society of America held in New York, November 11, 1948 (Vol. 39). Geological Society of America. https://books.google.iq/books/about/Sedimentary_Facies_in_Geologic_History.html?id=rvGq4Ezu6fsC&redir_esc=y

Maitima, J. M., Mugatha, S. M., Reid, R. S., Gachimbi,

L. N., Majule, A., Lyaruu, H., Pomery, D., Mathai, S., & Mugisha, S. (2009). The linkages between land use change, land degradation and biodiversity across East Africa. African Journal of Environmental Science and Technology, 3(10). Website: https://www.researchgate.net/publication/228913785_The_linkages_between_land_use_change_land_degradation_and_biodiversity_across_East_Africa

Minelli, S. (2016). Land degradation neutrality target setting programme. United Nations Convention to Combat Desertification (UNCCD). Website: https://www.unccd.int/sites/default/files/2018-08/LDN%20TS%20Technical%20Guide_Draft_English.pdf

Mukhlif, H. N. (2015). Monitoring & evaluation status of land degradation in RATGA valley basin in west Iraq using RS & GIS [Master's thesis, University of Anbar].

Mussumeci, G., Mangiameli, M., Costa, R., Piccione, V., Schilirò, M., & Tomarchio, D. (2024). Remote sensing approach for monitoring of macrofactors climate, soil and vegetation (Me.DAL Us. protocol) in the desertification process in Sicily. AIP Conference Proceedings. https://doi.org/10.1063/5.0215558

Pal, S. C., Chatterjee, U., Chakrabortty, R., Roy, P., Chowdhuri, I., Saha, A., Islam, A. R. M. T., Alam, E., & Islam, M. K. (2023). Anthropogenic drivers induced desertification under changing climate: Issues, policy interventions, and the way forward. Progress in Disaster Science, 20, 100303. https://doi.org/10.1016/j.pdisas.2023.100303

Rasmussen, M. (2024). The influence of time, rock properties, and climate on mechanical weathering [Doctoral dissertation, University of North Carolina at Charlotte]. Linke: https://www.proquest.com/openview/8ad53193fbd2a435eefe7e0cfed0d864/1?pq-origsite=gscholar&cbl=18750&diss=y

Rasul, G. (2016). Managing the food, water, and energy nexus for achieving the Sustainable Development Goals in South Asia. Environmental Development, 18, 14–25. https://doi.org/10.1016/j.envdev.2015.12.001

Rasul, G. (2016). Managing the risks of climate-induced desertification in fragile environments. Environmental Development, 20, 1–10.

Reynolds James F. (2013) Desertification. In: Levin S.A. (ed.) Encyclopedia of Biodiversity, second edition, Volume 2, pp. 479-494. Waltham, MA: Academic Press.

Reynolds, J.F., Maestre, F.T., Kemp, P.R., Stafford-Smith, D.M., Lambin, E. (2007). Natural and Human Dimensions of Land Degradation in Drylands: Causes and Consequences. In: Canadell, J.G., Pataki, D.E., Pitelka, L.F. (eds) Terrestrial Ecosystems in a Changing World. Global Change — The IGBP Series. Springer, Berlin, Heidelberg. https://doi.org/10.1007/978-3-540-32730-1_20.

Safriel, U. (2009). Deserts and desertification: Challenges for sustainable development. Land Degradation & Development, 20(3), 221–239. https://doi.org/10.1002/ldr.907

Salahat, M. A., & Al-Qinna, M. I. (2015). Rainfall fluctuation for exploring desertification and climate change: New aridity classification. Jordan Journal of Earth and Environmental Sciences, 7(1), 27–35. Website: https://jjees.hu.edu.jo/files/Vol7N1/Vol7N1_HQ_P27-35.pdf

Scherr, S. J., & Yadav, I. S. (1996). Land degradation in the developing world: Implications for food, agriculture, and the environment to the year 2020. International Food Policy Research Institute. https://doi.org/10.22004/ag.econ.42280

Shahid, S. A., & Alsumaiti, T. S. (2022). Soil conservation practices and efforts made to combat desertification in the United Arab Emirates. In Global degradation of soil and water resources: Regional assessment and strategies (pp. 273–286). Springer. https://doi.org/10.1007/978-981-16-7916-2_19

Sissakian, V., Al-Ansari, N., & Knutsson, S. (2013). Sand and dust storm events in Iraq. Journal of Natural Science, 5(10), 1084–1094. https://doi.org/10.4236/ns.2013.510133

Sivakumar, M. V. (2007). Interactions between climate and desertification. Agricultural and Forest Meteorology, 142(2–4), 143–155. https://doi.org/10.1016/j.agrformet.2006.03.025

Sombroek, W., & Sene, E. H. (1993). Land degradation in arid, semi-arid and dry sub-humid areas: Rainfed and irrigated lands, rangelands and woodlands. Published by: Food and Agriculture Organization (FAO) of the United Nations, including articles, books, meeting reports, proceedings and studies published by FAO, or prepared in collaboration with FAO. Website: http://agris.fao.org/agris-search/search.do?recordID=XF9657077

Stone, R. O. (1967). A desert glossary. Earth-Science Reviews, 3, 211–268. https://doi.org/10.1016/0012-8252(67)90378-9

Thomas, D. S. (1997). Science and the desertification debate. Journal of Arid Environments, 37(4), 599–608. https://doi.org/10.1006/jare.1997.0293

Tokbergenova, A., Nyussupova, G., Arslan, M., & Kiyassova, S. K. L. (2018). Causes and impacts of land degradation and desertification: Case study from Kazakhstan. In Vegetation of Central Asia and Environs (pp. 291–302). https://doi.org/10.1007/978-3-319-99728-5_11.

UNCCD. (2024). Global Land Outlook – Regional Report: Middle East and North Africa. United Nations Convention to Combat Desertification. UNCCD. (2024). Global Land Outlook – Regional Report: Middle East and North Africa. United Nations Convention to Combat Desertification. https://www.unccd.int

Vogt, J., Safriel, U., Von Maltitz, G., Sokona, Y., Zougmore, R., Bastin, G., & Hill, J. (2011). Monitoring and assessment of land degradation and desertification: Towards new conceptual and integrated approaches. Land Degradation & Development, 22(2), 150–165. https://doi.org/10.1002/ldr.1075

Wairiu, M. (2017). Land degradation and sustainable land management practices in Pacific Island countries. Regional Environmental Change, 17, 1053–1064. https://doi.org/10.1007/s10113-016-1041-0

Wang, X., Dong, Z., Zhang, J., & Chen, G. (2002). Geomorphology of sand dunes in the Northeast Taklimakan Desert. Geomorphology, 42(3–4), 183–195. https://doi.org/10.1016/S0169-555X(01)00085-X

World Health Organization. (1992). Our planet, our health: Report of the WHO Commission on Health and Environment. WHO. https://apps.who.int/iris/handle/10665/37933

Yousef, G. S., Dibs, H., & Naje, A. S. (2025). A Review of Environmental Monitoring for Land Desertification Using Geospatial Analysis and Remote Sensing. Nature Environment & Pollution Technology, 24(2). https://doi.org/10.46488/NEPT.2025.v24i02.D1697

Zade, S., Gourkhede, P., Vaidya, P., Singh, R. S., Sinha, S., Kumar, A., & Kumar, V. (2021). Problem soils and their management practices. Publisher: Mr.Gajendra Parmar, Web Site:www.parmarpublisher.com, ISBN: 978-81-925878-3-5

JJEES

JJEES (2026) 17 (3): 338-350
ISSN 1995-6681

Jordan Journal of Earth and Environmental Sciences

Metal Oxide Nanoparticles in Diesel: Emission Impact Study

Chirag S. Trivedi[1*], Anil M. Bisen[2], Balkrishna P. Shah[3]

[1] *Research Scholar, ITM Vocational University, Vadodara - 391760, Gujarat, India*
[2] *Affiliation: Mechanical Engineering Department, ITM Vocational University, Vadodara – 391760, Gujarat, India*
[3] *Physics Department – The Mahraja Sayajirao University of Baroda, India*

Received on 16 July 2025; Accepted on 2 April 2026

Abstract

The use of metal oxide nanoparticles as diesel fuel additives has emerged as an effective strategy to enhance combustion and mitigate emissions. In this study, Cupric Oxide (CuO) and Aluminum Oxide (Al_2O_3) nanoparticles were dispersed in diesel at concentrations of 25, 50, and 75 ppm, and their effects on engine emissions were evaluated under varying load conditions. The results indicate a consistent reduction in carbon monoxide (CO) and hydrocarbon (HC) emissions, with HC levels reduced to ~7–11 ppm for Al_2O_3 blends and ~8–12 ppm for CuO blends at higher loads, compared to neat diesel. Carbon dioxide (CO_2) emissions increased by up to ~6.6%, confirming improved combustion efficiency. However, nitrogen oxides (NO_x) emissions increased significantly, reaching peak values of ~1200 ppm for nanoparticle blends, compared to ~1068 ppm for neat diesel, due to elevated in-cylinder temperatures and enhanced oxidation kinetics. Among the tested conditions, CuO at 25 ppm demonstrated the most favorable trade-off, offering reduced CO, HC, and smoke emissions with a comparatively lower increase in NO_x, whereas Al_2O_3 at 75 ppm exhibited superior combustion efficiency but the highest NO_x emissions. The study highlights the inherent trade-off between improved combustion and NO_x formation, emphasizing the need for optimized nanoparticle dosing to achieve cleaner and more efficient diesel engine operation.

Keywords: *Emission Analysis, Aluminum Oxide, Cupric Oxide, Diesel fuel, Environmental Impact*

1. Introduction

The global demand for energy is increasing rapidly due to population growth, industrialization, and urbanization, placing significant pressure on conventional fossil fuel resources and raising concerns about sustainability and environmental impact (Khalife et al., 2017; Saxena et al., 2017). Diesel engines, widely used in transportation, power generation, agriculture, and industry, play a crucial role in meeting this demand because of their high efficiency and reliability. However, their extensive use contributes significantly to environmental pollution through emissions of nitrogen oxides (NO_x), particulate matter (PM), carbon monoxide (CO), and unburned hydrocarbons (HC) (Reşitoğlu et al., 2015; Geng et al., 2017). These emissions pose serious risks to human health, including respiratory diseases, cardiovascular disorders, and premature mortality (World Health Organization, 2021; Zhang & Balasubramanian, 2015). Among these pollutants, particulate matter (PM), particularly fine and ultrafine particles, plays a critical role in atmospheric processes such as particle growth, droplet formation, and deposition, thereby significantly affecting air quality and public health.

In response to these challenges, alternative fuels, such as biodiesel, have gained considerable attention as sustainable energy sources. Biodiesel offers advantages, such as renewability, biodegradability, and reduced emissions. However, its application may lead to slight compromises in engine performance and combustion efficiency (Dewangan et al., 2020). To overcome these limitations, recent research has focused on enhancing fuel properties by incorporating metal oxide nanoparticles.

Fuel additives with at least one dimension below 100 nm are classified as nanoscale additives (Khan et al., 2019; Ağbulut & Sarıdemir, 2020). Due to their high surface area-to-volume ratio and unique catalytic properties, nanoparticles promote more complete combustion, thereby improving engine performance and reducing pollutant emissions. Metallic nanoparticles are particularly attractive for their high reactivity and energy density. Studies have shown that nanoparticle-assisted combustion can significantly enhance oxidation reactions and improve overall combustion characteristics (Bergthorson et al., 2015).

Recent investigations have demonstrated the effectiveness of various metal oxide nanoparticles as fuel additives. Özgür (2021) studied nickel iron oxide ($NiFe_2O_4$) and nickel zinc iron oxide ($Zn_{0.5}Ni_{0.5}Fe_2O_4$) nanoparticles in a turbocharged diesel engine and reported significant emission reductions at optimized concentrations. Similarly, Fayad et al. (2023) investigated titanium dioxide (TiO_2) nanoparticles blended with biodiesel in a common-rail direct-injection engine and observed reductions in NO_x emissions and particulate matter when combined with exhaust gas recirculation. Husain et al. (2020) reported that cerium-coated zinc oxide (Ce–ZnO) nanoparticles improved brake thermal efficiency and reduced CO, HC, and smoke emissions in soybean biodiesel blends. Furthermore, Mehta et al. (2014) demonstrated that the addition of metallic nanoparticles, including aluminum, iron, and boron, significantly reduced ignition delay and

* Corresponding author e-mail: ctrivedi16101997@gmail.com

enhanced combustion in diesel engines. These findings indicate that adding nanoparticles to fuel acts as a combustion catalyst, improving combustion efficiency and reducing pollutant emissions. However, despite extensive studies on various nanoparticle additives, a comparative understanding of CuO and Al_2O_3 nanoparticles at low concentrations under varying engine load conditions remains limited. In particular, the underlying mechanisms governing emission variations, especially particulate matter and NO_x trade-offs, require further investigation.

Therefore, the present study aims to investigate the effects of CuO and Al_2O_3 nanoparticles on diesel engine emission characteristics under different operating conditions. The study focuses on understanding how nanoparticle additives enhance combustion behavior and mitigate harmful emissions, with particular emphasis on particulate matter and nitrogen oxides.

2. Materials and Methods

2.1 Materials

Cupric Oxide (CuO) and Aluminum Oxide (Al_2O_3) nanoparticles (with a specific surface area of approximately 30-50 m^2/g and an average particle size of 20-30 nm) were selected as fuel additives for their distinct physicochemical properties and their ability to enhance combustion through multiple catalytic and thermal mechanisms.

1. Lattice Oxygen Donation → Catalytic Oxidation (Bitire et al., 2022)

   CuO has a non-stoichiometric crystal structure that can release bound oxygen ions from its lattice into the combustion zone. This additional oxygen oxidizes CO → CO_2 and unburned HC → H_2O + CO_2, even in fuel-rich zones where free oxygen is locally scarce. Furthermore, CuO reduces particulate matter (PM) formation through a dual pathway: (i) lattice oxygen oxidizes soot precursors, such as acetylene (C_2H_2) and polycyclic aromatic hydrocarbons (PAHs) before they nucleate into primary soot particles, and (ii) a catalytic Cu^{2+}/Cu^{+} redox cycle continuously oxidizes deposited soot via $C + 2CuO \rightarrow CO_2 + Cu_2O$, followed by regeneration: $Cu_2O + ½O_2 \rightarrow 2CuO$. This cyclic oxidation mechanism enhances in-situ soot burnout and reduces overall smoke emissions.

2. High Thermal Conductivity → Heat Transfer Boost (Zhu et al., 2018)

   CuO has one of the highest thermal conductivities among metal oxides (~76 W/m·K for bulk Cu-based materials). When suspended in fuel, it improves heat distribution within the cylinder, ensuring the entire fuel charge heats uniformly and ignites more completely.

3. Higher Calorific Value → Lower Activation Energy (Ramachandran et al., 2023)

   CuO nanoparticles have intrinsic stored chemical energy that contributes to the overall heat release of the blended fuel. They also lower the activation energy barrier for combustion reactions, meaning fuel molecules ignite faster and at lower temperatures. Smoke and PM reductions of approximately 17–21% have been reported at a dosage of 50–75 ppm.

4. Secondary Atomization → Finer Fuel Spray (Li et al., 2024)

   Al_2O_3 nanoparticles adsorb onto fuel droplet surfaces and create surface tension instabilities, causing large droplets to break into much finer ones. This in turn eliminates fuel-rich droplet cores, which are primary sites for soot nucleation. The resulting finer droplets evaporate rapidly and mix more uniformly with air, significantly reducing PM formation.

5. Active Surface Sites → Catalytic Oxidation (Gad et al., 2021)

   The high surface area of Al_2O_3 nanoparticles provides abundant reactive adsorption sites for CO and HC molecules. These molecules are adsorbed and oxidized on the nanoparticle surface, functioning as distributed micro-catalysts within the combustion chamber.

6. Micro Heat Sink → Thermal Redistribution (Chohan et al., 2026)

   Al_2O_3 absorbs localized thermal spikes in the combustion chamber and re-radiates heat more uniformly. This eliminates dangerous "hot spots" —high-temperature zones (>1800 K) where the Zeldovich mechanism drives thermal NO_x formation

2.2 Preparation of Fuel Blends

The fuel blends were formulated by dispersing the nanoparticles in commercially available diesel fuel using a magnetic stirrer. The nanoparticle concentration used was 25, 50, and 75 ppm (parts per million) by weight in the diesel fuel.

From here on, the fuel blends will be denoted as follows:

Neat Diesel	Run 0
Diesel + 25 ppm CuO	Run 1
Diesel + 50 ppm CuO	Run 2
Diesel + 75 ppm CuO	Run 3
Diesel + 25 ppm Al_2O_3	Run 4
Diesel + 50 ppm Al_2O_3	Run 5
Diesel + 75 ppm Al_2O_3	Run 6

Engine Setup and Testing:

A single-cylinder, four-stroke, direct-injection diesel engine was used for the emission tests. The engine was coupled to a dynamometer to control load and speed. Engine operating conditions were carefully controlled. The engine was run at various load levels (0 %, 25%, 50%, 75%, and 100% of rated load) at a constant speed of 1500 rpm.

It should be noted that the present experimental study was conducted under steady-state operating conditions and did not consider cold-start behavior. Cold-start conditions are known to significantly influence emission characteristics due to lower combustion temperatures and incomplete fuel oxidation, particularly affecting particulate matter (PM) and hydrocarbon (HC) emissions.

Exhaust Emission Measurement:

Carbon dioxide (CO2), carbon monoxide (CO), nitrous oxide (NOx), sulfuric compounds, particulate matter (PM), and unburned hydrocarbons (UHCs) are the most prevalent emissions from fossil fuels (Reşitoğlu et al., 2015) ((Geng et al., 2017)

The high temperature in the combustion chamber and the surplus availability of oxygen are the causes of the formation of NOx emissions (Sudalaimuthu et al., 2018).

CO2 is formed during the complete combustion of fuel when oxygen is adequate, whereas CO emissions result from incomplete combustion or a deficiency of oxygen (Dey and Dhal, 2019; Bradley et al., 1999).

Due to environmental concerns, PM emissions are a major concern. PM is usually a complex mixture of sulfur compounds, various HCs, elemental carbon, and other species (Wang et al., 2016; Wei and Geng, 2016). UHCs, considered a main pollutant that significantly affects the environment, result from incomplete combustion (Reşitoğlu et al., 2015).

In the present study, an Exhaust Gas Analyzer(AVL444N) was used to measure the concentrations of gaseous pollutants, including CO, HC, CO_2, O_2, and NOx; a smoke meter (AVL437) was used to measure the smoke emission.

Figure 1. Smoke meter (AVL437) & Exhaust gas analyzer (AVL444N)

3. Results & Discussion

The detailed interpretation of the individual runs along with their experimental data (represented graphically) is as follows:

1- Run 0 (Neat Diesel)

Carbon monoxide (CO) levels initially drop from 0.08% at no load to 0.03% at 9 kg, suggesting improved combustion efficiency. However, at 12 kg, CO slightly increases to 0.04%, indicating incomplete combustion under peak-load conditions. Hydrocarbon (HC) emissions show a steady rise, increasing from 1 ppm at no load to 9 ppm at 12 kg, indicating higher levels of unburned fuel residues with increasing load. Carbon dioxide (CO_2) levels increase from 1.3% at no load to 6.1% at 12 kg, indicating more complete combustion. Simultaneously, oxygen (O_2) levels decline from 18.93% to 12.18%, demonstrating greater oxygen consumption with higher loads. Nitric oxide (NO) emissions surge significantly, from 80 ppm to 1068 ppm, likely due to elevated combustion temperatures at increased loads. Smoke emissions, which remain low at lower loads, rise sharply from 0.2 at no load to 33.2 at 12 kg, suggesting increased particulate formation and incomplete combustion at higher loads. These trends indicate that while higher loads enhance combustion efficiency, they also lead to substantial increases in NO and smoke emissions, which can adversely affect both environmental quality and engine performance.

2- Run 1 (Diesel + 25 ppm CuO)

Carbon monoxide (CO) content decreases from 0.12% at no load to 0.04% at 9 kg, reflecting improved combustion efficiency. At 12 kg, CO increases marginally to 0.05%, which may result from incomplete combustion at maximum load. Hydrocarbon (HC) emissions gradually increase from 6 ppm at no load to 15 ppm at 12 kg, reflecting increased unburned fuel content with rising load. Carbon dioxide (CO_2) content increases steadily from 1.4% at no load to 6.6% at 12 kg, indicating better combustion. Oxygen (O_2) content decreases from 18.9% to 11.62%, showing greater oxygen consumption. Nitric oxide (NO) emissions rise sharply from 38 ppm at no load to 1244 ppm at 12 kg, probably due to increased combustion temperatures. Smoke emissions also trend similarly, increasing from 0.9 to 22.9, reflecting greater particulate formation at higher loads.

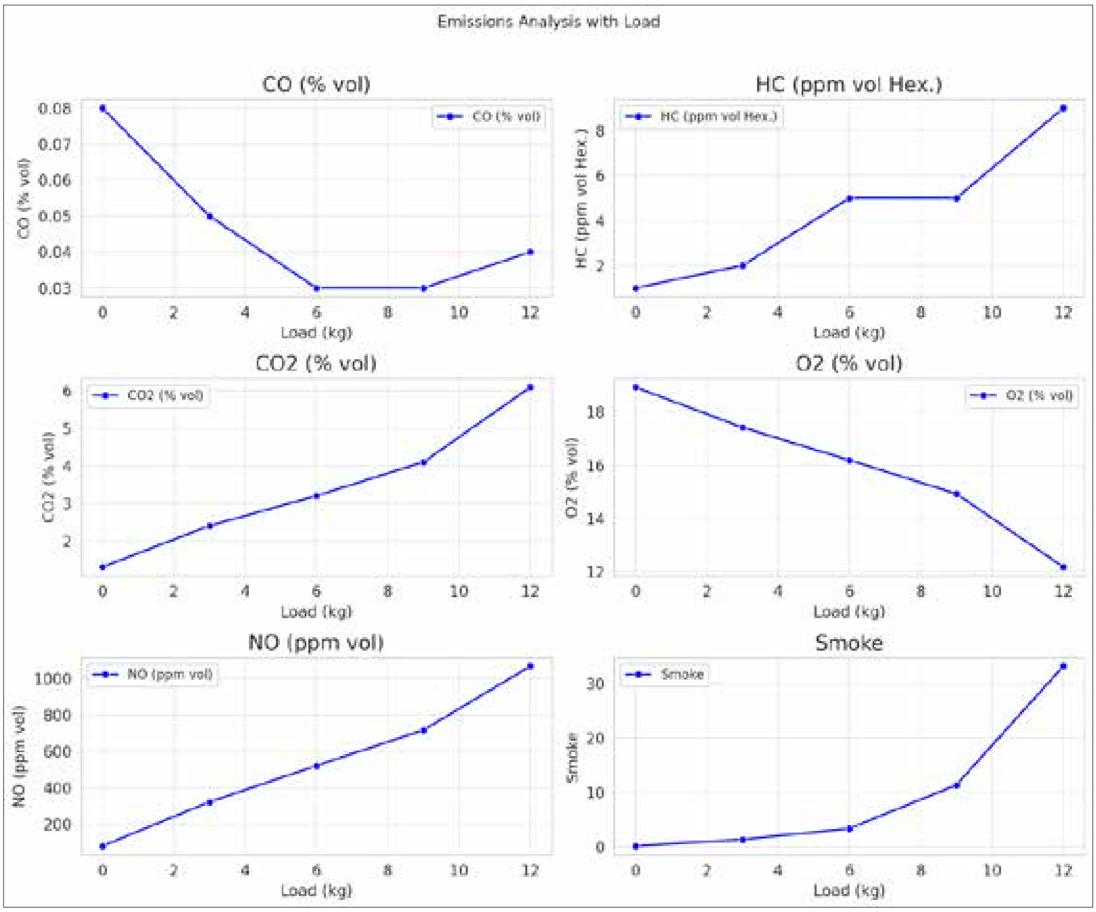

Figure 2. Variation of exhaust emission parameters with engine load for neat diesel fuel (Run 0)

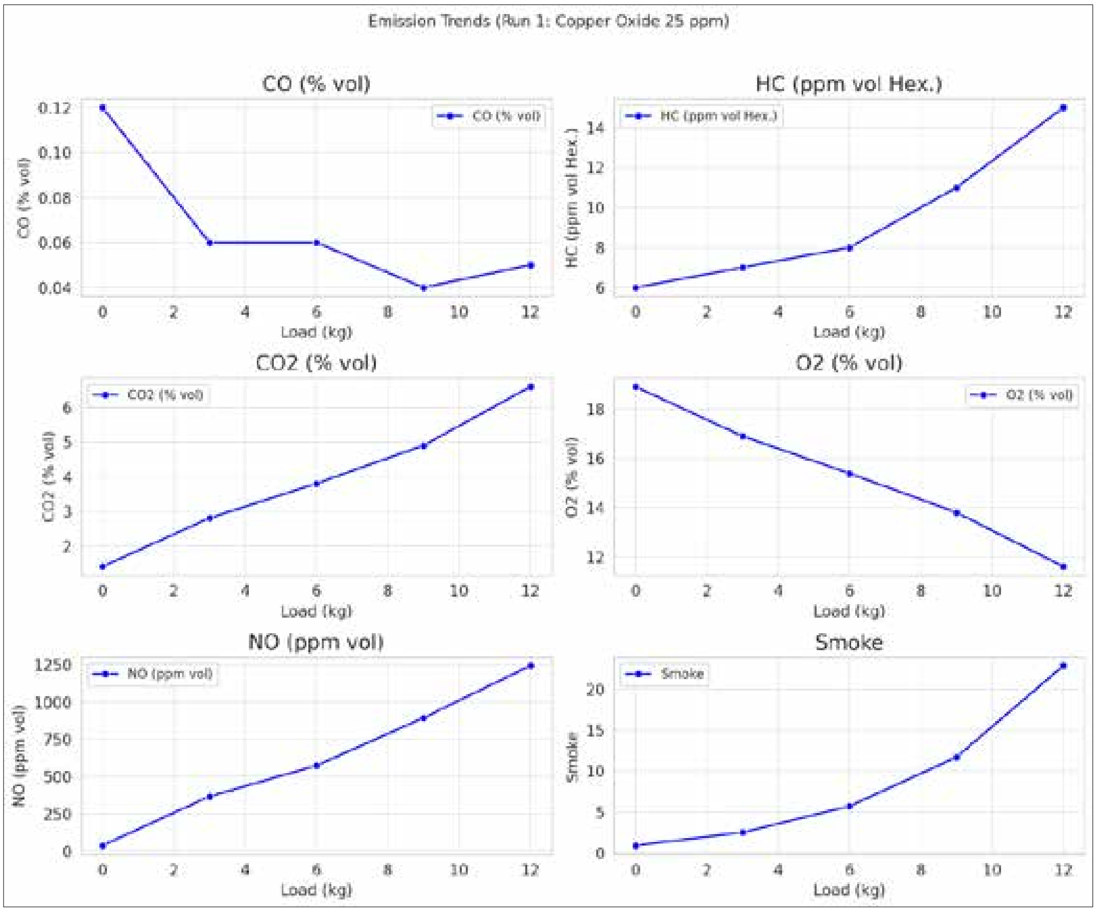

Figure 3. Emission characteristics of diesel blended with 25 ppm CuO nanoparticles (Run 1)

3- Run 2 (Diesel + 50 ppm CuO)

CO emissions decrease with load, from 0.13% at no load to 0.06% at 12 kg, indicating better combustion efficiency. HC emissions are fairly constant but rise slightly with increasing load, reaching 12 ppm vol Hex. at 12 kg, likely due to incomplete combustion at extreme loads. CO2 emissions increase from 1.4% at no load to 6.5% at 12 kg, confirming greater fuel oxidation and improved combustion. O2 decreases with load, from 18.73% to 11.68%, indicating more oxygen is consumed during combustion. NO emissions increase substantially with load, from 39 ppm at no load to 1207 ppm at 12 kg, as expected with higher combustion temperatures with CuO. Smoke emissions also increase steeply from 0.5 to 26.2, reflecting elevated particulate matter generation at high loads.

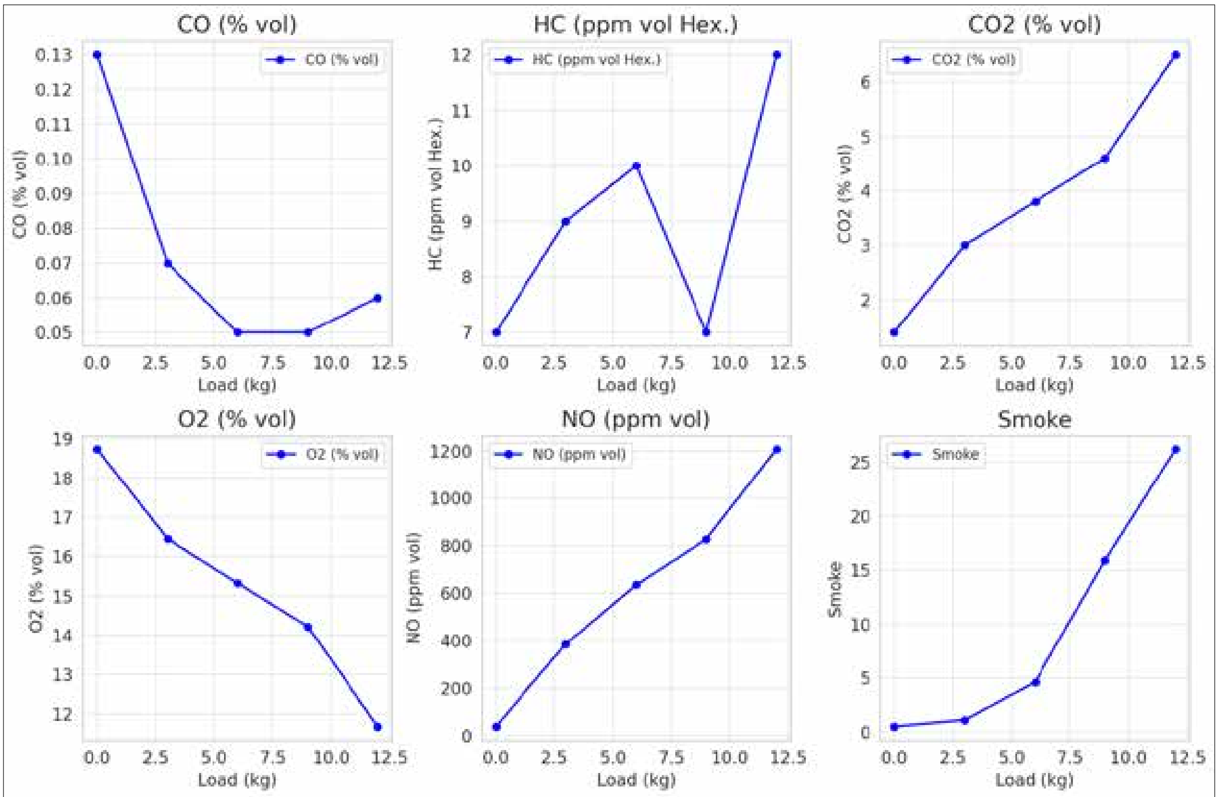

Figure 4. Emission characteristics of diesel blended with 50 ppm CuO nanoparticles (Run 2)

4- Run 3 (Diesel + 75 ppm CuO)

CO emissions initially rise to 0.17% at zero load but decrease significantly as load increases, stabilizing at 0.05%–0.06% beyond 6 kg. This indicates better oxidation of CO at higher loads. HC emissions remain relatively stable at lower loads (7–9 ppm) but rise slightly to 11 ppm at 12 kg, suggesting some incomplete combustion at higher loads. CO2 levels increase steadily from 1.6% at 0 kg to 6% at 12 kg, reflecting improved combustion efficiency as load increases. O2 levels show a consistent decline from 18.35% to 12.32%, indicating increased oxygen consumption during combustion. NO emissions rise significantly from 34 ppm to 1117 ppm as load increases, due to the higher combustion temperature. Lastly, smoke emissions rise from 0.6 at no load to 28.3 at full load, suggesting increased soot formation with increased load due to a richer fuel-air mixture.

Comparative Analysis of Emission Trends: Run 0 vs. Run 1 (CuO 25 ppm) vs. Run 2 (CuO 50 ppm) vs. Run 3 (CuO 75 ppm)

CO Emissions: Run 3 (CuO 75 ppm) shows slightly higher CO emissions at low loads compared to the other runs, especially at 0 kg load (0.17% vol). However, at higher loads, CO levels remain similar to those in Runs 1 and 2, suggesting that CuO improves oxidation at higher temperatures.

HC Emissions: Hydrocarbon (HC) emissions remain relatively stable across all CuO-doped runs, with Run 3 showing an average of 8.8 ppm. This is slightly lower than Run 1 (9.4 ppm) and Run 2 (9 ppm), suggesting moderate effectiveness in reducing unburned hydrocarbons.

CO_2 Emissions: CO_2 emissions increase with load in all runs, indicating better combustion efficiency with CuO addition. Run 3 shows slightly lower CO_2 levels than Run 2 but still higher than Run 0, suggesting that the combustion-efficiency gain starts to saturate at higher CuO concentrations.

O_2 Levels: Oxygen levels decrease with increasing load, as expected. Run 3 maintains an average O_2 of 15.516%, slightly higher than Run 2 but lower than Run 0, indicating that more oxygen is being utilized in combustion, albeit at a diminishing rate beyond 50 ppm CuO.

NO Emissions: NO levels rise significantly as CuO concentration increases. Run 3 averages 573.4 ppm, slightly lower than Run 2 (619 ppm) but still much higher than Run 0. This suggests that excessive CuO concentrations may reach a threshold beyond which additional oxidation no longer increases NO formation.

Smoke Emissions: Smoke emissions continue to increase at higher loads, with Run 3 averaging 10.44, higher than Runs 1 and 2. The high smoke levels at full load (28.3) suggest that 75 ppm CuO may cause incomplete combustion due to excessive nanoparticle agglomeration.

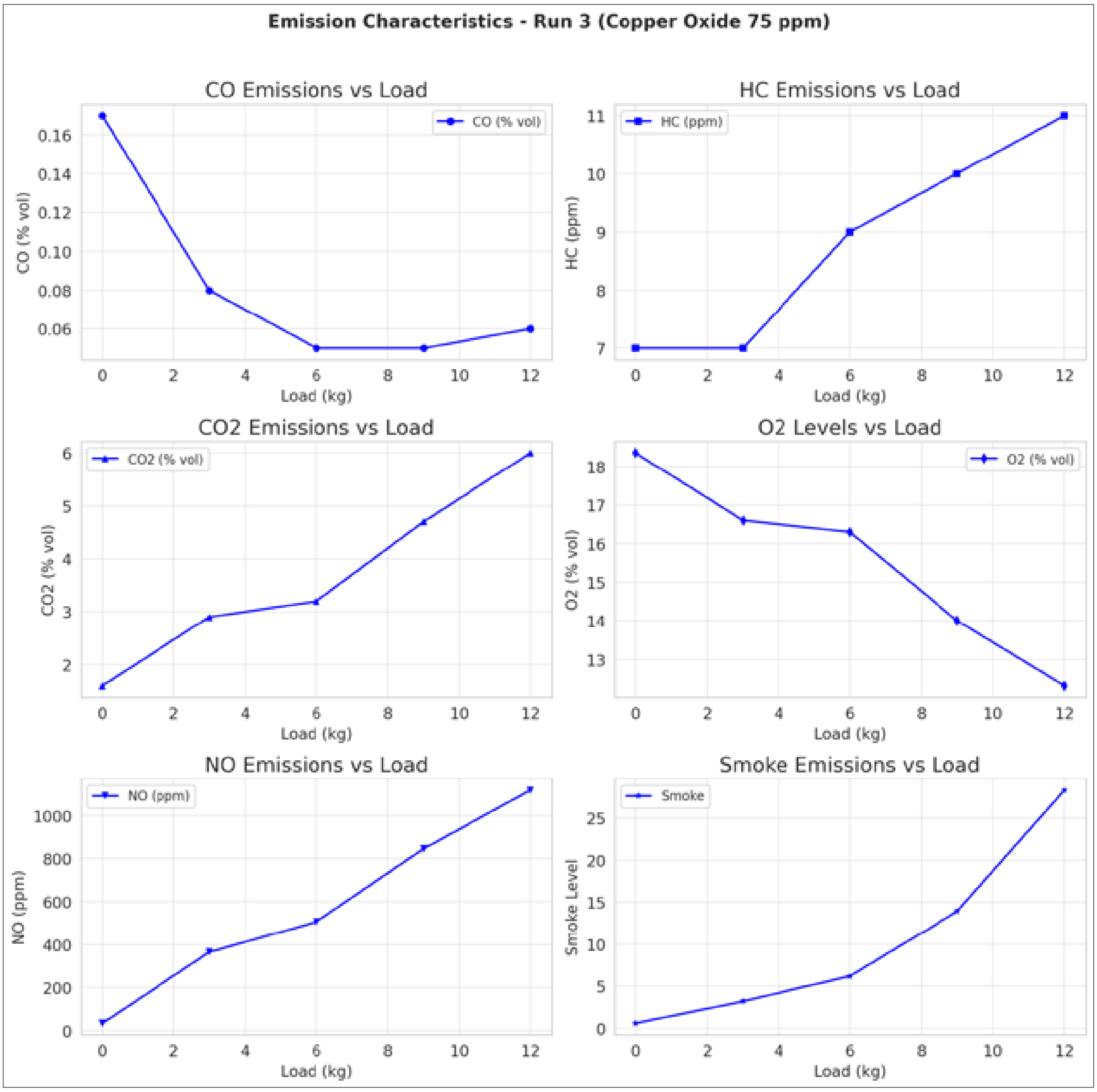

Figure 5. Emission characteristics of diesel blended with 75 ppm CuO nanoparticles (Run 3)

Concluding Remark:

While CuO additives improve combustion efficiency by increasing CO_2 production and reducing unburned HC and O_2 levels, diminishing returns beyond 50 ppm indicate that excessive CuO does not further enhance performance. Instead, it increases NO emissions and smoke levels at higher loads. Run 1 (CuO 25 ppm) remains the most balanced option, offering a good trade-off between efficiency and emissions control.

5- Run 4 (Diesel + 25 ppm Al_2O_3)

CO emissions decrease from 0.12% at 0 kg load to 0.04% at 12 kg, showing improved combustion efficiency at higher loads. The HC emissions start at 3 ppm at a 0 kg load and rise to 7 ppm at a 12 kg load, indicating increased unburned hydrocarbons at higher loads. The CO_2 levels increase with load, peaking at 6.4% at 12 kg, suggesting more complete combustion. The O_2 concentration decreases from 18.48% at 0 kg to 11.58% at 12 kg, consistent with fuel consumption. The NO emissions increase significantly with load, from 59 ppm at 0 kg to 1176 ppm at 12 kg, due to higher combustion temperatures. Smoke emissions also increase from 0 at no load to 22.8 at full load, indicating increased particulate matter formation.

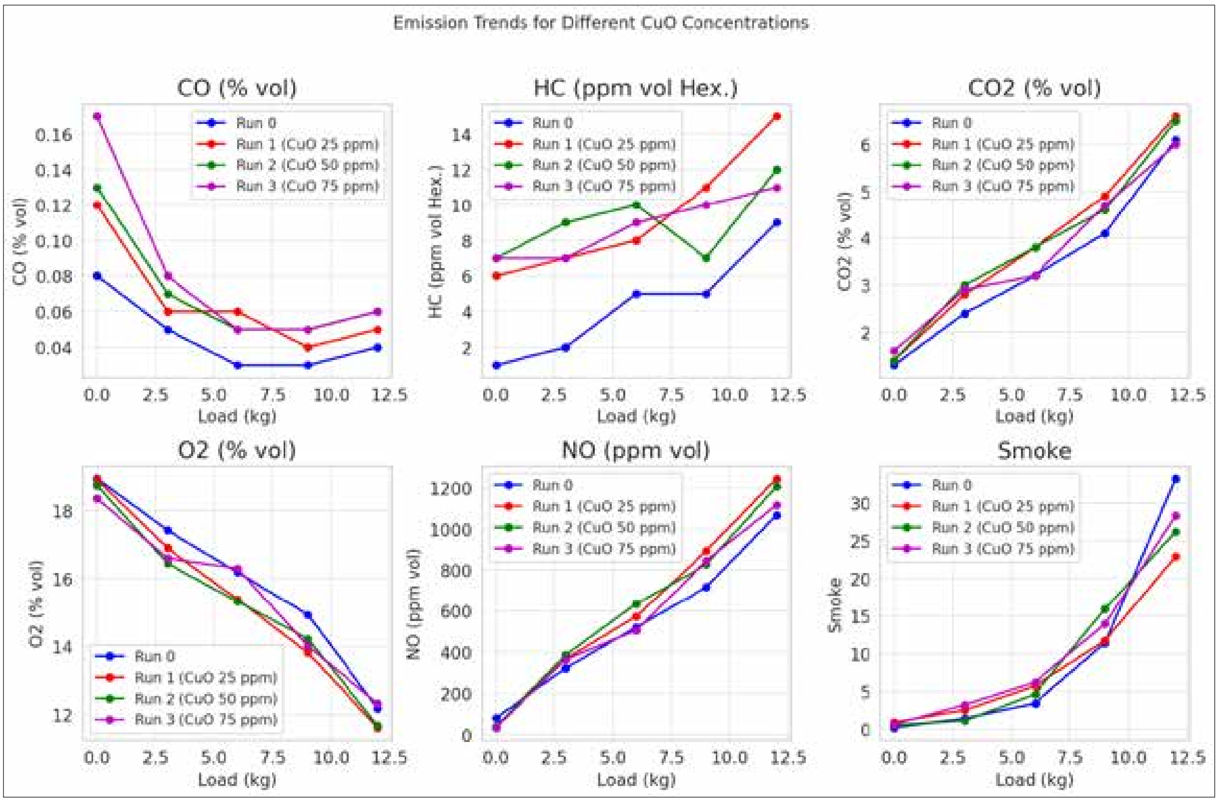

Figure 6. Comparative analysis of emission parameters for neat diesel (Run 0) and CuO nanoparticle blends (25, 50, and 75 ppm)

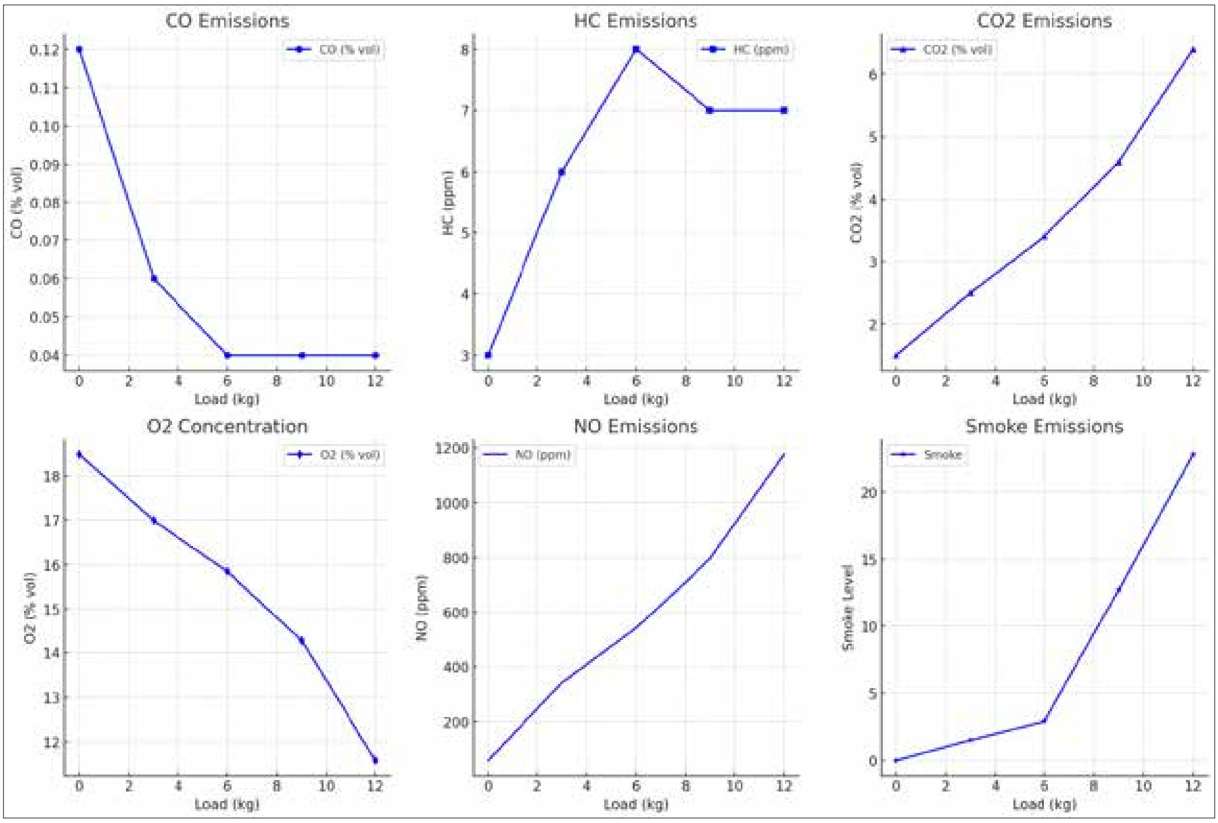

Figure 7. Emission characteristics of diesel blended with 25 ppm Al_2O_3 nanoparticles (Run 4)

6- Run 5 (Diesel + 50 ppm Al_2O_3)

Carbon Monoxide (CO) emissions decreased from 0.11% vol at 0 kg load to 0.04 - 0.05% vol at higher loads, indicating improved combustion efficiency at elevated loads. Hydrocarbon (HC) emissions increased with load, rising from 7 ppm at 0 kg to 13 ppm at 12 kg, suggesting increased fuel decomposition at higher engine loads. Carbon Dioxide (CO_2) emissions increased, peaking at 6.6% vol at a 12 kg load, indicating enhanced combustion efficiency. Conversely, Oxygen (O_2) levels decreased from 18.61% vol at no load to 11.43% vol at full load, further confirming better fuel utilization. Nitric Oxide (NO) emissions increased significantly from 54 ppm at 0 kg to 1213 ppm at 12 kg, which is a result of higher combustion temperatures at higher loads. Lastly, smoke emissions rose sharply from 0.5 at no load to 39.9 at full load, indicating incomplete combustion and increased soot formation under heavy-load conditions.

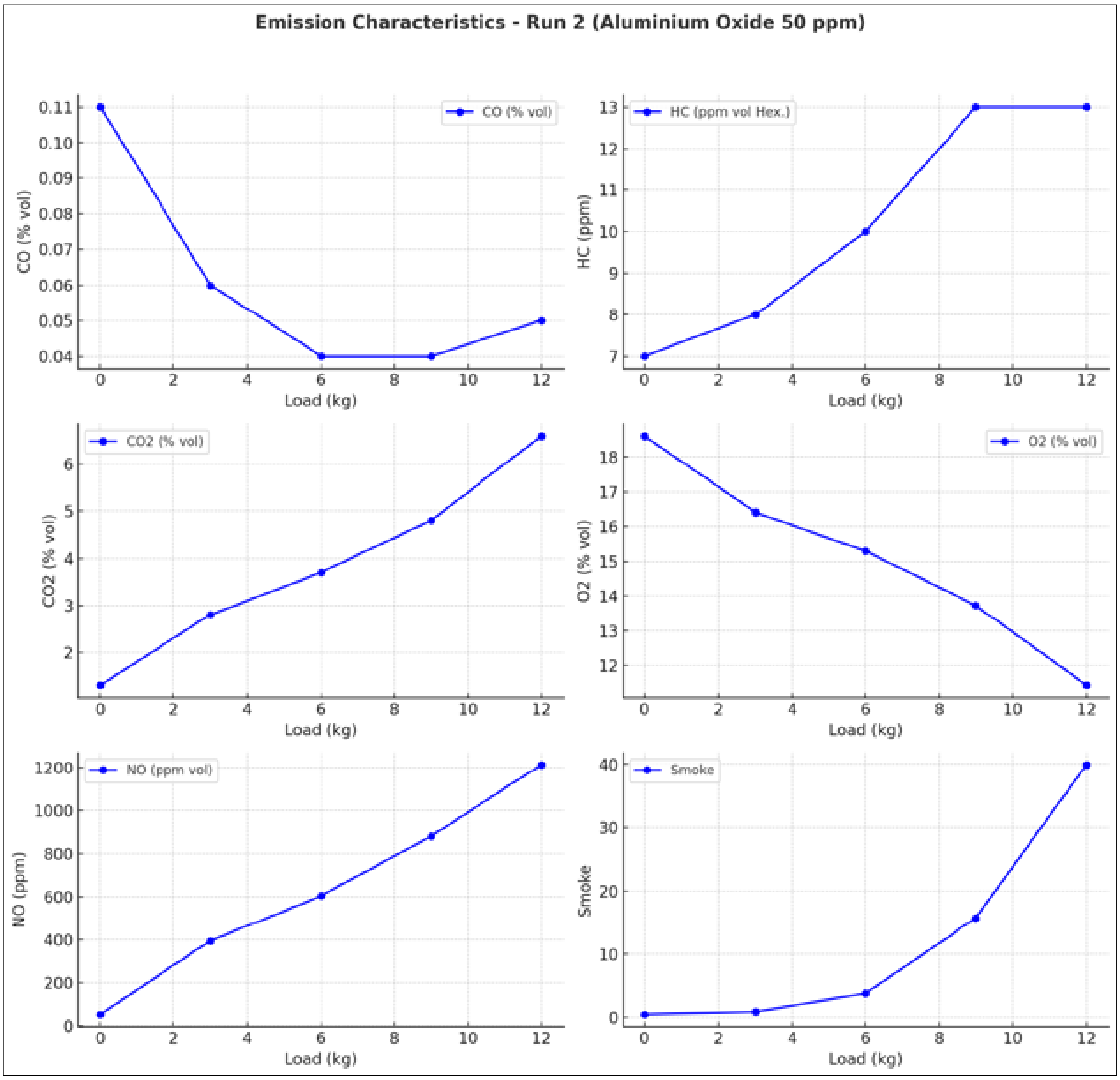

Figure 8. Emission characteristics of diesel blended with 50 ppm Al_2O_3 nanoparticles (Run 5)

7- Run 6 (Diesel + 75 ppm Al_2O_3)

Carbon Monoxide (CO) emissions gradually decrease from 0.09% at 0 kg to 0.05% at 9 kg, indicating better combustion efficiency at moderate loads, but a slight rise to 0.06% at 12 kg suggests incomplete combustion at higher fuel injection rates. Hydrocarbon (HC) emissions remain relatively low, ranging from 0 to 11 ppm, with slight increase at 12 kg, possibly due to incomplete oxidation. Carbon Dioxide (CO_2) levels increase from 0.9% at 0 kg to 6.4% at 12 kg, confirming improved fuel combustion at higher loads. Oxygen (O_2) concentration decreases as load increases, showing higher oxygen consumption due to more complete combustion. Nitric Oxide (NO) emissions rise significantly from 25 ppm at 0 kg to 1192 ppm at 12 kg, indicating higher combustion temperatures at greater loads. Smoke levels increase from 0.1 at no load to 28.2 at full load, which may be attributed to incomplete combustion and increased particulate matter formation at higher loads.

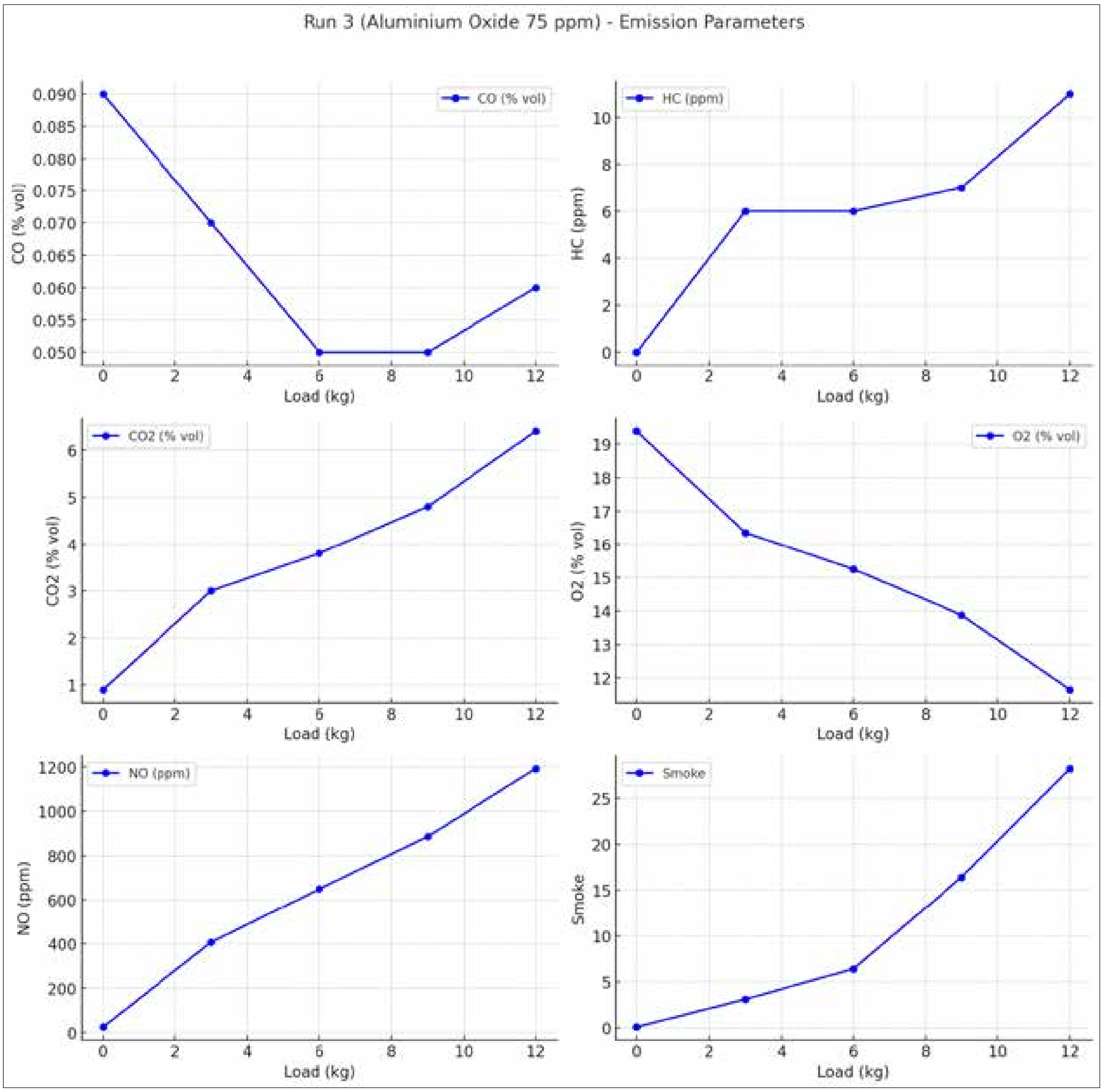

Figure 9. Emission characteristics of diesel blended with 75 ppm Al_2O_3 nanoparticles (Run 6)

Comparative Analysis of Emission Trends: Run 0 vs. Run 1 (Al_2O_3 25 ppm) vs. Run 2 (Al_2O_3 50 ppm) vs. Run 3 (Al_2O_3 75 ppm)

1. CO Emission: The emission trends of Carbon Monoxide (CO) indicate that Run 0 (Baseline) had the highest CO emissions. With the introduction of Al_2O_3 at 25 ppm (Run 4), a noticeable reduction in CO levels was observed, highlighting its catalytic effect. A further decrease in CO emissions was observed in Run 5 (Al_2O_3 50 ppm), with the average emission level stabilizing at 0.06% vol. In Run 6 (Al_2O_3 75 ppm), a slightly lower CO emission trend was observed compared to Run 5, suggesting a diminishing effect with increasing dosage.

2. HC Emission: The HC levels exhibited a decreasing trend with increasing Al_2O_3 concentration. Run 4 showed a moderate reduction in HC emissions, while Runs 5 and 6 showed a significant decline. Among them, Run 6 (Al_2O_3 75 ppm) recorded the lowest HC emissions, indicating enhanced combustion efficiency.

3. CO_2 Emissions: A progressive increase in CO_2 emissions was observed, indicating improved combustion efficiency. Run 6 recorded the highest CO_2 emission levels, confirming enhanced oxidation of CO and HC into CO_2.

4. O_2 Concentration: As the load increased, O_2 levels decreased across all runs, indicating improved fuel utilization. Run 6 recorded the lowest O_2 levels, signifying the highest combustion efficiency among all runs.

5. NO Emission: NO emissions exhibited an increasing trend with rising Al_2O_3 concentration. Run 6 recorded the highest NO emissions (1192 ppm at 12 kg load), attributed to higher combustion temperatures. This highlights a trade-off: Al_2O_3 enhances combustion efficiency but also increases NO formation.

6. Smoke Opacity Trends:

A significant reduction in smoke was observed as the Al2O3 concentration increased.

Run 6 had the lowest smoke emissions, confirming better fuel combustion and reduced soot formation.

Concluding Remark:

The comparative analysis shows that Al_2O_3, as a fuel additive, significantly improves combustion efficiency by reducing CO, HC, and smoke emissions, while increasing CO_2 and NO emissions. Run 6 (Al_2O_3 75 ppm) showed the best results in terms of reduced CO, HC, and smoke but had the highest NO emissions. Future optimizations can focus on balancing combustion efficiency with NO emission control.

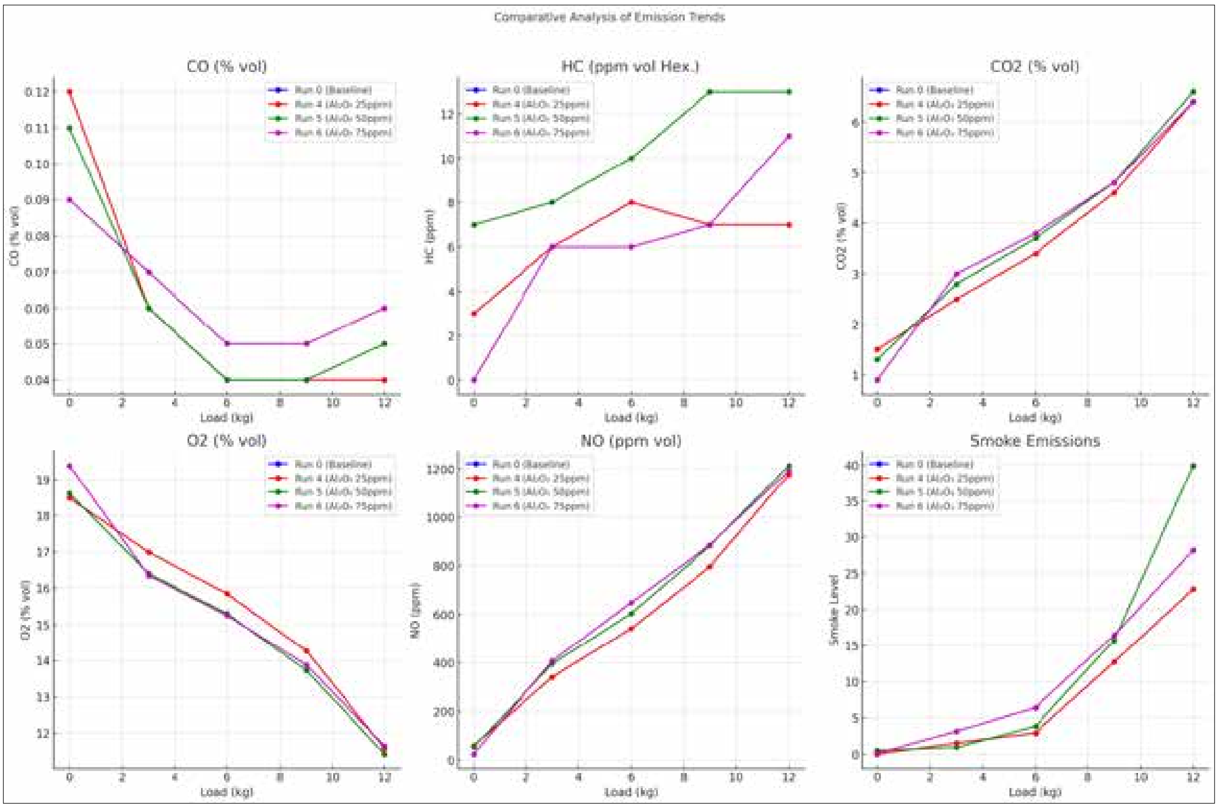

Figure 10. Comparative analysis of emission parameters for neat diesel (Run 0) and Al_2O_3 nanoparticle blends (25, 50, and 75 ppm)

Comparative Analysis: Run 1 (CuO 25 ppm) vs. Run 6 (Al_2O_3 75 ppm)

Carbon Monoxide (CO) Emissions : Run 1 has slightly higher CO emissions at lower loads compared to Run 6.

Both runs show a decreasing trend in CO emissions as the load increases, stabilizing at around 0.05-0.06% vol.

Hydrocarbon (HC) Emissions: Run 6 shows consistently lower HC levels than Run 1, except at 12 kg load, where both converge.

This indicates that Al_2O_3 (75 ppm) may improve combustion compared to CuO (25 ppm).

Carbon Dioxide (CO_2) Emissions: CO_2 increases with load in both runs.

Run 6 has slightly higher CO_2 emissions, which indicates better combustion efficiency.

Oxygen (O_2) Levels : O_2 levels decrease with increasing load, as expected.

Run 6 shows a faster decline in O_2 levels, which aligns with its higher CO_2 emissions and reinforces the idea of improved combustion efficiency.

Nitric Oxide (NO) Emissions: NO emissions increase significantly with load in both runs.

Run 6 has higher NO levels, suggesting a higher combustion temperature compared to Run 1.

Smoke Opacity: Run 6 shows higher smoke emissions at higher loads than Run 1, possibly due to incomplete combustion at peak loads.

This suggests a need to optimize the fuel-air ratio for Al_2O_3 (75 ppm) at higher loads.

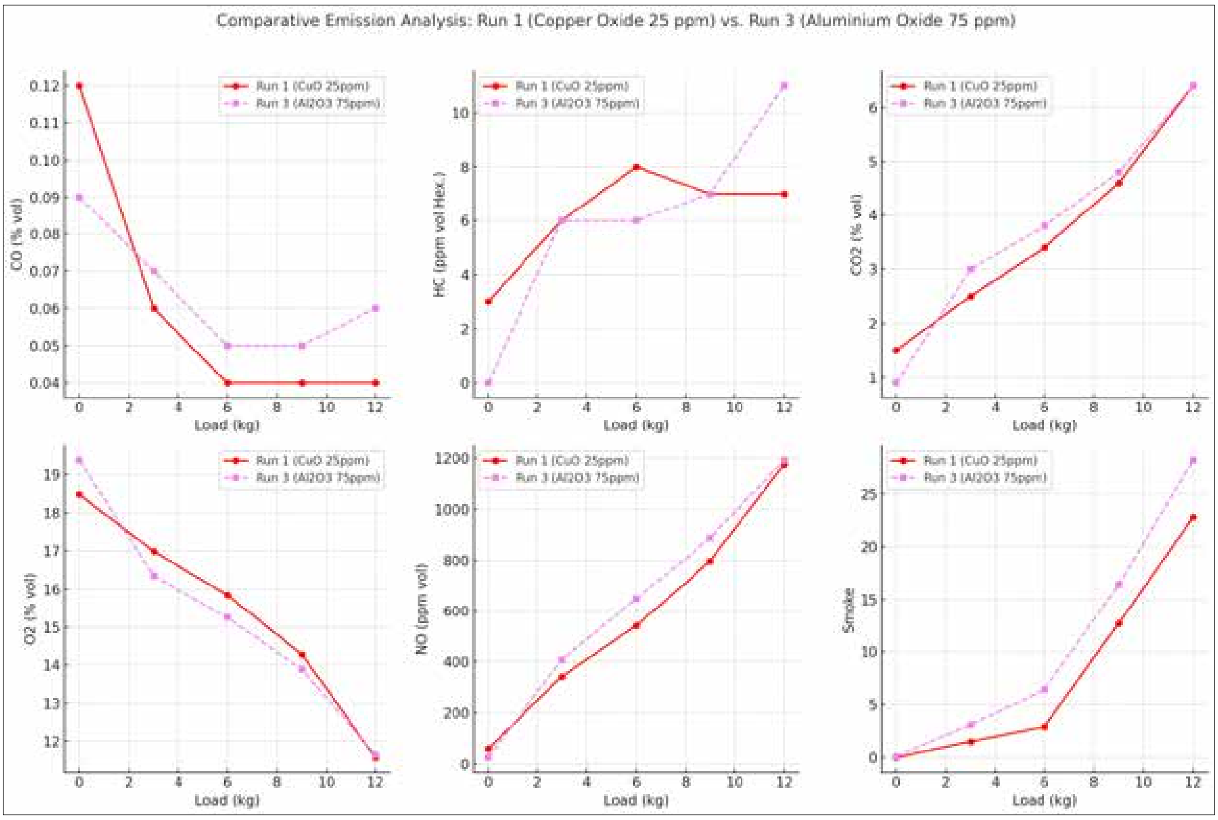

Figure 11. Comparative analysis of emission parameters for diesel blended with 25 ppm CuO nanoparticles (Run 1) and diesel blended with 75 ppm Al_2O_3 nanoparticles (Run 6)

Best Run: Run 1 (CuO 25 ppm) vs. Run 6 (Al2O3 75 ppm)

To determine the best run, we have evaluated the key emission parameters as follows:

1. Carbon Monoxide (CO): Lower CO is better (indicating better combustion)

Run 6 (Al_2O_3 75 ppm) has slightly lower CO emissions than Run 1 (CuO 25 ppm) at lower loads, indicating better oxidation of CO.

2. Hydrocarbons (HC) : Lower HC is better (indicating better fuel combustion).

Run 1 (CuO 25 ppm) has lower overall HC levels, indicating it burns fuel more completely than Run 6.

3. Carbon Dioxide (CO_2) : Higher CO_2 indicates better combustion but also more greenhouse gas emissions.

Run 6 (Al_2O_3 75 ppm) has slightly higher CO_2 levels, meaning better combustion efficiency but at the cost of more emissions.

4. Oxygen (O_2) Levels: Lower O_2 in exhaust suggests better combustion efficiency.

Run 6 has lower O_2 levels, indicating that it utilizes more oxygen for combustion than Run 1.

5. Nitric Oxide (NO) Emissions: Lower NO is better (since high NO emissions contribute to air pollution).

Run 6 (Al_2O_3 75 ppm) has higher NO emissions, which suggests a higher combustion temperature. Run 1 is better in this aspect.

6. Smoke Emissions: Lower smoke levels are preferred (indicating complete combustion).

Run 1 has lower smoke emissions at high loads, making it a cleaner option.

To summarize, if the goal is better combustion efficiency, Run 6 (Al_2O_3 75 ppm) is superior because it has lower CO, higher CO_2, and better oxygen utilization.

If the goal is lower emissions and environmental impact, Run 1 (CuO 25 ppm) is better due to lower NO and smoke emissions.

According to us, the Best Overall Choice is Run 1 (CuO 25 ppm), which maintains a better balance between efficiency and emissions. However, if maximizing combustion efficiency is the priority, Run 6 would be the preferred choice.

4. Challenges & Future Scope

Undoubtedly, the nanoparticle additives in diesel fuel reduce the engine emissions significantly. Further experimental efforts are needed to fill the knowledge gap about the type of nanoparticle used and its optimum dosage in fuel so that it serves the purpose of Complete Combustion as well as Lower Emissions and Environmental Impact. In addition, the stability characteristics of nanofluid fuels under various operating conditions should be addressed from a technical standpoint.

It is worth noting that, beyond engine emissions, performance, and combustion characteristics, most existing reviews have focused primarily on dispersion stability, wear and friction loss, corrosion, and cost-related issues with nanoparticles, with limited discussion of a very important aspect of these nano-additives, namely their toxicity and health impacts when they come into contact with humans and animals over a period of exposure. There is substantial evidence supporting the toxicity of these nanoparticles and the potential harm they could pose to an individual's health (Doshi et al., 2008; Karlsson et al.; Lin and Xing, 2007; Long, 2006a, 2006b; AZoNano). The harmful effects of exhaust emissions become more concerning when nanosize fuel additives are used (Zhang and Balasubramanian, 2015). The most probable entry sites for nanoparticles are the skin, gastrointestinal system, and lungs (Buzea et al., 2007). Nanoparticles, whether released or naturally occurring, can infiltrate and move within living organisms. Their minuscule size allows them to penetrate physiological barriers and enter the body (Kabir et al., 2018). According to reports, nanoparticles interact with several bodily systems, including the skin, brain, lungs, liver, kidneys, and blood, and may disrupt their normal functions (Schrand et al., 2010). Mauro et al. [31] demonstrated in a study that the skin is a negligible route for nanoparticle penetration and permeation. However, they found that Al2O3 nanoparticles can slightly permeate the skin (Mauro et al., 2019).

The present study does not account for cold-start conditions, which are critical in determining real-world emission performance. Future work should include transient and cold-start analysis to evaluate the effectiveness of nanoparticle additives under practical operating scenarios.

5. Conclusion

The concept of blending Aluminum Oxide and Copper Oxide Nanoparticles into neat diesel on the emission patterns was investigated in this study, and the results obtained during the trials are summarized.

1. A significant reduction in all emissions was observed by doping additives to diesel since metal oxide nanoparticles provide extra oxygen during combustion, and hence complete combustion was achieved.

2. It was observed that the NOx emissions were increased with the usage of metal oxide nanoparticles due to the liberation of extra oxygen.

3. As far as the experimental results are concerned, Run 6 (Al_2O_3 75 ppm) demonstrates higher combustion efficiency with better CO, CO_2, and O_2 emissions but at the expense of higher NO and smoke emissions, especially at higher loads. This run turned out to be more efficient in terms of fuel consumption, but it contributes to higher pollution levels. Run 1 (CuO 25 ppm), on the other hand, is cleaner overall, with lower HC, NO, and smoke emissions, making it a better option for minimizing pollution, especially at higher loads. While its CO and CO_2 emissions are slightly higher, it represents a more environmentally friendly choice.

4. Ultimately, Run 1 (CuO 25 ppm) appears to be the better option for cleaner combustion, particularly in reducing NO emissions and smoke opacity, while Run 6 (Al_2O_3 75 ppm) excels in combustion efficiency but requires optimization to reduce pollution at higher loads.

References

Ağbulut, Ü., & Sarıdemir, S. (2020). International Journal of Ambient Energy, 1. https://doi.org/10.1080/01430750.2018.1563822

Bergthorson, J. M., Goroshin, S., Soo, M. J., Julien, P., Palecka, J., Frost, D. L., & Jarvis, D. J. (2015). Applied Energy, 160, 368. https://doi.org/10.1016/j.apenergy.2015.09.037

Bitire, S. O., Nwanna, E. C., & Jen, T. (2022). The impact of CuO nanoparticles as fuel additives in biodiesel-blend fuelled diesel engine: A review. Energy & Environment, 34(7), 2259–2289. https://doi.org/10.1177/0958305x221089217

Bradley, K. S., Stedman, D. H., & Bishop, G. A. (1999). Chemosphere – Global Change Science, 1, 65. https://doi.org/10.1016/S1465-9972(99)00017-3

Buzea, C., Pacheco, I. I., & Robbie, K. (2007). Biointerphases, 2, MR17. https://doi.org/10.1116/1.2815690

Chohan, J. S., Prakash, K., Vijay, P., Aravindan, M. K., Pradhan, P., Jacob, A., Bisht, Y. S., Bhowmik, A., & Tamene, Y. (2026). Experimental evaluation of alumina nanoparticle additives in sunflower oil methyl ester for enhanced CI engine performance and emission control. Scientific Reports, 16(1), 4789. https://doi.org/10.1038/s41598-026-35034-2

Dewangan, A., Mallick, A., Yadav, A. K., & Richhariya, A. K. (2020). Effect of metal oxide nanoparticles and engine parameters on the performance of a diesel engine: A review. Materials Today: Proceedings, 21, 1722–1727. https://doi.org/10.1016/j.matpr.2019.12.117

Dey, S., & Dhal, G. C. (2019). Materials Science for Energy Technologies, 2, 575. https://doi.org/10.1016/j.mset.2019.06.003

Doshi, R., Braida, W., Christodoulatos, C., Wazne, M., & O'Connor, G. (2008). Nano-aluminum: Transport through sand columns and environmental effects on plants and soil communities. Environmental Research, 106, 296–303. https://doi.org/10.1016/j.envres.2007.04.006

Fayad, M. A., Sobhi, M., Chaichan, M. T., Badawy, T., Abdul-Lateef, W. E., Dhahad, H. A., Yusaf, T., Isahak, W. N. R. W., Takriff, M. S., & Al-Amiery, A. A. (2023). Reducing soot nanoparticles and NOX emissions in CRDI diesel engine by incorporating TiO2 nano-additives into biodiesel blends and using high rate of EGR. Energies, 16(9), 3921. https://doi.org/10.3390/en16093921

Gad, M. S., Razek, S. M. A., Manu, P., & Jayaraj, S. (2021). Experimental investigations on diesel engine using alumina nanoparticle fuel additive. Advances in Mechanical Engineering, 13(2). https://doi.org/10.1177/1687814020988402

Geng, P., Cao, E., Tan, Q., & Wei, L. (2017). Renewable and Sustainable Energy Reviews, 71, 523. https://doi.org/10.1016/j.rser.2016.12.080

Hussain, F., Soudagar, M. E. M., Afzal, A., Mujtaba, M., Fattah, I. R., Naik, B., Mulla, M. H., Badruddin, I. A., Khan, T. M. Y., Raju, V. D., Gavhane, R. S., & Rahman, S. A. (2020). Enhancement in combustion, performance, and emission characteristics of a diesel engine fueled with Ce-ZnO nanoparticle additive added to soybean biodiesel blends. Energies, 13(17), 4578. https://doi.org/10.3390/en13174578

Kabir, E., Kumar, V., Kim, K. H., Yip, A. C., & Sohn, J. R. (2018). Journal of Environmental Management, 225, 261. https://doi.org/10.1016/j.jenvman.2018.07.087

Karlsson, H. L., Cronholm, P., Gustafsson, J., & Möller, L. (2008). Copper oxide nanoparticles are highly toxic: A comparison between metal oxide nanoparticles and carbon nanotubes. Chemical Research in Toxicology, 21, 1726–1732. https://doi.org/10.1021/tx800064j

Khalife, E., Tabatabaei, M., Demirbas, A., & Aghbashlo, M. (2017). Progress in Energy and Combustion Science, 59, 32. https://doi.org/10.1016/j.pecs.2016.10.001

Khan, S., Dewang, Y., Raghuwanshi, J., & Sharma, V. (2019). AIP Conference Proceedings, 2100, 020146.

Li, S., Liu, Z., Yang, Q., Wang, Z., Huang, X., & Luo, D. (2024). Secondary atomization and Micro-Explosion effect induced by surfactant and nanoparticles on enhancing the combustion performance of AL/JP-10/OA nanofluid fuel. Molecules, 29(8), 1806. https://doi.org/10.3390/molecules29081806

Lin, D., & Xing, B. (2007). Phytotoxicity of nanoparticles: Inhibition of seed germination and root growth. Environmental Pollution, 150, 243–250. https://doi.org/10.1016/j.envpol.2007.01.016

Long, T. C., Saleh, N., Tilton, R. D., Lowry, G. V., & Veronesi, B. (2006). Titanium dioxide (P25) produces reactive oxygen species in immortalized brain microglia (BV2): Implications for nanoparticle neurotoxicity. Environmental Science & Technology, 40, 4346–4352. https://doi.org/10.1021/es060589n

Long, T. C., Tajuba, J., Sama, P., Saleh, N., Swartz, C., Parker, J., Hester, S., Lowry, G. V., & Veronesi, B. (2007). Nanosize titanium dioxide stimulates reactive oxygen species in brain microglia and damages neurons in vitro. Environmental Health Perspectives, 115, 1631–1637. https://doi.org/10.1289/ehp.10216

Mauro, M., Crosera, M., Bovenzi, M., Adami, G., Maina, G., Baracchini, E., & Filon, F. L. (2019). Toxicology In Vitro, 59, 275. https://doi.org/10.1016/j.tiv.2019.04.015

Mehta, R. N., Chakraborty, M., & Parikh, P. A. (2014). Nanofuels: Combustion, engine performance and emissions. Fuel, 120, 91–97.

Özgür, C. (2021). Influence of NiFe2O4 and Zn0.5Ni0.5Fe2O4 nanoparticles on exhaust emissions of 4 stroke-6 cylinders turbocharged diesel engine. International Journal of Automotive Engineering and Technologies, 10(1), 42–49. https://doi.org/10.18245/ijaet.781493

Ramachandran, E., Krishnaiah, R., Venkatesan, E. P., Shaik, S., Saleel, C. A., & Hussain, F. (2023). Investigation into the Ideal Concoction for Performance and Emissions Enhancement of Jatropha Biodiesel-Diesel with CuO Nanoparticles Using Response Surface Methodology. ACS Omega, 8(42), 39067–39079. https://doi.org/10.1021/acsomega.3c03890

Reşitoğlu, İ. A., Altinişik, K., & Keskin, A. (2015). Clean Technologies and Environmental Policy, 17, 15. https://doi.org/10.1007/s10098-014-0793-9

Saxena, V., Kumar, N., & Saxena, V. K. (2017). Renewable and Sustainable Energy Reviews, 70, 563. https://doi.org/10.1016/j.rser.2016.11.067

Schrand, A. M., Rahman, M. F., Hussain, S. M., Schlager, J. J., Smith, D. A., & Syed, A. F. (2010). Wiley Interdisciplinary Reviews: Nanomedicine and Nanobiotechnology, 2, 544. https://doi.org/10.1002/wics.106

Soutter, W. (2021, August 25). Nanoparticles as fuel additives. AZoNano. https://www.azonano.com/article.aspx?ArticleID=3085

Sudalaimuthu, G., Rathinam, S., Munuswamy, D. B., & Thirugnanasambandam, A. (2018). Testing and evaluation of performance and emissions characteristics of water-biodiesel aspirated research engine. Journal of Testing and Evaluation, 48(5), 20180306. https://doi.org/10.1520/jte20180306

Wang, Y., Liu, H., & Lee, C. F. F. (2016). Renewable and Sustainable Energy Reviews, 64, 569.

Wei, L., & Geng, P. (2016). Fuel Processing Technology, 142, 264. https://doi.org/10.1016/j.fuproc.2015.09.018

Zhang, Z. H., & Balasubramanian, R. (2015). Applied Energy, 146, 270. https://doi.org/10.1016/j.apenergy.2015.02.029

Zhu, D., Wang, L., Yu, W., & Xie, H. (2018). Intriguingly high thermal conductivity increment for CuO nanowires contained nanofluids with low viscosity. Scientific Reports, 8(1), 5282. https://doi.org/10.1038/s41598-018-23174-z

JJEES

JJEES (2026) 17 (3): 351-363
ISSN 1995-6681

Jordan Journal of Earth and Environmental Sciences

A Geospatial Analysis of Coal Mining-Induced Land Use Transformation in the Saleki Reserve Forest, Assam, India

Shyamal Borah* and Monjit Borthakur

Department of Geography, Cotton University, Guwahati, India

Received on 23 June 2025, Accepted on 29 April 2026

Abstract

This study employed supervised classification using multi-temporal ResourceSat imagery (2012, 2018, and 2024) to map land use and land cover (LU/LC) changes in the Saleki Reserve Forest, achieving high overall accuracy (94–96%) and QADI values of 0.06, 0.0283, and 0.0447, respectively. Despite some misclassifications among spectrally similar classes (e.g., built-up, mining, and barren land). The results revealed a substantial increase in coal mining, with mining area expanding by 396 ha (189%), including key hotspots, such as the 4-sq-mile lease (+77.4%) and Tirap grant (+54.7%), while the Ledo OCP area declined by 60.7%. This expansion coincided with a 16.5% loss in forest cover, a 303.8% rise in bare land, and a 40.9% reduction in water bodies. The Landscape Transformation Index rose significantly from 14.7 (2012–2018) to 38.6 (2012–2024), indicating intensified anthropogenic pressure. Canopy density analysis (2018–2024) revealed regeneration in some degraded areas, and forest cover density over trends 12 years highlighted partial conservation success. Overall, the findings emphasize the conflict between mining-driven deforestation and ecosystem resilience, underlining the need for integrated land-use planning, legal enforcement, and sustainable mining. A key limitation was the exclusive use of visible-band data, affecting class separability.

Keywords: *Coal mining, land use/ land cover, forest degradation, forest cover density, Makum Coalfields, Saleki*

1. Introduction

The land use (LU) is defined as human activity taking place on land; and the land cover (LC) is defined as the physical substance that is on or above (in the case of vegetation) the Earth's surface (Chang et al., 2018; Comber et al., 2005; Nedd et al., 2021; Pandey et al., 2021; Trautwein and Pletterbauer, 2018). Land use/land cover (LU/LC) change is now a focal point of environmental monitoring and natural resource management due to the rigid relationship between LU/LC change, anthropogenic changes, and ecosystem processes (Abusmier and Al-Kofahi, 2025; Akhtar et al., 2025; Mishra et al., 2020)particularly in developing countries, where cities generally lack adequate planning. Nowadays, the majority of Jordan's population lives in cities. Zarqa governorate is among the most populated governorates in Jordan and is located within the boundaries of a major hydrological basin. Therefore, the objectives of this study were to explore the spatial and temporal varying dynamics in the urban area and agricultural areas over the past two decades (2001-2021. Several factors are influencing LU/LC, like urbanization, climate change, and land conversion (Fitriani et al., 2025; Okoduwa et al., 2025). Still, very uniquely, mining activities have caused compounding limits to LU/LC globally, resulting in deforestation, loss of biodiversity, and environmental collapse as shown in Odisha (M. Mishra et al., 2022), Cameroon (Tamfuh et al., 2024), Ghana (Gbedzi et al., 2022), Rwanda (Niyonsenga and Sibomana, 2024), Bangladesh, Mongolia (Guan et al., 2017), Germany, and China's Loess Plateau (Cioc, 1998; Lin et al., 2021). In India, coal mining has forced profound LU/LC changes in Ramagundam (Kiran et al., 2022), Godavari (Garai and Narayana, 2018), Singrauli (Khan and Javed, 2012), Jharhia (Uddin Siddiqui and Kumar Jain, 2022), and Raniganj (Patra et al., 2022)India. Owing to its multifaceted consequences on soil, water, and landholders, assessment of spatio-temporal changes in mining areas has become important. The oldest coal mine of India, Raniganj coalfield has been producing superior quality non-coking coal for the last 246 years. To reduce the cost per unit production of coal, the mining authority prefers the opencast method over underground mining. The mushrooming growth of opencast mines in this coalfield causing huge waste dumps, depletion of vegetated surface, changing slope and drainage pattern, soil erosion, and degradation of environmental quality. With this background, the present study examines the spatio-temporal changes and evolution of opencast mines using multi-temporal Landsat Thematic Mapper (TM resulting in dramatic loss of vegetation and forest.

LU/LC transformations, caused by mining, negatively impact forest canopy density (FCD), which reflects the composition, structure, and preservation levels of forests about ecosystem stability. Research has demonstrated that canopy cover has been drastically diminished, with the canopy code at some mining sites dropping from >80% cover to <30% (Galiatsatos et al., 2020; Liu et al., 2024)reporting and verification (MRV. Similar declines in canopy density occurred in Indian states that are major coal producers, such as Jharkhand, Odisha, Chhattisgarh, and Madhya Pradesh (Joshi et al., 2006; Khan and Javed, 2012; Mohanty et al., 2020; Thakur et al., 2022). Compensatory afforestation has

* Corresponding author e-mail: shyamalborahsb106@gmail.com

not been able to fully restore canopy cover to levels recorded before the forest was cleared, due to limits imposed at each site by soil, species selections, and ecological suitability. In this context, socio-ecological systems that depend on forests for sustainable livelihoods further contribute to instability and fragility (López-Bedoya et al., 2022). In the coalfields of Assam, there are indications that mining expanded by 194 ha between 2000 and 2020, leading to growing problems with acid mine drainage, heavy metal leaching, and soil erosion (Kumar et al., 2023; Yadav et al., 2018). The North Eastern Coalfield (NEC), a unit of Coal India Limited, has produced or delivered an estimated 13.68 million tons of coal between 2003 and 2021, across 9 Mining Leases, totaling 5,377.82 ha since the NEC sale of coal began (Katakey, 2021).

The Saleki Reserve Forest (RF) in the Makum coalfields faces the threat of mining encroachment due to increased mining activity. There are currently six active mining leases within Saleki RF, equaling 1,308.22 ha of land, namely, 4 sq. mile (1032.27), 4.48 Sq. Mile (4.97), Tirap Coal Grant (27.28 ha), Namdang Coal Grant (150.24 ha), Ledo OCP (27.06 ha), and Tikok OCP (67.47 ha), with the current leases running from 2023 to 2029. Mining activity within the Reserve Forest entailed occupation within a reserve forest of 183 ha in 2003, to 1043.2 ha in 2020; and mining activities not inside the reserve increased from 9 ha in 2003 to 415.6 in 2020. Mining areas totaled 192 ha in 2003 and increased to 1,458.8 ha in 2020. Within this same time frame, opencast mining has increased in area from 192 ha in 2003 to 479.1 ha in 2020, rat-hole mining increased in area from 0 ha in 2003 to 979.7 ha in 2020 (Katakey, 2021). Even though many studies have documented LU/LC changes in coal mining regions, there is little spatiotemporal analysis of protected reserve forests such as the Saleki RF, where fragile ecosystems are threatened by rapid, localized degradation from opencast and rat-hole coal mining. The current study serves to address this by assessing LU/LC and FCD spatial-temporal changes in Saleki RF from 2012 to 2012, in the context of the Ledo OCP, 4 Sq. Mile lease, and Tirap Coal Grant, using geospatial tools to synoptically assess the ecological consequences of continued expansion and exploitation of coal resources.

2. Study Area and Methodology

2.1 Study area

Saleki Reserve Forest is a part of the Dehing Patkai Elephant Reserve located in Tinsukia District in Assam (Figure 1). It has an area of approximately 40 sq km (27°15′N to 24°19′ N latitudes 95°42′E to 95°49′E longitudes). It was proposed as a reserve forest in 1976 and was notified on the 9 March, 2022. The reserve forest is situated within the Namdang coal grant and the Tikok open-cast project, while the Ledo open-cast project and the Tirap coal grant are located to the east. Total annual rainfall exceeds 4,000 mm and it is often the highest in the month of June. The climatic means are generally between 6 and 38°C. Structural hills with elevations between 143-492 meters characterize the area; there are approximately 119-164 days of rain in a year with a prolonged drier season from October to February.

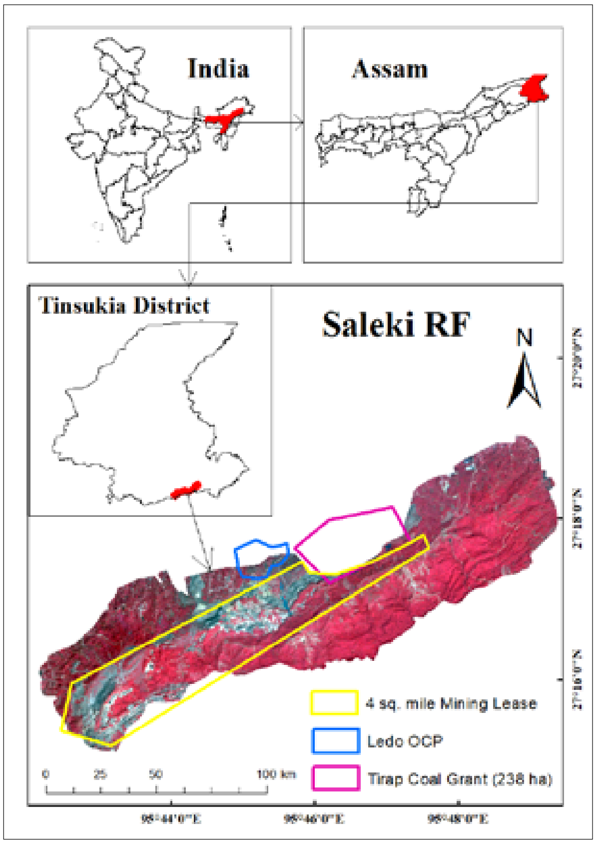

Figure 1. The Saleki RF is indicated in false color composite (LISS-4,8th March 2024)

2.2 Data collection and sources

The present study employed ResourceSat LISS-4 sensor data for LU/LC pattern analyses, utilizing specific datasets (Table 1). Focusing on the recent decade (2012-2024), the study investigated extensive mining activities in the region. The corresponding satellite datasets were obtained from Bhuvan's Bhoonidhi, ISRO's Earth Observation (EO) data hub.

Table 1. Details of satellite data

Acquisition Date	Satellite	Sensor	Path/row	Spatial resolution (m)	Source
01-11-2012	ResourceSat-2	LISS-4	114/052	5	NRSC
04-04-2018	ResourceSat-2A	LISS-4	114/052	5	NRSC
08-03-2024	ResourceSat-2A	LISS-4	114/052	5	NRSC

Source: Authors

Due to the limited spatial extent of the Saleki RF, high-resolution satellite data are essential for precise land use/land cover study. However, high-resolution LISS-4 sensor databases have only been available from 2012 onward for this specific location. To supplement the analysis and validate LU/LC statistics, this study relied on the following secondary data sources:

- The Report of the 'One Man Commission of

Inquiry' (Vol. I & II) by Brojendra Prasad Katakey, published on April 7, 2021, by the Assam State Government.

- Relevant existing literature, including:

  - Newspaper articles

  - Journal articles

These secondary sources provide valuable context and insights to support the primary satellite data analysis.

2.3 Methodology

2.3.1 Land use/land cover classification

The current study's workflow includes satellite data acquisition, image preprocessing, image classification, accuracy assessment, change-detection analysis, and forest canopy density mapping (Figure 2). A supervised classification method was employed to classify satellite images. The following sections provide extensive explanations of the various steps.

Image pre-processing and classification

The necessary image pre-processing was performed on the data for the three specified years (2012, 2018, and 2024). Image pre-processing, classification and analysis were conducted using Geospatial software (ERDAS Imagine and ArcGIS). Supervised image classification (maximum likelihood method) was performed in ERDAS Imagine. To identify the changes, images were broadly classified into five categories: built-up area, mining, forest area, bare land and water body (Table 2). Training samples for supervised classification were selected using a combination of high-resolution Google Earth imagery and field observations. Mining areas were identified based on characteristic features such as excavation pits, overburden dumps, and haul roads, distinguishing them from non-mining open land. Only spectrally homogeneous and clearly identifiable areas were used as training data to minimize misclassification in LISS-4 imagery.

Table 2. Land use Classification scheme

Sl. No	Class name	Description
1	Water body	Reservoirs, rivers, open water, ponds, etc.
2	Mining	Coal mines, abandoned mines, dumped yards, etc.
3	Forest area	Dense forest and open forest.
4	Bare land	Exposed soils, barren area, etc.
5	Built-up area	Residential, commercial, transportation, roads, pavements, etc.

Accuracy assessment

The Ground Truth Points (GTPs) were selected independently from training samples and were evenly distributed across the study area. They were derived from field observations and high-resolution Google Earth imagery, including both homogeneous and mixed pixels rather than only pure pixels. This ensured independent and unbiased accuracy assessment. The accuracy assessment methods include the standard Kappa coefficient, overall accuracy, producer's accuracy and user's accuracy. Overall accuracy indicates the number of pixels that are properly identified. The frequency of occurrence of a map class on the ground is determined by the user's accuracy. The producer's accuracy indicates the number of classified pixels in a class that accurately fits into that class. Equation 1 shows estimations for accurate Kappa statistics for the stratified random.

$$\text{Kappa coefficient} = (T \times C) - G/T2 - G \qquad (1)$$

(Arumugam et al., 2021; Vieira et al., 2010)

Where T is the test pixels, C is the correctly classified pixels observations and G is the sum of the multiplied total value.

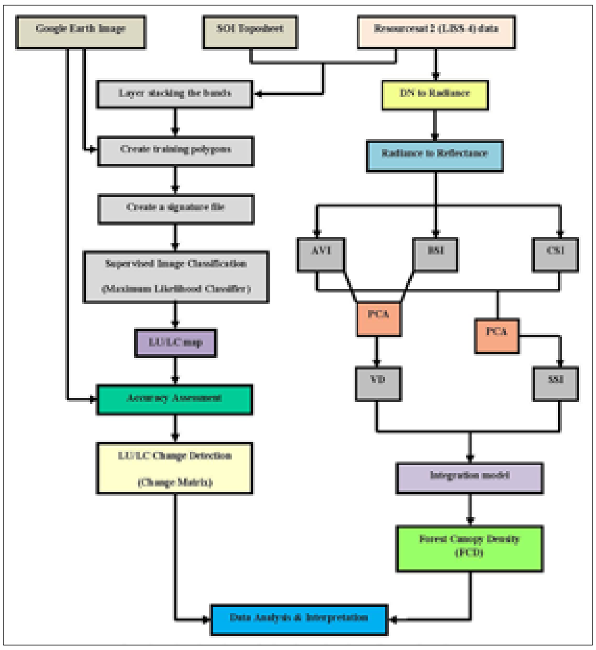

Figure 2. Flowchart showing the methods adopted to determine LU/LC change

The overall accuracy is calculated by dividing the sum of the values along the major diagonal by the total number of reference pixels (Equation 2). The traditional accuracy assessment methods included the standard Kappa coefficient followed by the overall accuracy equation, producer's accuracy and user's accuracy as indicated in equations 3 and 4 (Arumugam et al., 2021).

$$Overall\ Accuracy = (1/N) \sum_{i=1}^{r} n_{ii} \qquad (2)$$

$$Producer's\ Accuracy = (n_{ii}/n_{icol}) \qquad (3)$$

$$User's\ Accuracy = (n\_ii/n\_irow) \qquad (4)$$

Where n_{ii} is the number of suitably classified pixels, N is the total number of pixels; r is the number of rows, n_{icol} is the column total, and n_{irow} is the row total.

Quantity and Allocation Disagreement Index (QADI): This index calculates the degree of disagreement between the classification results and reference maps by keeping incorrectly labeled pixels as A and the difference in the pixel count (for each class) between the classified map and reference data as Q (Feizizadeh et al., 2022)various alternative measures have been investigated with minimal success in practice. In this article, we introduce a novel index that overcomes the limitations. Unlike Kappa, it is not sensitive to asymmetric distributions. The quantity and allocation disagreement index (QADI. The QADI index, which measures the degree of disagreement and variation, is then calculated from these values. Additionally, it can be used to create a graph showing how much each component contributes to the disagreement (Feizizadeh et al., 2022) various alternative measures have been investigated with minimal success in practice. In this article, we introduce a novel index that overcomes the limitations. Unlike Kappa, it is not sensitive to asymmetric distributions. The quantity and allocation disagreement index (QADI. The equation 5 for the QADI index is as follows:

$$QADI = \sqrt{\left(\frac{A}{N}\right)^2 + \left(\frac{Q}{N}\right)^2} \tag{5}$$

The resulting QADI value varies between 0and 1 (Feizizadeh et al., 2022)various alternative measures have been investigated with minimal success in practice. In this article, we introduce a novel index that overcomes the limitations. Unlike Kappa, it is not sensitive to asymmetric distributions. The quantity and allocation disagreement index (QADI.

2.3.2 Forest Canopy Density

Radiometric correction

Radiometric correction takes raw Digital Numbers (DN) and converts them to physical values to accurately represent a surface. Equation 6 shows the steps to convert DN to at-sensor radiance.

$$L\lambda = SR_k / DN_{max} \times DN \tag{6}$$

Where, Lλ: At-sensor spectral radiance (W/m²/sr/µm)

SR_k: Saturation radiance for the kth band (provided in metadata)

DN: Digital Number of the pixel

DN_{max}: Maximum possible value of pixel

To obtain at-sensor (TOA) reflectance, radiance values were converted using Equation 7:

$$Rsensor = \frac{L_\lambda \times \pi \times d^2}{E_{sun} \times cos\theta_z} \tag{7}$$

Where pi =3.14159

Rsensor = reflectance at the sensor

L_λ = spectral radiance at the sensor's aperture

E_{sun} = mean solar exo-atmospheric irradiance

θ_z = solar zenith angle

d = Earth-Sun distance

Advanced Vegetation Index (AVI)

The Advanced Vegetation Index (AVI) is a vegetation metric that was developed to increase sensitivity to vegetation density, especially when working in conditions of dense canopy cover, while minimizing the signal from background soil noise. The AVI can be computed using equation 8.

$$AVI = \sqrt[3]{(B4 \times (DN_{max} - B3) \times (B4 - B3) + 1} \tag{8}$$

Bare Soil index (BSI)

The Bare Soil Index (BSI) identifies bare soil areas from satellite imagery. We have provided a simple model of the BSI for LISS-4 in equation 9.

$$BSI = \frac{((B4 + B2) - B3)}{((B4 + B2) + B3} \tag{9}$$

Canopy Shadow Index (CSI)

The Canopy Shadow Index (CSI) identifies shadowed areas beneath dense vegetation canopies, typically indicating healthy forests. The formula for CSI is shown in equation 10.

$$CSI = \sqrt{((DN_{max} - B2) \times (DN_{max} - B3)} \tag{10}$$

To form a Vegetation Density (VD) calculation, we will find Principal Component Analysis (PCA) performance between the AVI and the BSI. Likewise, to form a Scaled Shadow Index (SSI) calculation, PCA will be performed between the CSI and AVI.

Forest Canopy Density

Forest Canopy Density (FCD) is defined as the percentage of land surface area covered by tree canopy in a forested area. One of the equations found in the literature is equation 11.

$$FCD = \sqrt{(VD \times SSI + 1)} - 1 \tag{11}$$

3. Results

3.1 Image classification and accuracy assessment

This study demonstrated the application of supervised classification for LU/LC mapping using multi-year ResourceSat series satellite data. To ensure reliability, accuracy assessments were performed for each year's classified maps using confusion matrices and test samples. The results showed consistent classification accuracy across years, with total accuracy levels of 94% and a Kappa coefficient of 0.86 (2012), 96% and a Kappa coefficient of 0.92 (2018), and 94% and a Kappa coefficient of 0.89 (2024) (Table 3). The producer's accuracy showed that water bodies and mining areas were classified with higher accuracy, while the user's accuracy indicated that water bodies and forest regions were classified with greater correctness. The QADI values for each year were 0.06, 0.02828, and 0.04472, respectively.

Although supervised classification achieved high accuracy, some misclassifications were observed in the classified maps, primarily due to mix-pixel effects, low image resolution, similar surface reflectance, and texture patterns. These misclassifications mostly occurred between built-up areas and mining regions. Accurate classification of coal mining areas, built-up areas, and bare lands using visible-band satellite data is challenging due to their similar spectral properties. However, this limitation can be overcome by utilizing SAR data or microwave satellite data, which offers enhanced feature discrimination based on backscattering intensity and dielectric properties (Forkuor et al., 2020; Ranjan et al., 2021; Ranjan and Parida, 2019). Unfortunately, historical microwave satellite sensor or SAR data are unavailable for this study, precluding its use for change detection.

Despite the difficulty in achieving 100% accuracy in differentiating mining areas from barren land and built-up areas using spectral signatures, the available data can still provide valuable insights for a representative study. Therefore, an analysis of change detection was carried out to recognize the impacts of coal mining activities on LU/LC patterns within the Saleki RF. The LU/LC maps, produced using supervised classification for 2012, 2018, and 2024, are shown in Figure 3.

Table 3. Confusion Matrix of Accuracy Assessment

	Reference Data							
	Class	***B***	***BA***	***W***	***M***	***F***	**Total**	**Au (%)**
	Year – 2012							
Classified Data	***B***	5	0	0	0	1	6	83.33
	BA	0	7	0	0	1	8	87.5
	W	0	0	4	0	0	4	100
	M	0	0	0	7	1	8	87.5
	F	3	0	0	0	71	74	95.94
	Total	8	7	4	7	74	100	
AP (%)	62.5	100	100	100	95.94			
AO (%)	94							
K	0.86201							
QADI	0.06							
	Year – 2018							
Classified Data	***B***	7	0	0	0	0	7	100
	BA	1	11	0	0	0	12	91.66
	W	0	0	3	0	0	3	100
	M	1	0	0	10	2	13	76.92
	F	0	0	0	0	65	65	100
	Total	9	11	3	10	67	100	
AP (%)	77.77	100	100	100	97.01			
AO (%)	96							
K	0.92468							
QADI	0.02828							
	Year – 2024							
Classified Data	***B***	11	1	0	0	3	15	73.33
	BA	1	8	0	0	0	9	88.88
	W	0	0	3	0	0	3	100
	M	0	0	0	10	0	10	100
	F	0	1	0	0	62	63	98.41
	Total	12	10	3	10	65	100	
AP (%)	91.66	80	100	100	95.38			
AO (%)	94							
K	0.89142							
QADI	0.04472							

B Bare land, *BA* Built-up area, *W* Water body, *M* Mining, *F* Forest area, AP the producer's accuracy, Au the user's accuracy, AO the overall accuracy, K = the kappa coefficient, QADI = Quantity and allocation disagreement index

Source: Calculated by the Authors

3.2 LU/LC mapping and change detection analysis of Saleki RF

After calculating the accuracy of prepared LU/LC maps, the areal coverage of each feature was analyzed. The areal coverage of coal mining was 137 ha, 213 ha, and 396 ha for the years 2012, 2018, and 2024, respectively (Table 4). It was observed that the areal coverage of coal mining expanded during 2012–2018, with a 55.47% change rate. However, the rate of increase in mining was recorded at 189.05% during 2012–2024 (Table 5).

A significant decrease rate (-16.48%) was noticed for the forest areas during 2012–2024 (Figure 5). The results show that the change rate of forest area was -8.42% and -8.8% during 2012–2018 and 2018–2024, respectively. The continued loss in forest area coverage suggests that mining activity has a detrimental influence on the forest ecology in the studied region. Moreover, a significant increase in bare land was noticed during 2012–2024 (303.77%). The rate of change in bare land was -1.89%, and 311.53% during 2012–2018 and 2018–2024 respectively. Built-up areas changed a lot over time, going up by 58.4% from 2012 to 2018 and then going down sharply by 77.27% from 2018 to 2024. Permanent settlements are not allowed in this area because it is part of a reserved forest. So, the mapped built-up land is mostly made up of temporary and semi-permanent buildings that coal miners use. These buildings are very close to active mining sites and are left empty or taken down when mining sites move or stop. The decrease in built-up area seen between 2018 and 2024 is due to people moving away from settlements and leaving them behind because of changes in mining activity, not because of planned or stable urban development. Similarly, the area under water bodies has decreased between 2012 and 2024 (-40.91%). The highest LU/LC conversion was in forest area to bare land (285 ha), followed by forest area to coal mining (232 ha) (Table 6). Thus, the lowest conversion was in the mining region to water bodies (0.22 ha). Most of the built-up area has gone back to being bare land (33 ha) and forest (35 ha). Most of the built-up areas are temporary mining labor camps that are left behind when mining shifts or slows down. Structures are taken apart or fall apart, turning into bare land first and then growing back naturally. This explains the change from developed land to forest. Overall, the LU/LC maps revealed that the land coverage of the mining area increased steadily across all classes from 2012 to 2024. As a result of widespread opencast coal mining activities, there has been a large reduction in forest cover, which includes herbs, shrubs and other vegetation (Figure 6). In between the study period, the amount of barren land expanded as well. The bare land consists of exposed soils, desolate areas, etc.

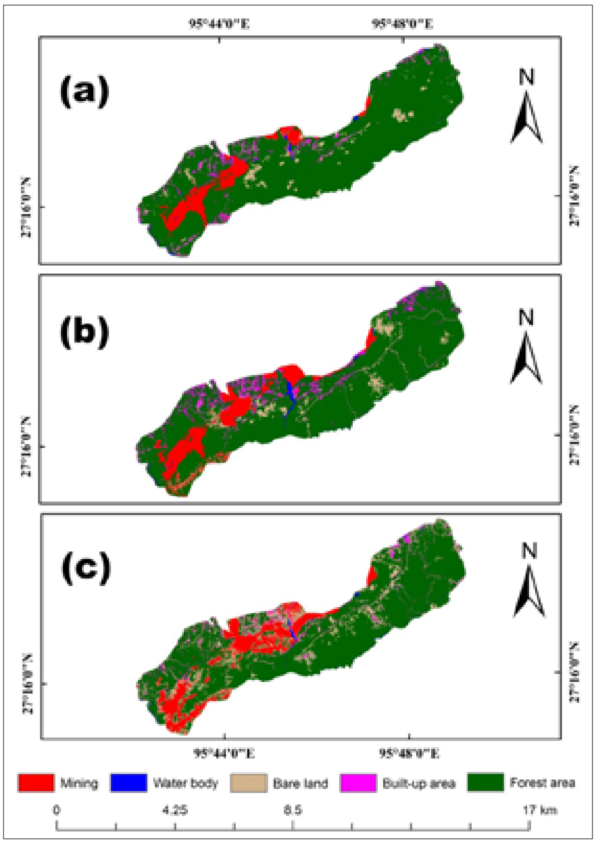

Figure 3. LU/LC map of the Saleki Reserve Forest for the years (a) 2012, (b) 2018, and (c) 2024

Table 4. Areal coverage of LU/LC classes

Year Classes	2012		2018		2024	
	Area (Ha)	Area (%)	Area (Ha)	Area (%)	Area (Ha)	Area (%)
Bare land	106	3.51	104	3.46	428	14.22
Built-up area	250	8.30	396	13.17	90	2.97
Water body	22	0.74	12	0.38	13	0.45
Mining	137	4.55	213	7.06	396	13.15
Forest area	2493	82.86	2283	75.91	2081	69.19
Total Area	3008	100	3008	100	3008	100

Source: Calculated by the Authors

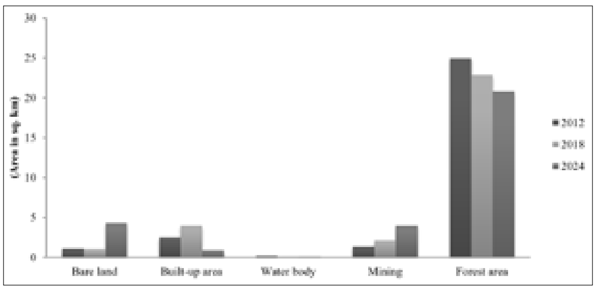

Figure 4. Comparative study of LU/LC change from 2012 to 2024

Table 5. Rate of change in areal coverage of different LU/LC classes

Year/Classes	2012-2018	2018-2024	2012-2024
Rate of change per year (%)			
Bare land	-1.89	311.53	303.77
Built-up area	58.4	-77.27	-64
Water body	-45.45	8.33	-40.91
Mining	55.47	85.91	189.05
Forest area	-8.42	-8.80	-16.48

Source: Calculated by the Authors

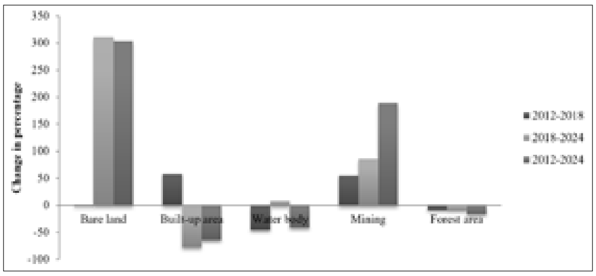

Figure 5. Net change of LU/LC from 2012 to 2024 in percentage

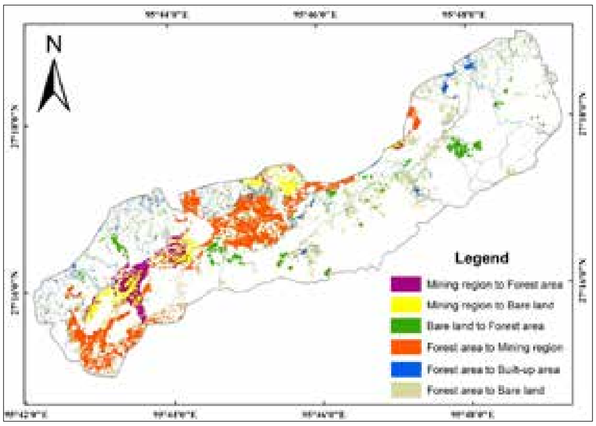

Figure 6. LU/LC conversion map of Saleki RF, 2012 – 2024

Table 6. Transition matrix of LU/LC change in the Saleki RF from 2012 to 2024 (Area in Ha)

Land use/land cover classes	Bare land	Built-up area	Water body	Mining	Forest area	Total in 2024
Bare land	33	7	0.7	24	72	136.7
Built-up area	33	10	0.9	27	35	105.9
Waterbody	2.8	0.8	5	3.6	2.7	14.9
Mining	70	7	0.2	107	57	241.2
Forest area	285	59	6	232	1909	2491
Total in 2012	423.8	83.8	12.8	393.6	2075.7	2989.7

Source: LANDSAT Satellite Image Processing

3.3 Forest Canopy Density in Saleki RF

In this section, changes in forest canopy density within the Saleki Reserve Forest between 2018 and 2024 are examined to assess patterns of forest degradation, regeneration, and broader ecological modification. The analysis focuses on shifts across different canopy density classes to understand spatial and temporal variations in forest condition during the study period. Forest Canopy Density (FCD) maps for the study area were generated using a multi-index approach that integrates the AVI and BSI (Figure 7) and CSI and SSI (Figure 8), each representing distinct biophysical characteristics of vegetation cover and surface conditions.

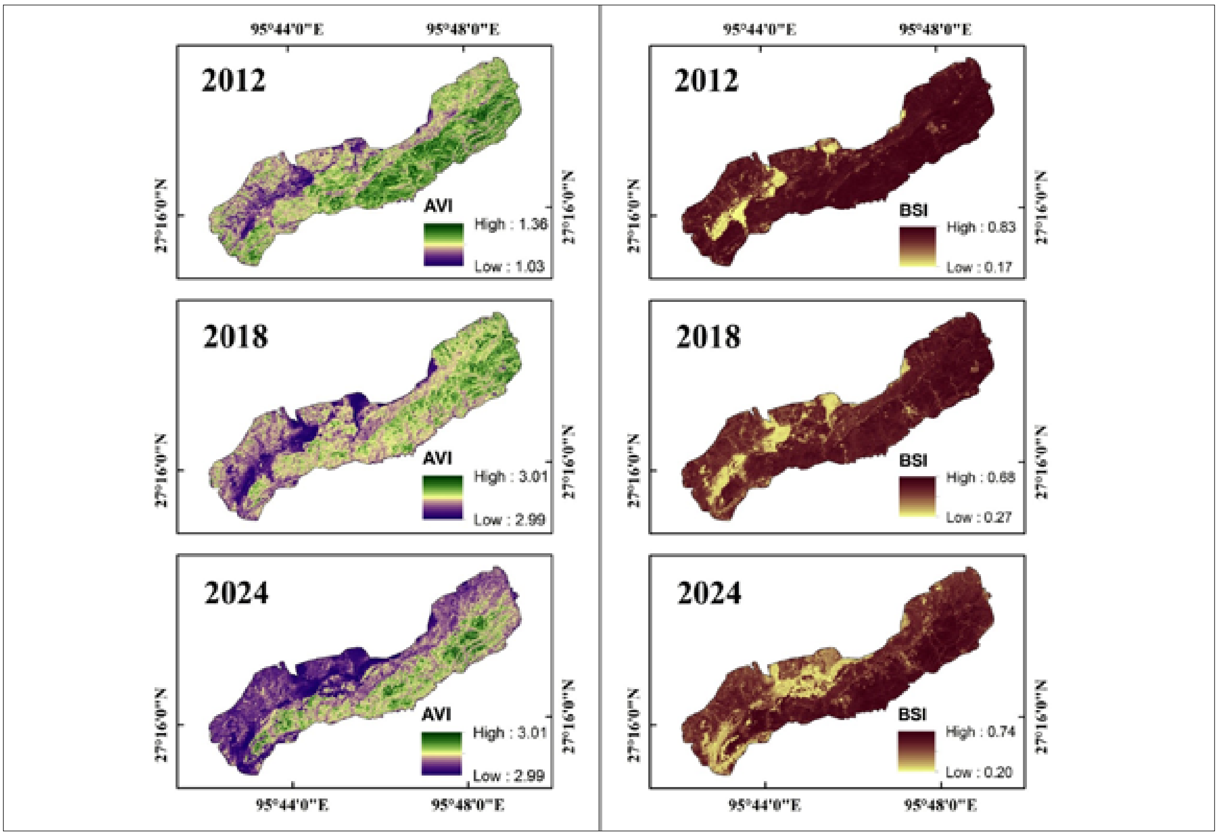

Figure 7. AVI and BSI of Saleki RF

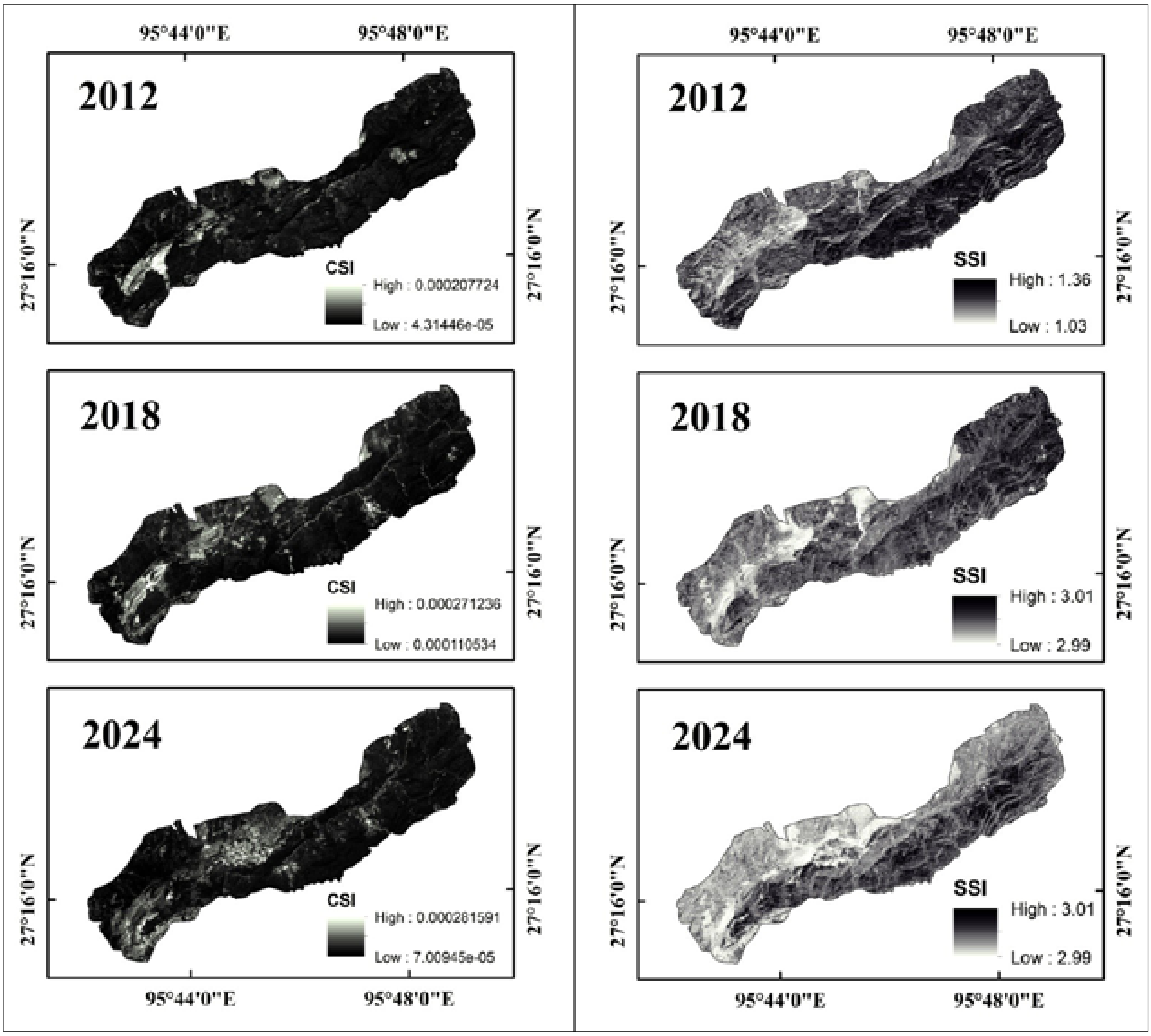

Figure 8. CSI and SSI of Saleki RF

Table 7 indicates the changes in canopy density of forests of Saleki Reserve Forest from 2012 to 2024. In the case of other natural cover like scrub and open forest, it can be concluded that scrub cover has reduced significantly from 1.63 ha to 0.1 ha, Open Forest-I decreased from 31.98 ha to 0.34 ha, and Open Forest-II has decreased sharply from 370.18 ha to 111.67 ha. While Moderately Dense Forest experienced a large decline by 2018, it has had a partial recovery by 2024. Medium Dense Forest increased from 2012 to 2018, then slightly decreased by 2024. The most noticeable cover of Highly Dense Forest has grown 107.12 ha in 2012 to 904.34 in 2024. Therefore, in general, there has been an obvious shift of forest cover density from sparse to denser canopy cover, indicating a successful forest regeneration or conservation efforts. The forest cover density maps for the study area for the year 2012, 2018 and 2024 are available in Figure 9.

Table 7. Category-wise area of Forest Canopy Density in Saleki RF

FCD Classes with FCD in %	2012		2018		2024	
	Area (in ha)	Area (in %)	Area (in ha)	Area (in %)	Area (in ha)	Area (in %)
Scrub land, 0-10	1.6275	0.054	0.02	0.0006	0.1	0.003
Open Forest-I, 11-20	31.9775	1.068	0.5625	0.018	0.3375	0.011
Open Forest-II, 21-40	370.18	12.371	199.84	6.67	111.6675	3.73
Moderately Dense, 41-60	1189.415	39.75	321.18	10.73	522.255	17.45
Medium Dense, 61-80	1291.8925	43.17	1948.69	65.12	1453.5175	48.57
Highly Dense, 81-100	107.1225	3.58	521.9225	17.44	904.335	30.22

Source: Calculated by the Authors

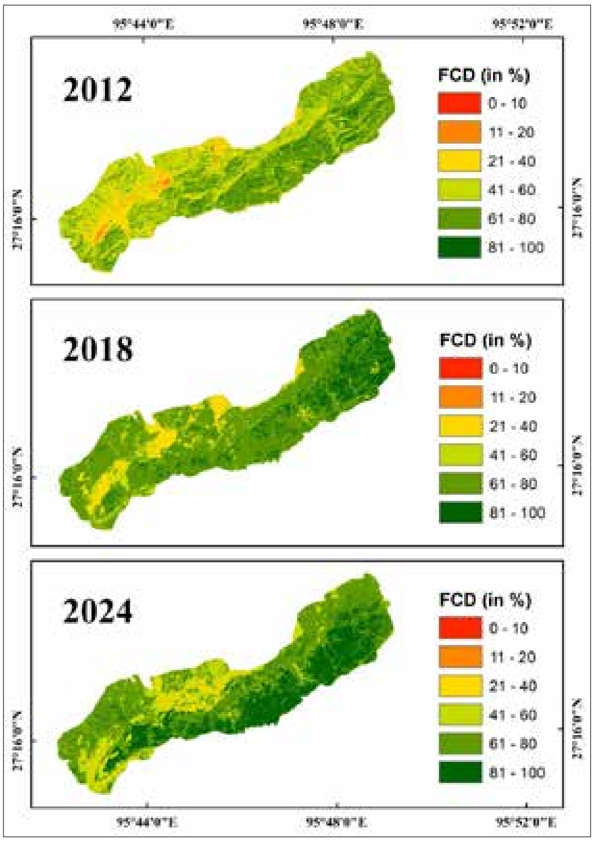

Figure 9. Forest Canopy Density map of Saleki RF

3.4 Expansion of coal mining inside Saleki RF

The unchecked expansion of coal mining activities within the Saleki RF poses a significant threat to its ecosystem. This section examines the spatial-temporal dynamics of coal mining expansion within the forest area. The mining projects inside the Saleki RF; i.e. Ledo Open Cast Project (Ledo OCP), 4 sq. mile mining lease and Tirap coal grant are considered as the critical hotspots of land cover degradation. Figure 10 illustrates the location of these three coal mining projects within the Saleki RF. These projects are overlaid on a false color composite image, providing a visual representation of their spatial distribution within the RF.

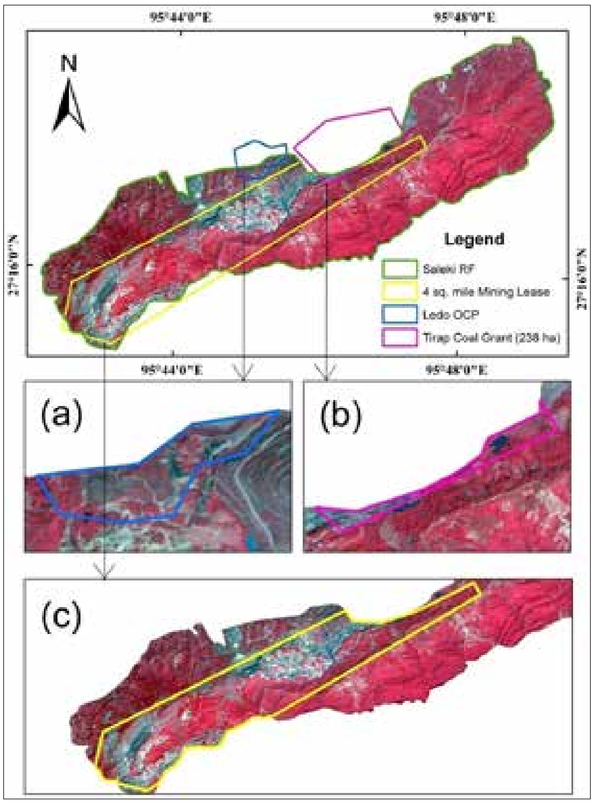

Figure 10. Coal Mining Projects inside Saleki RF, (a) Ledo OCP, (b) Tirap coal grant and (c) 4 sq. mile mining lease are shown in false color composite (LISS-4, dated 8th March 2024)

Table 8. Areal coverage of coal mining inside the Saleki RF in different study years obtained from supervised classification

Name of mining region	2012 (Area in ha)	2018 (Area in ha)	2024 (Area in ha)
Ledo OCP	14.9175	15.7925	5.845
Tirap Coal Grant	5.4525	7.9675	8.44
4 sq. mile mining lease	171.14	229.05	303.4275
Total	191.51	252.81	317.7125

Source: Calculated by the Authors

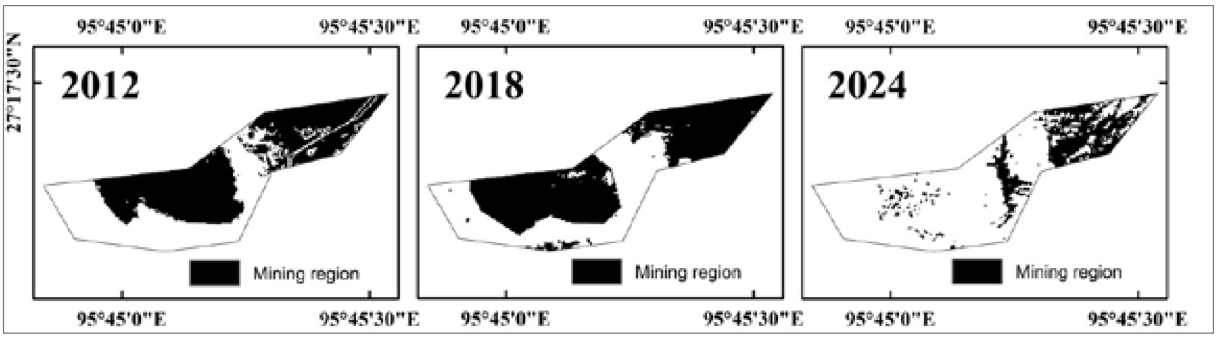

Figure 11. Coal mining region at Ledo OCP inside the Saleki RF in (i) 2012, (ii) 2018, and (iii) 2024

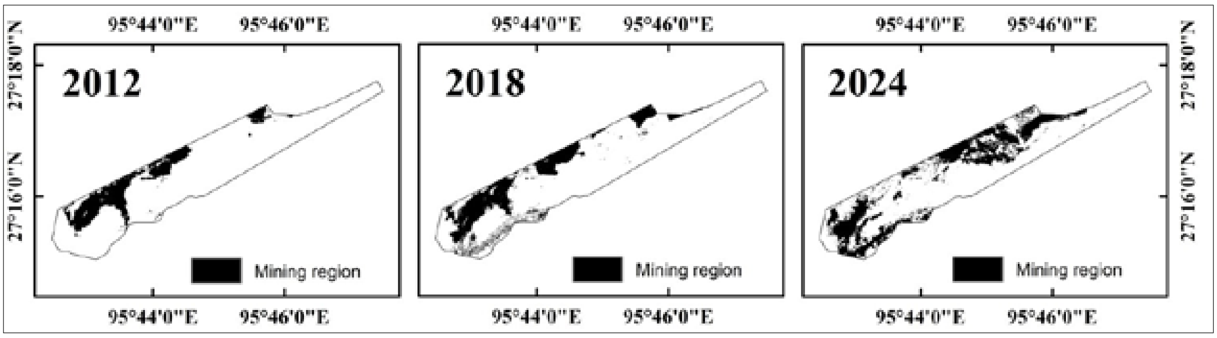

Figure 12. Coal mining region at 4 sq. mile mining lease inside the Saleki RF in (a) 2012, (b) 2018, and (c) 2024

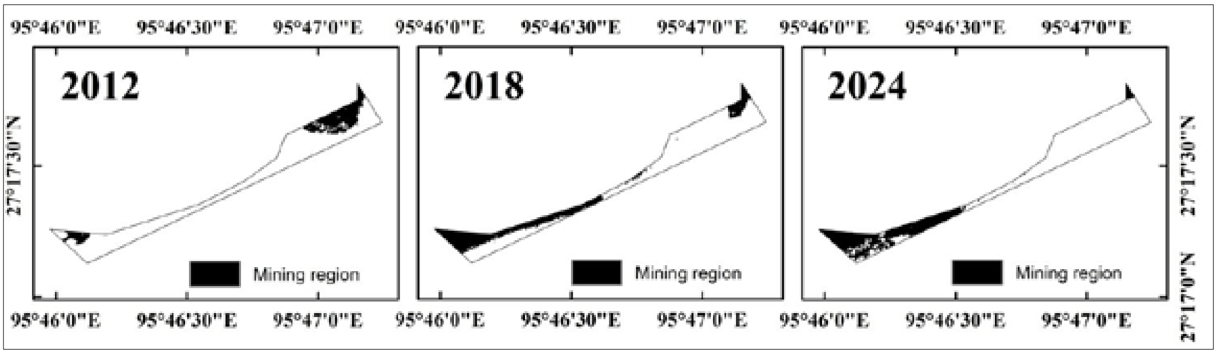

Figure 13. Coal mining region at Tirap coal grant inside the Saleki RF in (a) 2012, (b) 2018, and (c) 2024

The coal mining area inside Saleki RF expanded significantly between 2012 and 2024. The total mining area increased by 66% from 191.51 ha in 2012 to 317.71 ha in 2024 (Table 8). Notably, the 4 sq. mile mining lease registered a 77.4% increase from 171.14 ha to 303.43 ha during this period (Figure 12). Similarly, Coal mining within the Tirap Coal Grant increased by 54.7% from 5.45 ha to 8.44 ha (Figure 13). In contrast, Ledo OCP decreased by 60.7% from 14.92 ha to 5.85 ha (Figure 11). The year-wise increase shows a 32.1% rise from 2012 to 2018 and a 25.6% rise from 2018 to 2024. The three areas are, therefore, considered as the hotspots of coal mining-induced land cover change within the Saleki RF.

3.5 Landscape transformation index of Saleki RF, 201224-

The Landscape Transformation Index (LTI) is a quantitative measure that assesses the magnitude of changes in LU/LC patterns over time. It provides a comprehensive framework for evaluating the degree and nature of landscape transformations, enabling researchers and policymakers to track and understand the dynamics of environmental change (Łowicki, 2008). The LTI is calculated using Equation 12 below:

$$\mathrm{LTI} = (\Sigma|\textit{change in land cover class}|)\ /\ \textit{total area} \quad (12)$$

where Σ of change in land cover class represents the sum of the absolute values of changes in each land cover class and total area represents the total area of the landscape being studied.

- LTI for 2012-2018:

= (|3.51-3.46| + |8.30-13.17| + |0.74-0.38| + |4.55-7.06| + |82.86-75.91|) / 100

= (0.05 + 4.87 + 0.36 + 2.51 + 6.95) / 100

= 14.74

- LTI for 2018-2024:

= (|3.46-14.22| + |13.17-2.97| + |0.38-0.45| + |7.06-13.15| + |75.91-69.19|) / 100

= (10.76 + 10.20 + 0.07 + 6.09 + 6.72) / 100

= 33.84

- LTI for 2012-2024:

= (|3.51-14.22| + |8.30-2.97| + |0.74-0.45| + |4.55-13.15| + |82.86-69.19|) / 100

= (10.71 + 5.33 + 0.29 + 8.60 + 13.67) / 100

= 38.60

The overall change in land cover classes indicates significant changes in the landscape. Bare land increased by 323 hectares (11.71%), while the built-up area decreased by 160 hectares (5.33%). Water bodies experienced a minor decrease by nine hectares (0.29% decrease). Mining areas increased by 259 hectares (8.60%). The forest areas have decreased by 412 hectares (13.67%) from 2012 to 2024. The major changes exemplify a dynamic landscape, which deserves continual monitoring and management of land cover classes to assess their environmental and ecological consequences.

The outputs from the Landscape Transformation Index (LTI) reveal significant changes in the landscape among the three time periods. The LTI values of 14.74, 33.84, and 38.60 during 2012-2018, 2018-2024, and 2012-2024, respectively, show a continuous increase in the landscape transformation within the area. We must note that the net change in land cover classes has resulted in a considerable increase in bare land and mining areas, and a decrease in built-up areas, water bodies, and forest areas.

4. Discussion

The analysis of LU/LC change indicates significant declines in forest cover derived from 2,493 hectares in 2012 to 2,081 hectares in 2024. Simultaneously, mining activity has rapidly and dramatically increased from 137 hectares in 2012 to 396 hectares in 2024. The findings of the present study show that coal mining activities have rapidly destroyed forest cover in Saleki RF during this time. Furthermore, the One Man Commission of Inquiry Report presented by Justice Brojendra Prasad Katakey (Katakey, 2021) supports the majority of these findings by indicating that the extent of encroachment by mining activities is vast in the reserved forest. There has been a similarly alarming trend noted in the BP Katakey report in areas occupied by mining in the reserve forest, which has increased significantly from 183 hectares in 2003 to a shocking 1,043.2 hectares in 2020, with a disproportionate increase from 2018 (474.7 ha) to 2020 (1,043.2 ha). This is suggestive of the significant decreases in tree cover, and increases in mining area established by the study at hand, showing that the encroachment of coal mining is now a consistent trend in underwent encroachment into the reserved forest. Nonetheless, the One Man Commission of Inquiry Report provided an extrapolated estimation on the extent of non-coal mining areas (estimated in hectares) within the reserve forest. Based on the report's classification of mining activity and the estimates, the Environment and Forest Department, Government of Assam, provides a preliminary estimation and has mentioned the need for a scientific study on the issue (Katakey, 2021).

Moreover, the analysis on forest canopy density in the Saleki Reserve Forest offers very an encouraging picture of recovery from 2018 and ending in 2024. The earlier years showed a clear trend of significant degradation, particularly in the open forest and scrub forest classes. The most recent data are very promising, showing high levels of regrowth, primarily in moderately to highly dense forest classes. There was a huge increase in highly dense forest cover across the region, even in the affected mining areas. Mining sites are either demonstrating some success of planned re-growth efforts or significant natural evolution. The recovery of highly dense forest areas and other classes of forest canopy throughout these historically disturbed spaces is promising, since it shows that conservation and rehabilitation strategies have been able to address and reverse the deleterious effects of anthropogenic influences such as mining. Not only that, but increases in forest composition, density, and canopy coverage demonstrate that human-assisted or unassisted forest management efforts can positively contribute to and support equitable transitions towards future ecological stability.

The study results align with existing literature on the impacts of coal mining on forest ecosystems. Studies have consistently shown that coal mining leads to widespread deforestation, habitat destruction, and environmental degradation (Goswami, 2015). The findings of this research also support the notion that the expansion of coal mining and coke coal industries is a significant driver of LU/LC dynamics (A. Mishra et al., 2022). Furthermore, the role of labor migration and settlement expansion in contributing to land cover alteration is consistent with the existing literature (Kutir et al., 2022). However, this study provides new insights into the specific context of Saleki RF, highlighting the need for localized solutions to address the land-use transformations driven by coal mining in this region.

5. Conclusion

This study demonstrates that coal-mining expansion has been a dominant driver of land-use and land-cover transformation in and around the Saleki Reserve Forest, leading to substantial forest degradation, a reduction in water bodies, and an expansion of bare land. Landscape-level indicators confirm continuous and intensifying anthropogenic pressure, particularly in active mining lease areas, while localized declines in some mining zones suggest spatially uneven extraction dynamics. At the same time, recent canopy-density patterns indicate early signs of forest regeneration on degraded lands, highlighting ecological resilience where direct disturbance has slowed. Despite minor spectral limitations in differentiating mining-related land classes, the classification accuracy provides confidence in the observed trends. Overall, the findings underscore the urgent need for integrated land-use planning, stricter enforcement of environmental regulations, adoption of sustainable mining and reclamation practices, and continuous monitoring to balance resource extraction with long-term ecological stability.

Future work can better connect ecological and socio-economic factors and generalize findings by incorporating SAR and multi-temporal data, with site validation within a longitudinal cross-site design.

Statements and Declarations

- Conflict of interest:

The corresponding author declares on behalf of all authors that there is no conflict of interest.

- Funding:

The authors declare that no funds, grants, or other support were received during the preparation of this manuscript.

- Declaration of generative AI and AI-assisted technologies in the writing process:

No AI tools were used in the writing of this work.

References

References

Abusmier, S.A., Al-Kofahi, S.D., 2025. Examining Land Use/ Land Cover Dynamics in Zarqa Governorate Major Districts: Implications for Urban and Environmental Sustainability. Jordan J. Earth Environ. Sci. 16, 1–10.

Akhtar, M.M., Khan, T., Khan, A.R., Akhtar, R., Raza, D., 2025. Assessing the Land Use/Land Cover and Climatic Changes Impacts on Static Groundwater Level: A Case Study of Quetta, Pakistan. Jordan J. Earth Environ. Sci. 16, 136–143.

Arumugam, T., Yadav, R.L., Kinattinkara, S., 2021. Assessment and Predicting of LULC by Kappa Analysis and CA Markov model using RS and GIS Techniques in Udham Singh Nagar District, India. https://doi.org/10.21203/rs.3.rs-141832/v1

Chang, Y., Hou, K., Li, X., Zhang, Y., Chen, P., 2018. Review of Land Use and Land Cover Change research progress. IOP Conf. Ser. Earth Environ. Sci. 113, 012087. https://doi.org/10.1088/1755-1315/113/1/012087

Cioc, M., 1998. The Impact of the Coal Age on the German Environment: A Review of the Historical Literature. Environ. Hist. Camb. 4, 105–124. https://doi.org/10.3197/096734098779555754

Comber, A., Fisher, P., Wadsworth, R., 2005. What is Land Cover? Environ. Plan. B Plan. Des. 32, 199–209. https://doi.org/10.1068/b31135

Feizizadeh, B., Darabi, S., Blaschke, T., Lakes, T., 2022. QADI as a New Method and Alternative to Kappa for Accuracy Assessment of Remote Sensing-Based Image Classification. Sensors 22, 4506. https://doi.org/10.3390/s22124506

Fitriani, Y., Abdullah, N., Ridwan, I., 2025. Spatiotemporal Analysis of Wetland Environmental Changes Using Machine Learning and Remote Sensing Data. Jordan J. Earth Environ. Sci. 16, 418–432.

Forkuor, G., Ullmann, T., Griesbeck, M., 2020. Mapping and Monitoring Small-Scale Mining Activities in Ghana using Sentinel-1 Time Series (2015–2019). Remote Sens. 12, 911. https://doi.org/10.3390/rs12060911

Galiatsatos, N., Donoghue, D.N.M., Watt, P., Bholanath, P., Pickering, J., Hansen, M.C., Mahmood, A.R.J., 2020. An Assessment of Global Forest Change Datasets for National Forest Monitoring and Reporting. Remote Sens. 12, 1790. https://doi.org/10.3390/rs12111790

Garai, D., Narayana, A.C., 2018. Land use/land cover changes in the mining area of Godavari coal fields of southern India. Egypt. J. Remote Sens. Sp. Sci. 21, 375–381. https://doi.org/10.1016/j.ejrs.2018.01.002

Gbedzi, D.D., Ofosu, E.A., Mortey, E.M., Obiri-Yeboah, A., Nyantakyi, E.K., Siabi, E.K., Abdallah, F., Domfeh, M.K., Amankwah-Minkah, A., 2022. Impact of mining on land use land cover change and water quality in the Asutifi North District of Ghana, West Africa. Environ. Challenges 6, 100441. https://doi.org/10.1016/j.envc.2022.100441

Goswami, S., 2015. Impact of Coal Mining on Environment. Eur. Res. 92, 185–196. https://doi.org/10.13187/er.2015.92.185

Guan, C., Zhang, B., Li, J., Zhao, J., 2017. Temporal and spatial changes of land use and landscape in a coal mining area in Xilingol grassland. IOP Conf. Ser. Earth Environ. Sci. 52, 012052. https://doi.org/10.1088/1742-6596/52/1/012052

Joshi, P.K., Kumar, M., Midha, N., Yanand, V., Wal, A.P., 2006. Assessing areas deforested by coal mining activities through satellite remote sensing images and gis in parts of Korba, Chattisgarh. J. Indian Soc. Remote Sens. 34, 415–421. https://doi.org/10.1007/BF02990926

Katakey, B.P., 2021. One Man Commission of Inquiry, Vol I. Guwahati.

Khan, I., Javed, A., 2012. Spatio-Temporal Land Cover Dynamics in Open Cast Coal Mine Area of Singrauli, M.P., India. J. Geogr. Inf. Syst. 04, 521–529. https://doi.org/10.4236/jgis.2012.46057

Kiran, S., Kumar, R., Gogoi, K., 2022. Land Use/Land Cover Dynamics During 2001 And 2021 Using Google Earth Engine and GIS in Ramagundam Coal Mining Area, A Part of Pranhita Godavari Valley, Southern India. J. Sci. Res. 66, 63–68. https://doi.org/10.37398/JSR.2022.660107

Kumar, M., Srivastava, M.K., Kishor, K., Singh, A.K., 2023. An Assessment of the Environmental Impact of Coal Mining through Acid Mine Drainage and Soil Degradation from Makum Coalfields, Upper Assam, India: A Case Study. J. Geol. Soc. India 99, 1113–1120. https://doi.org/10.1007/s12594-023-2437-3

Kutir, C., Agblorti, S.K.M., Campion, B.B., 2022. Migration and Estuarine Land Use/Land Cover (LULC) Change along Ghana's Coast. Reg. Stud. Mar. Sci. 54, 102488. https://doi.org/10.1016/j.rsma.2022.102488

Lin, B., Wang, Y., Wang, H., Xiao, W., 2021. Quantifying the Impacts of Coal Mining and Soil-Water Conservation on Runoff in a Typical Watershed on the Loess Plateau, China. Water 13, 3229. https://doi.org/10.3390/w13223229

Liu, Y., Liu, R., Chen, J., Wei, X., Qi, L., Zhao, L., 2024. A global annual fractional tree cover dataset during 2000–2021 generated from realigned MODIS seasonal data. Sci. Data 11, 832. https://doi.org/10.1038/s41597-024-03671-9

López-Bedoya, P.A., Bohada-Murillo, M., Ángel-Vallejo, M.C., Audino, L.D., Davis, A.L. V., Gurr, G., Noriega, J.A., 2022. Primary forest loss and degradation reduces biodiversity and ecosystem functioning: A global meta-analysis using dung beetles as an indicator taxon. J. Appl. Ecol. 59, 1572–1585. https://doi.org/10.1111/1365-2664.14167

Łowicki, D., 2008. Land use changes in Poland during transformation. Landsc. Urban Plan. 87, 279–288. https://doi.org/10.1016/j.landurbplan.2008.06.010

Mishra, A., Swamy, S.L., Thakur, T.K., Kumar, A., Pandey, M., 2022. Impact of coal mining on land use changes, deforestation, biomass, and C losses in Central India: Implications for offsetting CO 2 emissions. L. Degrad. Dev. 33, 3731–3747. https://doi.org/10.1002/ldr.4419

Mishra, M., Santos, C.A.G., Nascimento, T.V.M. do, Dash, M.K., Silva, R.M.D., Kar, D., Acharyya, T., 2022. Mining impacts on forest cover change in a tropical forest using remote sensing and spatial information from 2001-2019: A case study of Odisha (India). J. Environ. Manage. 302. https://doi.org/https://doi.org/10.1016/j.jenvman.2021.114067

Mishra, P.K., Rai, A., Rai, S.C., 2020. Land use and land cover change detection using geospatial techniques in the Sikkim Himalaya, India. Egypt. J. Remote Sens. Sp. Sci. 23, 133–143. https://doi.org/10.1016/j.ejrs.2019.02.001

Mohanty, B., Mohanty, P., Mahalik, G., 2020. Effect of Coal Mining on Vegetation of Talcher Area of Odisha, India. Int. J. Mod. Agric. 9, 325–331.

Nedd, R., Light, K., Owens, M., James, N., Johnson, E., Anandhi, A., 2021. A Synthesis of Land Use/Land Cover Studies: Definitions, Classification Systems, Meta-Studies, Challenges and Knowledge Gaps on a Global Landscape. Land 10, 994. https://doi.org/10.3390/land10090994

Niyonsenga, J., Sibomana, E., 2024. The Impact of Mining Activities on Land Use and Land Cover Change in Rwamagana District, the Case of Muhazi Sector, Rwanda. J. Agric. 8. https://doi.org/10.53819/81018102t2419

Okoduwa, A.K., Amaechi, C.F., Enuneku, A.A., 2025. Assessing Land Use/Land Cover and Predicting Future Scenarios in Kano Metropolis, Northern Nigeria. Jordan J. Earth Environ. Sci. 16, 267–275.

Pandey, P.C., Koutsias, N., Petropoulos, G.P., Srivastava, P.K., Ben Dor, E., 2021. Land use/land cover in view of earth observation: data sources, input dimensions, and classifiers—a review of the state of the art. Geocarto Int. 36, 957–988. https://doi.org/10.1080/10106049.2019.1629647

Patra, T., Duttaa, D., Kundu, A., Kumar, M., Hossain, S.S., Chattoraj, K.K., 2022. Evolution of Opencast Mines in the Raniganj Coalfield (India): An Assessment through Multi-temporal Satellite Data. J. Geol. Soc. India 98, 387–394. https://doi.org/10.1007/s12594-022-1990-5

Ranjan, A.K., Parida, B.R., 2019. Paddy acreage mapping and yield prediction using sentinel-based optical and SAR data in Sahibganj district, Jharkhand (India). Spat. Inf. Res. 27, 399–410. https://doi.org/10.1007/s41324-019-00246-4

Ranjan, A.K., Sahoo, D., Gorai, A.K., 2021. Quantitative assessment of landscape transformation due to coal mining activity using earth observation satellite data in Jharsuguda coal mining region, Odisha, India. Environ. Dev. Sustain. 23, 4484–4499. https://doi.org/10.1007/s10668-020-00784-0

Tamfuh, P.A., Musi, E.N., Fils, S.C.N., Ateh, K.I., Aye, A.B., Tata, E., Mamdem, L.E., Kenzong, B., Nono, G.D.K., Bitom, D., 2024. Mapping Land use/Land Cover Changes Caused by Mining Activities from 2018 to 2022 Using Sentinel-2 Imagery in Bétaré-Oya (East-Cameroon). J. Geosci. Geomatics 12, 12–23. https://doi.org/10.12691/jgg-12-1-3

Thakur, T.K., Dutta, J., Upadhyay, P., Patel, D.K., Thakur, A., Kumar, M., Kumar, A., 2022. Assessment of land degradation and restoration in coal mines of central India: A time series analysis. Ecol. Eng. 175, 106493. https://doi.org/10.1016/j.ecoleng.2021.106493

Trautwein, C., Pletterbauer, F., 2018. Land Use, in: Riverine Ecosystem Management. Springer International Publishing, Cham, pp. 241–252. https://doi.org/10.1007/978-3-319-73250-3_13

Uddin Siddiqui, A., Kumar Jain, M., 2022. Change analysis in land use land cover due to surface mining in Jharia coalfield through Landsat time series data. Mater. Today Proc. 49, 3462–3468. https://doi.org/10.1016/j.matpr.2021.04.277

Vieira, S.M., Kaymak, U., Sousa, J.M.C., 2010. Cohen's kappa coefficient as a performance measure for feature selection, in: International Conference on Fuzzy Systems. IEEE, pp. 1–8. https://doi.org/10.1109/FUZZY.2010.5584447

Yadav, S., Kumar, A., Raj, H., Bora, H.R., 2018. Lichen diversity in coal mining affected areas of Makum coalfield, Magherita, Assam. Trop. Plant Res. 5, 243–249. https://doi.org/10.22271/tpr.2018.v5.i2.031

JJEES

Jordan Journal of Earth and Environmental Sciences

JJEES (2026) 17 (3): 364-369
ISSN 1995-6681

An Integrated Multivariate Statistical Framework for Detecting Structural Climate Shifts in Saudi Arabia

Alshaikh A. Shokeralla*

Department of Mathematics, Al-Baha University, Al-Aqiq 65931, Saudi Arabia

Received on 23 June 2025, Accepted on 29 April 2026

Abstract

Understanding climate change dynamics in Saudi Arabia is vital given the region's acute exposure to rising temperatures, water scarcity, and ecosystem vulnerability. This study applies an integrated multivariate statistical framework to identify persistent climate patterns, abrupt regime transitions, and the temporal evolution of climatic states over 1950–2023, leveraging ERA5 reanalysis datasets. Our analytical approach integrates the non-parametric Mann–Kendall test and Sen's slope estimator for trend quantification, the Pettitt and Bai–Perron algorithms for breakpoint detection, and a combined PCA–EMD framework to uncover latent multivariate dynamics and non-linear oscillations.

The results reveal a significant warming trend with a major structural breakpoint in 1995, indicating a transition to a warmer climate regime. Relative humidity and precipitation show greater variability, with potential shifts around 1970. PCA clearly separates thermal and hydrological signals, while STL and EMD reveal cyclic patterns that are not apparent in traditional analyses. These findings highlight the importance of incorporating climate regime shift detection into national adaptation strategies under Saudi Vision 2030, particularly water security, agricultural resilience, and public health planning in arid regions.

Keywords: *Climate change; ERA5; EMD; PCA; Multivariate Statistical; Saudi Arabia; STL; Structural break; Trend analysis*

1. Introduction

The phenomenon of climate change has been shown to pose escalating risks to arid and semi-arid regions. Saudi Arabia, in particular, has been identified as being among the most vulnerable of these regions. This vulnerability is attributed to a combination of factors, including extreme heat, limited water resources, and rapid socio-economic development. [1, 2] In recent decades, rising temperatures, erratic rainfall, and declining humidity have had deleterious effects on water supplies, agriculture, and human health [3–6]. This assertion is corroborated by findings from regional assessments by the IPCC AR6 [7] and WMO [8], which substantiate increased climate variability and exposure to extremes throughout the Arabian Peninsula.

To characterize climate variability, researchers commonly apply the Mann–Kendall test

In conjunction with Sen's slope estimation method, a robust, nonparametric trend-detection approach is employed. [9–11]. These univariate approaches are often complemented by multivariate and decomposition techniques, such as for seasonal trend decomposition, there is the Loess (STL) method [12], the Empirical Mode Decomposition (EMD) method [13], and the Principal Component Analysis (PCA) method [14,15]—which collectively reveal non-linear dynamics, seasonal cycles, and co-variability among climate variables. [14,15]—help isolate non-linear patterns, seasonal signals, and multivariate interactions. Structural break. The identification of abrupt regime shifts is critical for understanding non-stationary climate behavior. Such shifts are identified by detection techniques, including Pettitt and Bai–Perron methods [16–18].

Despite these advances, the majority of studies in Saudi Arabia remain univariate or short-term, lacking an integrated framework that simultaneously addresses trends, breakpoints, and multivariate dynamics over multi-decadal scales [5,19]. This discrepancy impedes the integration of evidence-based practices. policy formulation under national strategies like Saudi Vision 2030.

To address this, we present a comprehensive analysis of the Saudi climate from 1950 to 2023, using ERA5 data, integrating trend detection, structural change diagnostics, and multivariate decomposition. Our goal is to reveal hidden patterns, confirm regime shifts, and provide actionable insights for climate adaptation in one of the world's most sensitive arid regions.

2. Literature Review

Trend detection via MK and Sen's slope is well-established for non-normal climate data [1,2], with applications confirming long-term warming across the Middle East [6,7]. However, linear trends often miss abrupt shifts, necessitating structural break methods, like Pettitt's test and Bai–Perron segmentation [9–11]. Rodionov's regime shift detection further captures sequential transitions in non-linear systems [18,20], though its use in the Arabian Peninsula remains limited [20,21].

* Corresponding author e-mail: sshokeralla@gmail.com

Multivariate approaches, such as PCA reduce dimensionality while revealing dominant climate modes [22,23]. Decomposition tools (STL, EMD) separate trends, seasonality, and noise, enabling deeper insight into intrinsic variability [24,25]. Yet, the combined application of these methods— particularly alongside breakpoint detection—is rare in Saudi climate studies [26].

This study bridges that gap by fusing these techniques into a unified framework, offering a holistic view of Saudi Arabia's evolving climate structure over seven decades.

3. Methodology

3.1 Data Description

We used ERA5 reanalysis data (1950–2023) for near-surface temperature (TAS), relative humidity (HURS), and total precipitation (PR). While ERA5 offers high spatiotemporal resolution, uncertainties in arid regions—particularly pre-1979—arise from sparse observational constraints and model smoothing [27]. Precipitation estimates may be less reliable at local scales, warranting cautious interpretation.

3.2 Study Area

Saudi Arabia (16°–32°N, 34°–56°E) spans diverse climatic zones: hyper-arid deserts (central), humid coastal zones (Red Sea), and mountainous highlands (Asir). This heterogeneity increases climate sensitivity and requires regionally nuanced analysis.

Figure 1. Study Area Map of Saudi Arabia (1950–2023)

The map shows the main cities (Riyadh, Jeddah, and Asir) and the major climatic zones (arid, coastal, and mountainous). It provides a geographic reference for the subsequent multivariate statistical analysis of structural climate shifts. The base map and climate data are sourced from the Copernicus ERA5 Reanalysis (C3S, 2023) [28].

3.3 Trend Detection

To quantify long-term changes in Saudi Arabia's climate, we applied the Mann–Kendall non-parametric trend test, which is robust to non-normality and outliers commonly found in climatic time series [9,10]. The statistical significance of each trend was evaluated at the 5% level ($p < 0.05$). Concurrently, the magnitude of temporal trends was quantified using Sen's slope estimator. This estimator provides a distribution-free estimate of the median annual rate of change. This estimate offers a physically interpretable metric for policy-relevant assessment [16].

3.4 Principal Component Analysis (PCA)

"Given the strong interdependence among temperature, humidity, and precipitation, we employed Principal Component Analysis (PCA) on standardized annual anomalies to isolate the dominant orthogonal modes of climate co-variability [14,29]." Components were retained based on the Kaiser criterion (eigenvalue >1) and scree plot inspection

- PCA was conducted on the standardized matrix X of variables:

$$Z = XW \tag{1}$$

W is the eigenvector matrix, and Z is the projection onto principal components.

- Eigenvalues λi represent the variance explained by each component:

$$\frac{\lambda_i}{\sum_{j=1}^{p} \lambda_j} \tag{2}$$

- Scree plots and the Kaiser criterion (λ>1). Following standard practice, we retained only components that met the Kaiser criterion ($\lambda > 1$) and exhibited a clear elbow in the scree plot, ensuring a parsimonious yet informative representation of climate variability [13].

3.5 Decomposition and Regime Clustering

STL decomposed the series into trend, seasonal, and residual components. EMD generated Intrinsic

Mode Functions (IMFs) to capture multi-scale oscillations

$$X_t = T_t + S_t + R_t \tag{3}$$

Decomposition Components:

The time series is partitioned into three additive components:

Where:

T_t the long-term trend, capturing secular changes.

S_t the seasonal cycle, representing periodic fluctuations.

R_t the residual, reflecting unexplained noise or extreme events [30].

Intrinsic Mode Functions via EMD:

To capture non-linear and non-stationary oscillations, we applied Empirical Mode Decomposition (EMD) is a technique that adaptively decomposes the signal into a set of Intrinsic Mode Functions (IMFs). —each representing a distinct temporal scale of variability.

$$x_t = \sum_{i=1}^{n} IMF_i(t) + r(t) \tag{4}$$

K-means clustering was applied to the PCA scores to group years into climate regimes. The clustering minimizes: [31]

$$\mathbf{argmin}_C \quad \sum_{i=1}^{k} \sum_{x \in C_i} \|x - \mu_i\|^2 \tag{5}$$

Where is the centroid of the cluster C_i.

3.6 Operational Framework and p-value Interpretation

All tests used p-values to assess significance:

We considered results statistically significant when $p < 0.05$, implying rejection of the null hypothesis of no trend or no breakpoint; otherwise, the null hypothesis was retained.

4. Results

4.1 Trend Analysis Results

To evaluate long-term directional changes, we implemented the non-parametric Mann–Kendall test alongside Sen's slope estimator—a robust combination for trend detection in non-normally distributed climate data — to assess monotonic trends in temperature, humidity, and precipitation from 1950 to 2023. The results of the trend detection are summarized in Table 1.

Table 1. Trend Detection Results

Variable	Kendall Tau	p-value (Trend)	Slope
TAS	0.721914	1.018778e-19	0.043255
HURS	-0.101500	2.009930e-01	-0.011263
PR	-0.141059	7.539951e-02	-0.197888

Temperature showed a significant upward trend ($\tau = 0.722$, $p < 0.001$, slope = +0.043°C/year). Humidity and precipitation exhibited non-significant declines ($p > 0.05$).

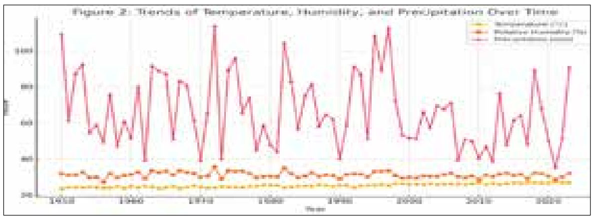

Figure 2. Trends of Temperature, Humidity, and Precipitation Over Time

Separate time series plots for (A) TAS, (B) HURS, and (C) PR (1950–2023), each with trend line and fixed axis units

4.2 Structural Break Detection

The analysis revealed significant changes in temperature and humidity between 1980 and 1995. These breaks mark shifts in climate patterns that could correspond to large-scale atmospheric events such as El Niño, or regional environmental changes

CUSUM and Pettitt's tests were used to identify structural shifts in the climate data. Significant breakpoints were detected in temperature and humidity, while precipitation showed no change in variance across time.

Table 2. Structural Change Detection Results

Variable	Break Year (Pettitt)	p-value
TAS	1995	<0.001
HURS	1970	0.191
PR	—	0.117

4.3 Spatial Climate Patterns (Moved from Section 5.1 per R2)

Regional analysis reveals contrasting trends:

Riyadh shows the strongest warming and drying, likely influenced by urbanization.

Table 3. Spatial Climate Summary (1950–2023)

Region	Latitude / Longitude	Mean TAS (°C)	TAS Trend (°C/decade)	Mean PR (mm)	PR Trend (mm/yr)
Riyadh	24.7°N, 46.7°E	27.1	0.35	11	-2.1
Jeddah	21.5°N, 39.2°E	28.3	0.28	53	0.8
Asir	18.2°N, 42.5°E	23.9	0.18	29	1.5

4.4 Principal Component Analysis (PCA)

Principal component analysis (PCA) was employed in this study to distill the multivariate climate record into its dominant modes of variability, focusing on the interplay between temperature, humidity, and precipitation

Table 4. PCA Loadings and Variance

Component	TAS	HURS	PR	Explained Variance
PC1	-0.437	0.629	0.642	69.50%
PC2	-0.897	-0.353	-0.264	24.90%

This table lists the loadings of the first two principal components for each climate variable. It provides insight into how much each variable contributes to the overall climate pattern. For example:

- **PC1:** 0.72 for temperature, -0.59 for humidity, and 0.34 for precipitation, indicating that temperature and humidity contribute strongly to the first principal component.
- **PC2:** -0.50 for temperature, 0.82 for humidity, and -0.29 for precipitation, suggesting that PC2 mainly represents a pattern of humidity variations.

"The first principal component (PC1) accounts for nearly 70% of the total variance, reflecting a dominant mode that couples moisture-related variables (HURS and PR) in opposition to temperature (TAS)."

This figure displays the eigenvalues of the first several principal components. The scree plot helps determine the number of components to retain for further analysis. It shows a clear elbow after the second component, suggesting that the first two components explain the preponderance of the observed variability in the data, which is attributable to the aforementioned factors.

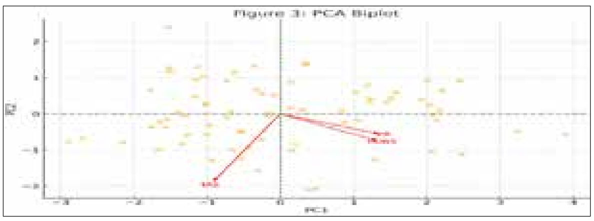

Figure 3. PCA Biplot

The biplot illustrates the present study seeks to examine the relationship between the variables of temperature, humidity, and precipitation) and the principal components. The vectors show how the variables correlate with each principal component, with temperature and humidity closely aligned along the first component.

4.5 Decomposition of Climate Variables

While trend analysis highlights long-term changes, it is also crucial to address extreme climate events, such as heatwaves, droughts, and intense rainfall, which have significant environmental impacts. Though not always captured in long-term trends, these events are key. It is imperative to comprehend the dynamics of climate variability and the associated risks. The increasing frequency of extreme heat and fluctuating precipitation patterns, leading to floods or droughts, exacerbates pressures on water resources and agriculture. The decomposition of temperature, humidity, and precipitation data reveals that while trends offer an overall perspective on climate change, the residuals unveil the sporadic nature of these extremes. It is imperative that future research concentrate on extreme event analysis using extreme value theory. Climate risks are better understood, and targeted adaptation strategies are developed.

We decomposed each climate variable using STL to extract trend, seasonal, and residual components, with results displayed in Figure 4

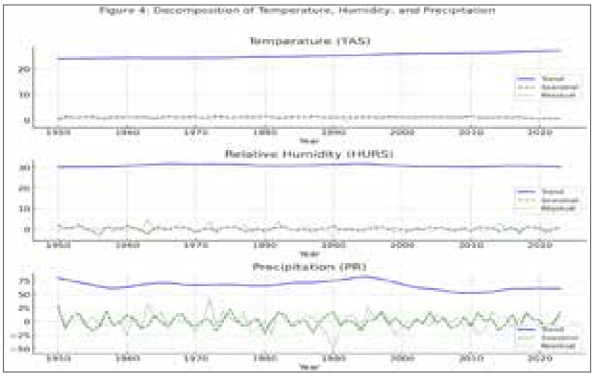

Figure 4. Decomposition of Temperature, Precipitation, and Humidity

This set of plots illustrates each variable's trend, seasonal, and residual components. In addition to the general trends, extreme climatic events such as heat waves and sudden rainfall have become more prevalent, especially during the summer. These events significantly exacerbate regional water scarcity and require deeper consideration for effective resource management.

4.5.1 Extreme Climate Events Analysis

While long-term trends reveal gradual climate shifts, extreme events, such as heat waves, pose immediate threats to ecosystems, health, and infrastructure. We used the Generalized Extreme Value (GEV) distribution to quantify these events, analyzing annual maxima of monthly temperature data (tas) from 1950 to 2023.

GEV Fit and Return Periods

The GEV model was fitted to the annual maximum temperatures to estimate return levels for rare, high-temperature events. The analysis revealed that:

- A 10-year return level corresponds to approximately 35.72 °C

- A 50-year return level is around 36.58 °C.

These thresholds indicate extreme heat events that are statistically expected once every 10 or 50 years, respectively.

Heatwave Frequency Indicator

A heatwave was defined as any month in which the temperature exceeded 35 °C. Using this definition, we found:

- A total of 38 heatwave months occurred from 1950 to 2023.

- A noticeable increase in frequency over the last two decades, particularly in 2010 and 2016, each of which recorded two extreme months, both years aligned with intense El Niño phases.

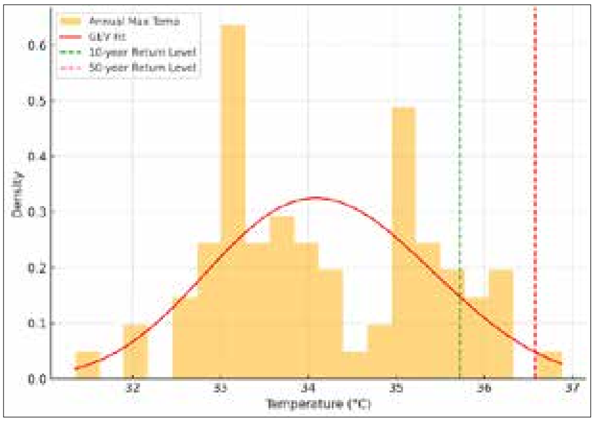

Figure 5. GEV Distribution with 10- and 50-Year Return Levels

Figure 6. Temporal Trend in Heatwave Months (>35°C)

GEV analysis indicates a 10-year return level of 35.7 °C for extreme heat. Heatwave months (>35°C) increased after 2000, peaking during El Niño years (2010, 2016). STL and EMD revealed low-frequency oscillations and residual extremes that trends alone did not capture.

4.6 Statistical Interpretation

The results indicate clear long-term temperature trends, with a consistent upward shift, suggesting global warming in the region. Humidity, however, slightly declined over time, possibly due to regional changes in atmospheric moisture content. On the other hand, precipitation did not exhibit a clear trend, decadal timescales.

The structural breaks detected in temperature and humidity suggest that climate regimes in Saudi Arabia shifted around 1980 and 1995, respectively. These shifts could be linked to global climate events such as the El Niño Southern Oscillation (ENSO) or regional phenomena such as the Arabian Peninsula monsoon.

PCA confirmed that temperature and humidity are the primary drivers of climate variability in the region, while precipitation plays a secondary role. The decomposition of climate variables further supports these findings, with the trend components showing clear changes in temperature over time, and the seasonal components highlighting the strong influence of seasonality on humidity.

Synthesis

- The analysis confirms **robust warming** in temperature trends, both statistically and structurally.
- **Moisture variables (HURS, PR)** behave differently: they are less stable but interrelated, possibly influenced by short-term climatic events and hydrological cycles.
- The **multivariate structure** (via PCA) reveals **two principal axes** of variability: temperature and moisture dynamics.

This multivariate representation supports the hypothesis of a regime shift in the mid-1990s.

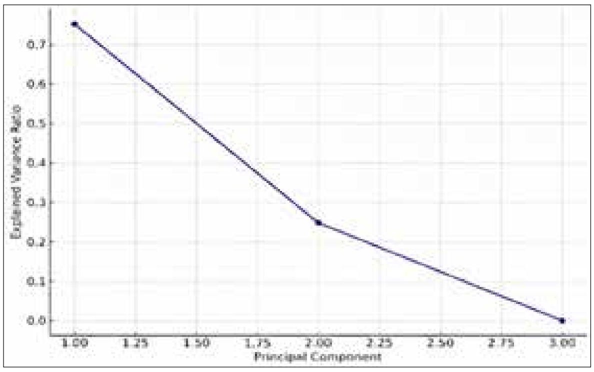

Figure 7. Scree Plot for PCA

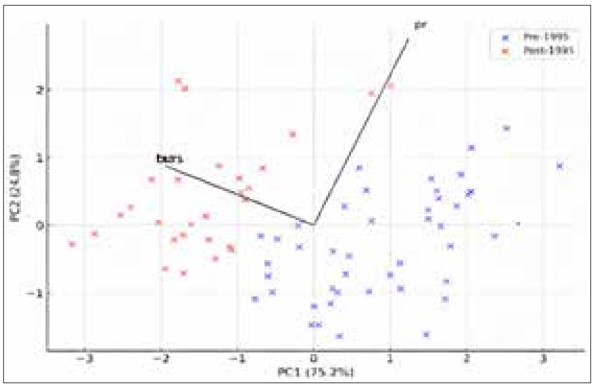

Figure 8. PCA Biplot

5. Discussion

This study confirms a robust warming trend in Saudi Arabia and a statistically significant regime shift in 1995—consistent with regional Gulf studies [e.g., Almazroui et al., 2020; Iqbal & Saleem, 2023]. The post-1995 clustering in PCA (Fig. 8) reinforces this transition.

Unlike global averages, precipitation shows no long-term trend, highlighting the region's high interannual variability—a feature also noted in studies from Kuwait and the UAE [Ahmad & Shahid, 2022].

The inverse TAS–HURS relationship (Fig. 8) suggests intensifying aridity, with implications for

evapotranspiration and soil moisture.

Critically, these findings align with Saudi Vision 2030's sustainability goals. The 1995 shift

coincides with accelerated urbanization and water demand, urging integration of climate

breakpoints into:

- Water security: Prioritize non-conventional sources (desalination, reuse).
- Agriculture: Shift to drought-resilient crops and precision irrigation.
- Public health: Implement heat action plans in cities like Riyadh.

The spatial contrasts (Table 3) further demand region-specific policies—e.g., flood management

in Asir vs. drought resilience in central regions.

The PCA biplot (Fig. 6) visualizes how climate variables interact and change over time... Years post-1995 (highlighted in red) cluster separately from earlier years, suggesting a structural shift

6. Conclusion and Recommendations

This study demonstrates that Saudi Arabia's climate underwent a structural shift toward warmer, drier conditions after 1995, with significant implications for water, agriculture, and health. The integrated framework successfully reveals hidden dynamics beyond conventional trend analysis.

We recommend that policymakers:

- Incorporate **regime shift detection** into national climate risk assessments.
- Strengthen **real-time monitoring** of hydrological stress indicators.
- Adopt **adaptive water management** strategies under Vision 2030.
- Develop **urban heat resilience plans**, especially for inland cities

Conflict of Interest

The author affirms that there are no financial, personal, or professional interests that could influence the work presented in this manuscript.

Funding

The present study was conducted with no external financial support.

Author Contributions

Alshaikh A. Shokeralla conceptualized the study, conducted all analyses, interpreted results, and wrote the manuscript

References

Almazroui, M. (2020). Temperature changes over the CORDEX-MENA domain in the 21st century using CMIP5 data. Atmospheric Research, 233, 104712. https://doi.org/10.1016/j.atmosres.2019.104712

Alghamdi, A. S., & Harrington, J. A. (2022). Climate change impacts in arid Saudi Arabia: A multi-decadal analysis. Climate Risk Management, 35, 100420. https://doi.org/10.1016/j.crm.2022.100420

IPCC. (2021). Climate Change 2021: The Physical Science Basis (AR6). Cambridge University Press. https://www.ipcc.ch/report/ar6/wg1/

World Meteorological Organization (WMO). (2023). State of the Global Climate 2022. https://library.wmo.int

Zhang, X., Zwiers, F. W., & Hegerl, G. (2020). Understanding and attributing climate change. Nature Climate Change, 10, 387–395. https://doi.org/10.1038/s41558-020-0742-1

AlSarmi, S., & Washington, R. (2016). Historical and future temperature and rainfall variability in Saudi Arabia. International Journal of Climatology, 36(4), 1573–1588. https://doi.org/10.1002/joc.4443

Gocic, M., & Trajkovic, S. (2016). Analysis of changes in meteorological variables using Mann–Kendall and Sen's slope estimator. Hydrological Sciences Journal, 61(2), 294–306. https://doi.org/10.1080/02626667.2014.967248

Fatima, A., & Wahab, M. A. (2022). Assessment of climate trends and variability in Saudi Arabia using ERA5 data. Arabian Journal of Geosciences, 15(9), 1–15. https://doi.org/10.1007/s12517-022-09918-6

Alghamdi, M., & Alwabel, M. (2021). Projected changes in temperature and precipitation across Saudi Arabia: CMIP6 ensemble. Sustainability, 13(14), 7719. https://doi.org/10.3390/su13147719

Hu, Z., & Si, B. C. (2020). Mann–Kendall trend test with consideration of pre-whitening and autocorrelation. Environmental Modelling & Software, 124, 104588. https://doi.org/10.1016/j.envsoft.2019.104588

Cleveland, R. B., Cleveland, W. S., McRae, J. E., & Terpenning, I. (1990). STL: A seasonal-trend decomposition procedure based on loess. Journal of Official Statistics, 6(1), 3–73.

Jolliffe, I. T., & Cadima, J. (2016). Principal component analysis: A review and recent developments. Philosophical Transactions of the Royal Society A, 379(2191), 20150202. https://doi.org/10.1098/rsta.2015.0202

Bai, J., & Perron, P. (2003). Computation and analysis of multiple structural change models. Journal of Applied Econometrics, 18(1), 1–22. https://doi.org/10.1002/jae.659

Ahmad, S., & Shahid, S. (2022). Changing rainfall and drought patterns in the Arabian Peninsula. Climatic Change, 170(1), 1–16. https://doi.org/10.1007/s10584-021-03259-4

Kendall, M. G. (1975). Rank correlation methods (4th ed.). Charles Griffin.

Sen, P. K. (1968). Estimates of the regression coefficient based on Kendall's tau. Journal of the American Statistical Association, 63(324), 1379–1389. https://doi.org/10.1080/01621459.1968.10480934

Kuglitsch, F. G., & Xoplaki, E. (2017). Recent and future trends of extreme temperatures and droughts in the Middle East. Climatic Change, 144, 137–151. https://doi.org/10.1007/s10584-017-2026-y

Iqbal, M., & Saleem, M. (2023). Trend and change-point detection in Saudi climate. Climate Dynamics, 60(3), 891–909. https://doi.org/10.1007/s00382-022-06321-2

NOAA. (2022). Global Annual Temperature Rankings. https://www.ncei.noaa.gov

Al-Juaidi, A., & Zubair, M. (2021). Spatiotemporal trends in precipitation in the western region of Saudi Arabia. Arabian Journal of Geosciences, 14(17), 1795. https://doi.org/10.1007/s12517-021-07722-7

Liu, M., & Xu, C. Y. (2018). Trend analysis in hydrology: A review. Stochastic Environmental Research and Risk Assessment, 32(9), 2637–2651. https://doi.org/10.1007/s00477-018-1548-7

Zare, M., & Ghaffari, G. (2020). Drought trend detection using Mann–Kendall and SPI in the Middle East. Environmental Earth Sciences, 79(6), 1–11.

ERA5 Climate Data. (2023). Copernicus Climate Change Service (C3S). https://cds.climate.copernicus.eu

WMO. (2022). Climate Indicators and Impacts. https://library.wmo.int

Li, Y., & Liu, H. (2017). PCA-based climate variability analysis. Environmental Modelling & Software, 93, 193–203. https://doi.org/10.1016/j.envsoft.2017.03.013

Abubakar, M. B., & Khan, S. (2020). Analysis of climate variability using PCA and trend tests. Journal of Environmental Management, 276, 111217.

Hamed, K. H. (2008). Trend detection in hydrologic data: The Mann–Kendall trend test under the scaling hypothesis. Journal of Hydrology, 349(3–4), 350–363.

El-Nesr, M. N., Abu-Zreig, M. M., & Alazba, A. A. (2010). Temperature trends and distribution in the Arabian Peninsula.

Alshamsi, N., & Badr, H. S. (2023). Climate change perception and policy in the GCC: A case from Saudi Arabia. Sustainability, 15(1), 423. https://doi.org/10.3390/su15010423

Alghamdi, A. S., & Hegazy, I. R. (2018). Long-term analysis of climate variability over Saudi Arabia using high-resolution gridded data. Theoretical and Applied Climatology, 134(1–2), 215–230.

Saudi Meteorology & Environment Protection Agency (MEPA). (2021). National Climate Assessment Report (in Arabic).

JJEES

JJEES (2026) 17 (3): 370-383
ISSN 1995-6681

Jordan Journal of Earth and Environmental Sciences

Groundwater (Borehole water) Pollution by Heavy Metals and Physicochemical Parameters in and around a Major Tertiary Institution in Akoka Area of Lagos-State, Nigeria.

Ojiodu, Chukwuwuba Chekwube[1*], Eruola, Adeyinka Olubunmi[2], Olumayede, Emmanuel Gbenga[3], Moses, Donatus, Ugochukwu[1], Ikegwu, Emmanuel Mmaduabuchi[4]

[1]College Central Research Laboratory, Yaba College of Technology, Yaba - Lagos, Nigeria.
[2]Department of Chemical Sciences, Yaba College of Technology, Yaba - Lagos, Nigeria.
[3]Department of Industrial Chemistry, Federal University, Oye, Ekiti, Nigeria.
[4]Department of Statistics, Yaba College of Technology, Yaba - Lagos, Nigeria.

Received on 23 June 2025, Accepted on 29 April 2026

Abstract

This study assessed the quality of borehole water in and around a tertiary institution in Akoka, Lagos State, Nigeria, by analyzing Heavy metals and Physicochemical parameters. Forty (40) Borehole water samples were collected from ten locations per month between June and November, 2023. Samples were digested with HNO_3 and analyzed using Atomic Absorption Spectrometry (AAS). Results showed that Lead (Pb) (1.22 - 3.44 mg/L) and Cadmium (Cd) (0.019 - 0.023 mg/L) exceeded WHO and NIS limits, while Zinc (Zn) (0.1015 - 0.1489 mg/L) remained within safe levels. Copper (Cu) and Nickel (Ni) were not detected. Pb (94%) was the most abundant metal, and Zn (4.98%) was the least. Kosoko Drive (KD) had the highest contamination, while Onos Hostel(OH) had the lowest. Physicochemical parameters - pH (4.50 - 6.83), temperature (29.2 - 30.1°C), total dissolved solids (106.2 - 436.7 mg/L), electrical conductivity (207 - 876 µS/cm), dissolved oxygen (4.18 - 5.09 mg/L), biological oxygen demand (0.38 - 1.10 mg/L), and chemical oxygen demand (2.48 - 5.24 mg/L) met WHO and NIS standards, although the water was acidic. Correlation analysis revealed a positive relationship between Heavy metals and Physicochemical parameters. Pollution indices (HPI, PI, MI) confirmed significant contamination. Therefore, the borehole water is polluted and unsafe for drinking or domestic use without adequate treatment.

Keywords: *Contamination, Pollution, Physicochemical, Heavy Metals, Concentration, Borehole.*

1. Introduction

The failure of Federal, State, and Local Governments, especially the Lagos State Water Corporation (LWC), to provide adequate water has forced Akoka residents in Lagos State to rely on groundwater (borehole water). Water, a transparent, tasteless, odorless, and colorless substance, is essential for life and socio-economic development, supporting food production, sanitation, and ecosystems (Talabi andKayode, 2021). Water sources are classified as -groundwater, such as boreholes, wells and surface water, including streams and reservoirs (Nnaji et al., 2016). Water from these sources serve domestic, agricultural, and industrial needs, each requiring specific quality standards to ensure safety and suitability (Saheed et al., 2021).

Akoka, located in Lagos Mainland Local Government Area, is a culturally diverse community with ethnic groups such as the Yoruba, Igbo, and Hausa, reflecting Nigeria's multicultural identity (Adeyemi, 2017). Bordered by Bariga, Shomolu, and Gbagada, it is known as a hub of academic excellence in Lagos State. The presence of a major university has spurred the growth of small and medium - sized businesses like cybercafés, shops, and transport services, boosting the local economy (Adeniran, 2019).

Groundwater in Akoka is primarily sourced from Lagos Lagoon and is part of the coastal aquifer system, a vital groundwater reserve in the region (Adeyemi, 2017). Boreholes typically access deeper confined aquifers, known for better water quality than shallow ones (wells). Due to the Lagos State Water Corporation's (LWC) inability to meet growing demand, residents increasingly rely on borehole water as a more dependable alternative to the often erratic municipal supply (Lagos State Ministry of Water Resources, 2020; University of Lagos, 2018).

Groundwater contamination by heavy metals, such as Copper (Cu), Zinc (Zn), Nickel (Ni), Cadmium (Cd), and Lead (Pb), along with other Physicochemical parameters, has become a significant environmental and public health concern in and around a tertiary institution in the Akoka area of Lagos State, Southwestern Nigeria. Even at low concentrations, long-term exposure to these metals poses serious health risks (Krishna et al., 2009). These contaminants originate from both natural and anthropogenic sources, including industrial activities, mining, agriculture, and improper waste disposal (Nawab et al., 2017; Bharati and Bhatnagar, 2018). Borehole water, polluted with these metals, may lead to serious health sicknesses, such as cancer, hypertension, gastrointestinal bleeding, neurological disorders, reproductive issues, and lung

* Corresponding author e-mail: ojioducc@yahoo.com

diseases (Lu et al., 2015; Nkpa et al., 2018). Lead is harmful, especially to children, as it can cause developmental delays, learning difficulties, and behavioral issues even at low levels of exposure (WHO, 2017). Adults, exposed to lead over time, may suffer from kidney damage, respiratory and skin problems, hypertension, and cognitive decline (Khan and Hanjra, 2009). Nickel, commonly found in industrial areas, especially in stainless steel and battery production, is a known carcinogen and often enters groundwater through industrial waste or plumbing. Copper contamination arises from corroded pipes, agricultural fungicides, and industrial discharges, leading to gastrointestinal problems in the short term and liver and kidney damage in the long term (Schaeffer and Frantzen, 2001). Zinc and Cadmium, mainly from mining, smelting, and battery production, also pollute groundwater and can cause kidney damage (WHO, 2017). Various laboratory methods are used to detect and quantify these metals in groundwater, they include inductively coupled plasma mass spectrometry (ICP-MS), flame atomic absorption spectrometry (FAAS), graphite furnace atomic absorption spectrophotometry (AAS-GF), and direct extraction/air acetylene flame methods (Faisal et al., 2014; Rahmanian et al., 2015). In addition to metal concentrations, physicochemical parameters, such as pH, temperature, turbidity, electrical conductivity (EC), total suspended solids (TSS), total dissolved solids (TDS), biological oxygen demand (BOD), chemical oxygen demand (COD), and dissolved oxygen (DO) are essential in assessing groundwater quality (WHO, 2011; Edwin et al., 2015). Deviations from WHO standards suggest pollution or environmental imbalance. For example, abnormal pH levels may signal acidic or alkaline contamination, while high EC and TDS indicate an excess of dissolved salts or pollutants. High levels of BOD and COD point out to organic or chemical contamination that could threaten aquatic life and public health (Tchounwou et al., 2012; Nriagu and Pacyna, 1988).

While numerous studies have assessed Heavy metals and Physicochemical parameters in groundwater across Lagos State and other areas of the world (Ezeribe et al., 2012; Behailu et al., 2017; Adefemi and Awokunmi, 2010; Shigut et al., 2017; Popoola et al., 2019), limited literature exists specifically in the Akoka area, with no literature particularly in and around a major tertiary institution located there (Adeniran, 2019; Olawole, 2015). Akoka was selected for this study due to its access to academic resources (Adeyemi and Ayodele, 2018), a diverse student population (Okunade and Olamide, 2017), a multicultural environment (Afolayan and Olumide, 2020), opportunities for collaboration (Anibueze, 2020; Oloyede and Abiola, 2022), and the presence of technological innovation (Abiodun and Madu, 2020). The influence of the institution on local developments (Uche and Bakare, 2021) also makes it a suitable case study. This research aims to assess the levels of heavy metals-Copper (Cu), Zinc (Zn), Nickel (Ni), Cadmium (Cd), Lead (Pb), and physicochemical parameters in borehole water and determine its safety for human consumption and domestic use without prior treatment.

2. Materials and Methods:

2.1 Description of Study Area/ Sampling Locations

This study was conducted in and around a tertiary institution in Akoka Area of Lagos State, Southwestern Nigeria. (N 6º 30' 00" and E 3º 23' 00"E - N 6º 31' 30" and E 3° 24' 30"). The area is located in the center of Lagos metropolis and is low-lying with variations in terrain relief, which makes it susceptible to flooding during rainfall. The study area includes Chapel (CH), Makama hostel (MAH), Moremi hostel (MH), Eni-Njoku hostel (EH), human resource (HR), Onos hostel (OH), Kosoko drive (KD), Anglican church (AC), Omitogun Onike (OO), and Mountain of Fire Ministry Onike (MFO).

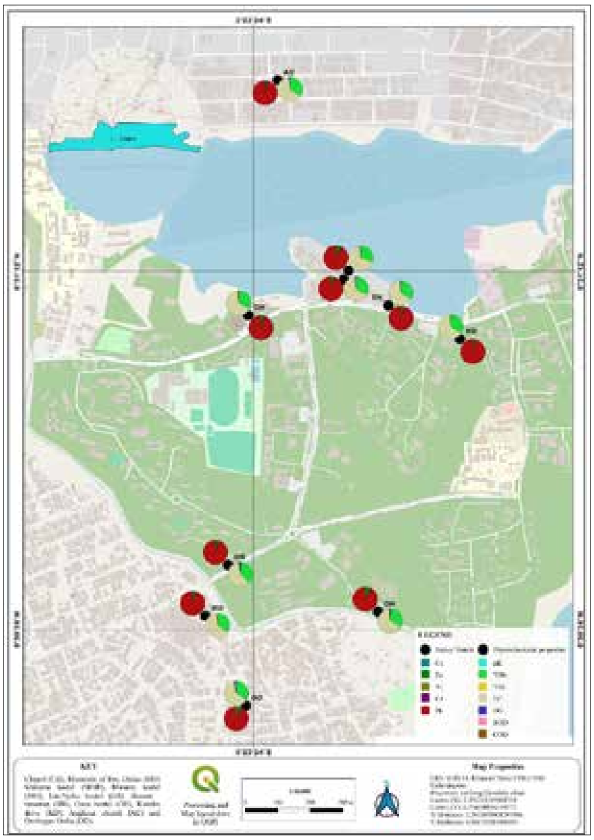

Figure 1. GIS Map showing the Sites and Concentrations of Heavy metals and Physicochemical parameters in the Study Area.

2.2 Selection of Sampling Sites/ Locations

Ten (10) Sampling sites were carefully chosen based on anthropogenic activities that may impact on the water quality in and around a tertiary institution in Akoka Area of Lagos - State, Southwestern-Nigeria. A Global Positioning System (GPS) device was used to record the coordinates for each sampling site.(GPS 76S Garmin)).

2.3 Sampling and Sample Collection

Ten borehole water Samples were collected in and around a tertiary institution in Akoka Area of Lagos-State, Southwesternn - Nigeria. Sampling was carried out for six months (June - November, 2023) and the samples were collected four times per month. The borehole water samples were collected with the aid of plastic bottles that has been previously washed and rinsed thoroughly with distilled water and suspended at one end to dry. The sample containers were first washed three times with each water sample before collection and the containers were tightly covered and labelled with appropriate identification codes. After collection, the samples were transported in an ice chest to the laboratory and analyzed for Heavy metals concentration (Cu, Zn, Ni, Cd, and Pb) and physicochemical parameters (pH, T0C, TDS, TSS, EC, DO, BOD, and COD).

2.4 Laboratory Analysis

All chemicals and reagents (Tetraoxosulphate (vi) acid (H2SO4), Trioxonitrate (v) acid (HNO3), Hydrochloric acid (HCl), Mercuric sulphate (HgSO4), Potassium dichromate (K2Cr2O7), Distilled water, Ferroin indicator, Ferrous ammonium sulphate (0.25 M FAS), Ethanol, Hydrogen peroxide) used for the laboratory analysis were of analytical grade and purchased from Lazco Scientific in Lagos, Lagos - State. Nigeria. Laboratory analysis were conducted inside the Analytical Chemistry Laboratory of the College Central Research Laboratory,Yaba College of Technology, Yaba - Lagos, Nigeria.

2.4.1 Digestion of Water Samples for Heavy metals Analysis

Borehole water samples were thoroughly shaken, and 100 mL of each was transferred to a 250 mL Pyrex beaker. Ten milliliters of concentrated HNO_3 were added, and the solution was gently heated and evaporated to about 20 mL. Then, 5 mL of concentrated HNO_3 and 5 mL of H_2O_2 were added, and the beaker was covered with a watch glass. The mixture was further heated until white fumes evolved and a clear solution formed. After cooling to room temperature, distilled water was added, and the solution was filtered using Whatman paper. The filtrate was transferred into a 100 mL volumetric flask, diluted to the mark with distilled water, mixed well, and stored in polypropylene bottles for analysis. Heavy metals (Cu, Zn, Ni, Cd, and Pb) were analyzed using an Agilent 240AA Atomic Absorption Spectrophotometer. All samples, including blanks and standards, were treated similarly. Triplicate analyses were performed for accuracy and precision (APHA, 2017; AOAC, 2000; Ajiwe and Eboagu, 2021).

2.5 Analysis of Physicochemical Parameters

2.5.1 Procedure for the Measurement of Temperatute, pH and Electrical Conductivity (EC)

The temperature, pH, and electrical conductivity of the water samples were determined by collecting 50 mL of each sample into a 100 mL beaker. The instrument used was an Adwa (AD 8000) pH/Conductivity/Temperature meter. The meter was inserted into the beaker, and readings were recorded. Electrical conductivity was expressed in µS/cm according to the machine's manual instructions. The meter was standardized using deionized water by inserting the electrodes into it. The water samples were analyzed for conductivity by immersing the probe in the beaker containing each sample, and the readings were taken (APHA, 2017; U.S. EPA, 2009; Baird et al., 2017; Perpetual et al., 2022).

2.5.2 Procedure for the Measurement of Dissolved (DO) and Biological Oxygen Demand(BOD)

The collected borehole water samples were tied in a black nylon immediately after collection to prevent light from penetrating into it and it was transported to the laboratory. Then, the initial dissolved oxygen (i.e. day zero (0) was measured using a portable dissolved oxygen meter (DO METER) and the values were recorded. Thereafter, the samples were incubated for five days in a dark cupboard, and date and time of incubation were noted. After incubation, the final dissolved oxygen (i.e. the quantity of oxygen used by the microbes within the five days) was measured using the same dissolved oxygen meter (DO METER) and the values were recorded. (APHA, 2017; U.S. EPA, 1993; Aliyu et al., 2018).

The Biological Oxygen Demand (BOD) were calculated, thus:

BOD (Mg/L) for day 5 = Final DO5 - Initial DO1

2.5.3 Procedure for the Measurement of Chemical Oxygen Demand(COD)

Chemical Oxygen Demand were determined using open reflux. 50.0 mL of each borehole water samples and distilled water (blank) were measured and transferred in a round bottom flask. 1g of Mecuric sulphate (HgSO4) and 25.0 mL K2Cr2O7 (0.00417M) were added and mixed. This was followed by slow addition of 75ml of Concentrated Tetraoxosulphate (vi) acid to the mixture. It was then heated at reflux for 2 hours and allowed to cool. The cooled solution was diluted with 350 ml distilled water and then cooled to room temperature. Then the excess Potassium dichromate (K2Cr2O7) in it was determined by titrating with 0.25 M Ferrous ammonium sulfate (FAS) using Ferroin indicator. A blank determination as above was done using 50ml of distilled water. (APHA, 2017;. U.S. EPA, 1983; Sawyer et al., 2003; Ovonkimwen, 2020).

The Chemical Oxygen Demand (COD) were calculated, thus:

$$\text{COD (mg/L)} = \frac{(\mathbf{A-B}) \times \mathbf{M} \times \mathbf{8000}}{\textbf{Volume of the sample (ml)}}$$

Where: A = mL of Ferrous ammonium sulphate (FAS) used for the blank; B = mL of FAS used for the sample;

M = Molarity of the FAS. :

2.5.4 Procedure for the Determination of Total Suspended Solids (TSS)

Total Suspended Solids (TSS) were obtained gravimetrically by filtration. An aliquot (100ml) of the water sample was filtered through dried pre-weighed 0.45 filter paper placed in a Buchner funnel. After wards, the filter paper was over dried at 1050c for one hour. Then the filter paper was cooled and weighed. The difference in filter paper weight before and after was used to calculate the total suspended solid. (APHA, 2017; U.S. EPA, 1979; Sawyer et al., 2003; Arafat et al., 2021).

The Total Suspended Solids (TSS) were thus:

TSS (mg/L) = (final wt - initial wt) × 1000 / amount of the sample taken.

2.5.5 Procedure for the Determination of Total Dissolved Solids (TDS)

Total Solids (TS) and Total Suspended Solids (TSS) were determined before calculating Total Dissolved Solids (TDS). A 100 mL borehole water sample was evaporated in a dish over a water bath. The residue was dried at 106 °C in an oven, cooled, and weighed. This process was repeated twice to achieve a constant weight. The difference in weight before and after drying gave the TS value. TDS was calculated by subtracting TSS from TS. (APHA (2017);U.S.EPA (1979)).

The Total Dissolved Solids (TDS) were calculated thus:

TDS (mg/L) = Total Solids (TS) - Total Suspended Solids (TSS):

2.6 Statistical Analysis

The Mean, Standard deviation, Analysis of variance (ANOVA) and Pearson's Correlation Coefficient Analyses were conducted. Significant differences in Heavy metals and Physicochemical parameters were compared using Duncan Multiple Range Test (DMRT), a post - ANOVA method for identifying which group means differ significantly. Differences were indicated using superscripts (a, b, etc.) in Table 1. The results showed no significant relationship ($p > 0.05$) between Heavy metals and Physicochemical parameters across all sites, except for electrical conductivity, which showed a significant correlation. (Table 1).

Table 1. Mean ± Standard Deviation of Heavy metals and Physicochemical parameters in and around a tertiary institution in Akoka Area of Lagos - State, Southwestern - Nigeria.

Location/ Site	pH	TEMP (°C)	Zn (mg/L)	Cd (mg/L)	Pb (mg/L)	TDS (mg/L)	TSS (mg/L)	EC (µS/cm)	DO (mg/L)	BOD (mg/L)	COD (mg/L)
CH	5.04±3.35^{a}	29.40±13.51^{a}	0.15±0.15^{a}	0.02±0.01^{a}	2.99±1.61^{a}	162.00±159.35^{a}	0.01±0.012^{a}	323.00±176.35^{b}	4.36±1.20^{a}	0.91±1.11^{a}	3.72±1.57^{a}
MFO	5.30±3.23^{a}	30.10±12.01^{a}	0.12±0.15^{a}	0.02±0.01^{a}	2.78±2.62^{a}	187.10±158.40^{a}	0.01±0.006^{a}	366.67±168.81^{b}	4.41±1.13^{a}	0.38±0.52^{a}	2.84±1.15^{a}
MAH	5.88±2.73^{a}	28.97±13.25^{a}	0.13±0.12^{a}	0.06±0.12^{a}	1.83±1.68^{a}	106.18±87.92^{a}	0.01±0.005^{a}	254.00±166.29^{b}	4.58±1.75^{a}	0.47±0.42^{a}	3.32±1.34^{a}
MH	5.23±2.64^{a}	29.40±9.50^{a}	0.12±0.11^{a}	0.02±0.01^{a}	2.10±1.29^{a}	151.90±120.04^{a}	0.01±0.004^{a}	296.00±164.69^{b}	5.09±1.35^{a}	0.37±0.49^{a}	3.08±1.43^{a}
EH	6.06±2.96^{a}	29.47±10.79^{a}	0.13±0.16^{a}	0.02±0.00^{a}	3.01±1.47^{a}	177.10±149.41^{a}	0.02±0.019^{a}	339.33±223.94^{b}	4.71±1.95^{a}	0.86±0.97^{a}	2.48±1.53^{a}
HR	4.50±2.73^{a}	29.70±11.10^{a}	0.11±0.15^{a}	0.02±0.00^{a}	2.41±1.32^{a}	126.50±124.23^{a}	0.01±0.01^{a}	220.67±150.89^{b}	4.18±1.70^{a}	0.69±0.68^{a}	3.08±1.45^{a}
KD	6.13±2.35^{a}	29.40±11.89^{a}	0.11±0.09^{a}	0.02±0.01^{a}	3.44±2.10^{a}	277.20±235.08^{a}	0.03±0.026^{a}	876.00±506.08^{a}	4.47±1.59^{a}	0.91±0.98^{a}	5.24±1.81^{a}
AC	6.50±2.89^{a}	29.50±12.94^{a}	0.11±0.12^{a}	0.02±0.00^{a}	3.12±1.93^{a}	176.20±134.79^{a}	0.01±0.009^{a}	348.00±312.24^{b}	4.51±1.91^{a}	0.92±0.97^{a}	3.72±1.71^{a}
OH	5.12±3.03^{a}	29.20±11.51^{a}	0.11±0.13^{a}	0.02±0.01^{a}	3.37±2.02^{a}	319.10±233.93^{a}	0.02±0.019^{a}	484.33±330.93^{b}	4.60±1.36^{a}	1.10±1.01^{a}	4.84±1.94^{a}
OO	6.83±3.32^{a}	29.40±13.25^{a}	0.11±0.11^{a}	0.02±0.01^{a}	1.33±0.94^{a}	117.60±124.38^{a}	0.01±0.006^{a}	233.00±179.20^{b}	4.67±1.50^{a}	0.90±1.09^{a}	3.64±1.40^{a}
F-Statistics (p)	0.414 (0.934)	0.003 (1.000)	0.067 (1.000)	0.813 (0.617)	1.336 (0.235)	1.200 (0.312)	1.995 (0.052)	3.259 (0.002)	0.212 (0.994)	0.730 (0.693)	1.758 (0.091)

3. Results and Discussion

3.1 Heavy metals in Borehole water Sample

Copper (Cu) is an essential heavy metal that supports bodily functions but becomes toxic at high levels. It can enter drinking water from copper pipes, industrial waste, or algal control additives. Cu may cause nausea, vomiting, diarrhea, and liver or kidney damage at high concentrations (Peter and Funmilayo, 2016). In this study, Cu was not detected in any of the water samples, possibly due to the absence of copper-related anthropogenic activities in the sampling areas (Figure 1).

Zinc (Zn) was the least abundant Heavy metal in the analyzed water samples, with concentrations ranging from 0.1015 mg/L to 0.1489 mg/L and an average of 0.1199 mg/L. The highest concentration was recorded at Chapel (CH), while the lowest was at Onus Hostel (OH). All Zn concentrations were below the permissible limits set by WHO (2015) and NIS (2007), with no significant differences between the sites ($p > 0.05$). The high levels of Zn at CH may results from natural sources or anthropogenic activities, such as the use of fertilizers and wood preservatives. Zinc, though essential for human and plant health, can cause stomach pain, vomiting, fever, fatigue, and diarrhea at toxic levels (Hassan, 2016). At moderate levels, Zinc is generally non-toxic (Peter and Funmilayo, 2016). Zinc enters groundwater through industrial processes, including the galvanic and battery industries, or from Zinc-containing fertilizers (Gopi et al., 2023; Bux et al., 2022) (Table 2).

Nickel (Ni) was not detected in all the borehole water samples (Table 2), likely due to the absence of sources such as steel alloys, electroplating, batteries, electronics, and related industrial or household activities at the sampling sites (Rashid et al., 2021).

Cadmium (Cd) concentrations in the analyzed water samples ranged from 0.019 to 0.023 mg/L, with an average of 0.019 mg/L. EH has the highest Cd levels, while MAH had the lowest (Table 2). All borehole water samples in the study sites have average values exceeding the maximum permissible limit for Cd in drinking water (WHO, 2015; NIS, 2007).

Table 2. Average Mean Concentration of Heavy metals and Physicochemical parameters of Borehole Water in and around a tertiary institution in Akoka Area of Lagos - State, Southwestern - Nigeria.

S/N	SAMPLE CODE	pH	Temp	HEAVY METALS					TDS	TSS	EC	DO	BOD	COD
				Cu	Zn	Ni	Cd	Pb						
			°C	*mg/L*					*mg/L*	*mg/L*	µs/cm	*mg/L*		
1	**CH**	5.04	29.4	ND	0.1489	ND	0.022	3.16	162.0	0.011	323	4.36	0.91	3.72
2	**MFO**	5.30	30.1	ND	0.1192	ND	0.020	2.90	187.1	0.008	370	4.41	0.38	2.84
3	**MAH**	5.88	29.3	ND	0.1281	ND	0.019	1.85	106.2	0.007	254	4.58	0.42	3.32
4	**MH**	5.23	29.4	ND	0.1175	ND	0.020	2.18	151.9	0.006	306	5.09	0.47	3.08
5	**EH**	6.06	29.5	ND	0.1321	ND	0.023	3.07	177.1	0.017	353	4.71	0.86	2.48
6	**HR**	4.50	29.7	ND	0.1094	ND	0.021	2.52	126.5	0.014	207	4.18	0.69	3.08
7	**KD**	6.13	29.4	ND	0.1131	ND	0.021	3.44	436.7	0.028	876	4.47	0.91	5.24
8	**AC**	6.50	29.5	ND	0.1222	ND	0.020	3.25	176.2	0.010	348	4.51	0.83	3.72
9	**OH**	5.12	29.2	ND	0.1015	ND	0.021	1.22	319.1	0.019	640	4.60	1.10	4.84
10	**OO**	6.83	29.4	ND	0.1062	ND	0.020	1.38	117.6	0.008	233	4.67	0.90	3.64
	MEAN	5.66	29.5	ND	0.1199	ND	0.019	2.50	196.04	0.013	391	4.56	0.75	3.60
	WHO, 2015	6.5 - 8.5	30- 32	2.00	5.00	0.02	0.003	0.01	500		<1000	5	6	10
	NIS, 2007	6.5 - 8.5	30 - 32	1.00	3.00	0.02	0.003	0.01	500		1000	3 - 5	1.34	32.0

ND = Not detected

The high concentration of Cd in the borehole water samples resulting from galvanized steel pipe corrosion, leaching of contaminated soil, or industrial discharges involving plastics and fertilizers in the study area may cause lung damage, severe stomach pain, vomiting, and diarrhea (Yusuf et al., 2018). There were no significant variation in Cd concentrations across the study sites ($p > 0.05$).

Lead (Pb) was the most abundant Heavy metal in the analyzed water samples, with concentrations ranging from 1.22 to 3.44 mg/L and an average of 2.50 mg/L. The highest level was recorded at KD (3.44 mg/L), while the lowest was at OH (1.22 mg/L) (Table 2). All the borehole water samples have the Pb levels exceeding the maximum allowable limits set by WHO (2015) and NIS (2007), indicating serious contamination (Table 2). The high concentrations of Pb resulting from nearby mechanic workshops and fuel leakage from cars and generators could be due to anthropogenic activities such as traffic congestion, vehicle emissions, and leaching of Pb - containing waste into groundwater(Figure 2). There is no significant differences in Pb concentrations across the study sites ($p > 0.05$).

Lead exposure poses serious health risks, including cancer, nervous system damage, and brain disorders (Yusuf et al., 2017).(Figure 1). High exposure may also lead to anemia, muscle weakness, and stomach pain (Alani et al., 2014). Even at lower levels, Pb can harm children's mental and physical development, causing learning disabilities and seizures. The findings underscore the need for urgent water treatment and regulation of lead - emitting activities in the study area. The high concentrations of Pb, Zn, and Cd in the borehole water samples indicate significant contamination. In contrast, the absence of Cu and Ni suggests minimal sources or the water's inability to retain these metals. While Cu and Ni were not detected, the concentrations of Pb, Zn, and Cd were comparable to values reported in previous studies in different cities/locations of the world, with Pb being higher (Table 3). Although, the Physicochemical parameters in the study area fall within WHO (2015) and NIS (2007) permissible limits, the values were generally lower than those reported in similar studies from other cities or locations in the world. (Table 4).

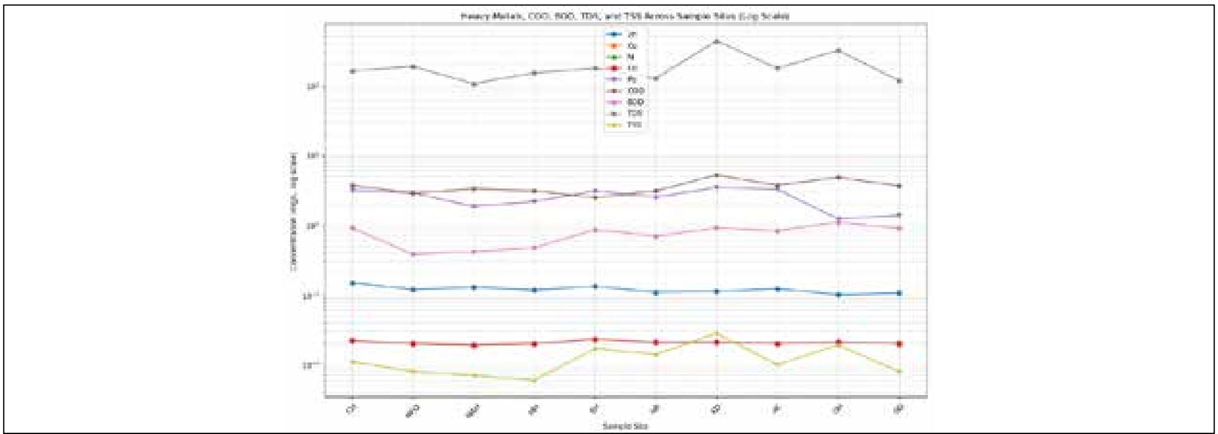

Figure 2. Line graph Showing the Concentrations of heavy metals and physicochemical parameters in the study Area.

Table 3. Data of Heavy metals in Borehole water in previous studies in different cities/locations of the world.

Heavy metals(mg/L)	Sample location										WHO permutable range	Previous studies / References
	CH	MFO	MAH	MH	EH	HR	KD	AC	OH	OO		
Cu	ND	ND	ND	ND	ND	ND	ND	ND	ND	ND	2.00	**ND -Not Detected - Present Study** 0.18 - 0.44 - Popoola et al., 2019. 8.04 - 24.0 - Ezeribe et al., 2012. 0.012 - 0.176 - Behailu et al., 2017. 0.26 - 0.38- Adefemi and Awokunmi,2010.
Zn	0.1489	0.1192	0.1281	0.1175	0.1321	0.1094	0.1131	0.1222	0.1015	0.1062	5.00	**0.1015 - 0.1489 - Present Study** 0.182 - 0.911 - Popoola et al., 2019. 0.001 - 1.054 - Birke et al., 2010. 5.692 - 12.421 - Fakayode, 2005.
Ni	ND	ND	ND	ND	ND	ND	ND	ND	ND	ND	0.02	**ND - Not Detected - Present Study** 0.006 - 0.49 - Dinakaron et al., 2021. 0.019 - 0.04 -Tadiboyina and Prasada, 2016)
Cd	0.022	0.020	0.019	0.020	0.023	0.021	0.021	0.020	0.021	0.020	0.003	**00.019 - 0.023 - Present Study** 0.000 - 0.0025 - Popoola et al., 2019. 0.013 - 0.026 - Shigut et al., 2017. 0.000 - 0. 006 - Dinakaran et al., 2021
Pb	3.16	2.90	1.85	2.18	3.07	2.52	3.44	3.25	1.22	1.38	0.01	**1.22 - 3.44 - Present Study** 0.082 - 0.374 - Popoola et al., 2019. 0.071 - 0.122 - Faisal et al., 2014. 0.068 - 0.103 - Saddozai et al., 2009. 0.001 - 0.002 - Eruola and Adedokun , 2012.

ND = Not detected

Table 4. Data of Physicochemical parameters in Borehole water in previous studies in different cities/locations of the world.

Physico-chemical	Sample Locations										WHO permutable range	Previous studies / References
Properties	CH	MFO	MAH	MH	EH	HR	KD	AC	OH	OO		
pH	5.04	5.30	5.88	5.23	6.06	4.50	6.13	6.50	5.12	6.83	6.5 - 8.5	**4.50 - 6.83 - Present Study** 6.35 - 8.31 - Popoola et al., 2019. 6.10 - 6.77 - Oyem et al., 2014. 5.80 - 7.50 - Edwin et al., 2016. 5.57 - 8.00 - Ayodeji et al., 2017.
T °C	29.4	30.1	29.3	29.4	29.5	29.7	29.4	29.5	29.2	29.4	30 - 32°C	**29.2 - 30.1 - Present Study** 18.90 - 29.37- Okeke et al., 2021.
TDS (mg/L)	162	187.1	106.2	151.9	179.1	126.5	436.7	176.2	319.1	117.6	500.00	**106.2 - 436.7 - Present Study** 247.5 - 589.7 - Popoola et al., 2019. 390 - 1756.67 - Behailu et al., 2017. 166 - 184 - Ezeribe et al., 2012. 450 - 1350 - Buridi and Gedala, 2014.
TSS (mg/L)	0.011	0.008	0.007	0.006	0.017	0.014	0.028	0.010	0.019	0.008		**0.006 - 0.028 - Present Study** 0.01 - 0.02 Igbemi et al, 2019
E_C (µs/cm)	323	370	254	306	353	207	876	348	640	233	<1000	30.15 - 109.33 Odu et al, 2020 **207 - 876 - Present Study** 450 - 1190 - Popoola et al., 2019. 42.69 - 320 - Okoro et al., 2012. 333 - 1527 - Ikeme et al., 2014. 566.33 - 627.33 - Shigut et al., 2017.
BOD (mg/L)	0.91	0.38	0.42	0.47	0.86	0.69	0.91	0.83	1.10	0.90	6	**0.38 - 1.10 - Present Study** 1.20 - 4.30 - Popoola et al., 2019. 4.70 - 8.90 - Obi and Okocha, 2007. 1.60 - 5.0 - Adefemi and Awokunmi, 2010.
COD (mg/L)	3.72	2.84	3.32	3.08	2.48	3.08	5.24	3.72	4.84	3.64	10	**2.48 - 5.24 - Present Study** 5.90 - 9.00 - Amaria, 2015 51.0 - 93.0 - Oyem et al., 2014 37.0 - 49.0 - Patil and Patil, 2010. 7.0 - 28.0 - Eid, 2019.
DO (mg/L)	4.36	4.41	4.58	5.09	4.71	4.18	4.47	4.51	4.60	4.67	5	**4.18 - 5.09 - Present Study** 6.48 - 7.15 - John et al, 2024. 6.6 - 7.5 - Adeogun et al, 2019.

The variations in heavy metal levels and Physicochemical parameters when compared with previous studies in different cities/locations of the world may be due to differences in human activities (waste burning/dumping), environmental policies, and technology use. The distribution pattern of heavy metals in the sampled borehole water follows the order: Pb > Zn > Cd, with mean concentrations of 2.50, 0.1199, and 0.019 mg/L respectively. Kosoko Drive (KD) (3.57 mg/L) was the most polluted site, while Onos Hostel (OH) (1.34 mg/L) was the least (Figure 3). The high pollution levels in KD may result from vehicular emissions and mechanic workshops, releasing metal particles and petroleum products into the environment. The trend and Percentage contribution of each site to pollution are as follows: KD > AC > CH > EH > MFO > HR > MH > MAH > OO > OH (Figure 4). There were significant differences in heavy metal levels across the sites ($p < 0.05$). These findings align with similar studies by Okorie et al., 2024; Igbemi et al., 2019; Popoola et al., 2019; Opaluwa et al., 2020; and Odu et al., 2020, confirming that anthropogenic activities significantly influence groundwater contamination.

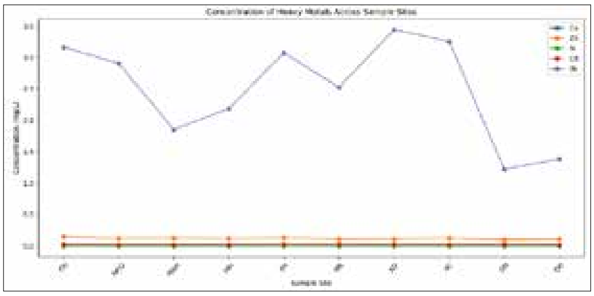

Figure 3. Line graph showing the distribution of heavy metals in the study area.

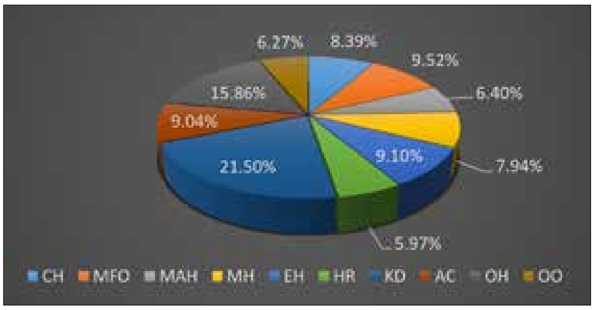

Figure 4. Percentage contribution of heavy metals and Physicochemical properties in each site.

3.2 Physicochemical Parameters of Borehole Water Sample

pH is a measure of the acidity or alkalinity of a solution, ranging from 0 to 14. In this study, borehole water pH ranged from 4.50 to 6.83, with an average of 5.66. The highest pH value was recorded at site OO, which was within WHO (2015) and NIS (2007) standards limits, while the lowest was at HR, falling below the acceptable limit (Table 2). Most water samples were acidic and below permissible limits, posing potential health risks. Acidic water can lead to the formation of carbonic acid in the body, making blood acidic and potentially harming health (Raji et al., 2019). There is no significant differences in pH values of the borehole water samples across the study sites ($p > 0.05$). The acidity of groundwater may be due to factors, such as increased temperature, high CO_2 concentrations from global warming, acidic soils, surrounding bedrock, and acid rain. Acidic conditions can also cause natural metals to dissolve, resulting in acid mine drainage and elevated metal concentrations in the water (Kitt, 2000).

Temperature is an important factor influencing metabolic activities, gas solubility, chemical reaction rates, and the distribution of aquatic organisms. In this study, borehole water temperatures ranged from 29.2°C to 30.1°C, with the highest value at MFO and the lowest at OH. These temperatures likely reflect the prevailing environmental and climatic conditions during sampling (Gebresilasie et al., 2021). All the borehole water temperature values were within the permissible limits set by WHO (2015) and NIS (2007). There was no significant difference in temperature across the study sites ($p > 0.05$). High water temperature will accelerate chemical reactions in aquifers, such as rock weathering, leading to the release of chemical contaminants. It can also reduce dissolved oxygen (DO) levels, potentially affecting aquatic ecosystems (Hassan et al., 2016; Maliki et al., 2020; Gebresilasie et al., 2021). Thus, monitoring temperature is essential for assessing water quality and its potential effects on both ecosystems and human health.

Total dissolved solids (TDS) are key indicators of drinking water quality. In the borehole samples, TDS ranged from 106.27 mg/L at MAH to 436.7 mg/L at KD, averaging 196.04 mg/L (Figure 5). High TDS may result from accumulated organic and inorganic solids, which can reduce water portability and cause gastrointestinal irritation or laxative effects. Therefore, the high TDS value in borehole water may be aesthetically displeasing for bathing and washing (Vincent, 2016). All TDS values in this study were within permissible limits set by WHO (2015) and NIS (2007), with no significant differences across sites ($p > 0.05$). TDS levels were consistently higher than total suspended solids (TSS) at all locations (Kaizer and Osakwe, 2010) (Figure 6). High TDS levels may indicate groundwater contamination from wastewater discharge into ponds and pits (Baloguru and Senthi, 2013).

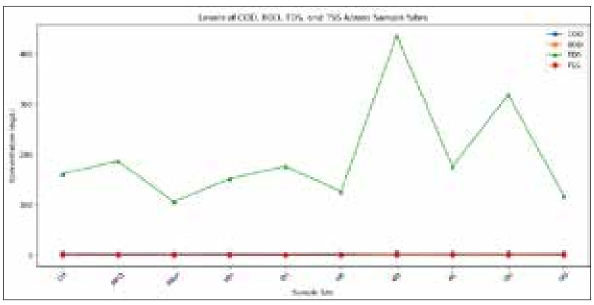

Figure 5. Line graph showing the distribution of Physicochemical parameters

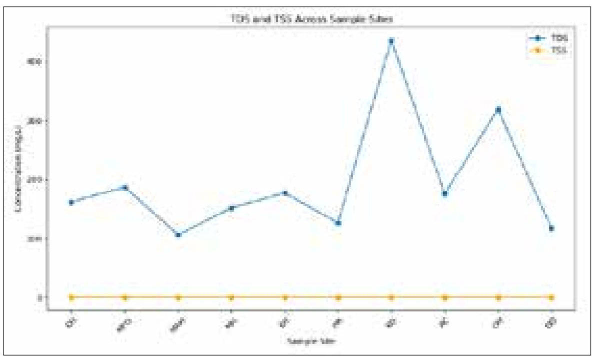

Figure 6. Line graph Showing the Levels of TDS and TSS in the Study Area

TSS is vital in determining water quality (Ndefo, 2011). It affects water clarity, so the higher the TSS value in a water source is, the lesser the clarity will be (WHO, 2017). The total suspended solids (TSS) values in the borehole water samples ranged from 0.006 mg/L at MH to 0.028 mg/L at KD, with an average value of 0.013 mg/L. In this study, the recorded results showed that TSS values were below the acceptable limit for drinking water quality(WHO, 2015; NIS, 2007). There is no significant difference in TSS levels in the study sites.($p > 0.05$).

Electrical conductivity (EC) measures water's ability to conduct electricity. It is determined by the presence of ionic species (Gebresilasie et al., 2021; Nriagu and Pacyna, 1988). Higher ion concentrations result in higher conductivity (Christine et al., 2018). EC values in this study ranged from 207 µS/cm at HR to 876 µS/cm at OH, averaging 391 µS/cm (Figure 7). All samples were within permissible limits set by WHO (2015) and NIS (2007) for drinking water. EC is directly related to total dissolved solids (TDS) because it reflects the ionic content of water, which determines its electrical conductivity (Figure 7). As TDS increases, ionic strength rises, causing higher EC values. High EC indicates contamination from dissolved ions, as EC is proportional to total dissolved solids (Gebresilasie et al., 2021). Monitoring EC helps assess water quality and detect possible pollution.

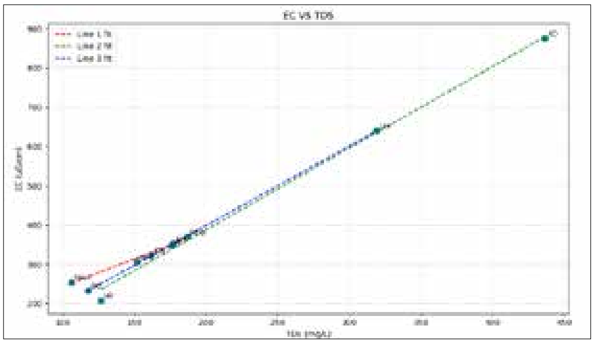

Figure 6. Line graph showing the relationship between EC against TDS

Dissolved oxygen (DO) is a key water quality indicator, reflecting contamination levels. Low DO suggests microbial contamination or chemical corrosion in the aquifer (Gebresilasie et al., 2021). DO concentrations ranged from 4.18 mg/L at HR to 5.09 mg/L at MH, averaging 4.56 mg/L. All the DO values in the borehole water samples were within acceptable limits (WHO, 2015; NIS, 2007) except at MH, which slightly exceeded the limit (Table 2). There was no significant difference in DO levels across all the sites ($p > 0.05$) (Table 1).

Biological oxygen demand (BOD) measures oxygen used by microorganisms to decompose organic matter, while chemical oxygen demand (COD) measures oxygen needed to oxidize both biodegradable and non-biodegradable materials. The BOD values in the borehole water samples ranged from 0.38 to 1.10 mg/L and COD from 2.48 to 5.24 mg/L, both were below permissible limits (WHO, 2015; NIS, 2007). There were no significant differences in BOD and COD levels across the study sites ($p > 0.05$) (Table 1).

3.3 Assessment of Pollution Status of Borehole Water Samples through Water Quality Indices

Water quality indices is a comprehensive tool used to assess water quality according to all metals present (Adano et al., 2023, Giri and Singh, 2014; Yadav et al., 2015).). To assess the pollution status, three water quality indices were applied this include: Heavy metals pollution index (HPI), Pollution index (PI), and Metal Index (MI).

3.3.1 Heavy Metal Pollution Index (HPI)

The Heavy Metal Pollution Index (HPI) is a ranking method used to assess the combined impact of individual heavy metals on overall water quality (Mohammed et al., 2014). The characterization of the borehole water from the study area with the use of the Heavy Metal Pollution index gives value to be compared with the critical value to evaluate the level of pollution (Yusuf et al., 2018) (Table 5).

Table 5. Mean of Heavy Metal Pollution of Borehole Water Samples in and around a Tertiary Institution in Akoka Area of Lagos - State, Southwestern - Nigeria.

S/N	Heavy metals	Mean Concentration MC (mg/L)	Highest Permissible value(Si), (NIS, 2007)	Unit weightage (Wi) Wi =	Sub index Qi =	Wi × Qi
1	Zinc (Zn)	0.11982	3.0	0.333	3.994	1.330
2	Cadmium(Cd)	0.0207	0.003	333.333	690	229999.77
3	Lead (Pb)	2.473	0.01	100	24730	2473000
4	Copper(Cu)	ND	ND	ND	ND	ND
5	Nickel	ND	ND	ND	ND	ND
HPI= $\frac{\sum Wi \times Qi}{\sum Wi}$ = 6232.91				$\sum$Wi=433.666		$\sum$Wi Qi =2703001.1

The mean HPI value was found to be 6232.91 which were far above the critical value of 100. This value indicates that the water from the study area is highly polluted with respect to Heavy metals and therefore unsuitable for consumption and domestic use.

3.3.2 Pollution Index (PI).

PI provides information on the relative pollution contributed by each sample. When the critical value is greater than 1.0. It shows a significant degree of pollution whereas value less than 1.0 indicates no pollution. The results showed high PI values for Cadmium (Cd) at 6.9 and Lead (Pb) at 247.3, both exceeding 1.0, indicating significant pollution (Ajiwe and Eboagu, 2021) (Table 6).

Table 6. Pollution Index (PI) of Borehole water Samples

S/N	Heavy metals	Mean Concentration	W.H.O Limit (2017)	PI = Concentration / Standard
1	**Zinc (Zn)**	0.11982	5.0	0.02
2	**Cadmium(Cd)**	0.0207	0.003	6.9
3	**Lead (Pb)**	2.473	0..01	247.3
4	**Copper (Cu)**	ND	ND	ND
5	**Nickel (Ni)**	ND	ND	ND
∑PI = 254.22				

In contrast, Zinc (Zn) had a pollution index of 0.02, suggesting no pollution. Since, the values of PI of Pb and Cd were above 1.0, suggesting that the borehole water samples if consume may cause serious health risks because the higher the values of PI, the higher the rate of the hazard risk on the human body (Girl and Singh, 2015).

3.3.3 Metal index (MI)

The Metal Index (MI) assesses the impact of heavy metals on human health and overall drinking water quality (Caeiro et al., 2005). The higher the concentration of a metal is when compared to its respective MAC value, the worse the quality of water will be. MI value > 1 is a threshold of warning (Yusuf et al., 2018). The MI values for Zn, Cd, and Pb are 0.02, 6.9 and 247.3 respectively, while Ni and Cu were not detected. The MI values for the Heavy metals showed that the water is seriously polluted with Pb and Cd. MI for the study area indicates low quality water with value 254.2 (Table 7). Therefore, the borehole water samples in the study area are considered unsafe for consumption and domestic use (Caerio et al., 2005).

Table 7. Metal index (MI)

S/N	Heavy metals	Mean^5 Concentration MC	Highest Permitted Limit (WHO, 2017)	$MC = \frac{MC}{HPI}$
1	**Zinc (Zn)**	0.11982	5.0	0.02
2	**Cadmium (Cd)**	0.0207	0.003	6.9
3	**Lead (Pb)**	2.473	0.01	247.3
4	**Copper (Cu)**	ND	ND	ND
5	**Nickel (Ni)**	ND	ND	ND
∑MI = 254.2				

Table 8. Water Quality Classification using MI (Caerio et al., 2005)

Metal index (MI)	Characteristics	Class
< 0.3	Very pure	1
0.3 – 1.0	Pure	11
1.0 – 2.0	Slightly affected	111
2.0 – 4.0	Moderately affected	1V
4.0 – 6.0	Strongly affected	V
>6.0	Seriously affected	VI

3.4 Correlation Coefficient Analysis.

Pearson's significant correlation analysis was employed to evaluate the relationship between the concentrations of heavy metals and physicochemical parameters in and around a tertiary institution in Akoka area of Lagos-State. The correlation coefficient values range from 0.052 to 0.946. There is a positive significant relationship between each of the heavy metals ($p < 0.05$) (Kaizer and Osakwe (2010); Zhang et al. (2021). Similarly, there is a positive significant relationship between each of physicochemical parameters ($p < 0.05$)(Orebiyi et al. (2022). Generally, here is positive significant relationship between the heavy metals and physicochemical parameters ($p < 0.05$) (Table 9).

Table 9. Correlation Coefficient Analysis of the heavy metals and physicochemical parameters in Borehole Water in and around a tertiary institution in Akoka Area of Lagos - State.

	pH	Temp (°C)	Zn (mg/L)	Cd (mg/L)	Pb (mg/L)	TDS(mg/L)	TSS(mg/L)	EC(µS/cm)	DO(mg/L)	BOD(mg/L)	COD(mg/L)
pH	1	.924** (<0.001)	.873** (<0.001)	.335** (<0.001)	.802** <0.001)	.707** (<0.001)	.592** (<0.001)	.579** (<0.001)	.881** (<0.001)	.780** (<0.001)	.794** (<0.001)
Temp (°C)		1	.946** (<0.001)	.389** (<0.001)	.823** <0.001)	.743** (<0.001)	.675** (<0.001)	.637** (<0.001)	.936** (<0.001)	.823** (<0.001)	.821** (<0.001)
Zn (mg/L)			1	.312* (0.011)	.810**(<0.001)	.754**(<0.001)	.648**(<0.001)	.563**(<0.001)	.910**(<0.001)	.804**(<0.001)	.745**(<0.001)
Cd (mg/L)				1	0.240(0.052)	0.181(0.145)	0.126(0.313)	0.186(0.134)	.365** (0.003)	0.052(0.680)	.251* (0.042)
Pb (mg/L)					1	.634** (<0.001)	.562** (<0.001)	.633** (<0.001)	.736** (<0.001)	.634** (<0.001)	.670** (<0.001)
TDS (mg/L)						1	.696**(<0.001)	.666**(<0.001)	.734**(<0.001)	.768**(<0.001)	.773**(<0.001)
TSS (mg/L)						.	1	.757** (<0.001)	.695** (<0.001)	.816** (<0.001)	.742** (<0.001)
EC (µS/cm)								1	.630**(<0.001)	.626**(<0.001)	.772*(<0.001)
DO (mg/L)									1	.802**(<0.001)	.778**(<0.001)
BOD (mg/L)										1	.794**(<0.001)
COD(mg/L)											1

4. Conclusion

Although the physicochemical parameters were below acceptable limits (WHO, 2015; NIS, 2007), Cu and Ni were absent, and Zn levels were within permissible limits. However, Pb and Cd levels exceeded the limits. Water quality indices (HPI, PI, MI) confirmed significant heavy metal pollution in borehole water samples in and around a tertiary institution in Akoka, Lagos, Nigeria. This indicates that the water is unsafe for consumption and domestic use. Additionally, the study showed the need to neutralize the borehole water, which is mostly consumed for drinking, due to its acidic nature.

Acknowledgements

Due acknowledgment is hereby given to the Management of Yaba College of Technology for the use of the College Central Research Laboratory.

References

Abiodun, O., and Madu, O. (2020). “The Role of Universities in Technology and Entrepreneurship Development in Lagos.” African Journal of Innovation and Technology, 22(1), 68 - 83.

Adano, A.J., Marcus, N. D., Magaji, J.I., and Opaluwa, O.D. (2023). “Assessment of Seasonal Variation in Heavy Metal Status of a Lotic Ecosystem in Federal Capital Territory, Abuja, North Central Nigeria,, Makara” Journal of Science: 27 (4).

Adefemi, S. O., Awokunmi, E. E. (2010). Determination of Physico-chemical parameters and Heavy metals in water samples from Itaogbolu area of Ondo - State, Nigeria. Afr. J. Environ. Sci. Technol. 4(3):145-148.

Adeniran, O. (2019). Economic Impact of Borehole Water in Urban Lagos: A Case Study of Akoka. Lagos: Lagos University Press.

Adeogun, O. Y., Adeoti, L., Jimoh, M. M., Adegbola, R. B., Oyeniran, T. A., Alli, S. A.(2019). Integrated Approach for Groundwater Assessment in Yetunde Brown, Ifako, Gbagada, Lagos State, Nigeria. J. Appl. Sci. Environ. Manage. 23 (4):593 - 602.

Adeyemi, A.(2017).Groundwater Resources and Sustainability in Lagos:Challenges and Opportunities. Lagos: Nigerian Water Resources Journal.

Adeyemi, A., and Ayodele, O. (2018). “The Role of University Libraries in Supporting Research and Academic Excellence in Nigerian Universities.” Library Management, 39(4), 255 - 269.

Afolayan, A., and Olumide, P. (2020). “Multiculturalism and Urbanization in Lagos: A Case Study of Ethnic and Cultural Diversity.” Nigerian Journal of Social Studies, 39(1), 112 -130.

Ajiwe, V.E., and Eboagu. N.C. (2021) “Health risk assessment of heavy metals contamination of ground water Nnewi in Nigeria”. Research square. 1 - 27.

Alani, R., Alo., B., and Ukoakonam, F.(2014). Preliminary investigation of the state of pollution of Ogun River at Kara Abattoir, Near Berger, Lagos. Int. J. Environ. Sci. Toxic., 2(2): 11- 23.

Aliyu, A.K., Birnin - Yauri, U.A., Umar, K.J., and Isa, S.A. (2018). “Assessment of Some Physicochemical Parameters and Heavy Metals in Ground Water From Sandy Areas of Argungu Emirate, Kebbi State, Nigeria”. Continental Journal of applied sciences. 13 (1):1 - 15.

Amaria, H. R. (2015). Assessment of Physicochemical quality of spring water in Arbaminch, Ethiopia. J. Environ. Anal. Chem. 2:157-163.

Anibueze, C. (2020). “The Importance of Academic

Collaborations in Lagos: Leveraging Networks for Research." Journal of Collaborative Research, 7(2), 25 - 39.

AOAC International (2000). Official Methods of Analysis, 17th Edition. Association of Official Analytical Chemists.

APHA (2017). Standard Methods for the Examination of Water and Wastewater, 23rd Edition. American Public Health Association, American Water Works Association, Water Environment Federation.

Arafat, R., Ishrat, J., and Yeasmin, N. J. (2021). "Assessment of Physicochemical properties of water and their seasonal variation in an urban river in Bangladesh". Water Science and Engineering. 14(2):139 - 148.

Ayodeji, A. S., Abubakar, S., Samuel, E. (2017). Physicochemical analysis of underground water in Zaria Metropolis, Kaduna State, Nigeria. Am. J. Chem. Eng. 5(6):158 - 162.

Baird, R.B., Eaton, A.D., and Rice, E.W. (Eds.) (2017). Standard Methods for the Examination of Water and Wastewater, 23rd Edition.

Balaguru, M., and Senthil Kumar, G. R. (2013). Groundwater quality impact assessment on lekkur sub basin using hych program: A case study from tamilnadu, India. International Journal of Current Research. 5(12): 3950 - 3956.

Behailu, T. W., Badessa, T. S., Tewodros, B. A. (2017). Analysis of Physical and Chemical parameters in groundwater used for drinking around Konso area, Southwestern Ethiopia. J. Anal. Bioanal. Tech. 8(5): 1 - 7.

Bharati, M., and Bhatnagar, A. (2018). "Assessment of Groundwater Quality Parameters and Contaminants in Urban Areas." Water Quality Reports, 15(2), 125 - 130.

Birke, M., Reimann, C., Demetriades, A., Rauch, U., Lorenz, H.(2010). Determination of major and trace elements in European bottled mineral water - analytical methods. J. Geochem. Explor. 107:217 - 226.

Buridi, K. R., Gedala, R. K. (2014). Study on determination of physicochemical parameters of groundwater in industrial area of pydibheema-varam, Vizianagaram District, Andhrapradesh, India. Austin. J. Public Health Epidemiol. 1(2):1 - 2.

Bux, R. K., Haider, S. I., Mallah, A., Solangi, A. R., Moradi, O., and Karimi - Maleh, H. (2022). "Spatial analysis and human health risk assessment of elements in ground water of District Hyderabad, Pakistan using ArcGIS and multivariate statistical analysis". Environmental Research. 11291.

Caerio, S., Costa, M. H., Ramos, T. B., Fernandes, F., Silveira, N., Coimbra, A and Painho, M.(2005). "Assessing heavy metal contamination in Sado Estuary sediment: An index analysis approach". Ecological Indicators 5: 155 - 169.

Christine, A. A., Kibet, J. K., Kiprop, A.K., and Were, M.L. (2018). "Assessment of Borehole water quality of Kakamega County, Kenya," Applied Water Science, 1(8): 47.

Dinakaran, J., Abbas, N.S., Shvetambri, A., Sujata, B., and Babeeta, C.K. (2021). "Assessment of Heavy Metals in Ground Water of Different Locations of National Capital Region, Delhi, India". Current World Environment. 16 (1); 143 -.150.

Dissmeyer, G. E.(2000). Drinking water from Forests and Grasslands, South Research Station, USDA Forest Service, Ashville, NC, USA.

Edwin, N., Ibiam, U. A., Igwenyi, I.O., Ude, V.C., Eko, S.N. (2015). Evaluation of physicochemical properties, mineral and heavy metal content of drinking water samples in two communities in South-East, Nigeria: A puplic health implication. J. Environ. Earth Sci. 5(9): 89 - 94.

Eid, B. I.(2017). Physicochemical properties and the concentration of anions, major and trace elements in groundwater, treated drink-ing water and bottled drinking water in Najran area, KSA. Appl. Water Sci. 7: 401 - 410.

Eruola, A. O., Adedokun, N. A. (2012). Analytical assessment of cadmium, lead and iron in hand dug wells of Ilaro, South Western Nigeria. Glob. J. Sci. Front Res. Chem. 12(6): 23 - 29.

Ezeribe, A. I., Oshieke, K. C., Jauro, A. (2012). Physicochemical properties of well water samples from some villages in Nigeria with cases of stained and mottle teeth. Sci. World J. 7(1):1 - 3.

Fakayode, S. O. (2005). Impact of industrial effluents on water quality of the receiving Alaro River in Ibadan, Nigeria. Ajeam Ragee. 10. 1 - 13.

Gebresilasie, K. G., Berhe, G. G., Tesfay, A.H.,and Gebre, S. E. (2021). "Assessment of Some Physicochemical Parameters and Heavy Metals in Hand - Dug Well Water Samples of Kafta Humera Woreda, Tigray, Ethiopia". International Journal of Analytical chemistry 9.

Giri, S.I., and Singh, A..K. (2014). "Assessment of Surface water quality using heavy metal pollution index in Subarnarekha River, India". Water Quality Exposure and Health (London). 5(4) :173 - 182.

Girl, S.I., and Singh, A. K.(2015). "Human health risk and ecological risk assessment of metals in fishes, shrimps and sediments from a tropical River".International Journal of Environmental Science Technology, 12, 2349 - 2362.

Gopia, C., Edward, A., Charlesa, A., Manivannanb, C., lakshmia, S., Jose, A., Muthiyan, M.(2023). "Physicochemical and Trace Metal Analysis in Groundwater of Nagapattinam Region in Nagapattinam District of Tamilnadu State" Journal of the Nigerian society of Physical sciences. 5(2): 1160.

Hassan, A.A.(2016). "Qualitative assessment of pollution Indices for heavy metals of the drinking water in Kirkuk, City, Northern Iraq". Journal of Environment and Earth Sciences 6(9): 2225 - 0948.

Hassan, M. R., Khan, M. Z. H., Khan, M., Aktar, S., Rahman, M., Hossain, F., and Hasan, A. S. M. (2016). "Heavy metals distribution and contamination in surface water of the Bay of Bengal coast". Cogent Environmental Science 2:1 - 12.

Igbemi I. A., Nwaogazie, I. L., Akaranta, O., Abu, G. O. (2019). Water Quality Assessment by Pollution Indices in Eastern Obolo Coastline Communities of Nigeria. American Journal of Water Resources, 7(3) : 111-120.

Ikeme, C. H., Dioha, I. J., Olasusi, K. A., Chukwu, P. U. (2014). Physicochemical analysis of selected borehole water in Umuihi, Town Imo State, Nigeria. Int. J. Sci. Eng. Res. 5(8): 680 - 689.

John, S.O.O., Olukotun, S. F., Kupi, T. G., Mathuthu, M.(2024). Health risk assessment of heavy metals and physicochemical parameters in natural mineral bottled drinking water using ICP - MS. in South Africa. Applied Water Science. 14: 202.

Kaizer, A. N., and Osakwe, S. A. (2010). Physicochemical characteristics and heavy metal levels in water samples from five river systems in Delta state, Nigeria. Journal of Applied Science and Environmental Management, 14(1): 83 - 87.

Khan, A., and Hanjra, M.(2009). "Effects of Pollution on Groundwater Quality in Urban Areas of Developing Countries." Environmental Monitoring and Assessment, 15(4): 333 - 340.

Kitt, F. P. (2000). Water Quality and Monitoring. Master Watershed Steward, Connecticut Department of Environmental Protection, 1 - 1.

Krishan, G. (2019). "Groundwater Salinity". Current World Environment. 14(2): 186 - 188.

Lagos State Ministry of Water Resources.(2020). Groundwater Management and Policy in Lagos: Challenges and Solutions. Lagos: Lagos State Government.

Lu, S. Y., Zhang, H. M., Sojinu, S.O., Liu, G. H., Zhang, J. Q., and Ni, H. G. (2015). Trace elements contamination and human health risk assessment in drinking water from Shenzhen, China. Environ. Monit. Assess. 2015.

Maliki, M., Inobeme, A., Kelani, T. and Eziukwu.(2020). "Physicochemical and Heavy Metals Analysis of Water from different Sources in Usen, Edo State, Nigeria". International Organization of Scientific Research - Journal of Applied Chemistry. 1(13): 34 - 37.

Mkadmi, Y., Benabbi, O., Fekhaoui, M., Benakkam, R., Bjijou, W., Elaz-zouzi, M., Kadourri, M., Chetouani, A. (2018). Study of the impact of heavy metals and physicochemical parameters on the quality of the wells and waters of the Holcim area (Oriental region of Morocco). J. Mater. Environ. Sci. 9(2) : 672 - 679.

Mohammed, A.G., Singh, G.P.,Olasehinde,A., and Saidu, A.D. (2014). "Study of the Physicochemical Characteristics of Groundwater in Michika Town and Environs. Northeastern, Nigeria".

Nawab, J., Khan, S., Khan, M.A., Sher, H., Rehamn, U. U., Ali, S., and Shah, S.M.(2017). Potentially toxic metals and biological contamination in drinking water sources in Chromite mining - impacted areas of Pakistan: a comparative study. Expo Health. 9 : 275 - 287.

Nigerian Industrial Standard (NIS) (2007). Nigerian Standard for Drinking Water Quality. Approved by the Standard Organization of Nigeria (SON) Governing Council. 14 - 18.

Nkpa, K. W., Amadi, B. A., and Wegwu, M. O. (2018). Hazardous metals levels in groundwater from Gokana, Rivers State, Nigeria. Non - Cancer and cancer health risk assessment. Human and Ecological Risk Assessment. An International Journal, 24(1): 214 - 224.

Nnaji, A.O., Idam, J. O., and Njoku, R. E. (2016). Assessment of variations in the concentration of heavy metals in groundwater within oil - producing communities of Rivers State Nigeria. Journal of Public Health & Environment Pollution, 1(1): 1-13.

Nriagu, J. O., and Pacyna, J. M. (1988). Quantitative assessment of worldwide contamination of air, water and soils by trace metals. Nature, 333 (6169), 134 -139.

Obi, C.N., and Okocha, C.O. (2007). Microbiological and physicochemical analysis of selected borehole waters. J. Eng. Appl. Sci. 257: 920 - 929.

Odu, N. N.,Omunakwe, A. L., and Millicent, M.(2020). Comparative Assessment on the Physicochemical Water Quality of Wells and Boreholes in Two Rivers State Communities, Nigeria. International Journal of Research Studies in Microbiology and Biotechnology (IJRSMB). 6(3) : 5 - 20.

Okeke, O.O., Jonathan, C.I., and Victor, C.E. (2021). "Determination of the levels of heavy metals and Physicochemical properties of borehole water within selected mining sites in Ebonyi State, Nigeria". Health Environment. 3(1): 162 - 168.

Okorie, M. N., Okechukwu, V. U., Omokpariola, ·D. O. (2024). Physicochemical properties and health risk assessment of selected heavy metals from soil and borehole water in Ifite-Awka, Anambra State, Nigeria. Discover Applied Sciences. 6:108. https://doi.org/10.1007/s42452-024-05767-8.

Okoro, H.K., Adeyinka, A., Jondiko, O. E., Ximba, B. J. (2012). Physicochemical analysis of selected groundwater samples of Ilorin town in Kwara State, Nigeria. Sci. Res. Essays, 7(23): 2063 - 2069.

Okunade, E., and Olamide, S. (2017). "The Impact of University Students on the Social and Economic Life of Lagos." International Journal of Sociology and Anthropology, 45(3), 193 - 203.

Olawole, A. (2015). Urban Water Supply and Groundwater Use: A Case Study of Akoka. Lagos: Lagos State University Press.

Olayemi, A., and Alabi, A. O.(2012). Assessment of Groundwater Quality in Lagos State, Nigeria. Water Quality Research Journal of Canada, 47(3): 307 - 317.

Oloyede, O., and Abiola, K. (2022). "Research Collaboration and Innovation in Nigerian Universities." African Research Journal, 8(3) : 119 -134.

Opaluwa, O.D., Mohammed, Y., Mamman, S., Ogah, A. T., and Danjuma Ali, D.(2020). Assessment of Water Quality Index and Heavy Metal Contents of Underground Water Sources in Doma Local Government Area, Nasarawa State, Nigeria. Asian Journal of Applied Chemistry Research. 6(3): 27- 40.

Orebiyi, E.O., Gbadebo, A.M., Taiwo, A.M., Idowu, O.A.(2022). Multivariate Analysis of Physico-chemical Parameters of Groundwater from Selected Communities in Yewa North Local Government Area of Ogun State, Southwestern, Nigeria. Science and Technology Publishing (SCI & TECH) ISSN: 2632 - 1017. 6(3):1096 - 1112.

Ovonramwen, O.B. (2020)."Physicochemical Analysis of Surface and Ground Water in Ugbomro and Iteregbi, Delta State, Nigeria". Journal of Applied. Science and. Environmental. Management. 24 (3): 511- 517.

Oyem, H.H., Oyem, I. M., Ezeweali, D. (2014). Temperature, pH, electrical conductivity, total dissolved solids and chemical oxygen demand of groundwater in Boji-Boji Agbor / Owa area and immediate suburbs. Res. J. Environ. Sci. 8(8): 444 - 450.

Patil, V. T., and Patil, R. R (2010). Physicochemical analysis of selected groundwater samples of Amalner Town in Jalgaon District, Maharashra, India. E. J. Chem., 7(1):111-116.

Perpetual, E., Jimoh, W., Abdulrahman, A., and Shuibu, Y.(2022)."Determination of Physicochemical Parameters of Water Samples in Active War Zones of Borno State, Nigeria" Nigerian Research Journal of Chemical Sciences 10(1): 1 - 24.

Peter, O.O., and Funmilayo, I.O.(2016). Assessment of some Heavy Metals in Groundwater. Department of Science Laboratory Technology, Federal College of Animal Health and Production Technology, Moor Plantation, Ibadan, Nigeria. 12 (3):1 - 7.

Popoola, L. T., Yusuff, A. S., Aderibigbe, T. A.(2019). Assessment of natural groundwater physicochemical properties in major industrial and residential locations of Lagos metropolis. Applied Water Science, 9 (191), 1 - 10.

Priti and Paul, (2016). "Assessment of heavy metal pollution in water resources and their impacts": A review. Journal of Basic and Applied Engineering Research. 8(3): 671- 675.

Rahmanian, N., Ali., S.H., Homayoonfard, M., Ali, N.J., Rehan, M., Sadef, Y., and Nizami, S. (2015). "Analysis of physiochemical parameters to evaluate the drinking water in the state of Perak, Malaysia". Journal of Chemistry, 1-10.

Raji, W.A., Anih, C.E., Obeta, P.O. (2019). "Assessment of Physicochemical Properties and Heavy metals in Borehole Water For Drinking In Okada Town, Edo State, Nigeria". Journal Applied Sciences and Environmental Management, 23 (12): 2205 - 2209.

Saddozai, A. A., Khalil, S., Hameed, T. (2009). Microbial quality of food snakes and drinking water in islamabad schools and colleges. Pak. J. Agric. Res. 22 (3 - 4): 144 - 149.

Saheed, A. G., Abimbola, T.O., and Azeem, A.A. (2021). "Assessment of heavy metals contamination and associated risks in shallow ground water sources from three different residential areas within Ibadan metropolis, southwest, Nigeria". Applied water Science. 11, 81.

Sawyer, C.N., McCarty, P.L., and Parkin, G. F. (2003). Chemistry for Environmental Engineering and Science, 5th Edition. McGraw - Hill.

Schaeffer, A., and Frantzen, K. (2001). "Groundwater Quality and Contamination Sources in Urban Areas." Journal of Environmental Management, 12(2) : 191 - 205.

Shigut, D. A., Liknew, G., Irge, D. D., Ahmad, T. (2017). Assessment of Physicochemical quality of borehole and spring water sources supplied to Robe Town, Oromia Region, Ethiopia. Appl. Water Sci. 7:155 -164. https://doi.org/10.1007/

s13201-016-0502 - 4.

Singh, R., Singh, S., Parihar, P., Singh, V.P., Prasad, S.M.(2015).“Arsenic contamination, consequences and remediation techniques: a review”. Ecotoxicology and Environmental Safety, 112, 247 - 270.

Singh, S., Ambawat, S. (2020). “Microbial diversity analysis and bioremediation to evade heavy metal toxicity”. International Journal of Chemical Studies 8(4): 3269 - 3274.

Tadiboyina and Rao ptsrk, (2018). “Trace Analysis of heavy metals in ground waters of Vijayawada Industrial Area”. International Journal of Environmental and Science Education. 11(10): 3215-3229.

Talabi, A.O.,and Kayode, T. J.(2019) “Groundwater pollution and remediation”. Journal of Water Resource and Protection 11, 1-19.

Tchounwou, P. B., Yedjou, C. G., Patlolla, A. K., and Sutton, D. J. (2012). Heavy metal toxicity and the environment. Mol. Clin. Environ. Toxicol. 101, 133 - 164.

Tiwari, A. K., Singh, A. K., Singh, A. K., Singh, M. P.(2015) Hydrogeochemical analysis and evaluation of surface water quality of Pratapgarh District. Appl Water Sci Uttar Pradesh. https://doi.org/10.1007/s13201-015-0313-z.

Uche, E., and Bakare, B.(2021). “Research and Local Development: The Role of Universities in Lagos State.” Urban Development and Policy Journal, 35(3), 200 - 215.

University of Lagos. (2018). Annual Report on Water Usage and Sustainability in Akoka. Lagos: University of Lagos, Press.

U.S.EPA.(1979).Methods for Chemical Analysis of Water and Wastes, EPA-600/4-79-020. Gravimetric procedures for measuring TS, TSS, and TDS in water samples.

U.S. EPA. (1983). EPA Method 410.2: Chemical Oxygen Demand (COD), Dichromate Reflux Method. Environmental Monitoring and Support Laboratory, Office of Research and Development, U.S. Environmental Protection Agency.

Vincent, J. (2016). “Physicochemical Analysis of Ground Water Municipal Solid Waste Dumping Sites in Arumuganeri Thoothukudi District, Tamilnadu, India”. Green Chemistry & Technology Letters 2(1): 35-37.

WHO. (2011). Guidelines for Drinking Water Quality, 4th ed., Acceptability aspects: taste odour and appearance, Geneva Switzerland. pp. 1-541.

WHO.(2015). Section 1: Managing the quality of drinking water sources. In: Schmoll, O., Howard, G., Chilton, G. (eds). Protecting groundwater for health. Managing the quality of drinking water. IWA Publishing for World Health Organization, Geneva.

WHO. (2017). Guidelines for drinking-water quality: Fourth edition incorporating the first addendum. Geneva:

Yadav, K. K., Gupta, N., Kumar, V., Sharma, S., Arya, S. (2015). “ Water quality assessment of Pahuj River using water quality index at Unnao Balaji, MP, and India”. The International Journal of Sciences: Basic and Applied Research. 19 (1): 241-250.

Yusuf, A.A., Olasehinde, M. N., Mboringong, R.,Tabele, P., and Daniel, E.P. (2017). Evaluation of Heavy Metals Concentration in Groundwater around Kashere and its Environs, Upper Benue Trough, Northeastern Nigeria. Global Journal of Geological Science. 16: 25-36.

Yusuf, A., Olasehinde, A., Mboringong, M. N., Tabale, R.P. and Daniel, E.P. (2018). “Evaluation of heavy metals concentration in ground water around Kashere and its environs, upper Benue trough, Northeastern Nigeria”. Global Journal of Geological Sciences 16: 25-36.

Zhang, X., Zhao, X., Li, R., Mao, G., Tillotson, M. R., Liao, X., Zhang, C., and Yi, Y. (2020). Evaluating the vulnerability of physical and virtual water resource networks in China’s megacities. Resources, Conservation and Recycling, 161, 104972.

المملكة الأردنية الهاشمية

صندوق دعم البحث العلمي والابتكار

الجامعة الهاشمية

المجلة الأردنية لعلوم الأرض والبيئة

JJEES

مجلة علمية عالمية محكمة

المجلد (١٧) العدد (٣)

https://jjees.hu.edu.jo/

ISSN 1995-6681

المملكة الأردنية الهاشمية
صندوق دعم البحث العلمي
الجامعة الهاشمية

JJEES

المجلة الأردنية لعلوم الأرض والبيئة

المجلد (17) العدد (3)

مجلة علمية عالمية محكمة تصدر بدعم من صندوق دعم البحث العلمي

أيلول 2026
jjees.hu.edu.jo
ISSN 1995-6681